MICRON- TO SUB-MICRON-SCALE TRACE ELEMENT ZONATIONS IN ZIRCON AND OLIVINE

Thesis by

Amy Elizabeth Hofmann

In Partial Fulfillment of the Requirements for the Degree of

Doctor of Philosophy

CALIFORNIA INSTITUTE OF TECHNOLOGY

Pasadena, California

2010

(Defended May 25, 2010)

Chapter 1 (pages 11 – 58) reprinted

with kind permission from Springer Science + Business Media:

Contributions to Mineralogy and Petrology, “Sub-micron scale distributions of trace elements in zircon,” **158 (**2009): 317-355 by A.E. Hofmann, J.W. Valley, E.B. Watson, A.J. Cavosie, and J.M. Eiler, Figures 1-7, © 2009

ACKNOWLEDGMENTS

To my parents, Ray and Joanne, whose genetic assemblage predisposed me to an insatiable curiosity and a fervent imagination and whose encouragement led me to push boundaries and to ask hard questions.

To my brother, Christopher, for keeping me company in my (in?)sanity, then, now, and in the years to come.

To my adviser, John Eiler, who thankfully shares my often dark and sardonic sense of humor, and who took me on as a student in spite of (or perhaps because of) my liberal arts background, which was both very liberal and rife with proclivities toward the humanities.

To Mike Baker, for transcending the roles of best friend and mentor these past five years and for patiently (and consistently) reminding me that a few years of graduate school should never be equated to over twenty years of accumulated wisdom and experience.

And finally: to all of the individuals who believed in me even when I didn't believe in myself, and to all of my mentors for challenging and supporting me along the way, this work barely begins to convey my gratitude.

We shall not cease from exploration

And the end of all our exploring

Will be to arrive where we started

And know the place for the first time.

– T.S. Eliot, "Little Gidding"

Thought is the thought of thought.

– James Joyce, Ulysses

ABSTRACT

Sub-micron-scale zoning of Ti concentrations and correlations between concentrations of Ti and other trace elements (P, Ce, and Y) and cathodoluminescent (CL) banding is observed in natural zircons of both unknown (e.g., Jack Hills) and known (e.g., Toba and Bishop Tuffs) provenance. Ion images were made using the Caltech Microanalysis Center's CAMECA NanoSIMS 50L with an O- primary beam focused to ~400–600 nm on the sample surface. The high spatial resolution of this technique allows for interrogation of chemical variations at or below the scale of CL banding in natural zircons. Images produced in this manner display several types of correlations among Ti, P, Ce, and Y (which appears to be a proxy for CL intensity): positive correlations between Ti concentrations, concentrations of some subset of the other trace elements (P, Ce, and Y), and cathodoluminescent (CL) zonations; Ti inversely correlated with P, Y, and Ce (all of which track oscillatory CL bands); no correlations between CL zones and either Ti or the other trace elements. Three possible causes for such correlations include: temperature-dependent equilibrium partitioning, trace-element partitioning limited by diffusion in the host melt, and surface-controlled, non-equilibrium growth. Comparison of our data with the expected results of these processes suggests that: 1) Ti partitioning in zircon is dependent upon non-equilibrium effects in addition to temperature and/or 2) the incorporation of elements that co-vary with Ti in zircon (e.g., Y, P and Ce) is also temperature-dependent.

To explore these hypotheses, we performed a series of experiments on synthetic and natural granitic compositions (enriched in TiO_2 and ZrO_2) at temperatures of 1400, 1300, and 1200°C. All liquids were zircon-saturated and 6 of the 16 experimental glasses were also saturated in rutile. NanoSIMS measurements of Ti in zircon overgrowth rims in our experiments range from 760 to 112 ppm and show a positive correlation with TiO_2 content of

the quenched glass and run temperature. Our Ti-in-zircon values when "adjusted" for SiO_2 and TiO_2 melt activities (i.e., log(Ti-in-zircon, ppm)+log(a_{SiO_2})-log(a_{TiO_2})) show a strong inverse correlation with 1/T; and least squares fits to the two sets of data generated in this study (synthetic bulk compositions and natural bulk compositions) yield equations with slopes that are statistically indistinguishable. This suggests that at temperatures above 1200°C other trace elements in the melt do not appear to have a substantial effect on Ti partitioning between zircon and silica-rich liquid. A weighted global fit to all of our experimental data is:

$$\log(\text{Ti-in-zircon, ppm})+\log(a_{SiO_2})-\log(a_{TiO_2}) = (6.21 \pm 0.43)-(5918 \pm 689)/T\ (K).$$

R^2 for this equation is 0.85. Our Ti glass contents coupled with measured zircon Ti concentrations from the same experiments allow us to calculate a zircon-melt Ti partition coefficient. Our measured $D_{Ti}^{zrc/melt}$ values are 0.014 to 0.029 and are broadly consistent with values determined from natural-zircon glass pairs. We note that, in the cases for which zircon-independent temperature constraints are known for a parental liquid, neither of the current Ti-in-zircon thermometry calibrations can explain Ti variations in natural zircons as documented by the NanoSIMS.

In Chapter 4, we document spatially correlated P, Al, and Cr zoning in 36 of 40 Gorgona komatiitic olivines from three textural units: a jointed flow top, two random spinifex zones, and two oriented plate spinifex zones. P zoning is observed to be decoupled from or inversely correlated with Al and Cr zoning in some olivines from all three units; the type of zoning observed (e.g., oscillatory, sector) varies depending on textural type. Cooling-rate experiments were performed on a synthetic haplo-komatiite bulk composition in order to evaluate the physical parameters governing incorporation of P, Al, and Sc (as a proxy for Cr) in spinifex komatiitic olivines. Cation-cation plots of data from the natural olivines reveal strong linear trends between Al and Cr and suggest that Al and Cr enter the olivine crystal lattice in a

2:1 ratio. Trends in P-Al and P-Cr composition space differ depending on the olivine textural type. With one exception, oriented plate spinifex olivines define a sub-horizontal P-Al and P-Cr trend, which suggests that P is being accommodated into the olivine lattice via a substitution mechanism involving both Al and Cr. The outlier from this population is a rare preserved plate spinifex tip, which records much higher P at low Al and Cr concentrations compared to the other plate spinifex grains; we interpret these data as suggestive of P incorporation in excess of equilibrium values due to rapid crystal growth.

TABLE OF CONTENTS

LIST OF FIGURES AND TABLES

Chapter 1

Chapter 2

Chapter 3

Chapter 4

Introduction

Although the specifics of trace element definitions differ, most geochemists would agree upon the following operational characterization, noting that these definitions are true for only a specified phase or system and thus a trace element in one phase may not be so classified in another: 1) Trace elements are non-stoichiometric constituents of a given phase; 2) Within a given system, trace elements act as "passive tracers" that do not affect the phase equilibria; 3) The activity of a trace element obeys Henry's Law within a given phase or system. Together, these characteristics establish trace elements' geochemical value. In igneous systems, like those examined in this thesis, trace elements do not affect the outcome of a magmatic event, whether it be melting, crystallization, and/or fractionation, to name a few; to a zeroth order, it is the innate properties of the elements that govern their behavior during magmatic processes. As a result of these combined characteristics, trace elements tend to be preferentially incorporated in one phase over another. Occasionally, the degree to which this "partitioning" occurs is identified as being highly dependent on a specific intensive variable (e.g., temperature) or the presence (or absence) of a specific crystalline phase. In these cases, the partitioning behavior (manifested most generally as the Nernst partition coefficient, the weight-basis ratio of the element of interest in one phase to that in another) is taken to be a signature of that process.

Zircon ($ZrSiO_4$) is a common accessory mineral found in wide array of igneous, metamorphic, and (as detrital grains) sedimentary rocks. Zircon's near ubiquity—particularly in felsic igneous rocks and metamorphic rocks that derive from felsic protoliths—coupled to its physical robustness and chemical retentivity against weathering and alteration makes zircon an essential component of most geochemical inquiries involving crustal igneous suites. Due to these characteristics, zircon is well-preserved throughout the geologic record: the oldest known autochthonous Earth materials are ca. 4.3 billion-year-old (Ga) detrital zircons separated from metasediments in the Jack Hills region of the Western Australian outback (Froude et al. 1983; Compston and Pidgeon 1986). Since their discovery and initial characterization, the Jack Hills zircon population has been barraged by geochemists seeking to understand the physical and chemical conditions of the early Earth (e.g., Compston and Pidgeon 1986; Maas et al. 1992; Amelin 1998; Cavosie et al. 2004; Cavosie 2005; Crowley et al. 2005; Dunn et al. 2005; Hoskin 2005; Nemchin et al. 2006; Menneken et al. 2007; Blichert-Toft and Albarede 2008; Caro et al. 2008; Nemchin et al. 2008; Ushikubo et al. 2008, to name a few). The oxygen isotope and trace element compositions of these zircons have been of particular interest because their signatures suggest whether liquid water and, as a corollary, something akin to continental crust was present on a cooling Hadean Earth (e.g., Peck et al. 2001; Wilde et al. 2001; Coogan and Hinton 2006).

To speak of "trace elements" in zircon is to reference on order ~ 20–25 elements (Hoskin and Schaltegger 2003) ranging from lithium (Li), phosphorus (P), and titanium (Ti) through yttrium (Y) and the rare earth elements (REEs) to uranium (U), thorium (Th), and—although it often occurs at the weight-percent level—hafnium (Hf). These elements enter the zircon lattice via substitutions (often coupled to one another in order to maintain charge balance and lattice neutrality) for silicon and zirconium, zircon's major constituents. Whereas U and Th are of interest predominantly for isotopic dating, concentrations of the other trace elements with respect to one another and to that retained by the parent melt from which the zircon crystallized are used to determine provenance and/or magmatic processes at work during zircon crystallization. In addition, subsets of the REEs have been implicated in both causing and quenching zircon cathodoluminescence (CL)—the emission of photons with characteristic wavelengths caused by electronic transitions resulting from the interaction between an electron beam and a solid characterized as having a band gap (Nasdala et al. 2003)—due to their role in altering the zircon lattice (e.g., Ohnenstetter et al. 1991; Remond et al. 1992; Yang et al. 1992; Hanchar and Miller 1993; Hanchar and Rudnick 1995; Remond et al. 1995; Belousova et al. 1998).

CL zonations are of particular interest in igneous zircons because they are frequently correlated with variations in trace element compositions (e.g., Corfu et al. (2003) and references therein). Zoning is frequently described as either "oscillatory" or "sector," although both can concomitantly exist within the same region of a crystal and resorption, dissolution, and reprecipitation can cause older zones to be abruptly truncated. Sector CL zoning is more consistently explained as having arisen from the attachment of less compatible cations to geometrically incomplete sites along a given crystal face due to differences in the free-energy of such sites as compared to fully coordinated sites within the zircon lattice (Nakamura 1973; Dowty 1976; Watson 1996) and/or different growth rates and mechanisms along different crystallographic faces (Nakamura 1973; Dowty 1976; Watson and Liang 1995; Watson 1996). Oscillatory CL zoning, on the other hand, can be interpreted as arising in response to 1) cyclically varying melt (or crystal) composition, temperature, and/or polymerization, 2) competition between crystal growth rates and cation diffusivities in both the melt and the solid state, and/or 3) dynamics and kinetics operating at the crystal-melt interface (most of which are addressed in Hoskin (2000).

The wavelengths of oscillatory CL zonations are on order of hundreds of nanometers to several microns; therefore, most microprobes (ion, electron, plasma) are capable of resolving trace element concentrations within zones only at the upper limit of this spatial range. As a result, analyses are frequently restricted to sectors, the largest oscillatory bands, and CL-homogeneous overgrowths (usually along the rim of the grain), although often researchers are left with little choice but to analyze (and thereby integrate over) areas that are multiply-zoned and hence may have large variations in their concentrations of a given trace element. With a primary beam diameter (and hence spatial resolution) on the order of 100s of nanometers compared to that of traditional ion microprobes, which operate with ~ 10–20 micron diameter primary beams, the NanoSIMS is well-suited for deconvolving trace element signatures from previously irresolvable small-scale domains.

In this thesis, I separately investigate the partitioning behavior of Ti and P, which enter the crystal lattices of zircon and olivine, respectively, at concentrations of approximately one part to several hundreds of parts per million. In both systems, previous researchers have investigated aspects of these elements' partitioning behaviors; the analytical and experimental work detailed here attempts to extend our understanding and interpretation of the trace element signatures of zircon and olivine. Observations in Chapters 1–3 utilize the high spatial resolution of the NanoSIMS to evaluate the partitioning behavior of Ti between zircon and granitic-to-rhyolitic melts in natural as well as experimental systems. Because of their Hollywood-esque "star appeal" and my interest in adding to our understanding of the early Earth, zircons from the Jack Hills were selected to be the guinea pigs of a NanoSIMS fishing expedition (to mix multiple metaphors) searching for correlations between trace elements typically measured in zircon (e.g., REEs, Y, P), CL zonations, and that latest dark horse of Zirconology, Ti. Our NanoSIMS analyses and observations of micron- to sub-micron-scale correlated trace element distributions—including Ti!—in zircons from the Jack Hills were previously published in *Contributions to Mineralogy and Petrology* and are reproduced with permission as Chapter 1. More generally, Chapters 1 and 3 document the first studies in which zircon trace element distributions were spatially resolved at the micron- to sub-micron scale.

The experiments detailed in Chapter 2 represent the first experimental zircon study in which zircons were grown from a melt of broadly natural granitic composition and, despite their small size (~ 5–15 microns in the longest dimension), could be analyzed for major and trace elements. This study in particular highlights how the spatial resolution of the NanoSIMS enables geochemists to evaluate trace element distributions and concentrations over distances closer to the growth scale. In turn, these observations may lead to fundamental insights into the processes and variables controlling zircon trace element chemistry. Together, the observations detailed in Chapters 1–3 are used to evaluate the assertion by Watson and Harrison (2005), Watson et al. (2006), and Ferry and Watson (2007) that Ti partitioning into zircon is an equilibrium process and therefore Ti concentrations in zircon can be used as a proxy for equilibrium growth and/or crystallization temperatures of zircons from systems for which the activities of SiO_2 with respect to quartz and TiO_2 with respect to rutile are either known or can be deduced. We assert, based on accumulated evidence, that Ti distributions in natural zircons are complex and may not record equilibrium crystallization temperatures. We recommend a re-evaluation of the lower-temperature regime of the existing Ti-in-zircon thermometry calibration curve in the context of long-duration, low-temperature experiments.

Although different in its mineral focus, Chapter 4 is of an intellectually similar lineage to Chapters 1-3; in Chapter 4, I examine the partitioning of P (and Cr and Al) between natural and synthetic olivines and komatiitic (high-magnesium, high temperature) melts and then evaluate the relationship of those trace elements distributions in komatiitic olivines to one another and to olivine crystallography. This work is an attempt to ascertain whether P zonations can aid us in further elucidating the physical parameters that govern the formation of spinifex textures in komatiites.

References

Amelin Y (1998) Geochronology of the Jack Hills detrital zircons by precise U-Pb isotope dilution analysis of crystal fragments. Chem Geol 146:25-38

Belousova EA, Griffin WL, Pearson NJ (1998) Trace element composition and cathodoluminescence properties of southern African kimberlitic zircons. Mineral Mag 62:355-366

Blichert-Toft J, Albarede F (2008) Hafnium isotopes in Jack Hills zircons and the formation of the Hadean crust. Earth Planet Sci Lett 265:686-702

Caro G, Bennett VC, Bourdon B, Harrison TM, von Quadt A, Mojzsis SJ, Harris JW (2008) Application of precise 142Nd/144Nd analysis of small samples to inclusions in diamonds (Finsch, South Africa) and Hadean zircons (Jack Hills, Western Australia). Chem Geol 247:253-265

Cavosie AJ (2005) Geochemistry of >3900 Ma detrital zircons from Jack Hills, Western Australia. Ph.D. thesis. University of Wisconsin-Madison, Madison, WI

Cavosie AJ, Wilde SA, Lui D, Wieblen PW, Valley JW (2004) Internal zoning and U-Th-Pb chemistry of Jack Hills detrital zircons: a mineral record of early Archean to Mesoproterozoic (4348-1576) magmatism. Precambrian Res 135:251-279

Compston W, Pidgeon RT (1986) Jack Hills, evidence of more very old detrital zircons in Western Australia. Nature 321:766-769

Coogan LA, Hinton RW (2006) Do the trace element compositions of detrital zircons require Hadean continental crust? Geology 34:633-636

Corfu F, Hanchar J, Hoskin PWO, Kinny P (2003) Atlas of zircon textures. In: Hanchar JM, Hoskin PWO (eds) Zircon, Reviews in Mineralogy and Geochemistry, vol. 53, pp 469-500

Crowley JL, Myers JS, Sylvester PJ, Cox RA (2005) Detrital zircon from the Jack Hills and Mount Narryer, Western Australia: Evidence for diverse >4.0 Ga source rocks. J Geol 113:239-263

Dowty E (1976) Crystal structure and crystal growth: II. Sector zoning in minerals. Am Mineral 61:460-469

Dunn SJ, Nemchin AA, Cawood PA, Pidgeon RT (2005) Provenance record of the Jack Hills metasedimentary belt: Source of the Earth's oldest zircons. Precambrian Res 138:235-254

Ferry JM, Watson EB (2007) New thermodynamic models and revised calibrations for the Ti-in-zircon and Zr-in-rutile thermometers. Contrib Mineral Petrol 154:429-437

Froude DO, Ireland TR, Kinny PD, Williams IS, Compston W, Williams IR, Myers JS (1983) Ion microprobe identification of 4,100-4,200 Myr-old terrestrial zircons. Nature 304:616-618

Hanchar JM, Miller CF (1993) Zircon zonation patters as revealed by cathodoluminescence and backscattered electron images: Implications for interpretation of complex crustal histories. Chem Geol 110:1-13

Hanchar JM, Rudnick RL (1995) Revealing hidden structures: The application of cathodoluminescence and back-scattered electron imaging to dating zircons from lower crustal xenoliths. Lithos 36:289-303

Hoskin PWO (2000) Patterns of chaos: Fractal statistics and the oscillatory chemistry of zircon. Geochim Cosmochim Acta 64:1905-1923

Hoskin PWO (2005) Trace-element composition of hydrothermal zircon and the alteration of Hadean zircon from the Jack Hills, Australia. Geochim Cosmochim Acta 69(3):637-648

Hoskin PWO, Schaltegger U (2003) The composition of zircon and igneous and metamorphic petrogenesis. In: Hanchar JM, Hoskin PWO (eds) Zircon, Reviews in Mineralogy and Geochemistry, vol. 53, pp 27-62

Maas R, Kinny PD, Williams IS, Froude DO, Compston W (1992) The Earth's oldest known crust: A geochronological and geochemical study of 3900 - 4200 Ma old detrital zircons from Mt. Narryer and Jack Hills, Western Australia. Geochim Cosmochim Acta 56:1281-1300

Menneken M, Nemchin AA, Geisler T, Pidgeon RT, Wilde SA (2007) Hadean diamonds in zircon from Jack Hills, Western Australia. Nature 448:917-921

Nakamura Y (1973) Origin of sector-zoning of igneous clinopyroxene. Am Mineral 58:986-990

Nasdala L, Zhang M, Kempe U, Panczer G, Gaft M, Andrut M, Plotze M (2003) Spectroscopic methods applied to zircon. In: Hanchar JM, Hoskin PWO (eds) Zircon, Reviews in Mineralogy and Geochemistry, vol., pp 427-467

Nemchin AA, Pidgeon RT, Whitehouse MJ (2006) Re-evaluation of the origin and evolution of >4.2 Ga zircons from the Jack Hills metasedimentary rocks. Earth Planet Sci Lett 244:218-233

Nemchin AA, Whitehouse MJ, Menneken M, Geisler T, Pidgeon RT, Wilde SA (2008) A light carbon reservoir recorded in zircon-hosted diamond from the Jack Hills. Nature 454:92-95

Ohnenstetter D, Cesbron F, Remond G, Caruba R, Claude J-M (1991) Emissions de cathodoluminescence se deux populations de zircons naturels: tentative d'interpretation. C. R. Acad. Sci. Paris 313:641-647

Peck WH, Valley JW, Wilde SA, Graham CM (2001) Oxygen isotope ratios and rare earth elements in 3.3 to 4.4 Ga zircons: Ion microprobe evidence for high $\delta^{18}O$ continental crust and oceans in the Early Archean. Geochim Cosmochim Acta 65:4215-4229

Remond G, Blanc P, Cesbron F, Ohnenstetter D, Rouer O (1995) Cathodoluminescence of rare earth doped zircons. II. Relationship between the distribution of the doping elements and the contrasts of images. Scanning Microsc Suppl 9:57-76

Remond G, Cesbron F, Chapoulie R, Ohnenstetter D, Roques-Carmes C, Schvoerer M (1992) Cathodoluminescence applied to the microcharacterization of mineral materials: A present status in experimentation and interpretation. Scanning Microsc 6(1):23-68

Ushikubo T, Kita NK, Cavosie AJ, Wilde SA, Rudnick RL, Valley JW (2008) Lithium in Jack Hills zircons: Evidence for extreme weathering of Earth's earliest crust. Earth Planet Sci Lett 272:666-676

Watson EB (1996) Surface enrichment and trace-element uptake during crystal growth. Geochim Cosmochim Acta 60(24):5013-5020

Watson EB, Harrison TM (2005) Zircon thermometer reveals minimum melting conditions on earliest Earth. Science 308:841-844

Watson EB, Liang Y (1995) A simple model for sector zoning in slowly grown crystals: Implications for growth rate and lattice diffusion, with emphasis on accessory minerals in crustal rocks. Am Mineral 80:1179-1187

Watson EB, Wark DA, Thomas JB (2006) Crystallization thermometers for zircon and rutile. Contrib Mineral Petrol 151:413-433

Wilde SA, Valley JW, Peck WH (2001) Evidence from detrital zircons for the existence of continental crust and oceans on the Earth 4.4 Gyr ago. Nature 409:175-178

Yang B, Luff BJ, Townsend PD (1992) Cathodoluminescence of natural zircons. J Phys-Condens Mat 4:5617-5624

Chapter 1

SUB-MICRON SCALE DISTRIBUTIONS OF TRACE ELEMENTS IN ZIRCON

Abstract

Sub-micron scale zoning of Ti concentrations and correlations between concentrations of Ti and other trace elements (P, Ce, and Y) and cathodoluminescent (CL) banding is observed in natural zircons. Ion images were made using the Caltech Microanalysis Center's CAMECA NanoSIMS 50L with an O- primary beam focused to ~ 300 nm on the sample surface. The high spatial resolution of this technique allows for interrogation of chemical variations at or below the scale of CL banding in natural zircons. Images produced in this manner display two types of correlations among Ti, P, Ce, and Y (which appears to be a proxy for CL intensity): strong (correlation coefficients > 0.8) and subtle (correlation coefficients ~0.15–0.4). Strongly correlated images, which display Ti variations of ca. a factor of 3 between adjacent CL bands and overall elevated trace element concentrations in CL-dark bands, were found within an oscillatory-zoned, trace-element enriched sector of a CL sector-zoned zircon. Three possible causes for such correlations include: temperature-dependent equilibrium partitioning, trace-element partitioning limited by diffusion in the host melt, and surface-controlled, non-equilibrium growth. Comparison of our data with the expected results of these processes suggests that: 1) Ti partitioning in zircon is dependent upon non-equilibrium effects in addition to temperature and/or 2) the incorporation of elements that co-vary with Ti in zircon (e.g., Y, P and Ce) is also temperature-dependent. Sub-micron scale, high-Ti regions are also found within Proterozoic Adirondack and > 4 Ga Jack Hills zircons as well as trace-element enrichments (including Ti) along cracks within Jack Hills zircons.

1. Introduction

The refractory nature of zircon makes it a valuable repository of geochemical information in igneous and metamorphic rocks (Watson and Harrison (2005) and references therein). The preservation of primary chemical signatures in zircon (e.g., oxygen and lithium isotope ratios, rare earth element profiles, Lu-Hf and U-Th-Pb isotope signatures) can provide information regarding provenance, petrogenesis and age (Maas et al. 1992; Valley et al. 1994; Hoskin and Ireland 2000; Peck et al. 2001; Hoskin 2005; Valley et al. 2005; Cavosie et al. 2006; Watson et al. 2006). The Ti-in-zircon geothermometer (Watson and Harrison 2005; Watson et al. 2006; Ferry and Watson 2007) is a recent addition to the compendium of geochemical proxies developed for zircon. It can constrain growth and/or re-equilibration temperatures of zircons, and it may be particularly useful in constraining the thermal state of the crust during events from which zircon is the only surviving mineral. Zircon crystallization temperatures based on the Ti thermometer should also complement geothermometry data based on other techniques from younger rocks for which thermal histories are better known.

Ti-in-zircon temperatures calculated for > 4 Ga detrital zircons from the Jack Hills metasedimentary belt in Western Australia yield average crystallization temperatures of ~700°C (Watson and Harrison 2005; Valley et al. 2006; Watson et al. 2006; Harrison and Schmitt 2007; Fu et al. 2008), consistent with growth from magmas resembling common continental granitoids. The protoliths of these zircons are unknown (although geochemical studies of nearby Archean gabbros and gneisses have been undertaken, e.g., Myers and Williams 1985; Fletcher et al. 1988; Myers 1988; Maas and McCullough 1991; Kinny and Nutman 1996). Therefore, the nature of the rocks from which these isolated crystals come must be inferred based only on their chemistry and mineral inclusion populations. These zircons are small (typically ca. < 200 μm in the long direction) and are characterized by sub-micron-scale zonations in cathodoluminescence (CL) brightness (visible by SEM), which presumably reflect zonations in CL-active elements (such as Y and the rare earth elements, REE). In this study, the NanoSIMS high-resolution ion microprobe is used to evaluate variations of Ti (as well as Y, P, and Ce) in these zircons over the scale of CL banding. These observations are key for the study of such grains because the discovery of μm-scale and finer zonation would require that accurate reconstructions of growth temperature and other petrologic variables be based on trace element measurements at similarly small scales. Furthermore, the discovery of such small-scale compositional complexity in zircons might expand the amount of information that could be recovered from their analysis.

Most of the previous measurements of Ti abundances in zircons have been determined by secondary ion mass spectrometry (SIMS), using a primary beam of O^- over areas from several microns to tens of microns across (Watson and Harrison 2005; Watson et al. 2006; Harrison and Schmitt 2007; Page et al. 2007; Fu et al. 2008). These measurements have demonstrated both variations of Ti within single zircon grains and the existence of high Ti concentrations in cracks of some grains. However, these analyses have averaged fine-scale (i.e., a few microns down to sub-micron) compositional zonations and inclusions. In order to increase the spatial resolution of their analyses, Harrison and Schmitt (2007) used a primary Cs^+ beam with a spot size of ~ 1 μm rastered over 25 × 25 μm areas. Images produced via this method show high Ti contents correlated with cracks and "crystal imperfections" at the micron scale but do not show correlations with CL banding (Harrison and Schmitt 2007). Yields for Ti^- ions produced in this manner are much lower than yields for Ti+ ions produced using a primary O^- beam. Given the low Ti concentrations ([Ti]) in many natural zircons (~ ppm level), this higher-resolution Cs^+ method may not be able to generate precise [Ti] measurements or discern spatially-organized Ti variations in low-Ti zones. Previous studies using a primary O- beam (e.g., Holden et al. 2005; Harrison and Schmitt 2007; Page et al. 2007; Fu et al. 2008) have demonstrated that Ti concentrations in some zircons correlate with relatively coarse (i.e., > 5 to 20 μm) cathodoluminescence (CL) banding. These studies do not resolve whether such Ti variations coincide with the smaller (~ μm)-scale CL banding typical of primary igneous zircon.

In this paper, we report Ti abundances in natural and synthetic zircons down to length scales of ~ 300 nm based on measurements made with the Caltech Microanalysis Center CAMECA NanoSIMS 50L. Detrital zircons from Archean metasediment in the Jack Hills (Australia) and from Proterozoic metapelite in the Adirondacks (New York) as well as synthetic high-Ti zircons are shown to exhibit positive correlations among concentrations of Ti, P, Y, and Ce. The Ti abundances and that of these other, correlated trace elements, can vary by factors of 2–3 over ~ 1 μm scales conformable to CL banding. High-magnification (i.e., 200,000×) backscatter images of these sharply banded high-amplitude trace element variations show no visible cracks or inclusions, suggesting they are intrinsic to primary (i.e., magmatic) zircon. These data suggest that: 1) Ti partitioning in zircon is dependent upon non-equilibrium effects in addition to temperature and/or 2) the incorporation of elements that co-vary with Ti in zircon (e.g., Y, P and Ce) is also temperature-dependent. Many zircons we have studied also contain 1–2 μm-wide zones or < 1 μm spots having Ti concentrations up to 40 times that of adjacent zircon, corresponding to apparent temperatures up to 1200°C. These Ti hot spots are associated with identifiable cracks or mineral inclusions and presumably reflect sampling of micron or sub-micron domains of Ti-rich phases.

2. Samples and Analytical Methods

2.1. Sample descriptions

We examined five detrital zircons from metasediment sample 01JH54b from the Jack Hills (first described in Cavosie et al. 2004). Zircons were prepared and mounted as described in Cavosie et al. (2004), and all were previously imaged by CL and dated as > 4.0 Ga by U-Pb geochronology using the SHRIMP II ion microprobe at Curtin University (Cavosie 2005). We also examined three zircons from the leucosome of a southern Adirondack migmatite metapelite; these zircons were previously characterized by CL and analyzed for $^{49}Ti/^{30}Si$ by ion microprobe but have not been dated (Watson et al. 2006). Based on reported U-Pb geochronology of Adirondack zircons (e.g., Wasteneys et al. 1999; McLelland et al. 2004; Heumann et al. 2006), the cores of these zircons, which are both oscillatory- and sector-zoned, are likely to be between ca. 1.3 and 1.1 Ga in age. In order to preserve pre-existing ion microprobe analysis pits generated during the prior geochronologic and trace-element studies of the grains, the existing gold coats were left intact. High-Ti synthetic zircons from 'Run 57' of Watson et al. (2006) were mounted in Araldite resin, polished with 0.25 μm diamond grit, and Au-coated prior to NanoSIMS analysis.

All samples examined in this study were imaged using Caltech's LEO 1550 VP FE-SEM before and after ion microprobe sessions in order to identify NanoSIMS analysis locations and to check for cracks and/or mineral inclusions within those regions that were analyzed. Inclusions greater than ~ 2 μm in diameter were identified prior to NanoSIMS analysis using SEM-EDS. Inclusions observed in Adirondack zircons include monazite, feldspar, and quartz, as well as an unidentified P-bearing phase or phases; quartz, rutile, and a Ti, Fe-bearing oxide were the only inclusion phases found within the Jack Hills zircons that were examined (though previous studies of related grains have reported K-feldspar, plagioclase, rutile, muscovite, biotite/chlorite, amphibole, apatite, monazite, and xenotime; (Maas et al. 1992; Mojzsis et al. 2001; Peck et al. 2001; Cavosie et al. 2004)). Inclusions less than 2 μm in diameter were only identified in our samples after SIMS analysis, either because they appeared as obvious anomalous features in ion images and/or because we recognized them during post-analytical SEM interrogation.

2.2. Ion microprobe analytical technique

Both natural and synthetic zircons were analyzed for Ti, P, Y, Ce, Zr, and Si contents by ion microprobe using the Caltech Microanalysis Center's CAMECA NanoSIMS 50L. This instrument can detect up to seven distinct species over a mass range up to a factor of 22 simultaneously, facilitating the generation of compositional maps showing coupled spatial variations of multiple elements. Although the NanoSIMS operates on principles broadly similar to more conventional SIMS instruments, its scale of analysis (spatial resolution down to tens of nanometers) and ion optics are sufficiently different that instrumental conditions during analysis are described to aid comparison with potential future work of a similar kind. The following parameters were typical of the tuning conditions used for data presented here: For both spot measurements and ion imaging, the primary beam aperture lenses, D0 and D1, were set at 100 μm and 300 μm, respectively, corresponding to a typical probe size of ~ 300 nm. Positive secondary ions were extracted at 8 kV and collected using electron multipliers. The QSA effect was not calculated. No energy offset was applied.

For spot analyses (i.e., measurements of average trace-element concentration within a μm-scale domain), a 200–500 nA O^- primary beam (~ 35–90 pA on the sample surface, after passing through the aperture D1 and the E0 immersion lens stack) was focused to a 2 × 2 μm rastered spot on the sample surface; collected counts were limited to the inner 1 × 1 μm square of the rastered area by electrostatic gating of the secondary ion beam in order to minimize sampling the outermost edges of the analysis area, which are affected by gradients in charge and topography. Zircons were pre-sputtered for 3–5 minutes prior to analysis in an attempt to achieve a relatively steady counting rate on $^{28}Si^{+}$ (though a strict steady state was not achieved; the raw $^{28}Si^{+}$ counting rates were observed to vary systematically by up to 15% between the first and final cycles).

Ion imaging was performed using a 250–350 nA O^{-} primary beam (~ 45–60 pA on the sample surface after passing through aperture D1 and the E0 stack) rastered over 10 × 10 μm (in the case of Adirondack zircons) or 20 × 20 μm (Jack Hills zircons) areas. In imaging mode, data are collected as linearly discretized spots within the analysis area; the total number of such "spots" is determined by the user prior to image collection and usually results in oversampling (i.e., discretized "spots" are selected to be smaller than the beam diameter; see §2.4 below for description of image processing). Zircons were pre-sputtered with a higher beam current, obtained by use of a wider primary beam aperture, for 15–30 minutes (depending on analysis area size) prior to imaging in order to establish a steady counting rate on $^{28}Si^{+}$.

The mass resolving power (MRP) varied by isotope (and varied slightly with tuning condition from session to session) within the range ~ 4000–10000. The MRP was determined using the Cameca definition, which relates mass line width to mass dispersion by dividing the mass (M) of the isotope of interest by the total range in mass differences (ΔM). Due to interferences by doubly charged ^{92}Zr, ^{94}Zr, and ^{96}Zr on singly charged ^{46}Ti, ^{47}Ti, and ^{48}Ti, as well as possible interference from ^{48}Ca and ^{50}Cr on ^{48}Ti and ^{50}Ti, respectively, ^{49}Ti (5.5% of natural, terrestrial Ti) was used to determine Ti concentration in all zircons analyzed as part of this study. Abundances of Zr were determined by analyzing ^{94}Zr (17.40% of natural terrestrial Zr). We selected ^{94}Zr instead of ^{90}Zr because the latter has an interference with ^{89}YH, which may be abundant in magmatic zircons. ^{94}Zr potentially suffers from interference from $^{31}P_2{}^{16}O_2$ and from $^{30}Si^{16}O_4$. Cerium variations were monitored through measurements of ^{140}Ce, both because it is the most abundant isotope of natural Ce (88.48%) and because it lacks substantial interferences in secondary ions sputtered from zircon. Silicon was also analyzed by its major isotope (^{28}Si, 92.23%), which showed no detectable interferences. Phosphorus and yttrium have only one isotope each, ^{31}P and ^{89}Y. Potential interferences with ^{89}Y include minor contributions from molecular silicon ($^{30}Si_2{}^{29}Si$) and appropriate isobaric combinations of Si_2O_2; similar interferences for ^{31}P include $^{94}Zr_3$ and ^{30}SiH. In all cases, molecular species such as these were presumed to be in abundances low enough so as not to cause percent-level interferences.

2.3. Calibration of Ti analyses

Two synthetic, Ti-doped zircons from experimental Run 57 of Watson et al. (2006) were used in conjunction with NIST 610 glass and the natural kimberlitic zircon, KIM-5 (Page et al. 2007; Fu et al. 2008), to calibrate ion microprobe Ti analyses. These zircons were imaged in backscatter electron mode on the SEM prior to analysis. High resolution SEM-EDS analysis was used to identify and thereby avoid Ti-rich inclusions. Each zircon standard was analyzed 20 times on the NanoSIMS; the sample mount was then removed from the NanoSIMS, its Au coat was removed, and a fresh carbon coat was applied. Then, each ion microprobe pit was analyzed twice by wavelength-dispersive spectroscopy on a JEOL JXA 8200 electron microprobe—once within each ion microprobe pit and once ~ 10 μm adjacent to each pit. Electron microprobe analyses (EMPA) within ion microprobe pits gave anomalous oxide totals, which is expected given that the path lengths for X-rays leaving the sample are not correctly modeled by the correction program, which assumes a flat surface;

therefore, the adjacent analyses (which gave oxide totals of 100.0 ± 2.0%) were used for calibration. Electron microprobe analyses were made using a focused electron beam (~ 1 μm in diameter) with an accelerating voltage of 15 kV, a beam current of 400 nA, and counting times of 20 s on peak and 10 s off-peak for standards and 60 s on peak and 30 s off-peak for samples (to account for multiple interferences with other analyzed elements: P, Ce, Si, Zr, Hf, and Sc). Electron microprobe data were reduced using CITZAF (Armstrong 1988). Oxygen was calculated by stoichiometry. Resulting Ti concentrations ([Ti]) for the Run 57 zircons were within the range previously reported (i.e., 1353 ± 245 ppm (2 s.e.)) by Watson et al. (2006) for these materials.

Each session of NanoSIMS analyses was preceded and followed by analyses of both of the synthetic, high-Ti zircons from Watson's Run 57 experimental charge and—for sessions in which Jack Hills zircon were analyzed—KIM-5, a megacrystic zircon from kimberlite (Page et al. 2007). Figure 1 illustrates average measurements of 1 × 1 μm spots on these three standard materials. During these sessions, the size of the primary beam on the sample surface was estimated to be ~ 300 nm in diameter. These data define a simple linear trend in a plot of $^{49}Ti^+$ vs. [Ti], suggesting the use of slopes from these trends to calibrate unknown zircons analyzed within the same time period (Figure 1). The use of this calibration line for A16 (an Adirondack zircon) and the Jack Hills zircons results in a [Ti] of ~ 10.8 ppm for A16 (9.0 ppm reported in Watson et al. 2006) and [Ti] between 2 and 10 ppm for regions within Jack Hills zircons free of cracks and hot spots. Reported values for similar regions in Jack Hills zircons analyzed by other labs range from ~ 2 to ~ 20 ppm (Watson and Harrison 2005; Harrison and Schmitt 2007; Trail et al. 2007; Fu et al. 2008). A 10 × 10 μm ion image of one standard (KIM-5 zircon) was integrated for all counts emitted from more than 500 nm from the image edge; the resulting $^{49}Ti^+/^{28}Si^+$ ratio is comparable to the spot measurement calibration, suggesting that secondary ion ratios from images can be interpreted as measures of concentration by comparison with conventional spot-measurement calibrations.

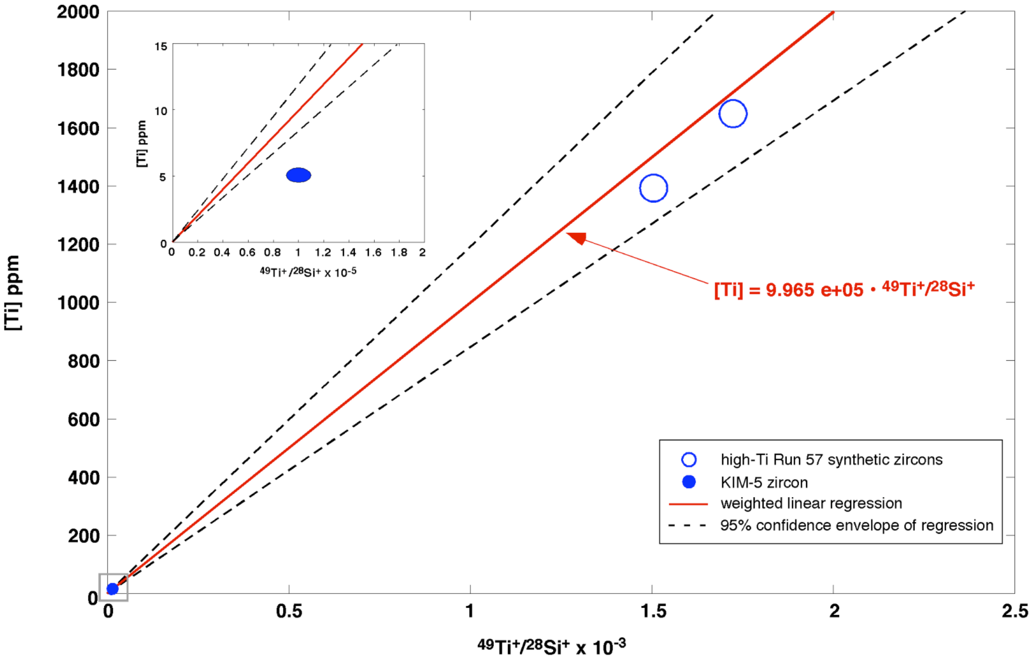

Figure 1. A representative example of measurements calibrating the analysis of Ti in zircon on the NanoSIMS 50L, based on measurements of ^{49}Ti^{+}/^{28}Si^{+} ratios of standards of known Ti content in June 2007. Plotted values are averages of 12 EMPA and NanoSIMS analyses of two Run 57 synthetic zircons and 20 NanoSIMS analyses of KIM-5 zircon. [Ti] for KIM-5 was assumed to be 5.1 ppm, based on 14 SIMS analyses of KIM-5 fragments published in Page et al. (2007). *Error bars* (one standard error) are indicated by the marker size. The data were fit with a least-square linear regression weighted for errors in both coordinates and forced through the origin; the 95% confidence envelope of this regression was calculated using bootstrap statistics. *Inset:* note that the data for Ti-poor KIM-5 zircon are resolved from the background but fall outside the 95% confidence envelope as a result of forcing the fit through the origin.

Sub-micron scale Ti concentrations and distributions were the focus of this study, and this is the only trace element whose yield was calibrated with independent standards. However, during analysis, the intensities of Y, P, and Ce were also monitored. These trace elements are therefore reported as measured isotope ratios to ^{28}Si^{+} (i.e., the data have been processed for dead time and background but not otherwise modified) rather than as concentrations. It is generally true that trace element abundance ratios measured by SIMS are approximately linearly proportional to their concentrations in the material being analyzed. Zircons from the

Jack Hills have previously been reported to contain between hundreds and thousands of ppm Y as well as Ce and P at concentrations from tens to hundreds of ppm (Maas et al. 1992; Peck et al. 2001; Cavosie et al. 2006).

2.4. Image processing

Images produced on the NanoSIMS can be output as ASCII matrices in which each matrix element is the number of counts recorded at the corresponding image x and y coordinates of the sample. These raw image files were processed using code written in MATLAB by the authors. Images were either 128 × 128 pixels (for images generated by rastering the beam over 10 × 10 μm areas) or 256 × 256 pixels (for 20 × 20 μm images). In both cases, the nominal beam diameter on the sample surface (~ 300 nm) was larger than the corresponding width of an individual pixel; therefore, images were smoothed with a 25-pixel moving-average window (i.e., a 5 × 5 pixel image domain; approximately the beam diameter on the sample surface) to account for over-sampling. Prior to smoothing, raw images for each element were ratioed pixel-by-pixel to the $^{28}Si^+$ image, in order to reduce variations caused by changes with time and location in primary beam intensity or variations across the image in the efficiency of secondary ion extraction. Line profiles (Figures 4–5) illustrate variations in element abundance ratios along one-dimensional transects of images. Each point along a line profile is either the concentration (in the case of Ti) or the ratio (e.g., $^{31}P^+/^{28}Si^+$) of the average of all ion counts within a rectangle 3–8 pixels long parallel to the line profile (length determined based on width of features of interest) and 80–200 pixels wide perpendicular to the line profile. The dimensions of the rectangular areas were selected in order to maximize the number of counts contributing to a line profile without 'projecting' obvious compositional variations at some non-perpendicular angle to that line profile. In any single line profile, the area integrated for each point on the line is constant. NanoSIMS ion maps were co-registered with post-analysis CL and SEM images using overlay features in Canvas. The linear offset of a sharp feature among all three image types suggests co-registration alignment errors less than 10%, relative.

3. Results

The following paragraphs briefly summarize the features that contribute to variations in Ti abundance in natural zircons from the Jack Hills and Adirondacks and in synthetic zircons from Watson's Run 57 experiment. The high-Ti inclusions and cracks observed in this study have also been described previously by other authors, albeit at a coarser scale (e.g., Harrison and Schmitt 2007). Features that are resolvable only with μm to sub-μm probe diameters—in particular, submicron chemical variations correlated with CL banding in Jack Hills zircons—have not been reported previously.

3.1. Micron-scale high-Ti regions ("hot spots")

Micron- to sub-micron-scale high-Ti regions were observed in one of three Adirondack zircons, two of five Jack Hills zircons, and all Run 57 synthetic zircons analyzed on the NanoSIMS. Figure 2 illustrates such a feature found within an Adirondack zircon. These regions, here called 'hot spots,' display Ti concentrations up to 40 times the background concentration of the host zircon and commonly account for approximately 50% of the total Ti counts within a 10 × 10 μm or 20 × 20 μm image—despite making up less than 5 percent of the total surface area of a grain. The identified hot spots do not correspond to observable features in CL but are visible as dark inclusions in backscatter electron images made at high magnification on the Caltech SEM. The inclusion imaged in Figure 2 could not be identified by SEM-EDS after NanoSIMS analysis because it had inadvertently been either polished or sputtered away.

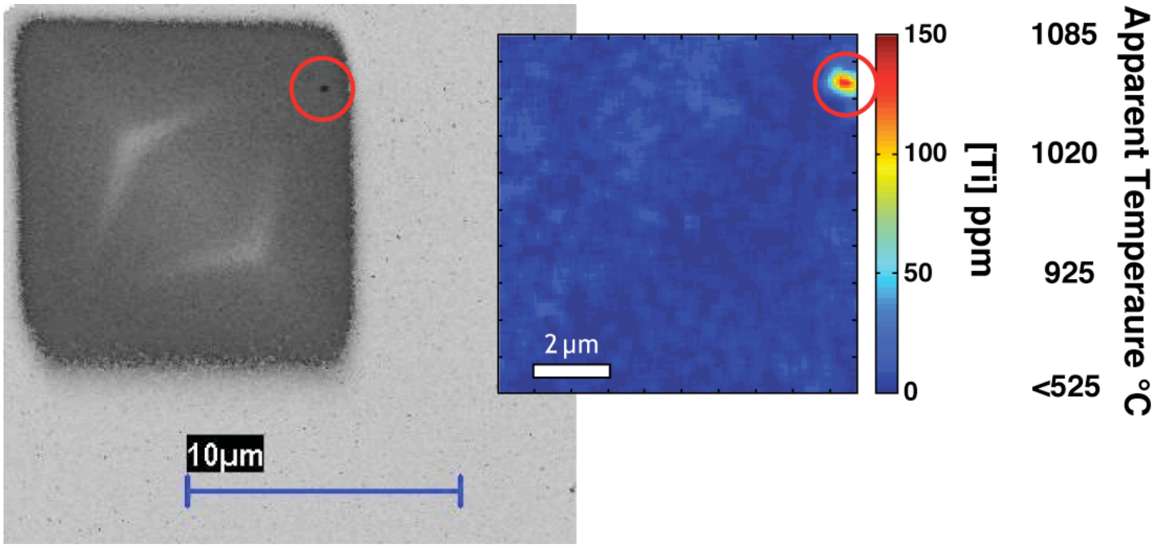

Figure 2. Analysis domain of a Proterozoic zircon from the Adirondacks (New York); the *right frame* is a Ti^+ ion image and the *left frame* is an SEM image of the same grain after ion imaging (the *dark square* marks the rastered region). The *light colored "diamond"* in the SEM image is a charging artifact. Note the sub-μm scale inclusion of a Ti-rich phase in the *upper right corner* of both frames (denoted within the *red circle*). This inclusion contains more than half of the Ti counts in the entire analyzed region.

When compared to backscatter images of the same features, smoothed NanoSIMS images of inclusions appear to have a larger radius; i.e., there appears to be a 'halo' ca. 300 nm wide of elevated Ti surrounding each small inclusion. It is unlikely that this halo is a result of chemical diffusion of Ti out of the inclusion into surrounding zircon. First, if the zircon grew from a melt that was saturated in that Ti-rich inclusion phase, then the zircon presumably already contains Ti in an abundance corresponding to saturation with respect to the TiO_2 activity buffered by the inclusion phase. Secondly, previous data constraining the diffusion coefficient of Ti in zircon (Cherniak and Watson 2007) suggest that the length scale of Ti mobility should be small relative to the analytical spot size in this study under most crustal conditions.

A more likely explanation for the observed Ti halos around inclusions is unavoidable broadening of the Ti-enrichment feature by the finite size of the primary ion beam. We find that inclusions that are ~ 400 nm across as viewed by SEM imaging appear to be ~ 1 μm across in the NanoSIMS images (either 'smoothed' with a 5 × 5 pixel moving window or in unsmoothed images). By evaluating the width of the $^{49}Ti^{+}/^{28}Si^{+}$ signal between 16 and 84% of its height, this increase in size is shown to be the expected result of imaging a perfectly sharp Ti gradient across the inclusion/host interface using a primary beam ~ 300 nm in diameter. As a result, the observed Ti enrichment factor of 40× between inclusions and host is an underestimate of the actual Ti content of the inclusion (although its integrated contribution to the Ti ion count over the entire image is unchanged). A similar observation regarding beam broadening of Ti anomalies associated with Ti-rich inclusions was made by Harrison and Schmitt (2007).

3.2. Cracks and recrystallized zircon

Several of the studied zircons were imaged in regions that are transected by cracks. The resulting NanoSIMS ion images illuminate in detail a phenomenon reported in other studies (e.g., Harrison and Schmitt 2007): [Ti] is often strongly elevated in and/or near cracks in natural zircons. As described in §3.1 above, beam broadening was determined to account for an apparent increase in crack width of ca. 850 nm in ion images. In this study, all images of cracks in natural zircons exhibited this phenomenon (i.e., all of three images); no ion images were made on synthetic zircons. Line profiles taken across cracks indicate that Ti concentrations within and/or adjacent to cracks (within < 1 μm of the crack edge) can be as high as a factor of 60 above the concentration of surrounding unfractured zircon. Cracks also display elevated Y, P, and Ce concentrations, although the proportional enrichment in these elements is generally less than that for Ti. For example, a line profile taken across the lower (horizontal) crack in Figure 3 indicates that Ti is enriched by a factor of 60 within and/or adjacent to the crack (i.e., within < 1 μm) as compared to the surrounding zircon whereas the same profile shows a factor of 3 increase in Y, a factor of 10 increase in P, and a factor of 30 increase in Ce. Other cracks show similar differences in relative enrichments of these elements.

Healed fractures that are bright in CL have been interpreted to be "zircon veins" produced either by solid-state recrystallization of zircon along cracks or by precipitation from hydrothermal solutions (Timms et al. 2006; Reddy et al. 2007; Rimsa et al. 2007). It seems possible that we have encountered a related phenomenon; however, the cracks in this study are not filled with any observable precipitate (Figure 3), and no obvious anomalies in CL banding were observed in association with these cracks. The open cracks we observed might have formed due to lattice damage induced volume increase following the decay of in situ radioactive isotopes, or they may have formed after both sedimentary transport and metamorphism, possibly during the exhumation and intense modern weathering of the Jack Hills. The ductility of quartz surrounding zircons in the Jack Hills metaconglomerates likely hampered brittle zircon deformation; this fact, combined with the absence of visible non-zircon precipitate in the cracks suggests it is unlikely that these zircons were deformed during metamorphism. The observation of 0.30–0.90 wt. % Fe as determined via SEM-EDS within these cracks also supports crack formation in a lateritic environment.

Post-ion microprobe examination of our samples at high magnification (200,000×) using Caltech's FE-SEM in backscatter, above-lens secondary electron, and in-lens secondary electron modes revealed no precipitates or inclusions in any of the imaged cracks. That is, the cracks appear to be open void spaces at the scale observed. One explanation of this

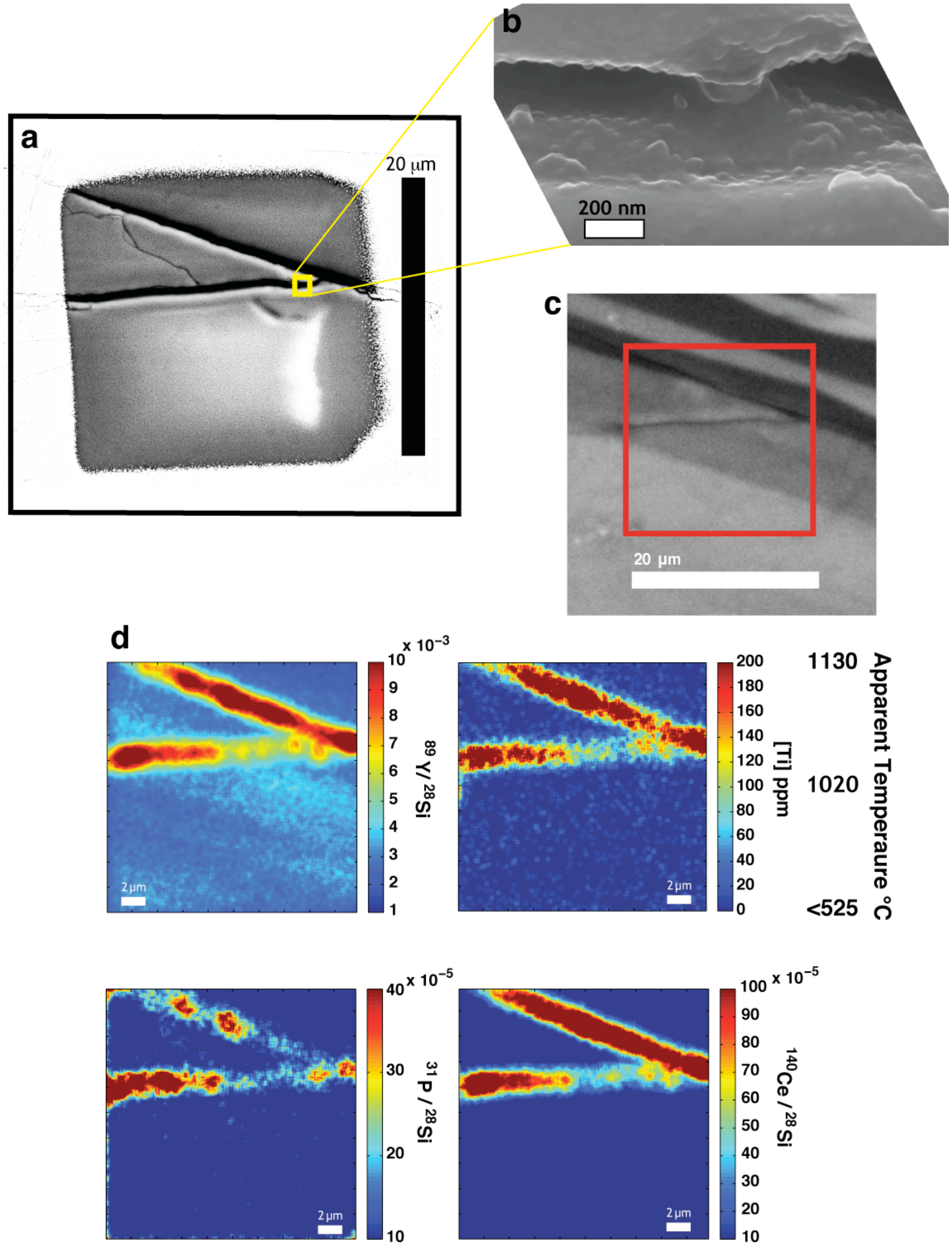

Figure 3. Cracks in Jack Hills zircon 01JH54b.4-1. **a.** Backscatter FE-SEM image of the analyzed region by SIMS; note that no visible precipitate or individual inclusions appear in the cracks. The *yellow box* indicates approximate location of imaged area given in (**b**). **b.** High-magnification in-lens secondary electron FE-SEM image of the *yellow boxed* region in (**a**) taken after NanoSIMS analysis. **c.** CL image of region mapped (outlined in *red*). **d.** Yttrium, phosphorus, and cerium ion maps ratioed to $^{28}Si^{+}$ and [Ti] map of the cracks. Note the faint presence of a yttrium-rich band crossing beneath the horizontal crack in the $^{89}Y^{+}/^{28}Si^{+}$ map. This band corresponds to a dark CL region visible in (**c**); the faintness is due to the high concentration of trace elements in the cracks themselves overwhelming the lower CL signal. The $^{49}Ti^{+}/^{28}Si^{+}$ map was converted to [Ti] using the calibration given in Figure 1.

observation is that high Ti, Y, P, and Ce abundances associated with cracks reflect a thin (<<1 μm) layer of secondary, trace-element-enriched zircon that has precipitated and/or recrystallized along the fracture wall, perhaps in response to infiltration of fluid through the crack. If these cracks formed after metamorphism, then the secondary zircon might have grown at very low temperatures. After correction for beam broadening, the [Ti] content of such secondary zircon would be on order > 250 ppm, which corresponds to a growth temperature in excess of 1100°C; given the observed textures within the crack, this interpretation seems unlikely. This observation may reflect the fact that Ti partitions strongly into secondary zircon relative to co-existing aqueous fluid, making the zircon far richer in Ti than expected for its growth temperature based on Ti-thermometry. Conversely, cracks may be partially filled or armored by an evenly distributed layer of Ti-, Y-, P- and Ce-rich phases that are always smaller than the smallest features that can be imaged by FE-SEM, and that have an average atomic number near that of zircon (so that the collection of minerals will not appear as an anomalous feature on a backscattered SEM image). This second hypothesis should be tested by detailed TEM studies of cracks in zircons.

Measured $^{94}Zr^{+}/^{28}Si^{+}$ ratios vary by ca. 10–20% across cracks; we infer that this reflects the amplitude of aberrations in element/element ratios produced by rastering the ion beam across topographic features like cracks and crystal edges (i.e., because the Zr/Si ratio is very nearly stoichiometric and hence approximately constant in zircon along the edges of the cracks). This variation is two or three orders of magnitude less than the trace-element enrichments observed near cracks, so such enrichments cannot be attributed to measurement conditions, charging, or gradients in surface topography (although their amplitude or distribution might be modified by such artifacts).

3.3. Correlations of Ti and other trace elements with CL banding

Growth features manifested in cathodoluminescence (e.g., sector and oscillatory zoning) were observed in all natural zircons analyzed in this study, and the NanoSIMS ion images generated in this study frequently overlapped those CL features. (See Cavosie (2005) for CL images of such features in Jack Hills zircons analyzed for this study, in addition to the figures shown here.) We observe that abundances of all trace elements analyzed in this study (Ti, P, Ce, and Y) spatially co-vary with CL bands, with high concentrations corresponding to CL-dark bands and visa versa (Figures 4 and 5). These correlations between CL bands and trace element concentrations are more pronounced in dark, generally trace-element rich regions of sector-zoned crystals (i.e., relative to CL-bright, trace-element poor sectors of the same crystal). Jack Hills zircons exhibit the highest trace element concentrations and strongest trace-element variations between oscillatory CL bands in CL-dark sector zones.

On a pixel-by-pixel basis, more secondary ion counts are detected per second for $^{89}Y^+$ than for $^{49}Ti^+$, $^{31}P^+$, or $^{140}Ce^+$, reflecting the relatively high concentrations of Y in the zircons analyzed; therefore, $^{89}Y^+$ ion images provide the best means of co-registering ion images with CL images. The $^{89}Y^+/^{28}Si^+$ ratios exhibit obvious spatial correlations with CL zones (dark CL regions correspond to high $^{89}Y^+/^{28}Si^+$ and vice versa). The $^{89}Y^+/^{28}Si^+$ ratio therefore was used as a proxy for CL bands for the purposes of establishing correlations with other, lower abundance, less precisely imaged trace elements (images for other trace elements are often not sufficiently sharp to clearly identify the edges of banded concentration variations).

Images that display $^{89}Y^+/^{28}Si^+$ variations concordant with oscillatory CL banding can be grouped into two qualitative classifications on the basis of the correlations with CL banding (using $^{89}Y^+/^{28}Si^+$ as a proxy) and Ti, P and Ce variations: Type 1) strong correlations (i.e., correlation coefficients > 0.8) between CL banding and P, Ce, and Ti concentrations, with

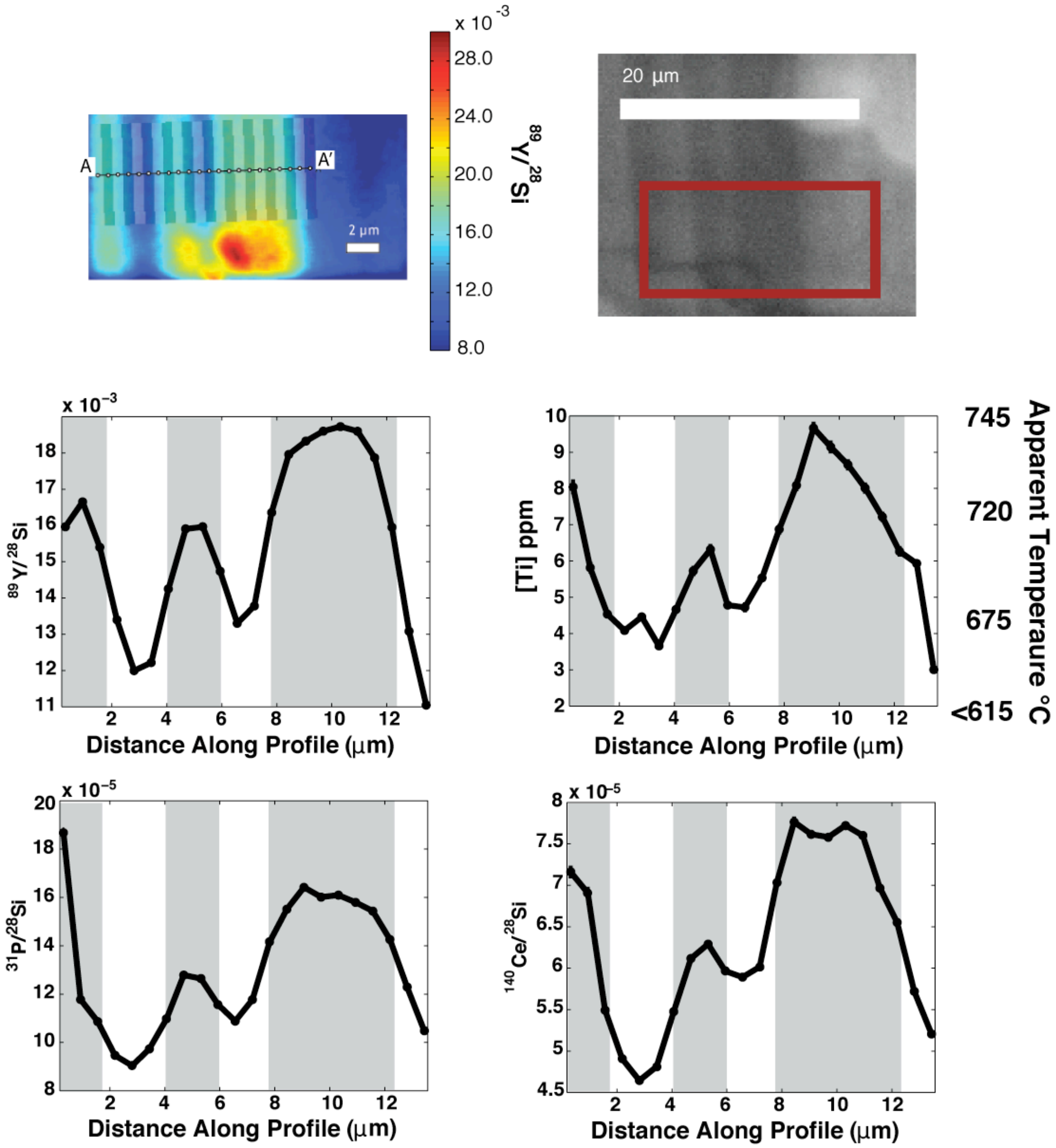

Figure 4. Jack Hills zircon 01JH54b.4-1 (~ 4.1-4.2 Ga) displaying strong correlations between oscillatory CL zones and trace elements. *Upper left:* $^{89}\text{Y}^{+}/^{28}\text{Si}^{+}$ ion map of lower 10 × 20 µm outlined in CL image. *Black line* across bands indicates location of line profile. The alternating *gray rectangles* indicate the integration areas (6 µm × 600 nm) for counts assigned to each profile point. See text for further details. The hot spot in Y (appearing beneath the analyzed area) is the edge of a crack that does not extend upward into the analyzed area. *Upper right:* CL image of region mapped (outlined in *red*) within the CL-dark sector. The CL-bright, rounded region in the *upper right corner* of the CL image is a surface-charging artifact. *Bottom:* Line profiles showing correlated CL and trace element concentrations. The *vertical gray bars* correlate to the CL-dark bands in the analyzed region.

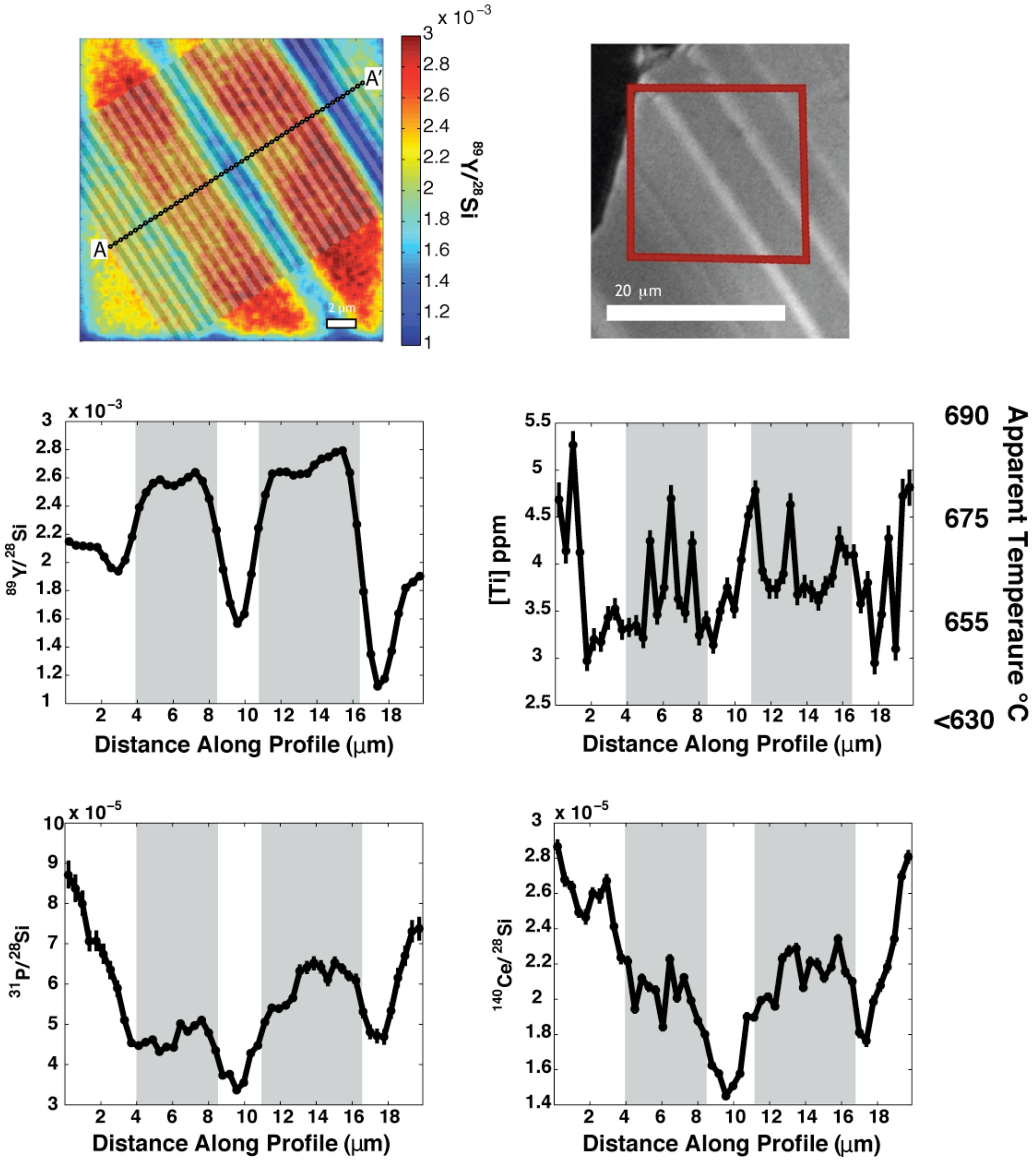

Figure 5. Jack Hills zircon 01JH54b.9-2 (~ 4.0-4.1 Ga) displaying subtle correlations between CL bands and trace elements. *Upper left:* $^{89}Y^+/^{28}Si^+$ ion map of region outlined in CL image. The *black line* across the bands indicates the location of the line profile. The alternating *gray rectangles* indicate the integration area (~ 15 μm × 500 nm) for counts assigned to each profile point. See text for further details. *Upper right:* CL image of region mapped (outlined in *red*). *Bottom:* Line profiles showing correlated CL and trace element concentrations. The *vertical gray bars* correlate to the CL-dark bands in the analyzed zircon.

dark CL regions corresponding to high trace element content; Type 2) similar but subtler correlations (i.e., correlation coefficients ~ 0.15–0.4) between CL banding and Ti, P, and Ce, with Ti generally displaying the weakest correlation. Based on a two-tailed t-test, these two image types are statistically different at the 99th percentile confidence level; i.e., they appear to represent substantively different patterns of correlated chemical zonation rather than extremes of a continuum. Similarly, using a one-tailed t-test, the correlation coefficients of Type 2 images were determined to be statistically different from zero above the 85th percentile (i.e., it is likely that correlations among elemental abundances in this second group are significant, even if they are more muted than those in Type 1 images). Both types of images can occur within a single zircon. Correlations described here are limited to the subset of elements analyzed; other trace elements may or may not show correlations with CL banding (e.g., Sc; Holden et al. 2005).

The compositional variations associated with CL-concordant banding in Type 1 and Type 2 images define linear trends in various plots of element/element ratios against one another (e.g., Ti/Si vs. Y/Si, etc.; see Figure 6). The plots reveal a bimodal distribution separating Type 1 (highly correlated) images from Type 2 (subtly correlated) images (the difference between these two populations is here statistically significant to better than 99% confidence). Although such plots are useful guides to compositional correlations, they may be incomplete or even misleading because they fail to simultaneously capture co-variations in all measured compositional variables. In order to more rigorously determine the quantitative relationships among P, Ce, Ti, and Y, we performed a principal component analysis on data for Types 1 and 2 CL-concordant zoning, as well as for data from a line profile oriented across a crack. In each case, data were grouped by textural type; all CL-concordant bands were grouped together into a single population. For each textural sub-group of data, each measured element/element ratio (e.g., $^{31}P^{+}/^{28}Si^{+}$) for all spatially discrete points were normalized such

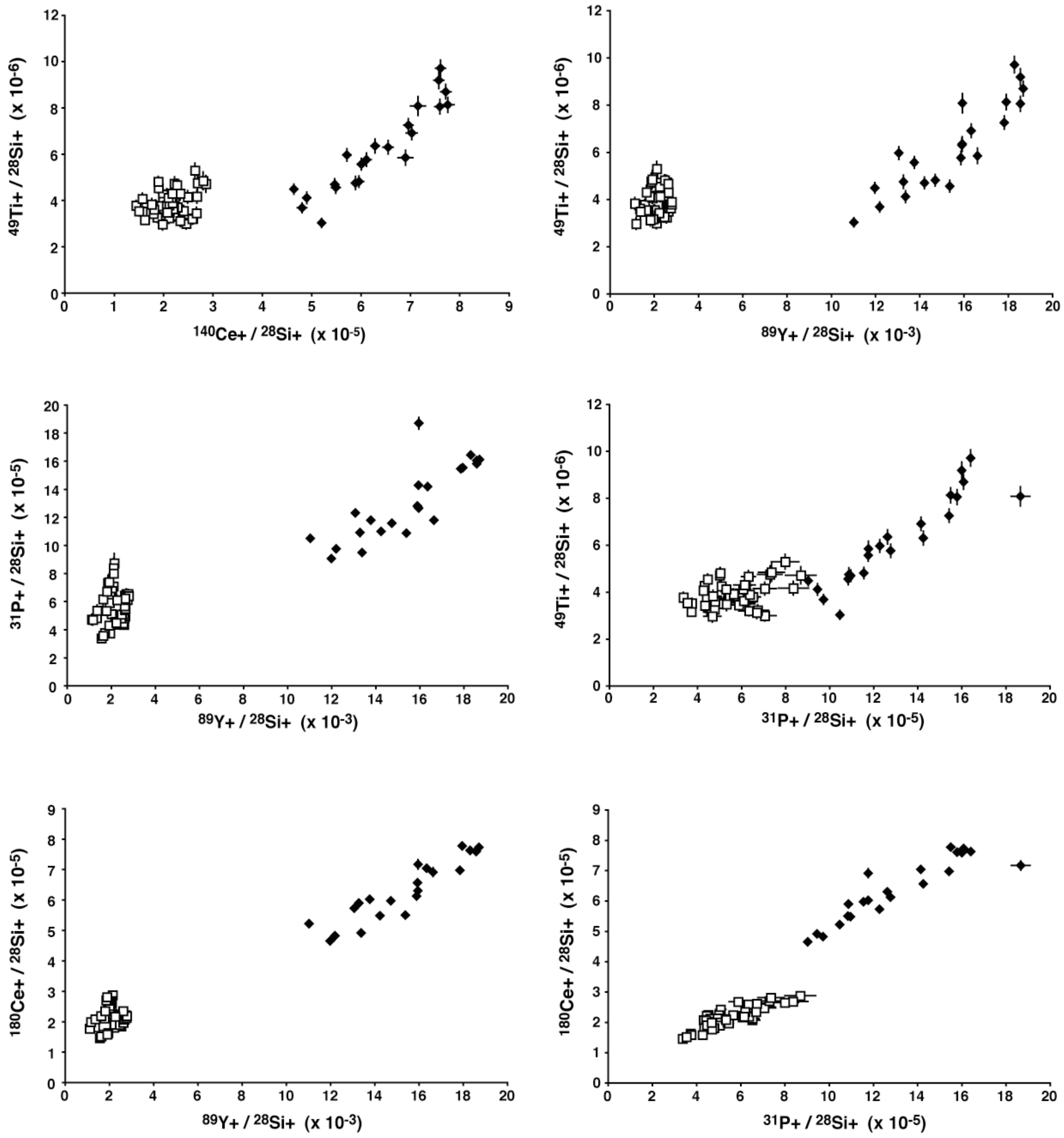

Figure 6. 2D plots of trace elements across CL banding in Type 1 (strongly correlated) and Type 2 (subtly correlated) images. *Filled diamonds* are data from the line profile taken across Jack Hills zircon 01JH54b.4-1 (see Figure 4), a Type 1 image. *Open squares* are data from the line profile taken across Jack Hills zircon 01JH54b.9-2 (see Figure 5), a Type 2 image. *Error bars* indicate two standard error (2 SE).

that their mean was zero and their standard deviation equaled one: that is, normalized $^{31}P^+/^{28}Si^+_i$ (i.e., x_i) for any point, *i*, equals $\left(x_i - \frac{1}{n}\cdot\sum_{i=1}^{n} x_i\right) \Big/ \sqrt{\frac{1}{n}\cdot\sum_{i=1}^{n}\left(x_i - \bar{x}\right)^2}$. This was done in order to weight all data equally in the principal component regression. Each point in composition space therefore corresponds to a point taken from the line profile of interest, in which the line profile points are discretized as detailed in §2.4 above.

Regression of the data for CL-concordant banding (fit without rotation) yielded one significant eigenvector that accounted for 88% of the variance observed (no one additional eigenvector accounted for more than 9.5% of the variance). This is consistent with the data for CL-concordant bands defining a single, shared, linear trend in composition space. The first principal component coefficients, which give relative amplitudes of the changes in each element ratio, were 0.52, 0.45, 0.51, and 0.52 for $^{31}P^{+}/^{28}Si^{+}$, $^{49}Ti^{+}/^{28}Si^{+}$, $^{89}Y^{+}/^{28}Si^{+}$, and $^{140}Ce^{+}/^{28}Si^{+}$, respectively; i.e., after normalization as defined above, the linear relationship among these variables has a slope ~1 among any two of these four compositional variables. Similarly, for the crack subjected to a principle component analysis, one eigenvector accounted for 99% of the variance and the first principal component coefficients were between 0.498-0.501 for all four of the compositional variables. Thus, the crack also defines a single linear trend in composition space. However, the trends for CL-concordant bands and the crack clearly differ from one another in plots of un-normalized element/element ratios (Figure 7). That is, each textural type defines a simple linear trend through composition space, but these trends differ strongly from one another in slope. The three-dimensional plot in Figure 7 clearly cannot capture all of the details of these relations (there are too many compositional variables to simultaneously depict them visually) but still captures the important features of these compositional trends.

a

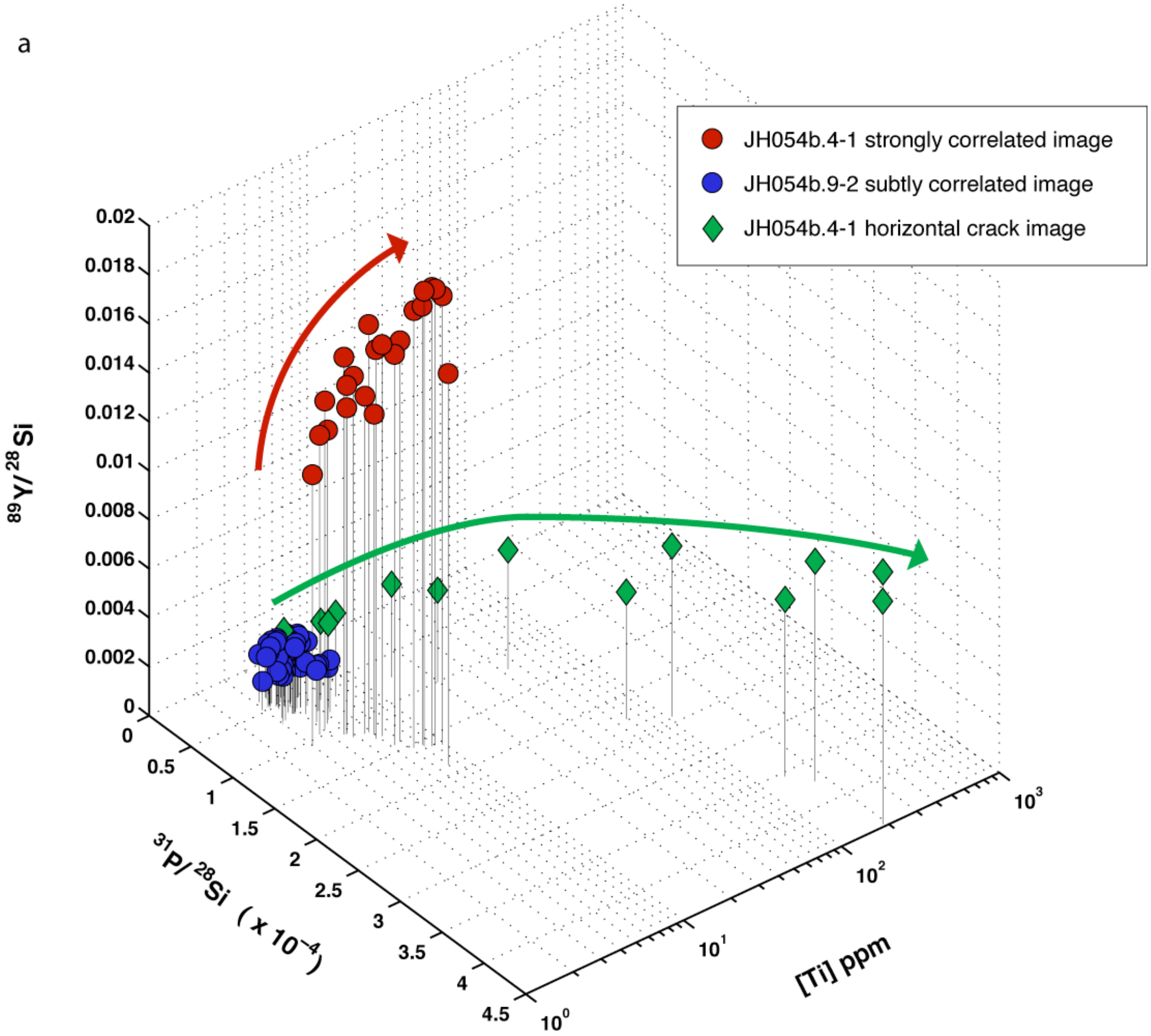
JH054b.4-1 strongly correlated image
JH054b.9-2 subtly correlated image
JH054b.4-1 horizontal crack image
^{89}Y/^{28}Si
0.02
0.018
0.016
0.014
0.012
0.01
0.008
0.006
0.004
0.002
0
0
0.5
1
1.5
2
2.5
3
3.5
4
4.5
^{31}P/^{28}Si (x 10^{-4})
10^{0}
10^{1}
10^{2}
10^{3}
[Ti] ppm

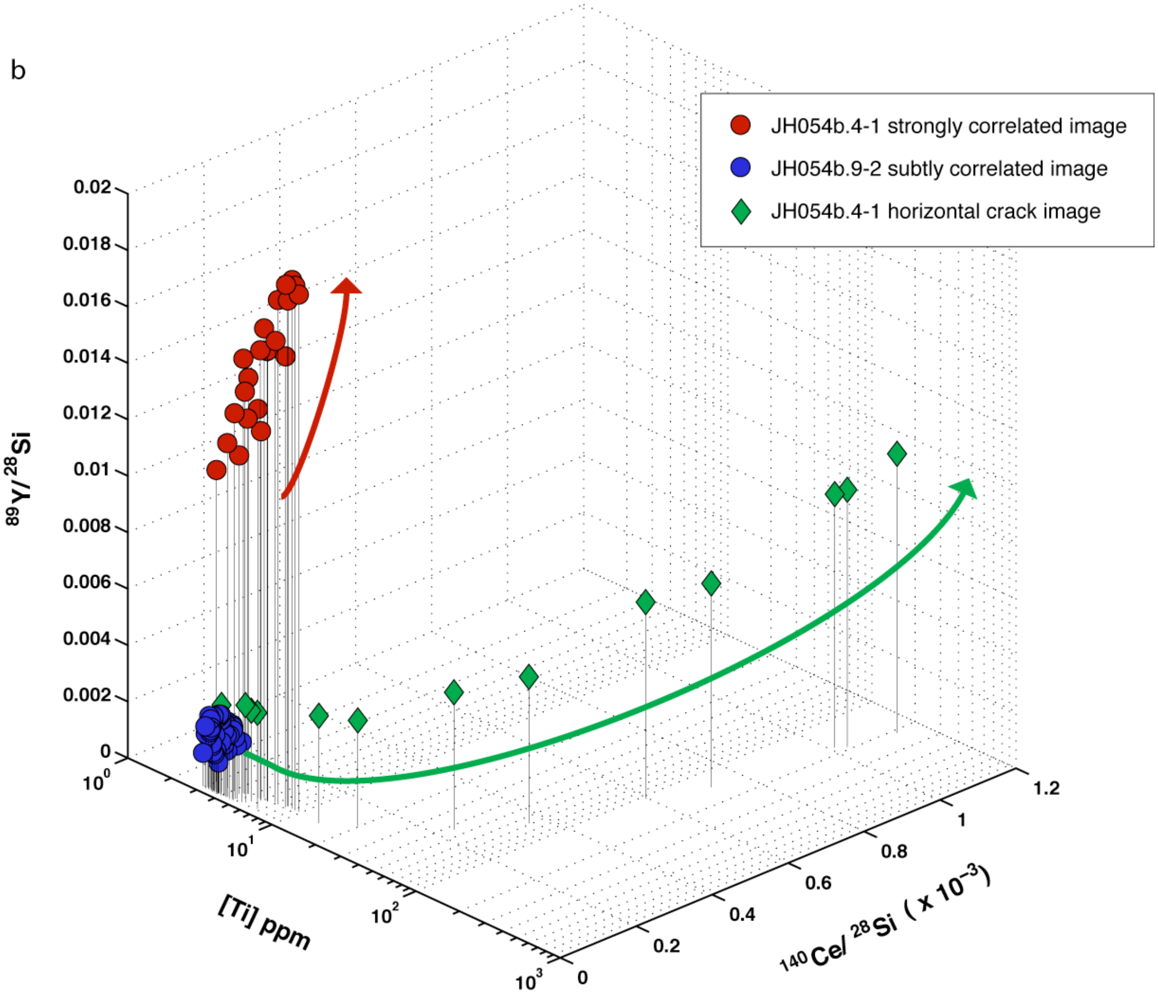

Figure 7. 3D composition space plots of trace elements in cracks and across CL banding. **a.** ^{89}Y$^+$/^{28}Si$^+$ versus ^{31}P$^+$/^{28}Si$^+$ versus [Ti]. **b.** ^{89}Y$^+$/^{28}Si$^+$ versus [Ti] versus ^{140}Ce$^+$/^{28}Si$^+$. The *blue circles* represent analyses across CL banding in Jack Hills zircon 01JH54b.9-2, which displays subtle correlations between CL banding and trace elements (see Figure 5). The *red circles* correspond to analysis of Jack Hills zircon 01JH54b.4-1 (Figure 4). The green diamonds are from a line profile taken across the horizontal crack in Jack Hills zircon 01JH54b.4-1 (Figure 3). The *red* and *green arrows* display general correlations seen among elements and across cracks, respectively.

4. Discussion

In this section, we first review physical-chemical constraints on the nature of trace-element partitioning into zircon and its relationship to CL banding, and then discuss three alternate (though not mutually exclusive) hypotheses as explanations of observed correlations between Ti, Y, P, and Ce concentrations exhibited by oscillatory-zoned domains. In particular, we consider whether such correlations may be due to one or more of: temperature-dependent equilibrium partitioning of all trace elements during rapid cycles in growth temperature and/or changes in bulk melt chemistry; episodic diffusion-limited enrichment of trace elements in the boundary layer of melt adjacent to growing crystals; and/or kinetically controlled, non-equilibrium crystal-melt partitioning of trace elements into relatively rapidly grown layers of crystals. Some correlations may also result from charge-balanced coupled substitutions into the zircon lattice. At the end of this section we comment on the origins and significance of elevated trace element abundances in cracks and on the role of Ti-rich inclusions in Ti-thermometry and ion imaging of zircon.

4.1.1. A brief review of Ti, P, Ce, and Y in zircon and the origins of CL banding

Phosphorus, cerium, and yttrium can enter the zircon lattice by the coupled xenotime-type substitution mechanism: $(Y, REE)^{3+} + P^{5+} = Zr^{4+} + Si^{4+}$ (Speer 1982), although this mechanism is only clearly known to control trace element incorporation in crystals doped with (or naturally enriched in) middle rare-earth elements (MREE), Y, and P (Finch et al. 2001; Hanchar et al. 2001). In general, however, P is not thought to completely charge balance (Y + REE) due to its typical low abundance in the melt (e.g., Hoskin and Schaltegger 2003). In natural crystals with high rare-earth element contents, charge compensation could also be accomplished via the interstitial incorporation of +1 ions like H and Li (Ushikubo et al. 2008).

Heavy rare earth elements are smaller in ionic radius than the LREE and MREE and therefore are more compatible in the small Zr site in the zircon structure. However, experimental investigation of the xenotime-type substitution suggests that deviations from the xenotime mechanism may occur as a result of three compositional factors: 1) displacement of Zr into the Si site, 2) lattice strain resulting from the incorporation of P (into the Si site) and HREE (into the Zr site), and 3) ratios of REE to P greater than one (in the case of HREE-dominated incorporation) or less than one (in the case of LREE-dominated incorporation) (Finch et al. 2001; Hanchar et al. 2001). These observations suggest that multiple mechanisms beyond the xenotime-type substitution are responsible for trace element incorporation into zircon. Accommodation of Y, P, and REE in zircon is known to be limited by strain accumulation at the Si site as the Si-O bond length decreases with increasing P incorporation (a result of the smaller ionic radius of P^{5+} in IV-fold coordination, 0.17 Å, compared to the Si^{4+} ionic radius of 0.26 Å; Shannon 1976). Incorporation of Ti^{4+}—IV-coordinated ionic radius of 0.42 Å (Shannon 1976)—into the Si site as evidenced by increasing [Ti] with decreasing a_{SiO_2} (Ferry and Watson 2007) and as predicted by quantum mechanical calculations (Harrison et al. 2005; Ferriss et al. 2008) could potentially offset strain caused by P^{5+} incorporation. Therefore, it seems plausible that Ti incorporation into the zircon lattice is enhanced (i.e., Ti becomes more compatible) with increasing charge-coupled substitutions of other trace elements (e.g., P, Y, REE) for major elements (Zr, Si).

CL emissions are most frequently attributed to the HREE, but may also result from lattice defects and non-stoichiometry (Ohnenstetter et al. 1991; Hanchar and Rudnick 1995; Remond et al. 1995; Corfu et al. 2003; Nasdala et al. 2003). CL-active elements (all at concentrations less than a weight percent) can vary in abundance across a single zircon grain, leading to banding, sector zoning and other textural features in CL images. These variations in abundances of CL-active elements can arise from a variety of equilibrium and kinetic phenomena that are discussed in detail in subsequent sections. Briefly, oscillatory zoning in CL brightness can reflect cyclically changing conditions in the melt (temperature, composition), diffusion-limited changes in melt composition adjacent to the growing crystal, and/or kinetic influences on partitioning at the crystal-melt interface. Sector zones of CL brightness can arise when less compatible cations attach to incomplete sites along the crystal surface because those sites, which are in equilibrium with the near-field liquid, have different free energy and geometry than fully-formed structural sites (Nakamura 1973; Dowty 1976; Watson 1996), and/or different growth rates or growth mechanisms along different crystal faces (Nakamura 1973; Dowty 1976; Watson and Liang 1995; Watson 1996). In addition to these mechanisms, trace zircon constituents like Li, Sc, P, REE, and Y are network-modifying species that affect the ordering and polymerization of the melt, which may in turn influence zonation patterns by changing diffusivities and/or partition coefficients (Hoskin 2000). Three different physical mechanisms that could influence the Ti zonation and its relation to CL banding will be discussed below.

4.1.2. Temperature-dependent equilibrium partitioning

Amplitude variations at least as great as a factor of ~ 3 in [Ti] are observed between adjacent CL bands in the strongly correlated (i.e., Type 1) images (Figure 4). These images have the highest absolute concentrations of all analyzed trace elements, are from sector-zoned CL grains, and display oscillatory zoning in CL. Overall, these observations suggest that Ti abundances of igneous zircons are controlled by the same processes that control CL banding, at least in trace-element enriched grain domains. The simplest possibility raised by these CL-correlated μm to sub-μm variations in [Ti] contents of zircons is that they grew at equilibrium with co-existing melt over a periodically or episodically fluctuating range in temperature, such as might result from injection of new magma into a cooling magma chamber or movement of the zircon from one region of a thermally zoned magma chamber to another. High [Ti] in a zircon core that decreases towards its rim has previously been interpreted as due to magma cooling (Harrison et al. 2007; Hiess et al. 2008). If the Ti distribution in zircon is highly temperature-dependent (Watson and Harrison 2005; Watson et al. 2006; Ferry and Watson

2007), then cooling at constant Ti activity would lead to monotonically decreasing Ti in zircon. It is possible (though perhaps unlikely) that temperature and melt composition could fluctuate so regularly, repetitively and commonly that they also cause the fine-scale (i.e., μm to sub-μm) oscillatory zonations in trace element contents in magmatic zircons. Assuming Ti-partitioning is both Henrian and temperature dependent, as indicated by Ferry and Watson (2007), and equilibrium between the crystal and the bulk host melt does occur and is maintained over the length scale of growth bands, then each compositionally distinct band of uniform [Ti] in such an oscillatory-zoned grain would indicate a period of equilibrium growth at a particular (and determinable) temperature.

In the context of an equilibrium-growth hypothesis, the observed positive correlations among Ti, Y, P, and Ce in trace-element-rich zircon domains (Figures 4-7) suggest that the abundances of Y, P, and Ce are also controlled by equilibrium crystal/melt partitioning, and thus that their variations also reflect the influence of varying temperature on the relevant partition coefficients. Given the complex crystal-chemical controls of P-Y-REE partitioning in zircon (§4.1.1 above), this may be unlikely. Nonetheless, this hypothesis is possible given current constraints and could be tested in part by experimentally determining the temperature dependences of partition coefficients for Y, P, and Ce between zircon and melt. If correlated variations in Ti, P, Ce, and Y are, in fact, an equilibrium phenomenon, then the relevant partition coefficients could be used to interpret the compositions of natural igneous zircons to reconstruct parent melt temperatures and, because this element set would provide multiple independent thermometers, one could use such data to determine components of parent melt compositions.

The grains we studied lack observable resorption textures, suggesting that their trace element zonation is not the result of magma mixing events or grain convection through a magma chamber that varied strongly in temperature. In addition, Ti abundances and the amplitudes of Ti banding vary between sector zones of a single crystal; i.e., presumably isochronous bands of zircon from different crystal faces can differ in Ti content. It is difficult to imagine how this could occur if crystal-melt partitioning is controlled only by extrinsic factors like temperature or melt composition.

One way to explain the positive correlations among Y, P, Ce, and Ti in areas enriched in these elements (as compared to areas with low total concentrations of these elements) is that their partition coefficients may also vary as a function of zircon composition—a response, in part, to intracrystalline strain resulting from cation substitutions (e.g., Finch et al. 2001; Hanchar et al. 2001). For example, perhaps Ti is more compatible in zircon that is rich in Y and REE. It is established that Y is compatible and Ce (and the other HREE) are moderately compatible in zircon; data from natural igneous rocks seem to strongly suggest that Ti and P are incompatible. There are currently little or no data on the concentrations of Y, P, and Ce in those zircons that have been used to evaluate Ti partitioning and, hence, on the effect that concentrations of Y, P, and/or Ce and the other REE may have in controlling Ti incorporation into zircon.

If we base our analysis on compositional data from natural zircons, then the highly compatible behavior of Y and predominantly incompatible behavior of Ti in zircon indicate that, during equilibrium partitioning, these two elements should behave oppositely at the crystal interface (in the absence of energetically driven preferential attachment to the crystal surface). Because we observe positive correlations between Y and Ti distributions (i.e., similar behavior), we suggest that equilibrium processes may not have governed the partitioning of these elements into the zircons we have analyzed.

4.1.3. Trace-element partitioning limited by diffusion in host melt

In the case that the linear growth rate of igneous zircon approaches the diffusivity of Ti, P, and/or Ce in parent melt, these incompatible trace elements will become enriched in a boundary layer of melt adjacent to the growing face of the crystal. In this case, these elements are excluded from the crystal, and diffusion is too slow to dilute the resulting enrichment into the adjacent melt (e.g., Smith et al. 1955). Compatible trace elements like Y will become depleted in the adjacent boundary layer. Even if crystal growth remains an equilibrium process immediately at the melt/crystal interface, this phenomenon can lead to disequilibrium trace-element partitioning between the crystal and the bulk melt—i.e., melt farther from that interface than the region of diffusion-limited enrichment (the additional possibility of non-equilibrium growth is discussed in §4.1.4, below). The simplest case assumes that less compatible elements in the zircon structure increase in concentration in the liquid as the zircon grows. As the crystal grows and rejects trace elements like P, Ti, and the rare earths, the concentrations of such elements in the liquid increases; therefore, with continued growth at the same rate, the trace element concentration in the solid crystal must also increase. At the same time, such growth depletes the near-field melt in zircon constituents (i.e., Zr), which slows zircon growth. If zircon growth slows enough, diffusion-limited enrichments of incompatible elements in surrounding melt can relax, so that their abundances in the next solid layer will be closer to that expected for equilibrium partitioning with the far-field melt. Similarly, the depletion gradient in Zr next to the zircon should also relax, and, if the factors that lead initially to the rapid growth rate still exist, then the cycle should repeat itself.

It has been suggested that diffusion-limited enrichment of incompatible elements in melt immediately adjacent to a growing crystal (i.e., in response to rapid crystal growth coupled with slow diffusion of incompatible elements in the melt) can cause crystallization of accessory minerals from melts that are not saturated in accessory components far from surfaces of growing phenocrysts (Green and Watson 1982; Harrison and Watson 1984; Bacon 1989). Nucleation of such accessory phases imposes a limit on the concentrations of their constituent elements in melt boundary layers. For example, the highest Ti contents observed in oscillatory bands in zircon cannot exceed equilibrium partitioning with a melt that is saturated with respect to rutile. It follows that the activity of TiO_2 in the bulk melt, far from the growing zircon surface must be no more than 1 divided by the amplitude of the Ti variations from CL bright to CL dark bands.

One can evaluate whether this process plausibly explains the data by comparing the enrichments of various trace elements (P, Ti, Y, and Ce) to their diffusion coefficients in the melt and to the diffusion coefficient for Zr. Zirconium is a trace constituent of most natural melts and is highly compatible in zircon. Therefore, Zr must diffuse to the crystal face in order for it to continue growing, so concentration gradients should only form at the solid-liquid interface for those trace elements that diffuse more slowly than Zr because faster diffusing species would maintain a homogeneous distribution in the melt over the time-scales of diffusion-limited zircon growth. That is, coupled oscillatory variations in Ti, Ce, P and Y observed in zircon can only reflect diffusive enrichment of melt boundary layers if diffusion rates of these elements in silicate melt are slower than that for Zr.

Within a wet (~ 6% H_2O) silicic melt at ca. 800ºC, Zr, P, and the rare earths diffuse at a similar rate (~ 10^{-15} m^2/sec for Zr, 10^{-17} m^2/sec for P and the REE) (Harrison and Watson 1983; Rapp and Watson 1986) whereas Ti diffuses much more quickly (~ 10^{-9} to 10^{-10} m^2/sec) (Hayden and Watson 2007). Within a silicic melt containing < 1% H_2O at a temperature of 800ºC, Zr, P, and the REE diffuse at approximately the same rate (~ 10^{-21} m^2/sec) (Harrison and Watson 1983; Rapp and Watson 1986). Titanium diffusivity in dry melts has not been determined. Thus, because P and the REE diffuse as slowly as Zr in a hydrous silicic melt, the boundary layer between crystal and melt would likely not be strongly enriched in either P or the REE, and the effects of these ions on changing a_{SiO_2} at the crystal surface (e.g., Ryerson and Hess 1980) would be minimal. Even if gradients did develop in REE and P, Ti diffuses ~8 orders of magnitude more quickly than these elements (~ 5 orders of magnitude more quickly than Zr) in the melt and therefore should maintain a homogeneous concentration adjacent to a growing zircon crystal. For these reasons, we suggest that concentration gradients controlled by melt diffusion do not plausibly explain the observations, unless diffusion-limited growth leads to variations in Y and other trace elements follow suit through a combination of charge compensation and lattice strain effects on distribution coefficients.

4.1.4. Surface-controlled, non-equilibrium growth

The variations in Ti concentration observed across oscillatory CL bands in zircon might be attributable to disequilibrium partitioning at the zircon-melt interface. Local disequilibrium would occur if sites on the surface of a growing zircon incorporate incompatible trace elements at abundances greater (or less) than those expected for equilibrium bulk partitioning (i.e., because surface sites differ in size and/or local charge from those in the grain interior), and continued growth effectively 'buries' those enriched (or depleted) layers within the grain interior before they can exclude their non-equilibrium complement of incompatible elements (or accumulate the equilibrium amount) (Watson 1996). This process could plausibly occur when growth rate exceeds the rate of solid-state diffusion within the crystal. Solid-state diffusion coefficients for all of the analyzed elements are slow relative to likely rates of phenocryst growth, so this mechanism seems plausible to us (although so little is known about non-equilibrium trace element partitioning that the hypothesis is effectively un-falsifiable at present).

We favor the interpretation that trace element zonation concordant with CL banding reflects the disequilibrium partitioning phenomena discussed in the previous paragraph, perhaps modified by diffusion-controlled enrichments of some elements with relatively slow diffusion coefficients (e.g., P) in melt adjacent to zircon. We think it is particularly significant that a single zircon can preserve trace-element variations concordant with both oscillatory and sector CL-zones (e.g., Jack Hills zircon 01JH54b.4-1; Figure 4). Sector zoning in minerals grown from a melt cannot be easily explained as a result of trace element zonation in the melt, because the diffusive processes that lead to such zonation next to growing crystals are isotropic in the melt, and growth rates of different faces on sub-equant grains must be roughly equal, at least when averaged over the history of grain growth. Thus, at least in the case of the sector-zoned grains, it seems most likely to us that trace-element zonation reflects the non-equilibrium, surface adsorption-driven uptake of some incompatible elements from the melt preferentially more on one growing crystal face than another.

4.2. Origins of high trace element concentrations associated with cracks

High [Ti] has been observed in cracks within zircon, both in this study (see, for example, Figure 3) and by other authors (e.g., Harrison and Schmitt 2007). The correlations observed in this study among [Ti], P, Y, and Ce (Figure 3) associated with cracks, and the absence of substantial variations in the $^{94}Zr^+/^{28}Si^+$ ratio near and in cracks, suggest that the cracks themselves may contain or are mantled by recrystallized or secondarily precipitated zircon. Secondary zircon formed via dissolution-reprecipitation has been reported as having a high degree of porosity that anneals over time (e.g., Martin et al. 2008 and references therein);

this texture has not been observed in or along the cracks in the samples we examined. Solid-state zircon recrystallization is frequently identified via regions of zircon that are featureless in CL and cross-cut pre-existing igneous zonation CL (or by the presence of "ghost" zoning—remnants of primary zoning that are observable but relatively weak (Hoskin and Black 2000)). At the scale of resolution for the CL images of zircons used in this study, there are no observable variations in CL intensity where primary magmatic CL banding is cross-cut by cracks.

As shown in Figure 7, the compositions of cracks display a markedly different trend in composition space from that associated with oscillatory, magmatic CL bands: elevations in Ce/Si and P/Si ratios near cracks are greater in magnitude than those associated with primary magmatic CL bands, whereas enrichments in Y/Si near cracks are proportionately smaller. If we interpret the composition vector defined by CL bands as a signature of igneous zircon, the elevated Ce/Si ratio associated with the crack in Figure 7 resembles that expected for metamorphic or hydrothermal zircon compared to magmatic zircon (e.g., Geisler et al. 2003; Hoskin 2005), but the increase in P/Si associated with the crack is too large. (Hoskin and Black (2000) suggest that recrystallized zircons are generally less enriched in P relative to igneous zircon.) Likewise, Y should be more enriched in the metamorphic/hydrothermal zircon (Hoskin 2005), but it appears to be less enriched in the crack relative to the trend for nominally igneous zircon. Thus, the geochemical signatures of trace-element-enriched zircon domains associated with cracks do not unambiguously identify them as belonging to a previously recognized class of metamorphic or hydrothermal zircons.

We are left with an ambiguous set of constraints regarding the origin of trace element enrichments associated with cracks in zircons: The regular, correlated enrichments in multiple elements, lack of associated anomalies in Zr/Si ratios, and lack of SEM evidence for discrete alteration phases seem to point strongly toward a generation of secondary zircon that grew or recrystallized along the surfaces of open (fluid filled?) fractures, or underwent chemical exchange with fluids in cracks. Yet, the composition of this crack-associated secondary zircon does not closely resemble that of known metamorphic and hydrothermal zircons, at least as sampled at the coarser scales accessible to conventional SIMS. We believe the most plausible explanations are either 1) that the thin veneer of secondary zircon in Jack Hills zircons samples a crustal fluid different in trace element composition from those common to previously studied younger zircons, or 2) that the process of creating thin zones of secondary zircon on crack surfaces differs in some fundamental way from those that control the compositions of coarser metamorphic and hydrothermal domains.

4.3. Micron-scale high-Ti regions ("hot spots")

Both Jack Hills and Adirondack zircons analyzed in this study contain small (≤ 1 μm) inclusions that are Ti-rich, as evidenced by NanoSIMS $^{49}Ti^+$ ion images (e.g., Figure 2). These inclusions have both a positive and negative impact on the accuracy of the Ti-in-zircon thermometer. On one hand, this thermometer yields accurate temperatures only in cases where one independently knows $a_{\mathrm{TiO_2}}$ and $a_{\mathrm{SiO_2}}$ of the melt and the pressure at which the zircon grew (Watson and Harrison 2005; Watson et al. 2006; Ferry and Watson 2007). Past applications of this thermometer have generally assumed $a_{\mathrm{TiO_2}} = 1$. The presence of Ti-rich inclusions in magmatic zircon supports the assumption that rutile activity is high (although our study does not demonstrate whether such inclusions are rutile, ilmenite or another Ti-rich phase). On the other hand, if one mistakenly included Ti-rich inclusions in zircon analyses the thermometer would provide spuriously high growth/crystallization temperatures. Large (> ~1 μm) inclusions of this kind might be easily recognized and avoided in routine optical imaging before or after analyses, but we find some examples of inclusions that would be difficult to detect without high-resolution ion imaging or unusually careful SEM imaging (e.g., Figure 3). The effects of sampling rutile or other high-Ti inclusions on apparent temperature as determined via [Ti] has been documented by several authors interested in applying Ti-thermometry to Hadean and Archean Jack Hills zircons (e.g., Harrison and Schmitt 2007; Page et al. 2007). In this study, submicron Ti-rich inclusions display [Ti] concentrations ~ 40 times that of the background (after correction for beam broadening), corresponding to temperatures in excess of 1100ºC for a background of 3 ppm Ti. Similarly, a conventional SIMS analysis of an analytical area of 20 × 20 μm containing one such inclusion would raise the apparent temperature by tens of degrees.

4.4. Comparisons with previous studies of trace-element zonation in zircon

Several authors have investigated potential relations between Ti and REE abundances in zircon and between trace-element abundances and CL banding. For example, Hanchar et al. (2001) conducted zircon synthesis experiments in which they noted increasingly pronounced sector zoning with increasing P and REE contents of product crystals. Similarly, Cavosie et al. (2006) noted higher abundances of REE in a dark CL sector of a doubly-zoned (e.g., oscillatory and sector zoning) concordant 3900 Ma Jack Hills zircon and Ushikubo et al. (2008) described higher [Li] in dark CL bands of several > 4 Ga Jack Hills zircons. It is also assumed that CL-dark bands, which are richer in U and Th relative to CL-bright bands, are dark (i.e., have quenched CL emissions) due to radiation damage to the crystal lattice (e.g., Nasdala et al. 2003 and references therein).

Ti variability in single zircons at multiple scales (e.g., << 300 μm and ~ 300 μm; Page et al. 2007) and undulating [Ti] that appears to correlate with other trace element concentrations (e.g., REE) or core/rim domains (as identified by CL imaging) have been attributed to disequilibrium partitioning at the solid-melt interface (Page et al. 2007; Fu et al. 2008; Hiess et al. 2008). Page et al. (2007) noted no clear correlation between CL banding and Ti content in a larger sample of the same megacryst (KIM-5) or in various other kimberlitic zircons. As with other studies reviewed here, these analyses are limited by the coarse resolution of conventional SIMS analyses (e.g., 5–20 μm). Very few cratonic and kimberlitic zircons showed positive correlations between [Ti] and REE contents; Page et al. (2007) suggested that trace element incorporation in those zircons which do show correlated, elevated values may be due to any of the following: zircon lattice defects, non-equilibrium processes, or non-Henrian partitioning behavior, in agreement with our observations above.

Using Ti-thermometry and SHRIMP REE data, Lowery Claiborne et al. (2006) showed a general depletion of MREE and LREE with decreasing [Ti] and concluded that this correlation reflects decreasing temperature. Compositional variations across tens of μm in zircons from the Nevada Spirit Batholith indicate positive correlations between [Ti] (and hence temperatures) and LREE and MREE concentrations (Lowery Claiborne et al. 2006). Such observations in zircons from regions other than the Jack Hills suggest that the trace-element correlations with Ti observed in this study may be common among zircon populations. Although the spot size of SHRIMP analyses (~ 20 μm beam diameter) did not allow Lowery Claiborne et al. (2006) to isolate individual oscillatory bands thinner than the beam diameter, they did note higher [Ti] in wide, bright CL zones and lower [Ti] in dark CL zones—a trend opposite that which we present here.

Harrison and Schmitt (2007) reported Ti concentration data for several Jack Hills zircons that display "complex CL-banding" yet preserve nearly homogeneous Ti compositions at the scale of measurement (O^- beam, 4 μm spot; Cs^+ beam, 1 μm spot, but with relatively poor sensitivity). They presented ion images from several grains that suggest that [Ti] does not correlate with CL growth bands at the scale of measurement. The authors suggested that complex internal CL patterns may mislead investigators into creating speculative complicated growth histories that are not borne out by Ti thermometry (they observed variations in Ti, averaged over ~ 10 μm scales, that correspond to variations in T of less than 50°C). Although not all NanoSIMS images of this study display strong correlations between CL bands and [Ti], we note that correlations occur at scales smaller than that which can be analyzed by a conventional SIMS O^- beam. In principle, the variations we observe could be spatially resolved on a conventional ion microprobe using a Cs^+ primary beam. The failure of Harrison and Schmitt to observe CL-concordant banding using this method might be due to the 4x lower yield of negative secondary $^{48}TiO^-$ ions relative to Ti^+ yields achievable with an O^- primary beam.

Hiess et al. (2008) also found no systematic relationship between Ti concentrations and CL banding in zircons from West Greenland, but they acknowledged that CL banding is frequently finer than the scale of their analyses. They presented [Ti] maps for three zircon crystals (see Figure 7 in Hiess et al. 2008): weak correlations between CL zoning and Ti distribution as well as cracks and high-Ti inclusions are observable despite the maps' coarse pixelation (1 pixel corresponds to an individually analyzed 5 × 5 micron area). Together with the data of Lowery Claiborne et al. (2006), the observations of correlated CL zoning and trace elements presented by Hiess et al. (2008) suggest that correlated Ti and REE distributions (as a proxy for CL banding) may be common among zircons, given the spatial and temporal domains distinctly different from those of the Jack Hills and Adirondack zircons presented here.

5. Conclusions

We find the following key features of trace element distributions in zircons:

(1) The NanoSIMS, with a linear spatial resolution of hundreds of nm while operating in scanning mode with a primary O^- beam, is well-suited for characterizing sub-micron chemical variations of order ppm and greater. Because the width of cathodoluminescent banding can range from several μm to tens of nm, the NanoSIMS enables analysis of individual bands rather than averaging over several CL domains, as is common in conventional ion microprobe analyses.

(2) As suggested by previous studies, Ti-thermometry should only be applied to regions of an individual zircon that are free of cracks and Ti-rich inclusions. Without a preliminary, high-resolution characterization of the zircon surface using SEM-EDS, thin cracks enriched in Ti as well as Ti-bearing inclusions several hundreds of nm in diameter may be inadvertently analyzed—particularly by larger, ca. 20 μm diameter beams characteristic of SHRIMP and traditional SIMS or by depth profiling down into inclusions initially below the surface during rastering—adding tens to hundreds of degrees to the nominal Ti temperature of zircon.

(3) Trace elements appear to be enriched in or along the edges of cracks in the Jack Hills zircons analyzed. The magnitude of these enrichments defines a trend distinctly different from the trend that characterizes trace-element enrichments correlative to CL banding and may therefore indicate a different mechanism of incorporation. Based solely on the relative enrichments of $^{89}Y^+/^{28}Si^+$, $^{49}Ti^+/^{28}Si^+$, $^{31}P^+/^{28}Si^+$, and $^{140}Ce^+/^{28}Si^+$, it is not possible to discern whether the apparent secondary zircon in or along the cracks is metamorphic or hydrothermal in origin.

(4) Abundances and distributions of the four trace elements analyzed in this study (i.e., Ti, Y, P, Ce) are spatially correlated to CL banding; the highest trace element concentrations correspond to CL-dark bands in sector-zoned areas of individual zircons. Two qualitative types of images were observed: those with strong correlations among the trace elements and CL banding and those with more subtle correlations among the trace elements and CL banding. These two populations were determined to be statistically different at the 99th percentile. The compositional variations associated with CL-concordant banding define linear trends in two-dimensional composition space, confirmed via principal component analysis.

At the low apparent temperatures of growth (i.e., 680–720°C) recorded by the Ti-in-zircon thermometer for most Jack Hills zircons, conditions at the crystal-melt interface may have deviated from thermodynamic equilibrium. For those sub-μm scale regions of concordant higher [Ti] and CL banding, there is a greater chance for diffusive re-equilibration based on rapid diffusivity of Ti in the melt; however, based on data for equilibrium partitioning, the sub-μm to μm scale of the variations and their association with sector zones suggest a crystal surface paired kinetic-diffusion effect leading to correlated growth entrapment of Y, P, Ce, and Ti.

Acknowledgments

The authors thank Yunbin Guan and Chi Ma for technical assistance on the NanoSIMS and FE-SEM, Mike Baker and Eric Essene for thoughtful comments on earlier versions of this manuscript, and M.E. Bickford and two anonymous reviewers for their constructive reviews. Financial support for this study was provided by a grant from the Moore Foundation to the Caltech Microanalysis Center.

References

Armstrong JT (1988) Quantitative analysis of silicate and oxide minerals: Comparison of Monte Carlo, ZAF, and Φ (ρz) procedures. In: Newbury DE (ed) Microbeam analysis—1988. San Francisco Press, San Francisco, pp 239-246

Bacon CR (1989) Crystallization of accessory phases in magmas by local saturation adjacent to phenocrysts. Geochim Cosmochim Acta 53:1055-1066

Cavosie AJ (2005) Geochemistry of >3900 Ma detrital zircons from Jack Hills, Western Australia. Ph.D. thesis. University of Wisconsin-Madison, Madison, WI

Cavosie AJ, Valley JW, Wilde SA, E.I.M.F. (2006) Correlated microanalysis of zircon: Trace element, $\delta^{18}O$, and U-Th-Pb isotopic constraints on the igneous origin of complex >3900 Ma detrital grains. Geochim Cosmochim Acta 70:5601-5616

Cavosie AJ, Wilde SA, Lui D, Wieblen PW, Valley JW (2004) Internal zoning and U-Th-Pb chemistry of Jack Hills detrital zircons: a mineral record of early Archean to Mesoproterozoic (4348-1576) magmatism. Precambrian Res 135:251-279

Cherniak DJ, Watson EB (2007) Ti diffusion in zircon. Chem Geol 242:470-483

Corfu F, Hanchar J, Hoskin PWO, Kinny P (2003) Atlas of zircon textures. In: Hanchar JM, Hoskin PWO (eds) Zircon. Rev Mineral Geochem 53:469-500

Dowty E (1976) Crystal structure and crystal growth: II. Sector zoning in minerals. Am Mineral 61:460-469

Ferriss EA, Essene EJ, Becker U (2008) Computational study of the effect of pressure on the Ti-in-zircon geothermometer. Eur J Mineral 20:745-755

Ferry JM, Watson EB (2007) New thermodynamic models and revised calibrations for the Ti-in-zircon and Zr-in-rutile thermometers. Contrib Mineral Petrol 154:429-437

Finch RJ, Hanchar JM, Hoskin PWO, Burns PC (2001) Rare-earth elements in synthetic zircon: Part 2. A single-crystal X-ray study of xenotime substitution. Am Mineral 86:681-689

Fletcher IR, Rosman KJR, Libby WG (1988) Sm-Nd, Pb-Pb, and Rb-Sr geochronology of the Manfred Complex, Mount Narryer, Western Australia. Precambrian Res 38:342-354

Fu B, Page FZ, Cavosie AJ, Fournelle J, Kita NK, Lackey JS, Wilde SA, Valley JW (2008) Ti-in-zircon thermometry: applications and limitations. Contrib Mineral Petrol 156:197-215

Geisler T, Rashwan AA, Rahn MKW, Poller U, Zwingmann H, Pidgeon RT, Schleicher H, Tomaschek F (2003) Low-temperature hydrothermal alteration of natural metamict zircons from the Eastern Desert, Egypt. Mineral Mag 67:485-508

Green TH, Watson EB (1982) Crystallization of apatite in natural magmas under high pressure hydrous conditions, with particular reference to orogenic rock series. Contrib Mineral Petrol 79:96-105

Hanchar JM, Finch RJ, Hoskin PWO, Watson EB, Cherniak DJ, Mariano AN (2001) Rare earth elements in synthetic zircon: Part 1. Synthesis, and rare earth element and phosphorus doping. Am Mineral 86:667-680

Hanchar JM, Rudnick RL (1995) Revealing hidden structures: The application of cathodoluminescence and back-scattered electron imaging to dating zircons from lower crustal xenoliths. Lithos 36:289-303

Harrison TM, Aikman A, Holden P, Walker AM, McFarlane C, Rubatto D, Watson EB (2005) Testing the Ti-in-zircon thermometer. Eos Trans AGU 86:Abstract V41F-1540

Harrison TM, Schmitt AK (2007) High sensitivity mapping of Ti distributions in Hadean zircons. Earth Planet Sci Lett 261:9-19

Harrison TM, Watson EB (1983) Kinetics of zircon dissolution and zirconium diffusion in granitic melts of variable water content. Contrib Mineral Petrol 84:66-72

Harrison TM, Watson EB (1984) The behavior of apatite during crustal anatexis: equilibrium and kinetic considerations. Geochim Cosmochim Acta 48:1467-1477

Harrison TM, Watson EB, Aikman AB (2007) Temperature spectra of zircon crystallization in plutonic rocks. Geology 35:635-638

Hayden LA, Watson EB (2007) Rutile saturation in hydrous silicate melts and its bearing on Ti-thermometry of quartz and zircon. Earth Planet Sci Lett 258:561-568

Heumann MJ, Bickford ME, Hill BM, McLelland JM, Selleck BW, Jercinovic MJ (2006) Timing of anatexis in metapelites from the Adirondack lowlands and southern highlands: A manifestation of the Shawinigan orogeny and subsequent anorthosite-mangerite-charnockite-granite magmatism. Geol Soc Am Bull 118:1283-1298

Hiess J, Nutman AP, Bennett VC, Holden P (2008) Ti-in-zircon thermometry applied to contrasting Archean metamorphic and igneous systems. Chem Geol 247:323-338

Holden P, Aikman A, Ireland TR, Hiess J (2005) Does Ti record the crystallization temperature of zircon? Eos Trans AGU 86:Abstract V41F-1539

Hoskin PWO (2000) Patterns of chaos: Fractal statistics and the oscillatory chemistry of zircon. Geochim Cosmochim Acta 64:1905-1923

Hoskin PWO (2005) Trace-element composition of hydrothermal zircon and the alteration of Hadean zircon from the Jack Hills, Australia. Geochim Cosmochim Acta 69(3):637-648

Hoskin PWO, Black LP (2000) Metamorphic zircon formation by solid-state recrystallization of protolith igneous zircon. J Metamorph Geol 18:423-439

Hoskin PWO, Ireland TR (2000) Rare earth element chemistry of zircon and its use as a provenance indicator. Geology 28:627-630

Hoskin PWO, Schaltegger U (2003) The composition of zircon and igneous and metamorphic petrogenesis. In: Hanchar JM, Hoskin PWO (eds) Zircon. Rev Mineral Geochem 53: 27-62

Kinny PD, Nutman AP (1996) Zirconology of the Meeberrie gneiss, Yilgarn Craton, Western Australia: an early Archaean migmatite. Precambrian Res 78:165-178

Lowery Claiborne L, Miller CF, Walker BA, Wooden JL, Mazdab FZ, Bea F (2006) Tracking magmatic processes through Zr/Hf ratios in rocks and Hf and Ti zoning in zircons: An example from the Spirit Mountain batholith, Nevada. Mineral Mag 70:517-543

Maas R, Kinny PD, Williams IS, Froude DO, Compston W (1992) The Earth's oldest known crust: A geochronological and geochemical study of 3900 - 4200 Ma old detrital zircons from Mt. Narryer and Jack Hills, Western Australia. Geochim Cosmochim Acta 56:1281-1300

Maas R, McCullough MT (1991) The provenance of Archean clastic metasediments in the Narryer Gneiss Complex, Western Australia: Trace element geochemistry, Nd isotopes, and U-Pb ages for detrital zircons. Geochim Cosmochim Acta 55:1915-1932

Martin LAJ, Duchene S, Deloule E, Vanderhaeghe O (2008) Mobility of trace elements and oxygen in zircon during metamorphism: Consequences for geochemical tracing. Earth Planet Sci Lett 267:161-174

McLelland JM, Bickford ME, Hill BM, Clechenko CC, Valley JW, Hamilton MA (2004) Direct dating of Adirondack massif anorthosite by U-Pb SHRIMP analysis of igneous zircon: Implications for AMCG complexes. Geol Soc Am Bull 116:1299-1317

Mojzsis SJ, Harrison TM, Pidgeon RT (2001) Oxygen-isotope evidence from ancient zircons for liquid water at the Earth's surface 4,300 Myr ago. Nature 409:178-181

Myers JS (1988) Early Archean Narryer Gneiss Complex, Yilgarn Craton, Western Australia. Precambrian Res 38:297-307

Myers JS, Williams IR (1985) Early Precambrian crustal evolution at Mount Narryer, Western Australia. Precambrian Res 27:153-163

Nakamura Y (1973) Origin of sector-zoning of igneous clinopyroxene. Am Mineral 58:986-990

Nasdala L, Zhang M, Kempe U, Panczer G, Gaft M, Andrut M, Plotze M (2003) Spectroscopic methods applied to zircon. In: Hanchar JM, Hoskin PWO (eds) Zircon. Rev Mineral Geochem 53: 427-467

Ohnenstetter D, Cesbron F, Remond G, Caruba R, Claude J-M (1991) Emissions de cathodoluminescence se deux populations de zircons naturels: tentative d'interpretation. C. R. Acad. Sci. Paris 313:641-647

Page FZ, Fu B, Kita NT, Fournelle J, Spicuzza MJ, Schulze DJ, Viljoen F, Basei MAS, Valley JW (2007) Zircons from kimberlite: new insights from oxygen isotopes, trace elements, and Ti in zircon thermometry. Geochim Cosmochim Acta 71:3887-3903

Peck WH, Valley JW, Wilde SA, Graham CM (2001) Oxygen isotope ratios and rare earth elements in 3.3 to 4.4 Ga zircons: Ion microprobe evidence for high δ^{18}O continental crust and oceans in the Early Archean. Geochim Cosmochim Acta 65:4215-4229

Rapp RP, Watson EB (1986) Monazite solubility and dissolution kinetics: implications for thorium and light rare earth chemistry of felsic magmas. Contrib Mineral Petrol 94:304-316

Reddy SM, Timms NE, Pantleon W, Trimby P (2007) Quantitative characterizations of plastic deformation of zircon and geological implications. Contrib Mineral Petrol 153:625-645

Remond G, Blanc P, Cesbron F, Ohnenstetter D, Rouer O (1995) Cathodoluminescence of rare earth doped zircons. II. Relationship between the distribution of the doping elements and the contrasts of images. Scanning Microscopy Supplement 9:57-76

Rimsa A, Whitehouse MJ, Johansson L, Piazolo S (2007) Brittle fracturing and fracture healing of zircon: An integrated cathodoluminescence, EBSD, U-Th-Pb, and REE study. Am Mineral 92:1213-1224

Ryerson FJ, Hess PC (1980) The role of P_2O_5 in silicate melts. Geochim Cosmochim Acta 44:611-624

Shannon RD (1976) Revised effective ionic radii and systematic studies of interatomic distances in halides and chalcogenides. Acta Crystallogr A32:751-767

Smith VG, Tiller WA, Rutter JW (1955) A mathematical analysis of solute redistribution during solidification. Can J Phys 33:723-745

Speer JA (1982) Zircon. In: Ribbe PH (ed) Orthosilicates. Rev Mineral 5: 67-112

Timms NE, Kinny PD, Reddy SM (2006) Enhanced diffusion of uranium and thorium linked to crystal plasticity in zircon. Geochemical Trans 7:10

Trail D, Mojzsis SJ, Harrison TM, Schmitt AK, Watson EB, Young ED (2007) Constraints on Hadean zircon protoliths from oxygen isotopes, Ti-thermometry, and rare earth elements. Geochem, Geophys, Geosy 8:1-22

Ushikubo T, Kita NK, Cavosie AJ, Wilde SA, Rudnick RL, Valley JW (2008) Lithium in Jack Hills zircons: Evidence for extreme weathering of Earth's earliest crust. Earth Planet Sci Lett 272:666-676

Valley JW, Cavosie AJ, Fu B, Peck WH, Wilde SA (2006) Comment on "Heterogeneous Hadean Hafnium: Evidence of continental crust at 4.4 to 4.5 Ga". Science 312:1139a

Valley JW, Chiarenzelli JR, McLelland JM (1994) Oxygen isotope geochemistry of zircon. Earth Planet Sci Lett 126:187-206

Valley JW, Lackey JS, Cavosie AJ, Clechenko CC, Spicuzza MJ, Basei MAS, Bindeman IN, Ferreira VP, Sial AN, King EM, Peck WH, Sinha AK, Wei CS (2005) 4.4 billion years of crustal maturation: oxygen isotope ratios of magmatic zircon. Contrib Mineral Petrol 150:561-580

Wasteneys H, McLelland J, Lumbers S (1999) Precise zircon geochronology in the Adirondack Lowlands and implications for revising plate-tectonic models of the Central Metasedimentary Belt and Adirondack Mountains, Grenville Province, Ontario and New York. Can J Earth Sci 36:967-984

Watson EB (1996) Surface enrichment and trace-element uptake during crystal growth. Geochim Cosmochim Acta 60(24):5013-5020

Watson EB, Harrison TM (2005) Zircon thermometer reveals minimum melting conditions on earliest Earth. Science 308:841-844

Watson EB, Liang Y (1995) A simple model for sector zoning in slowly grown crystals: Implications for growth rate and lattice diffusion, with emphasis on accessory minerals in crustal rocks. Am Mineral 80:1179-1187

Watson EB, Wark DA, Thomas JB (2006) Crystallization thermometers for zircon and rutile. Contrib Mineral Petrol 151:413-433

Chapter 2

AN EXPERIMENTAL STUDY OF TI PARTITIONING BETWEEN ZIRCON AND COEXISTING GRANITIC MELT

Abstract

We conducted 10 kbar experiments on a series of synthetic and natural granitic compositions (enriched in TiO_2 and ZrO_2) at temperatures of 1400, 1300, and 1200°C. All liquids were zircon-saturated and 6 of the 16 experimental glasses were also saturated in rutile. SiO_2 contents of the quenched glasses range from 64.2 to 70.7 wt. % and water varied from 0.4 to 7 wt. %. TiO_2 contents of the rutile-saturated quenched melts are positively correlated with run temperature and vary from 1.9 to 5.1 wt. %; ZrO_2 concentrations in the glasses also show a broad positive correlation with run temperature. At a given temperature, ZrO_2 contents of the liquids are strongly correlated with the cation-based melt parameter (Na+K+2Ca)/(Si•Al). ZrO_2 contents of the rutiles in our experiments are positively correlated with temperature and range from 7.2 to 3.2 wt. %. NanoSIMS measurements of Ti in zircon overgrowths rims in our experiments range from 760 to 112 ppm and show a positive correlation with TiO_2 content of the quenched glass and run temperature. Our Ti-in-zircon values when "adjusted" for SiO_2 and TiO_2 melt activities (i.e., log(Ti-in-zircon, ppm)+log(a_{SiO_2})-log(a_{TiO_2}) show a strong inverse correlation with 1/T; and least squares fits to the two sets of data generated in this study (synthetic bulk compositions and natural bulk compositions) yield equations with slopes that are statistically indistinguishable. This suggests that at temperatures above 1200°C other trace elements in the melt do not appear to have a substantial effect on Ti partitioning between zircon and silica-rich liquid. A weighted global fit to all of our experimental data is:

$\log(\text{Ti-in-zircon, ppm}) + \log(a_{SiO_2}) - \log(a_{TiO_2}) = (6.21 \pm 0.43) - (5918 \pm 689)/T\ (K)$. R^2 for this equation is 0.85. Our Zr-in-rutile data also yields a regression line in composition vs. 1/T space:

$\log(\text{Zr-in-rutile, ppm}) + \log(a_{SiO_2}) = (7.723 \pm 0.178) - (5184 \pm 284)/T\ (K)$; $R^2 = 0.98$. Our Ti glass contents coupled with measured zircon Ti concentrations from the same experiments allow us to calculate a zircon-melt Ti partition coefficient. Our measured $D_{Ti}^{zrc/melt}$ values are 0.014 to 0.029 and are broadly consistent with values determined from natural-zircon glass pairs.

1. Introduction

The mineral zircon ($ZrSiO_4$) is a common accessory constituent of most felsic rocks, in which it is often the most abundant structural repository of elements used to date magmatic processes (e.g., U, Hf, Th) and to make inferences concerning petrogenesis (e.g., REEs). Given the robustness of zircon against physical and chemical alteration as well as diffusive re-equilibration, it is often the only material that remains of a given rock suite, thus making it a suitable target for a wide array of geochemical applications. These applications include geothermometry, which has become feasible via the Ti-in-zircon thermometer (Watson et al. 2006; Ferry and Watson 2007), in which the Ti content of zircon, after adjusting for the SiO_2 and TiO_2 activities in the coexisting melt, has been shown to be a linear function of reciprocal absolute temperature. In the cases of ancient zircon (e.g., Jack Hills; Maas et al. 1992; Menneken et al. 2007), it is often possible to infer the activities of SiO_2 and TiO_2 in the now non-existent melt based on mineral inclusions in the zircons. The relatively low temperatures calculated for these ancient zircons have been used to make fundamental inferences concerning the nature of the early Earth (Watson and Harrison 2005). However, recent work has called into question the calibration of the thermometer (Ferriss et al. 2008; Reid et al. 2009) as well as its usefulness as an indicator of zircon parental melt composition (Fu et al. 2008) or crystallization temperature (Hiess et al. 2008). In addition, several authors have noted correlations at the scale of 10s of microns between Ti and other minor and trace element concentrations: Ti inversely correlated with Hf and U in some zircons from the Spirit batholith (Lowery Claiborne et al. 2006) and Ti positively correlated with zones of high REE concentrations in some zircons from kimberlites (Page et al. 2007).

A NanoSIMS study of several Jack Hills zircons (Hofmann et al. 2009a) revealed that, at least in some oscillatory- and sector-zoned zircons, Ti distributions were spatially correlated at the sub-micron scale with distributions of Y, P, and Ce, all of which increased in concentration within dark cathodoluminescent (CL) bands and decreased in concentration within adjacent light CL bands. Similar observations were made on zircons of known provenance (e.g., zircons from the Sierra Nevada batholith and the Quottoon Igneous Complex) (Hofmann et al. 2009b). While the growth rates of zircons in magmatic systems are poorly constrained, it is difficult to accept that oscillations in Ti by factors of 2 over length scales of 100s of nm really reflect temperature oscillations in the granitic system in which the zircon grew. These fine-scale variations of Ti in zircon and the fact that Ti is generally positively coupled with other trace elements led Hofmann et al. (2009a) to conclude that kinetic effects at the crystal-melt interface may be important in at least partially controlling the concentration of trace elements in zircon. If true, such processes would greatly complicate inferring temperatures from Ti in zircon.

The fine-scale variations in Ti observed in many natural zircons and the fact that these variations are almost universally positively coupled with concentrations of other trace elements has direct implications for the current calibration of the Ti-in-zircon thermometer: (1) zircons from granitic systems where temperatures could be independently estimated from mineral-melt or mineral-mineral equilibria were used to help define the calibration line at temperatures below ~ 800°C (Watson et al. 2006; Ferry and Watson 2007). The conventional SIMS techniques used to analyze these grains would have averaged any sub-micron oscillatory zoning in Ti if it were present; the meaning of such an average Ti value in terms of equilibrium crystal-liquid partitioning is unclear. (2) The experiments of Watson et al. (2006) and Ferry and Watson (2007) used in constraining the high-temperature end of the calibration line were conducted using synthetic bulk compositions that were essentially free of trace elements. If Ti partitioning between zircon and liquid is coupled with the partitioning of trace elements such as Y, P, etc., then the results of such experiments might not be applicable to natural zircons. Finally, the need to grow crystals large enough to be analyzable using conventional SIMS and electron microprobe techniques (i.e., at least 20 μm in diameter; Watson et al. 2006) required bulk compositions with extremely high water and K_2O contents potentially making it difficult to estimate the silica activity of these quartz-free melts.

The purpose of this study was to investigate experimentally the partitioning of Ti between zircon and a series of granitic melt compositions that were either free of trace elements or contained them at concentrations of order ca. 100s to 1000s of parts per million (ppm) by weight. Because all the bulk compositions had relatively similar SiO_2, Al_2O_3, and alkali contents and Na_2O/K_2O values, any observed variation in zircon-liquid Ti partitioning between the synthetic bulk compositions (trace-element free) and the natural bulk compositions would point to the possible effect of trace elements on Ti partitioning between zircon and melt. Further, unlike earlier experimental studies in which the bulk compositions were vapor-saturated at 10 kbar and the coexisting liquids could not be analyzed (Watson et al. 2006; Ferry and Watson 2007), the liquids in our experiments quenched to large, easily analyzed regions of glass allowing us for the first time to determine zircon-liquid Ti partition coefficients. The ability to analyze the small overgrowth rims on our zircon run products was only made possible by the use of Caltech's CAMECA NanoSIMS 50L. The high spatial resolution of the NanoSIMS (~ 100–500 nm diameter beam on the sample surface while operating with a Cs+ primary beam) removes the restriction of having to grow zircons that are 10s of microns in size and the need to flux the experimental charge either with very high water contents or lead- or lithium-molybdenate-based fluxes, thereby enabling zircons to be synthesized from melts closer in composition to natural granites.

2. Experimental and Analytical Techniques

2.1 Starting Materials

The bulk starting compositions used in this study were constructed to be close to that of Westerly granite—a two-mica, plagioclase-microcline-quartz granite for which the onset of melting occurs close to the quartz-albite-orthoclase ternary minimum (Tuttle and Bowen 1958). A minimum-melt granite bulk composition was chosen for several reasons: 1) experiments can be performed over a large range in temperatures without intersecting a quartz or feldspar primary phase volume, which would lead to significant changes in liquid composition; 2) the absence of any major crystallizing phases means that the experimental charges are mostly liquid, thus minimizing any potential quench effects and providing large areas of quenched glass for analysis; 3) the first application of the Ti-in-zircon thermometer was to Hadean Jack Hills zircons (Watson and Harrison 2005), and the results of that study were interpreted as evidence for minimum melting on the early Earth.

Three series of starting materials were created: a synthetic, nominally anhydrous series of mixes (labeled MMG for minimum-melt granite), a synthetic hydrated series of mixes (containing up to 6.4 wt. % H_2O, labeled MMGh), and a series of modified natural granite compositions (identified as "GO") that are based on USGS granite G-2 powder (Gladney et al. 1992; Govindaraju 1994) and synthetic orthoclase glass. The bulk compositions of all mixes are listed in Table 1. MMG-1 was constructed using high-purity oxide and carbonate powders and ground for ~ 3 h under ethanol in an automated alumina mortar. After decarbonation, splits of this mix were used to construct the starting mixes MMG-2, -3, -4, and -5, which consisted of varying proportions of MMG-1 plus SiO_2, TiO_2, ZrO_2, and natural zircon. The proportions of ZrO_2 and zircon were adjusted so as to ensure that each bulk composition would be zircon saturated at the appropriate run temperature; ZrO_2 and zircon proportions were determined based on the zircon saturation model of Watson and Harrison (1983). The TiO_2 contents were chosen so as to produce a mix that would be either rutile-saturated or undersaturated at run temperature as predicted by the rutile saturation model of Gaetani et al. (2008). Each of these mixes was ground by hand in an alumina mortar under ethanol for ~ 30 min.

In order to make the MMGh series of bulk compositions, we first constructed a hydrous composition (H-2) with a nominal H_2O content of 6.6 wt. % using high-purity oxides, carbonates, and hydroxides ($Al(OH)_3$ and $Mg(OH)_2$); the oxide + carbonate portion of the mix was ground for ~ 3 h and decarbonated and then the hydroxides were added and the powder was ground for an additional 2 h. MMGh-1, -2, and -3 bulk compositions were constructed by mixing together one of the MMG bulk compositions (depending on the anticipated run temperature) plus H-2 + zircon ± ZrO_2 ± TiO_2. MMGh-4 consisted of H-2, SiO_2, ZrO_2, and zircon. All MMGh-series starting compositions were designed to be zircon saturated and each was mixed by hand under ethanol in an alumina mortar for ~ 30 min.

Table 1. Nominal starting mix compositions (in weight percent on a volatile-free basis) and zircon seed crystal composition

Mix	SiO_2	TiO_2	Al_2O_3	FeO*	MnO	MgO	CaO	Na_2O	K_2O	P_2O_5	ZrO_2	HfO_2	TE
MMG-1	71.15	2.00	14.10	1.71	-	0.36	1.49	3.31	5.38	-	0.50	-	-
MMG-2	68.73	5.09	12.48	1.51	-	0.32	1.32	2.93	4.76	-	2.84	0.02	-
MMG-3	68.84	2.73	13.73	1.65	-	0.34	1.43	3.19	5.18	-	2.89	0.02	-
MMG-4	69.25	3.57	13.21	1.60	-	0.34	1.39	3.10	5.04	-	2.49	0.02	-
MMG-5	71.16	1.84	12.95	1.57	-	0.33	1.37	3.04	4.94	-	2.80	0.02	-
MMGh-1	68.74	4.08	13.09	1.19	-	0.34	1.41	3.12	5.08	-	2.93	0.02	-
MMGh-2	70.85	1.90	13.18	1.21	-	0.34	1.41	3.14	5.11	-	2.83	0.02	-
MMGh-3	70.58	3.00	13.14	1.22	-	0.34	1.41	3.13	5.09	-	2.06	0.02	-
MMGh-4	73.00	1.84	12.56	0.79	-	0.33	1.37	3.04	4.95	-	2.10	0.02	-
GO-0	68.39	0.40	15.92	1.99	0.02	0.62	1.61	3.35	6.70	0.12	0.03	0.001	0.52
GO-1	68.62	5.20	12.04	1.50	0.02	0.47	1.22	2.54	5.07	0.09	2.90	0.02	0.32
GO-2	69.89	1.92	13.16	1.64	0.02	0.51	1.33	2.77	5.54	0.10	2.70	0.06	0.35
GO-3	68.88	3.51	13.16	1.58	0.02	0.49	1.34	2.82	5.48	0.08	2.30	0.04	0.30
GO-4	72.02	1.71	12.46	1.49	0.02	0.46	1.27	2.68	5.18	0.08	2.33	0.02	0.28
GO-5	70.08	2.95	13.18	1.52	0.01	0.46	1.36	2.88	5.42	0.07	1.80	0.02	0.25
GO-6	71.84	0.89	13.49	1.40	0.01	0.46	1.40	2.99	5.55	0.06	1.64	0.02	0.24
H-2	72.09	2.03	13.84	0.87	-	0.36	1.51	3.35	5.45	-	0.50	-	-
G-2	69.56	0.48	15.48	2.41	0.03	0.75	1.97	4.10	4.51	0.14	0.04	<0.01	0.51
Westerly granite	72.34	0.26	14.34	1.74	-	0.37	1.52	3.37	5.47	-	-	-	-
zircon seeds	32.87	see footnote									65.90	1.15	0.07

FeO* = all Fe as FeO. Nominal water contents (wt. %) in the hydrous mixes: MMGh-1: 3.55; MMGh-2: 3.45; MMGh-3: 3.31; MMGh-4: 6.37; GO-1: 0.32; GO-2: 0.34; GO-3: 0.79; GO -4: 0.81; GO-5: 1.24; GO-6: 2.65. Dash in an oxide column indicates that the oxide was not included in mix or, in the case of Westerly granite, not reported. TE = trace elements converted to wt. % oxides. G-2 = USGS granite powder. Westerly granite composition reported in Tuttle and Bowen (1958). Average zircon seed composition determined by electron microprobe on a mm-sized zircon fragment of the same material used to generate the seeds; trace element content determined by difference; Ti determined via conversion of NanoSIMS $^{48}Ti^{16}O^-$ spot analyses to be 7 ± 2 ppm.

The base GO mix (GO-0) consisted of ~ 82% G-2 granite plus 18% synthetic orthoclase glass and was ground for ~ 2 h under ethanol. The remaining bulk compositions in the GO-series (-1, -2, -3, -4, -5, and -6) were constructed by mixing together GO-0 plus some combination of SiO_2, TiO_2, ZrO_2, and zircon and one of the MMGh powders if the bulk composition was going to be run at 1200 or 1300°C; nominal water contents of the GO-series mixes ranged from 0.3 to 2.6 wt. %. In all cases, each of the GO-series mixes consisted of at least 45% of the G-2 granite. Final GO bulk compositions were ground under ethanol by hand for ~ 30 min.

Approximately 1% finely ground zircon crystal fragments were added to each of the starting mixes to act as seeds. The source of these fragments is a large ~ 13 × 10.5 ×15 mm, translucent brownish-red crystal with a visible square pyramidal termination at one end. Although the provenance of this particular grain is uncertain, it is very similar in physical properties and composition to Mud Tank zircons (B. Watson, personal communication). A fragment of the original crystal was mounted in epoxy, polished using 0.25 μm diamond powder, and analyzed for major and minor elements on Caltech's JEOL JXA-8200 electron microprobe; the composition is listed in Table 1. Finely ground fragments were produced by first crushing < 1 mm slabs cut from this grain in a percussion mortar and then grinding the resulting pieces in an alumina mortar under ethanol for 20 min (prior to grinding, a magnet was used to remove any metal slivers that may have been introduced from the percussion mortar). The resulting slurry was poured through a 10 μm mesh attached to a vibration sieve. Material that passed through the sieve was dried overnight in a 110°C oven and stored for use as seed crystals; material that did not pass through the sieve was reground in ethanol and the process repeated. A representative sample of the fragments used as seeds (Figure 1) was imaged on Caltech's LEO 1550 VP FE-SEM under backscatter, secondary electron, and

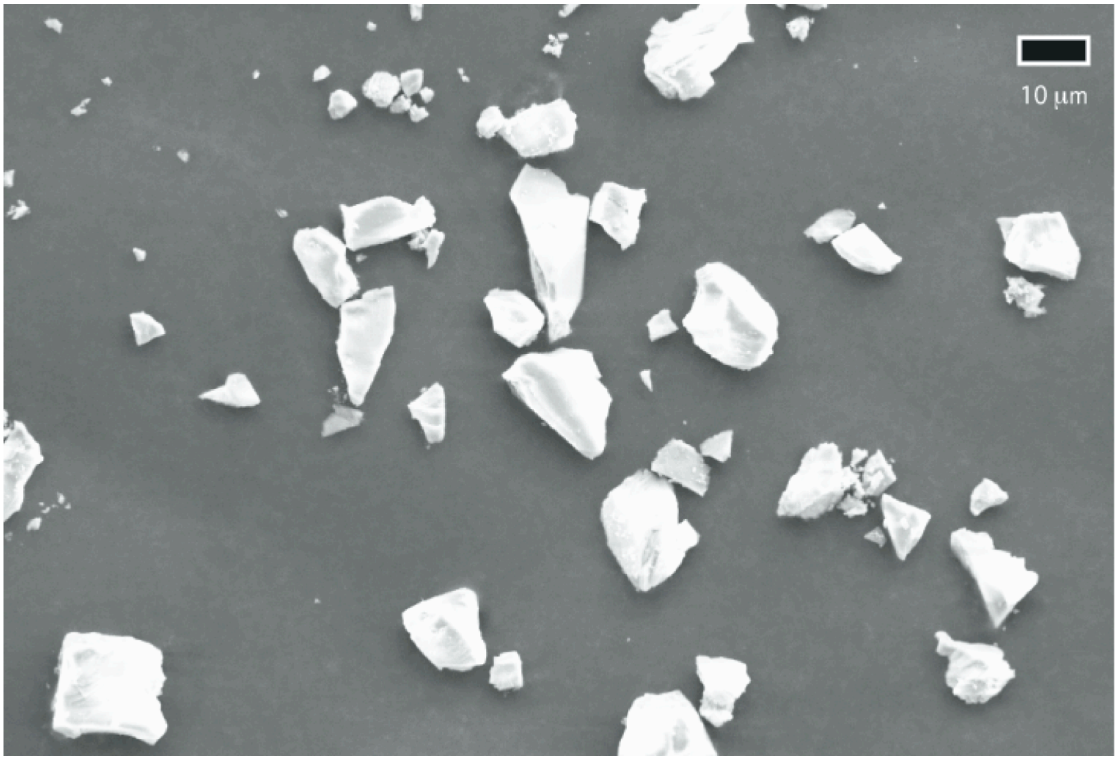

Figure 1. FE-SEM secondary electron image of seed crystals added to experimental starting powders. Scale bar is 10 microns. Note that the zircon fragments do not display characteristic igneous zircon morphology (i.e., faceted terminations, prismatic crystal faces) unlike the zircon run products (see Figure 4 for examples).

cathodoluminescence (CL) modes in order to ascertain seed morphology. Note that the fragments are generally ≤ 10 µm in longest dimension and—more importantly—display none of the crystal-face terminations seen in zircons that grow from silicate liquids.

The compositions of all of the starting mixes are listed in Table 1. For those mixes used in zircon synthesis experiments (MMG-2 to -5; MMGh-1 to -4; and GO-1 to -6), silica contents on an anhydrous basis range from 69 to 73 wt. %, Al_2O_3 contents vary between 12.5 and 13.7 wt. %, and total alkalis lie in the range 7.6 to 8.4 wt. %; Na_2O/K_2O values are 0.52 to 0.62. These values are similar to our target composition, Westerly granite, which has SiO_2, Al_2O_3, Na_2O+K_2O, and Na_2O/K_2O values of 72.3, 14.3, 8.8, and 0.62, respectively. Figure 2, a ternary plot of normative Quartz, Orthoclase, and Plagioclase, compares our starting compositions to those used in other recent experimental studies of element partitioning

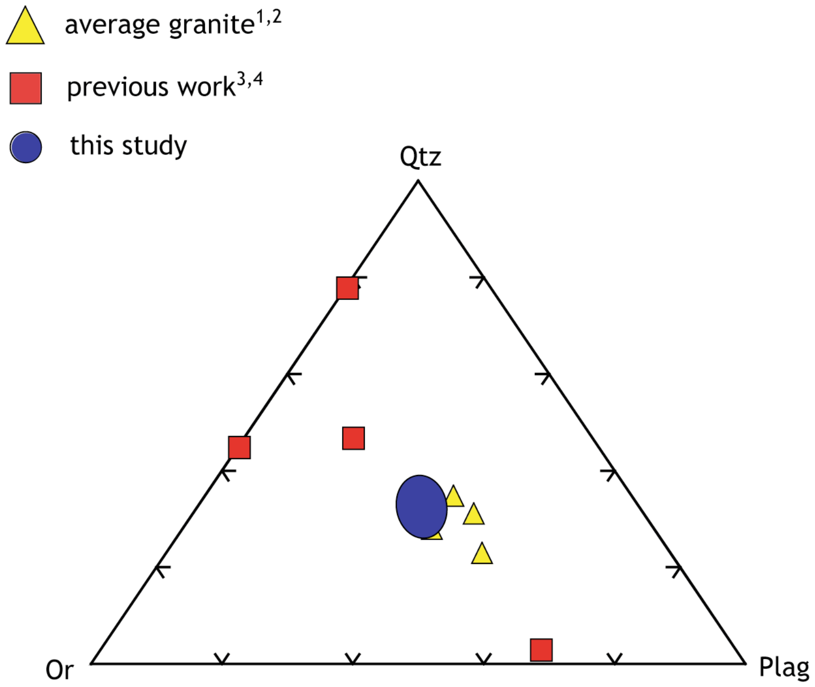

Figure 2. Normative quartz (Qtz) - orthoclase (Or) - plagioclase (Plag) ternary showing the projected locations of bulk compositions used in this study (Table 1; all lie within the blue oval); compositions of "average" granites (yellow triangles); and bulk starting compositions utilized in other experimental studies of zircon growth (red squares). Average granite compositions are from [1]Tuttle and Bowen (1958) and [2]Le Maitre (1976). "Previous work" represents the following studies: [3]Watson et al. (2006) and [4]Luo and Ayers (2009).

between zircon and silicate melt (Watson et al. 2006; Luo and Ayers 2009) and with those of average granite (Tuttle and Bowen 1958; Le Maitre 1976). Our starting mix compositions, unlike those from earlier experiments, overlap or plot close to the compositions of average granite. Finally, the nominal water contents of our starting bulk compositions range from ~ 0.3 to 6.4 wt. %.

2.2 Experimental method

All experiments were run at temperatures of 1450 to 1200°C and a pressure of 10 kbar using a piston cylinder; temperatures, run durations, coexisting phases, and phase proportions are listed in Table 2. Run assemblies consisted of inner pieces of crushable MgO, straight-walled graphite furnaces, and pressed CaF_2 outer sleeves. All starting mixes were contained within a graphite crucible sealed inside a Pt capsule: ~ 10–15 mg of starting powder was weighed into a graphite crucible, which was then placed into a Pt capsule that had been welded shut at one end; graphite powder was packed on top of the crucible, and the open end of the Pt capsule was coned and welded shut. Electron microprobe analyses of the glass from the first experiment with mix MMGh-1 (nominally 3.6 wt. % H_2O) suggested that the run had lost appreciable water either during the final weld and/or during the actual run. In order to minimize any water loss from the hydroxide powders during the final weld, capsules were partially immersed in a water bath at room temperature for the second and final weld. We address the question of water loss during a run in §3.3. Although the oxygen fugacity (f_{O_2}) was not buffered in these experiments, the graphite crucible restricts f_{O_2} in our capsules to lie on or below the graphite-C-O vapor (GCO) buffer, which is approximately QFM-1.5 at 1200°C and QFM-1.8 at 1400°C at 10 kbar (Jakobsson and Oskarsson 1994). These f_{O_2} values indicate that the majority of the Fe in our experimental glasses will be present as FeO (Kress and Carmichael 1991) and that all Ti will be present as TiO_2 (Krawczynski et al. 2009).

Pressure in these experiments was applied using the hot-piston-in technique and was controlled using a mechanical pump to within ± 30 bars of the target pressure (10 kbar). Run temperatures were monitored and controlled to within ± 2°C using a $W_3Re/W_{25}Re$ thermocouple and no pressure correction was applied to the thermocouple EMF. Based on previous determinations of the thermal profile of this piston-cylinder assembly, we estimate that our temperatures are accurate to within ± 15°C. Total run times ranged from 3-193 hours. Experiments were quenched by shutting off power to the furnace and initial quench rates were of the order of 100°C/s. After quenching, each Pt capsule was removed from the

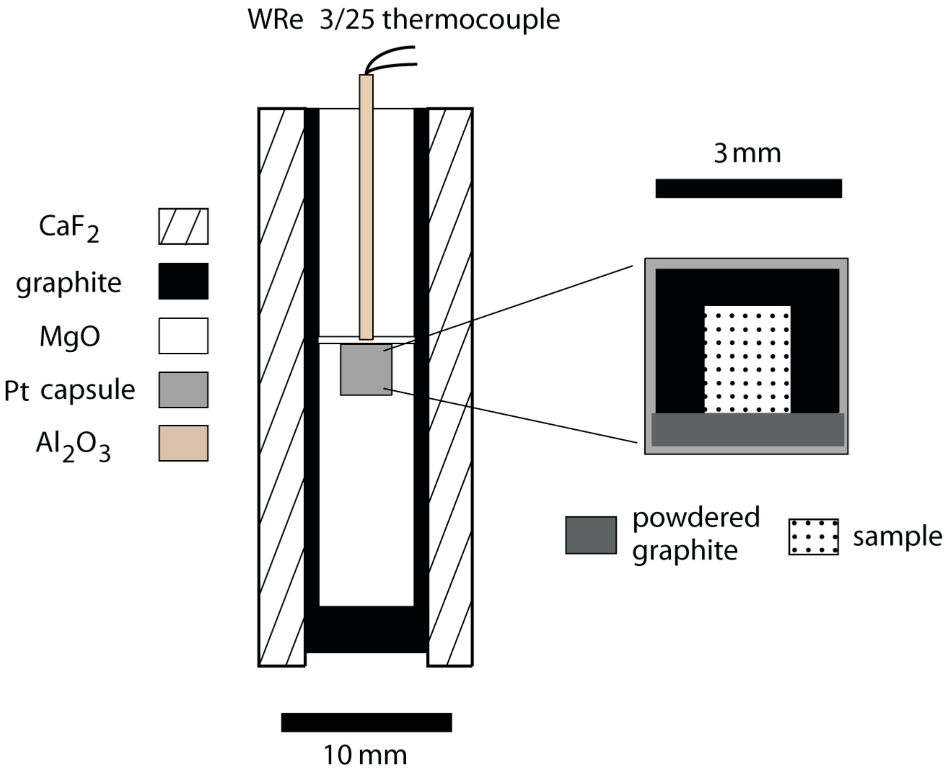

Figure 3. Schematic representation of piston-cylinder run assemblage (left) and capsule (right)

furnace assembly, mounted in epoxy, and polished for SEM, microprobe, and SIMS analysis. In all cases the final polishing was done with 0.25 μm diamond grit. Figure 3 gives a to-scale schematic of a run assemblage as well as a cross-section of a typical capsule prior to an experiment.

2.3 Analytical techniques

Mounted and polished capsules were initially viewed under reflected light and were then carbon-coated and examined using Caltech's LEO 1550 VP FE-SEM under backscatter, secondary electron, and cathodoluminescence (CL) modes in order to identify crystalline phases and to document zircon overgrowths (visible in CL). The samples were later transferred to Caltech's JEOL JXA-8200 electron microprobe for analyses of the coexisting glass and crystals in each charge. Samples were repolished with 0.25 μm diamond grit before being Au-coated in preparation for SIMS analyses.

2.3.1 Electron microprobe

Quantitative analyses of the oxides SiO_2, TiO_2, Al_2O_3, FeO*—all Fe as FeO, MnO, MgO, CaO, Na_2O, K_2O, P_2O_5, and BaO in the experimental glasses and SiO_2, TiO_2, Al_2O_3, FeO*, MgO, CaO, Na_2O, K_2O, P_2O_5, HfO_2, Y_2O_3, and Ce_2O_3 in the coexisting zircons and (if present) rutiles from all experimental products were acquired using Caltech's JEOL JXA-8200 electron microprobe. Analyses were performed using an accelerating voltage of 15 kV, a 10 nA beam current, and either a 10 μm beam for glass or a < 1 μm beam for zircon and rutile. Preliminary analyses of glasses from a subset of experiments with the GO-series bulk compositions showed that HfO_2 (the most abundant trace element in the zircon seeds) was below the detection for these analytical conditions and thus Hf was dropped from the list of elements analyzed in the glasses. Standards consisted of synthetic and natural glasses and minerals: Smithsonian rhyolite VG568 (Si for glass); zircon (Zr, Si for zircons); Shankland forsterite (Mg); TiO_2 (Ti); anorthite (Al, Ca); fayalite (Fe); Amelia albite (Na); hafnium metal (Hf); microcline (K); Durango apatite (P); YPO_4 (Y); $CePO_4$ (Ce). Counting times and spectrometer assignments per element were chosen to minimize interferences and maximize precision. Data were reduced using a modified ZAF procedure (CITZAF; Armstrong 1988).

During the analysis session for the experimental glasses three glasses were analyzed as secondary standards: rhyolite VG568, QLO-1-1, and QLO-1-2. The last two were produced for this study; QLO-1-2 is a fused sample of USGS reference powder QLO-1, a quartz latite (Gladney and Roelandts 1988). QLO-1-1 is a glassed sample of QLO-1 with sufficient TiO_2 and ZrO_2 to generate a bulk mix with ~ 2 wt. % TiO_2 and ZrO_2. It was produced in order to have a relatively high-silica secondary standard glass with TiO_2 and ZrO_2 contents comparable to those in our experimental glasses. Both were fused at 1500°C and 10 kbar for 4 h.

All three glasses were analyzed multiple times throughout each probe session. Ten analyses were made on QLO-1-1 and QLO-1-2 after every three experimental glasses, and averaged and accepted compositions for all three secondary glass standards are given in Table 4. Based on the analyses of the rhyolite glass, QLO-1-1, and QLO-1-2, relative errors ($100 \cdot 1\sigma$/mean value) for the major oxides are: 0.38% SiO_2, 0.60% Al_2O_3, 3.0% FeO*, 3.0% CaO, 4.5% Na_2O, and 1.1% K_2O. Using just the 49 analyses of QLO-1-2, relative errors for TiO_2 and ZrO_2 are 2.7% and 5.1%, respectively. At the end of the glass analysis session we also collected five analyses on the rutile and zircon standards: relative errors for TiO_2 and ZrO_2 were both ~ 0.3%. During the analysis sessions for the crystals in the experimental charges, the rutile and zircon standards were repeatedly analyzed as unknowns. Based on 36 rutile and 35 zircon analyses, fractional errors on TiO_2, SiO_2 and ZrO_2 were 0.35%, 0.71%, and 1.1%, respectively, and the average compositions (see Table 3) overlap with their accepted compositions at the 1-sigma level.

2.3.2 Fourier Transform Infrared Spectroscopy (FTIR)

A subset of our experimental glasses was analyzed for water and CO_2 using FTIR. Doubly polished wafers cut from the experimental charges were ultrasonicated in acetone followed by ethanol. Data were collected using Caltech's Nicolet Continuμm infrared microscope attached to a Magna860 FTIR with a liquid nitrogen-cooled MCT-A detector, CaF_2 beamsplitter, and incandescent SiC source. The sample chamber was purged with dry air throughout the analysis, and transmission spectra were obtained in the near-infrared region of the electromagnetic spectrum between 8000 and 1200 cm^{-1}. A total of five spectra were collected on each sample. The standard deviations for these measurements were of order ≤ 5%.

Dissolved water and CO_2 concentrations were calculated at a given absorption band using the Beer-Lambert law, which requires FTIR absorption peak heights, appropriate molar absorption coefficients, and sample thickness and density. Peak heights for the molecular water band at ~ 5230 cm^{-1} and the hydroxyl group band at ~ 4520 cm^{-1} were determined by subtracting off straight-line backgrounds; following Newman et al. (1986) total water content was taken as the sum of these two bands. Compositionally dependent extinction coefficients for these peaks were calculated using expressions in Ohlhorst et al. (2001) and the composition of the glass normalized to a volatile-free basis (note that the compositionally-dependent extinction coefficients of Ohlhorst et al. (2001) were determined using straight-line background corrections). In one sample with very low water concentrations (< 0.1 wt %), we were required to use the extinction coefficient given for the OH stretching vibration band at ~3550 cm^{-1} (Behrens and Stuke 2003). Carbon dioxide concentrations were determined in the same way using an absorption coefficient for molecular CO_2 at ~ 2350 cm^{-1} (Behrens et al. 2004). Sample thickness was determined to within ± 2 μm using a digital indicator. In order to calculate the densities of our water bearing glasses, we followed the approach of Stolper (1982) and modified the compositionally dependent glass density expression of Huggins (1940). Using nearly 200 published glass compositions for which total water content and density had been independently determined, we refit the FeO-term in the Huggins (1940) expression and calculated values for an H_2O term and a pressure term. The modified equation calculates the densities of the calibration data set with a mean error of ~ 0.9%. Because glass density is a function of major-element composition (which for our samples is known from electron microprobe analyses) and water contents, determining the dissolved water concentration in a given sample is a simple minimization problem (two equations: Beer-Lambert law expression and the modified Huggins expression; and two unknowns: water content and glass density).

2.3.3 7fGEO SIMS

The majority of the experimental glasses were analyzed for water content by collecting $^{1}H^{+}$ and $^{30}Si^{+}$ on Caltech's Cameca 7fGEO SIMS and comparing these values to a calibration curve created on standards of known composition and water content. Analyses of both the standards and experimental glasses utilized a 4.5 nA $^{16}O^{-}$ primary beam and magnetic peak switching, counting for 4.96 s at mass 1.008 amu and 2.00 s at mass 29.974 amu for a total of 4 minutes including peak switching. In order to avoid any small crystals, the magnetic field was switched to identify zircons at mass ^{90}Zr and rutile at ^{48}Ti. The primary beam was focused using field and transmission apertures to a diameter of 8–10 μm on the sample surface. Positive secondary ions were extracted at 10 kV and collected using electron multipliers. Five points were collected on each standard; each point (standards and unknowns) was presputtered for 6 minutes in order to get a near constant counting rate on $^{1}H^{+}$. A -75 V offset was applied to isolate the high energy H^{+} tail from the intense (high counts per second) peak in the H^{+} spectrum at low initial kinetic energies due to electron- or ion-stimulated desorption (see Ihinger et al. 1994).

2.3.4 NanoSIMS

Zircons were analyzed for Ti, Hf, Zr, and Si contents by ion microprobe using Caltech's CAMECA NanoSIMS 50L and the following isotopes: $^{28}Si^{-}$, $^{48}Ti^{16}O^{-}$, $^{94}Zr^{-}$, $^{94}Zr^{16}O^{-}$, and $^{180}Hf^{16}O^{-}$. The following parameters were typical of the tuning conditions used for data presented here: the primary beam aperture lens D1 was set at 100 μm, corresponding to a predicted probe size of < 100 nm. However, the beam diameter was independently measured to be ~ 400 nm by making a traverse across the interface between a Pt bead embedded within one of the sample charges and the surrounding glass and evaluating the width of the signal between 16 and 84% of its height. The difference between the predicted and actual beam diameters is likely to result from differences in the primary tuning parameter values used in the Cameca prediction and the actual tuning parameters used during analysis. Negative secondary ions were extracted at -8 kV and collected using electron multipliers. Analyses utilized a ~ 20 nA Cs^+ primary beam (~ 1–2 pA on the sample surface, after passing through the aperture D1 and the E0 immersion lens stack) focused to a spot the diameter of the primary beam on the sample surface; the electron gun was simultaneously employed at a voltage of -7950 to -7960 V to aid in ion extraction and to minimize sample charging. A square area 8 to 15 μm on a side incorporating each zircon and some of the surrounding quenched glass was pre-sputtered for ~ 20 min using a 5–10 pA beam prior to analysis in an attempt to achieve a relatively steady counting rate on $^{28}Si^-$ and $^{94}Zr^{16}O^-$. Analyses were performed by rastering the beam over the pre-sputtered area to create an image of the area of interest. The beam was then moved linearly across the sample at ~ 200 nm intervals, creating a line profile either 10 to 12 μm long (i.e., starting within the glass on one side of a grain, moving across the entire grain and into surrounding glass on the opposite side) or ~ 5 μm long (across half a grain and into the surrounding glass). At least two zircons from each experimental charge were analyzed in this manner. The QSA effect was not calculated and no energy offset was applied.

2.4 Calibration of Ti analyses

Two synthetic, Ti-doped zircons from experimental Run 57 of Watson et al. (2006) were used in conjunction with the natural zircon 91500 (Wiedenbeck et al. 2004) to calibrate the ion microprobe Ti analyses. As reported in Hofmann et al. (2009a), Ti concentrations for the Run 57 zircons were analyzed at Caltech using the JEOL JXA-8200 electron microprobe and yielded Ti contents of 1393 ± 45 (1σ) and 1646 ± 118 ppm (1σ), within the range previously reported by Watson et al. (2006) for zircons from this experimental run. A value of 5.2 ppm Ti (given in Fu et al. 2008) was used for 91500. Each session of NanoSIMS analyses was followed by analyses of both of the synthetic, high-Ti zircons from Watson's Run 57 experimental charge as well as zircon 91500; with one exception, $^{48}\mathrm{Ti}^{16}\mathrm{O}^{-}/^{94}\mathrm{Zr}^{16}\mathrm{O}^{-}$ vs. Ti ppm calibration curves had correlation coefficients > 0.97; the lowest value was 0.93. Conversion of $^{180}\mathrm{Hf}^{16}\mathrm{O}^{-}/^{94}\mathrm{Zr}^{16}\mathrm{O}^{-}$ ratios to Hf concentrations relied on a two-point calibration (a linear fit to the 91500 value of 5325 ppm given in Wiedenbeck et al. 2004 regressed through the origin) and was used as an approximation to determine whether correlations between Ti and Hf existed in zircon overgrowths from different bulk composition suites; because no correlations were observed and the errors on $^{180}\mathrm{Hf}^{16}\mathrm{O}^{-}/^{94}\mathrm{Zr}^{16}\mathrm{O}^{-}$ ratios are high, Hf data are not included in any of the tables.

3. Results and Discussion

The temperature, run duration, phase assemblage, and phase proportions of each experiment is reported in Table 2. Table 2 also reports the Ti contents as measured using the NanoSIMS in zircons from these runs. Average compositions (determined by microprobe) of the experimental glasses, zircons, and rutile (when present) are listed in Tables 3 and 4.

3.1 Run products and phase compositions

3.1.1 Zircon

Zircons are present in all of our subliquidus experiments (see Table 2) and range in size from 5 to 15 μm in longest dimension. Note the prismatic shapes of all the larger zircon crystals to which we restricted our analyses (Figure 4a-f), as compared to the zircon fragments (imaged in Figure 1) that were added to our starting materials as nucleation sites for zircon growth. The CL images of zircon run products (panels g-i in Figure 4) are suggestive of "new" zircon growth (denoted as CL-bright in these images as in Figure 2c of Watson et al. 2006) over CL-dark zircon cores (i.e., the original seeds). In our low-water (nominally anhydrous) experiments, the CL-bright signal appears to bleed out into the surrounding glass matrix; this effect may be the result of topography associated with the zircon-glass interface or it may simply be limited to the resolution of the SEM variable pressure secondary electron detector (used for CL imaging) on these smallest zircons. Thus it is difficult to say with certainty the actual spatial extent of the overgrowth as demarcated by CL-bright regions in these experiments. The angular appearance of dark cores in the larger zircon grains suggests that minimal dissolution occurred prior to overgrowth of "new" zircon.

Microprobe analyses were collected from interiors of the larger grains and for the smaller grains were often within several microns of the edge, and thus in these instances all the analyzed elements other than Si, Zr, and Hf are probably affected by fluorescence from the surrounding glass. For example, microprobe TiO_2 contents varied from the detection limit (~ 0.07) to 0.2 wt. %; as we discuss below, TiO_2 contents determined by NanoSIMS varied from ~ 0.02 to 0.13 wt. %. HfO_2 concentrations are on the order of 0.7 to 1 wt. % and almost certainly reflect that of the initial seed fragments (see Table 1). Very small (≤ 1 μm) semi-rounded "grains" are also present in all of the experiments. We suspect that these are

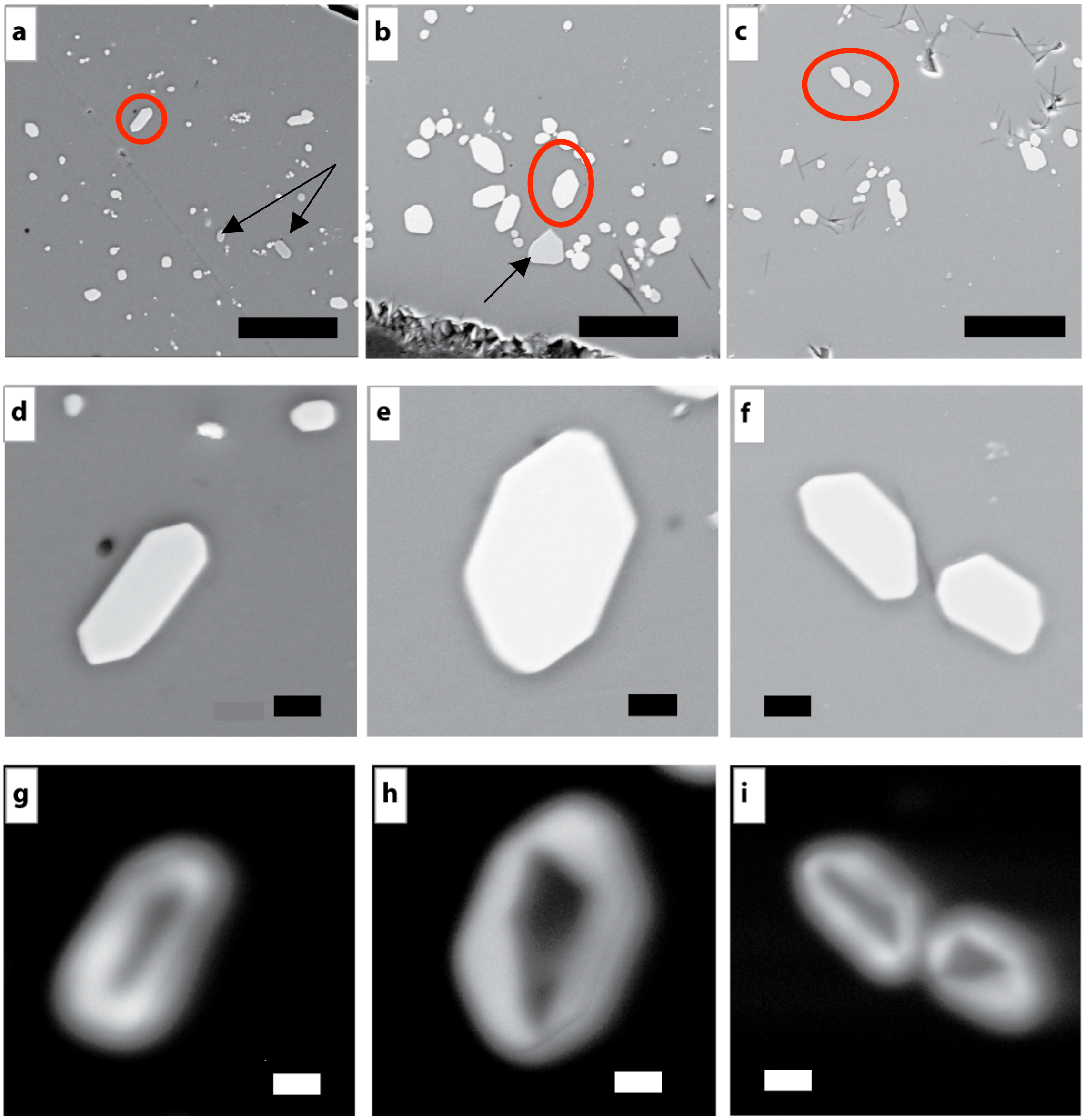

Figure 4. Representative images of experimental run products. In the secondary electron (SE) images, white objects are zircons, light gray objects (denoted by arrows when present) are rutiles, and the gray background is glass. **a.** SE image of a portion of MMG-2-2, a nominally anhydrous, rutile- and zircon-saturated, synthetic oxide mix run at 1400°C for 191 h. Red circle surrounds the zircon illustrated in panels **(d)** and **(g)**. Scale bar is 30 μm. **b.** SE image of a portion of MMGh-3-1, a hydrated, rutile- and zircon-saturated, synthetic oxide mix run at 1300°C for 98 h. Red circle surrounds the zircon illustrated in panels **(e)** and **(h)**. Scale bar is 30 μm. **c.** SE image of a portion of GO-6-1, a hydrated, rutile-undersaturated composition predominantly comprised of natural G-2 granite powder and synthetic orthoclase that was run at 1200°C for 169.5 h. Red circle surrounds the zircons illustrated in panels **(f)** and **(i)**. Scale bar is 30 μm. **d.-f.** SE image of zircons denoted by red circles in upper panels. Note the faceted terminations. Scale bar is 2 μm in all 3 images. **g-i.** CL images of the same zircons imaged in panels **(d-f)**. Note the apparent presence of seed crystals (dark gray) surrounded by new zircon overgrowth (white). In smaller zircons, the CL-bright area appears to spill over into the glass (black), perhaps due to edge-effects like topographic relief. Scale bar is 2 μm in all three images.

baddeleyite, but they are too small to analyze. This supposition is consistent with the fact that all of the starting mixes contained ZrO_2.

Zircon Ti concentrations by NanoSIMS were determined by first identifying plateaus in each $^{48}Ti^{16}O^-/^{94}Zr^{16}O^-$ line profile that spanned either an entire grain or approximately half of a grain. Plateaus varied in width from ~ 400 nm to 1 μm. The points contributing to a given plateau were averaged and a standard deviation was calculated; the resulting ion ratio was then converted to a Ti concentration using the $^{48}Ti^{16}O^-/^{94}Zr^{16}O^-$ vs. Ti ppm calibration curve determined using our three zircon standards. A calibration curve from a given NanoSIMS session was only applied to zircons in our experimental charges that had been analyzed during that session. Errors on the calculated Ti content reflect the standard deviation on the $^{48}Ti^{16}O^-/^{94}Zr^{16}O^-$ ratio and the uncertainty on the slope of the calibration curve. Since all of our experiments are synthesis runs and since the overgrowth rims always contain more Ti than the cores, we have selected the highest average Ti content from a given profile as representing the closest approach to an equilibrium value for that experiment. Ti contents vary from ~ 700 to 760 ppm for our 1400°C rutile-saturated experiments to 112 ppm in one of our rutile-undersaturated 1200°C runs.

3.1.2 Rutile

When present, rutiles formed grains that are, on average, ~ 5 to 15 μm in longest dimension. As in the case with the zircons, microprobe analyses were collected from the interiors of the larger grains and from near the grain boundaries (within several microns) of the smaller grains. Average SiO_2, Na_2O and K_2O concentrations in rutiles analyzed as part of this study are 0.28, 0.02, and 0.15 wt. %, respectively, suggesting some partial beam overlap with the quenched glass and/or secondary X-ray excitation. ZrO_2 contents as measured by

Table 2. Experimental results

Run #	Temp (°C)	Time (hrs)	Run products	Phase proportions	Ti concentration in zircon overgrowth (ppm)	One standard deviation (ppm)
MMG-1-1	1400	23.57	liq	100	-	-
MMG-2-1	1400	114.50	liq, zrc, rt	97.0, 2.9 , 0.1	707	145
MMG-2-2	1400	191.08	liq, zrc, rt	97.0, 2.9 , 0.1	761	148
MMG-3-1	1400	113.35	liq, zrc	96.9, 3.1	377	61
MMG-4-1	1300	192.13	liq, zrc, rt	96.1, 3.0 , 0.9	487	139
MMG-5-1	1300	193.50	liq, zrc	n.a.	n.a.	n.a.
MMGh-1-1	1300	47.67	liq, zrc, rt	96.3, 3.2 , 0.5	357	85
MMGh-1-2	1300	48.10	liq, zrc, rt	96.8, 2.9 , 0.3	544	84
MMGh-2-1	1300	48.18	liq, zrc	96.7, 3.3	296	47
MMGh-3-1	1200	98.00	liq, zrc, rt	97.3, 2.3 , 0.4	277	41
MMGh-4-1	1200	84.67	liq, zrc	97.6, 2.4	206	44
GO-1-1	1400	71.58	liq, zrc, rt	96.6, 2.9 , 0.5	146	21
GO-1-2	1400	71.83	liq, zrc, rt	97.0, 2.8 , 0.2	520	47
GO-2-1	1400	72.08	liq, zrc	97.7, 2.3	239	28
GO-3-1	1300	120.00	liq, zrc, rt	96.9, 2.7 , 0.4	170	108
GO-4-1	1300	119.98	liq, zrc	97.8, 2.2	247	23
GO-5-1	1200	168.27	liq, zrc, rt	96.7, 2.2 , 1.1	219	76
GO-6-1	1200	169.47	liq, zrc	98.2, 1.8	112	24
G-2-3	1450	7.98	liq	100		
H-2-2	1200	21.00	liq	100		
H-2-3	1200	3.08	liq	100		
H-2-4	1200	95.63	liq	100		
H-2-5	1450	7.45	liq	100		

Mineral abbreviations: liq = liquid; rt = rutile; zrc = zircon; n.a. = not analyzed; all subliquidus MMG-series, MMGh-series, and GO-series experiments also contain ≤1 μm semi-rounded grains of what we infer to be baddeleyite.

Table 3. Average compositions of zircon and rutile run products (wt. %)

Run #	phase	SiO_2	TiO_2	Al_2O_3	FeO*	MgO	CaO	Na_2O	K_2O	P_2O_5	ZrO_2	HfO_2	Y_2O_3	SUM
MMG-2-1	zrc	32.6(2)	0.16(3)	0.03(3)	0.15(4)	-	0.02(1)	0.02(1)	0.06 (1)	0.05(4)	66.0(5)	0.8(3)	-	99.9
	rt	0.4(1)	90.0(5)	0.75(4)	0.12(4)	-	0.06(1)	-	0.14(3)	0.02(2)	7.3(2)	-	-	98.8
MMG-2-2	zrc	32.10(7)	0.19(4)	0.02(2)	0.12(4)	-	0.027(6)	0.02(2)	0.05(1)	0.06(3)	66.0(5)	1.0(1)	-	99.6
	rt	0.35(8)	90.3(8)	0.66(4)	0.13(2)	-	0.070(5)	-	0.15(1)	0.03(2)	7.5(2)	-	-	99.2
MMG-3-1	zrc	32.4(1)	0.11(3)	0.04(4)	0.15(4)	-	0.02(1)	0.02(2)	0.06(2)	0.02(2)	66.2(5)	1.1(3)	-	100.1
MMG-4-1	zrc	32.2(2)	0.09(3)	0.08(5)	0.14(2)	-	0.026(1)	0.014(7)	0.06(2)	0.03(2)	66.0(4)	1.0(2)	-	99.6
	rt	0.5(2)	93.6(4)	0.59(3)	0.14(4)	-	0.076(4)	0.03(3)	0.18(2)	0.03(1)	4.1(2)	-	-	99.2
MMGh-1-1	zrc	31.98(7)	0.2(2)	-	0.05(3)	-	0.03(2)	0.04(3)	0.07(2)	-	66.2(7)	0.7(5)	-	99.3
	rt	0.24(6)	92.0(3)	0.83(4)	0.17(5)	-	0.06(2)	0.02(2)	0.16(1)	-	5.5(2)	0.04(4)	-	99.0
MMGh-1-2	zrc	32.3(1)	0.12(7)	0.03(1)	0.07(4)	-	0.01(1)	-	0.03(1)	-	66.2(8)	1.0(2)	-	99.8
	rt	0.14(3)	91.6(3)	0.89(1)	0.17(4)	-	0.06(1)	-	0.13(2)	0.02(2)	5.7(1)	-	-	98.7
MMGh-2-1	zrc	32.2(1)	0.06(3)	-	0.11(3)	-	0.01(1)	-	0.04(1)	0.04(4)	66.2(6)	1.0(1)	-	99.7
MMGh-3-1	zrc	32.4(2)	0.08(2)	0.01(1)	0.07(2)	0.01(1)	0.02(1)	0.02(2)	0.04(1)	-	65.9(8)	1.04(5)	-	99.6
	rt	0.11(2)	93.5(4)	0.83(5)	0.23(4)	0.01(1)	0.06(1)	-	0.11(1)	-	3.6(1)	-	-	98.4
MMGh-4-1	zrc	31.8(2)	0.05(4)	0.02(2)	0.04(2)	-	0.02(1)	-	0.05(2)	-	66.4(8)	0.8(4)	-	99.2
GO-1-1	zrc	32.2(1)	0.16(2)	0.04(4)	0.13(5)	-	0.03(1)	0.02(1)	0.05(2)	0.05(4)	66.4(4)	1.0(1)	-	100.1
	rt	0.4(2)	91.2(2)	0.47(1)	0.12(5)	-	0.06(2)	0.02(2)	0.16(4)	0.02(2)	6.7(2)	-	-	99.2
GO-1-2	zrc	32.8(3)	0.16(6)	0.02(2)	0.09(3)	-	0.01(1)	-	0.04(1)	0.04(3)	66.7(6)	1.1(2)	-	101.0
	rt	0.23(6)	91.3(5)	0.46(5)	0.12(4)	-	0.05(2)	0.02(1)	0.12(1)	-	7.3(3)	-	0.02(2)	99.6
GO-2-1	zrc	32.6(1)	0.07(3)	-	0.12(2)	-	0.02(1)	0.01(1)	0.05(1)	-	66.4(7)	1.0(2)	-	100.3
GO-3-1	zrc	32.5(2)	0.06(4)	-	0.07(3)	-	0.01(1)	0.04(3)	0.06(2)	0.07(6)	66.4(7)	1.1(2)	-	100.3
	rt	0.2(1)	93.3(4)	0.49(4)	0.17(2)	-	0.06(1)	0.05(4)	0.16(2)	0.02(2)	4.4(1)	-	-	98.8
GO-4-1	zrc	31.9(2)	0.07(5)	0.05(3)	0.08(4)	-	0.01(1)	-	0.03(1)	0.06(4)	66.8(8)	0.4(4)	-	99.4
GO-5-1	zrc	32.3(3)	0.05(3)	0.02(2)	0.08(2)	-	0.02(1)	-	0.05(1)	0.04(4)	66.7(7)	1.2(1)	-	1005
	rt	0.20(3)	95.6(3)	0.48(4)	0.15(3)	0.01(1)	0.05(1)	0.01(1)	0.15(1)	-	2.8(2)	-	-	99.5
GO-6-1	zrc	32.4(1)	0.01(1)	0.01(1)	0.10(5)	-	0.02(1)	-	0.05(1)	0.04(4)	66.5(6)	1.0(1)	-	100.1

Mineral abbreviations: zrc = zircon; rt = rutile. Numbers in parentheses are 1σ in terms of the least units cited; e.g., 32.6(2) is 36.6 ± 0.2; dashes indicate that the mean oxide value was < the corresponding standard deviation; averages based on 4 to 8 analyses; 36 analyses of the zircon standard yield: 32.3(2), SiO_2; 66.2(7), ZrO_2; accepted values: 32.40 and 66.32 ; 35 analyses of the rutile standard yield: 100.2(4), TiO_2; accepted value: 100.

microprobe decrease monotonically with decreasing temperature from ~ 7.2 ± 0.3 wt. % at 1400°C to 3.2 ± 0.5 wt. % at 1200°C. These ZrO_2 contents are substantially lower than those reported by Ferry and Watson (2007) but comparable to those reported in Watson et al. (2006) for rutile coexisting with zircon over a similar range of temperatures (1200 to 1400°C). The Ferry and Watson ZrO_2 values range from 14 wt. % at 1400°C to 8.6 wt. % at 1280°C. Some of these differences may reflect differences in the silica activities in the melts generated in the two experimental studies, but as we describe below, estimating silica activities for our experimental melts does not allow us to reconcile these differences in ZrO_2 in rutile.

3.1.3 Glass

Our experimental glasses contain between 64.2 and 70.7 wt. % SiO_2, 12.3 to 15.4 wt. % Al_2O_3, 2.5 to 3.2 wt. Na_2O, and 4.7 to 5.6 wt. % K_2O. H_2O values range from 0.4 to 7.0 wt. %. The nominally anhydrous runs contain 0.4 to 0.7 wt. % water—not unexpected given that we did not dry the loaded capsules prior to the final welding. A number of the hydrous runs contain substantially more water than the nominal H_2O content of their starting mixtures. For example, the glass from run MMGh-3-1 contains 6.9 wt. % H_2O, although the starting mix is calculated to have 3.31 wt. % water. We suspect that we accidentally introduced water into the capsules during their final welding within a water bath. This was perhaps a serendipitous occurrence in that there is a crude correlation between the thickness of the zircon overgrowths as determined by the NanoSIMS and the water content of the coexisting quenched glass. TiO_2 contents in the glasses vary from 0.9 to 5.1 wt. %, and for the rutile-saturated glasses decrease monotonically with decreasing temperature. ZrO_2 contents also generally decrease with decreasing temperature and range from 0.3 to 1.1 wt. % (all of the above oxide values are based on glass compositions that include water and that have been normalized to 100%).

Table 4. Compositions of experimental glasses and secondary standards (wt. %)

Run #	SiO_2	TiO_2	Al_2O_3	FeO*	MnO	MgO	CaO	Na_2O	K_2O	P_2O_5	ZrO_2	H_2O	SUM
MMG-1-1 [§]	70.3(5)	2.04(8)	14.0(4)	1.64(6)	-	0.32(2)	1.39(7)	3.10(9)	5.10(5)	-	0.48(6)	n.a.	98.3
MMG-2-1	68.5(2)	5.1(1)	13.8(2)	1.51(4)	-	0.30(2)	1.34(4)	3.0(2)	4.66(3)	-	0.90(8)	0.39	99.5
MMG-2-2	68.1(4)	5.0(1)	13.66(9)	1.50(5)	-	0.30(2)	1.33(4)	2.9(2)	4.61(4)	-	0.89(8)	0.49	98.9
MMG-3-1	68.4(3)	2.77(7)	15.0(1)	1.62(5)	-	0.34(2)	1.44(4)	3.12(8)	5.00(5)	-	0.84(8)	0.49	99.1
MMG-4-1	68.9(4)	2.77(7)	14.7(1)	1.42(4)	-	0.32(2)	1.43(3)	2.97(8)	4.90(4)	-	0.41(4)	0.74	98.6
MMG-5-1	71.2(3)	1.93(7)	13.8(1)	1.55(4)	-	0.32(1)	1.41(3)	3.0(4)	4.83(6)	-	0.40(4)	n.a.	98.5
MMGh-1-1	65.5(3)	3.46(8)	15.22(9)	1.13(4)	-	0.32(3)	1.39(4)	2.8(2)	4.77(4)	-	0.56(7)	3.22	98.3
MMGh-1-2	62.8(4)	3.53(8)	14.6(1)	0.96(5)	-	0.30(2)	1.34(5)	2.33(6)	4.52(5)	-	0.66(7)	6.11	97.1
MMGh-2-1	67.6(3)	1.90(5)	14.6(1)	1.00(6)	-	0.32(2)	1.40(4)	2.7(4)	4.79(3)	-	0.52(8)	3.57	98.4
MMGh-3-1	63.8(4)	2.34(4)	13.6(1)	0.91(4)	-	0.31(2)	1.35(4)	2.09(5)	4.47(4)	-	0.34(6)	6.89	96.1
MMGh-4-1	65.4(5)	1.89(6)	13.2(1)	0.42(4)	-	0.27(2)	1.27(4)	1.96(6)	4.31(4)	-	0.27(6)	6.97	96.0
GO-1-1	69.2(6)	4.8(1)	12.6(1)	1.51(6)	0.02(2)	0.46(2)	1.22(4)	2.50(7)	5.06(6)	0.08(3)	0.86(9)	0.44	98.7
GO-1-2	68.8(5)	5.0(1)	12.41(8)	1.34(5)	0.03(2)	0.45(2)	1.18(4)	2.44(7)	5.03(5)	0.07(2)	1.0(1)	0.66	98.3
GO-2-1	68.3(2)	1.94(5)	13.3(1)	1.38(4)	0.02(2)	0.49(2)	1.28(4)	2.54(5)	5.34(4)	0.08(4)	1.12(5)	2.56	98.4
GO-3-1	68.5(2)	3.12(6)	13.82(8)	1.19(5)	0.02(2)	0.47(2)	1.34(3)	2.7(1)	5.35(3)	0.09(3)	0.48(9)	1.50	98.6
GO-4-1	67.0(2)	1.79(5)	12.1(2)	0.96(5)	0.02(2)	0.40(2)	1.22(5)	1.85(5)	4.69(5)	0.08(3)	0.65(6)	6.68	97.4
GO-5-1	70.1(3)	1.92(8)	13.9(1)	1.1(2)	0.02(2)	0.43(2)	1.35(4)	2.77(6)	5.31(6)	0.07(2)	0.28(6)	1.58	98.9
GO-6-1	67.3(2)	0.87(3)	13.8(1)	1.16(5)	0.01(1)	0.44(2)	1.32(3)	2.36(5)	5.07(4)	0.06(3)	0.33(4)	5.25	98.0
QLO-1-1 (49)**	64.4(2)	2.14(6)	15.2(1)	3.50(8)	0.09(3)	0.90(3)	2.88(5)	3.8(1)	3.21(3)	0.23(3)	1.9(1)	n.a.	98.4
normalized	65.3	2.17	15.4	3.55	0.09	0.91	2.92	3.8	3.26	0.23	2.0		99.8
accepted value	65.5	2.14	14.9	3.57	0.09	0.92	2.91	3.9	3.31	0.23	2.0	0.31	99.8
QLO-1-2 (48)	66.0(2)	0.64(3)	16.15(9)	3.90(7)	0.09(2)	0.97(3)	3.18(5)	4.2(1)	3.57(4)	0.25(3)	0.04(4)	n.a.	99.2
normalized	66.5	0.64	16.26	3.92	0.09	0.98	3.20	4.2	3.59	0.25	0.04	-	99.8
accepted value	66.2	0.63	16.34	3.93	0.09	1.01	3.20	4.2	3.64	0.26	0.03	0.07	99.8
VG568 (10)	76.7(3)	0.08(2)	11.95(5)	1.15(6)	0.03(1)	0.026(7)	0.43(3)	4.0(3)	4.84(6)	0.002(5)	0.02(3)	-	99.3
accepted value	76.7	0.12	12.06	1.23	0.03	0.000	0.50	3.8	4.89	0.000	0.000	-	99.4

Unless otherwise stated, between 18 and 20 analyses were averaged for each experiment. Numbers in parentheses adjacent to the analyses are 1σ in terms of the least units cited; e.g., 70.3(5) represents 70.3 ± 0.5; dash in an oxide column indicates that the oxide was not included in mix or, in the case of VG568, not reported; n.a. = not analyzed. H_2O calculated based on the following linear calibration: wt% $H_2O = -0.0778 + 3.847 * [({}^1H^+/{}^{30}Si^+)*SiO_{2\,anhydrous}]$; $R^2 = 0.999$. Adjusted Na_2O and K_2O contents (by mass balance; see text) for glasses with >0.5 wt. H_2O are: 3.13, 5.09, MMG-4-1; 3.02, 4.92, MMGh-1-1; 2.90, 4.71, MMGh-1-2; 3.05, 4.96, MMGh-2-1; 2.87, 4.66, MMGh-3-1; 2.78, 4.51, MMGh-4-1; 2.54, 5.03, GO-1-2; 2.74, 5.47, GO-2-1; 2.84, 5.52, GO-3-1; 2.50, 4.87, GO-4-1; 2.92, 5.47, GO-5-1; 2.82, 5.25, GO-6-1. For QLO-1-1, QLO-1-2, and VG568, number of analyses given in parentheses; because the oxide sums were systematically low for QLO-1-1 and QLO-1-2, oxide values normalized to the accepted sums are also given. Analyzed BaO contents for QLO-1-1 and QLO-1-2 are 0.16(6) and 0.17(6), respectively and are included in the reported oxide sum; accepted values are 0.14 and 0.16; CO_2 contents in QLO-1-1 and QLO-1-2 are 0.06 and 0.03 wt. %, respectively. VG568 also contains 0.13 wt. % Cl.

Figure 5 compares the TiO_2 contents in our rutile-saturated glasses with the values predicted by the rutile-saturation model of Gaetani et al. (2008). The measured TiO_2 concentrations in the experimental glasses lie on or very near the 1:1 line in Figure 5, suggesting that the TiO_2 contents of our rutile-saturated glasses are consistent with the much larger body of experimental data used by Gaetani et al. (2008) to calibrate their model. In contrast, the other recent model for estimating titanium contents of rutile-saturated melts (Hayden and Watson 2007) predicts TiO_2 contents in our 1400°C experimental liquids of ~ 16 wt. %; however, calculations at these temperatures represents a substantial extrapolation of their model.

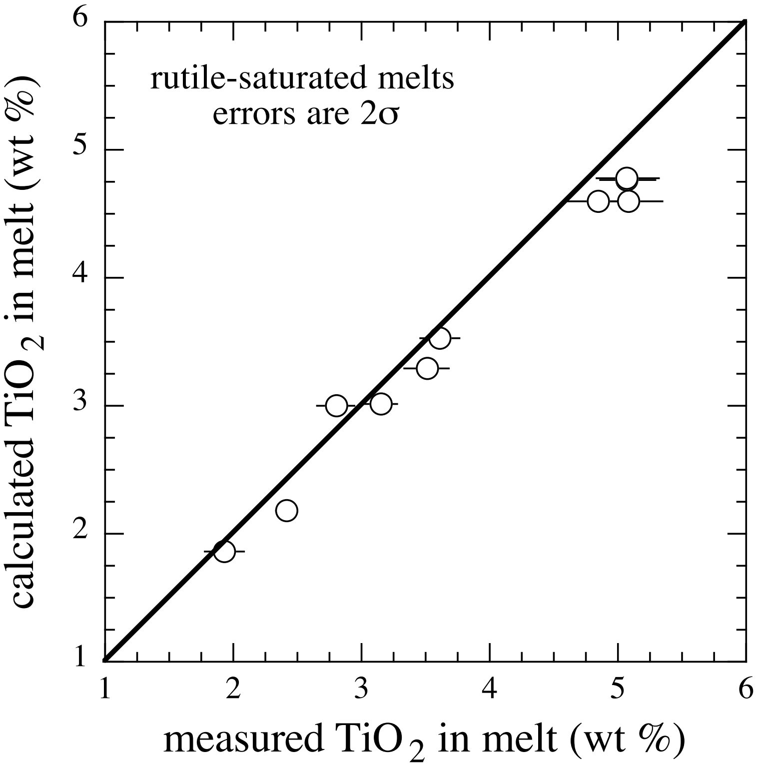

Figure 5. Plot of the measured TiO_2 concentration (by electron microprobe) in experimental glasses (open circles) from this study vs. the concentration of TiO_2 predicted by the Gaetani et al. (2008) model for rutile-saturated silica-rich melts. Following Gaetani et al. (2008), liquid TiO_2 contents were calculated assuming a mole fraction of TiO_2 in the rutiles of 1.

In a similar vein, Figure 6a compares measured ZrO_2 contents in our zircon-saturated melts with ZrO_2 concentrations predicted by the model of Watson and Harrison (1983). All of our glasses plot above the 1:1 line, suggesting that they should be undersaturated in zircon; however, visual inspection of our experimental glasses and quantitative microprobe analyses confirms that zircon is present in all of the charges. One interpretation of Figure 6a is that our experiments are in fact undersaturated with respect to zircon, but that run durations were insufficient for all the zircon to dissolve. This hypothesis is unlikely given that our run times are longer (in some cases by a factor of two) than those of the lower temperature experiments of Watson and Harrison (1983). A more likely explanation is that we have extrapolated their model substantially outside its calibration range (750–1020°C and pressures of 1.2–6 kbar). Nevertheless, Figure 6b shows that variations in the ZrO_2 contents of our quenched glasses are well described by the melt parameter (Na+K+2•Ca)/(Si•Al) used by Watson and Harrison to fit their own experimental data (element abbreviations in the above expression denote cation fractions). The isotherms in Figure 6b are best-fit lines to each set of constant temperature experiments; each set of experiments overlaps with its respective isotherm at the 1-sigma level.

3.2 Phase proportions

Phase proportions were determined by mass balance using the least-square fitting approach described by Albarede and Provost (1977) and the average electron microprobe analyses of coexisting rutile (when present), zircon, and glass (Tables 3 and 4); results are given in Table 2. Because measured water contents in our quenched glasses were in many cases inconsistent with the nominal water contents of the starting mixes for reasons discussed above, we allowed the bulk water content to be a variable, and we also allowed the bulk Al_2O_3

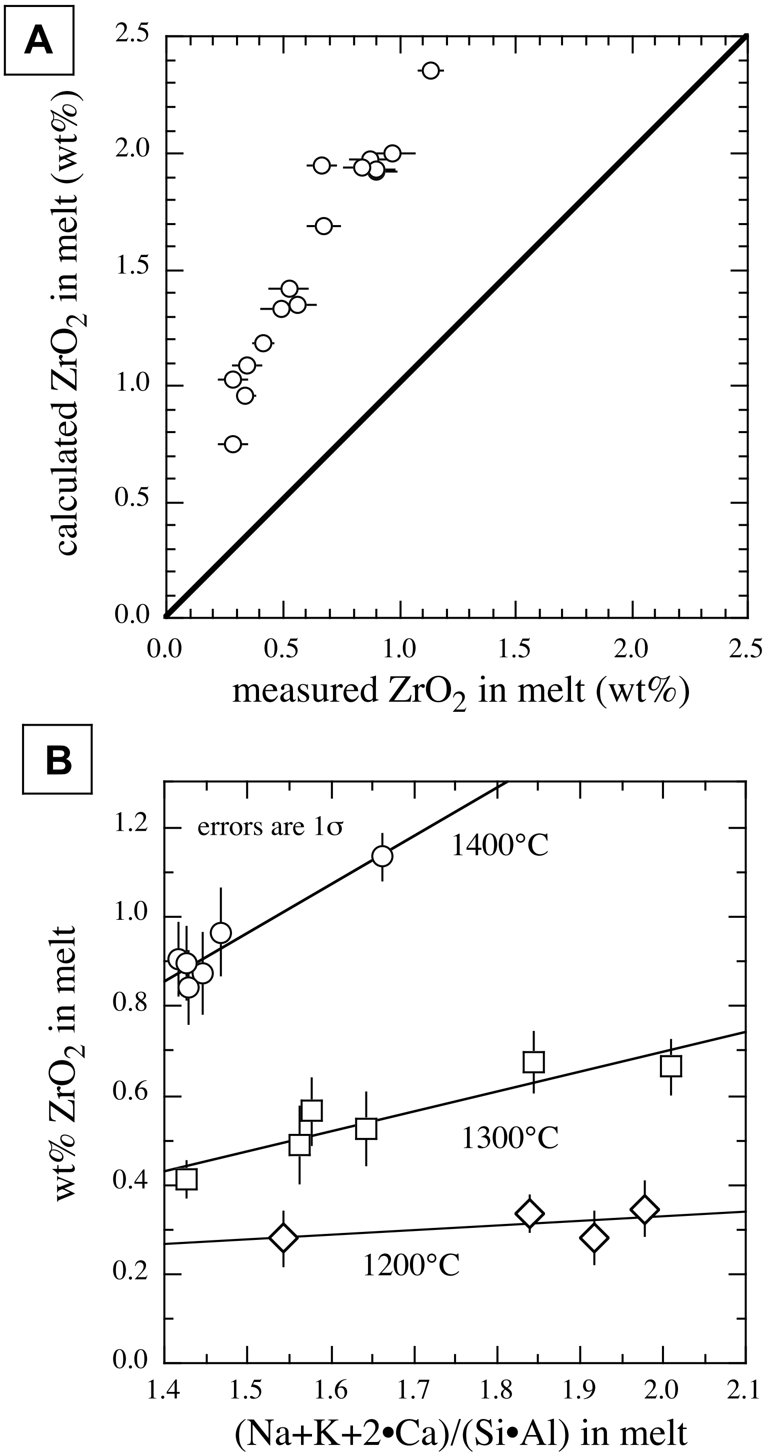

Figure 6. Comparison of experimental ZrO_2 concentrations to predicted values required for zircon saturation **a.** Plot of the measured ZrO_2 concentration (by electron microprobe; Table 3) in experimental glasses (open circles; error bars are one standard deviation) from this study v. the concentration of ZrO_2 predicted for these same glass compositions by the Watson and Harrison (1983) model for zircon-saturated melts. The Watson and Harrison model predicts that all of our experiments, despite having abundant zircon (~ 2–3 % by mass; see Table 2) are undersaturated in zircon. This prediction is likely the result of extrapolation of the Watson and Harrison model to this study's experimental temperatures, which all lie outside the model's calibration range (max: 1020°C). **b.** Plot of experimental glass compositions showing a strong linear correlation at a given

temperature between measured ZrO_2 concentration in the glass and the coexisting cation fraction parameter (x-axis) determined by Watson and Harrison (1983) to affect zircon solubility.

content to vary since preliminary mass balance calculations yielded large mismatches in Al_2O_3. These mismatches in Al_2O_3 were much larger with the synthetic mixes (i.e., the MMG-series and the MMGh-series) than with the GO-series experiments. Note that the glass is the only repository of Al_2O_3 in our experiments. We suspect that the form of the alumina used to construct these powders (Al_2O_3) leads to more extensive alumina addition during the grinding process (in an alumina mortar and pestle), than the feldspar and orthoclase glass used in the GO-series bulk compositions. Matzen et al. (2010) also observed that the Al_2O_3 contents of their synthetic glasses were greater than the Al_2O_3 content of the starting bulk composition presumably due to addition of Al_2O_3 from the alumina crucible in which the starting powders were ground. Finally, the Na_2O and K_2O contents of the glasses in the water-rich experiments were allowed to vary in the mass balance calculations because these oxides are known to be mobile in high-water glasses under bombardment with an electron beam (e.g., Hanson et al. 1996; Morgan and London 1996). During each of the calculation, the anhydrous oxide sum of the bulk composition was held constant at 100%, and any changes to the bulk concentrations of H_2O and Al_2O_3 required to minimize χ^2 were compensated for by corresponding proportional changes to the concentrations of the remaining oxides. The number of equations varied from 12 (for the synthetic bulk compositions) to 14 for the GO-series experiments and the number of variables was at most 7; thus all of our mass balance calculations were over-determined, and all are statistically significant at the 95% confidence level (i.e., $P \geq 0.05$).

Glass comprises between ~ 96 to 98 wt. % of our experimental charges; calculated zircon abundances vary from ~ 1.8 to 3.3 wt. %; and rutile abundance are ≤ 1.1 wt. %. We tried including baddeleyite in our mass balance calculations; however, the result was that either the zircon or the ZrO_2 was calculated to have a negative abundance. We suspect that this reflects the near linearity in composition space of high-silica glass, zircon, and ZrO_2, and thus the calculated zircon abundances may be slightly overestimated. For the MMG- and MMGh-series experiments, calculated increases in bulk Al_2O_3 ranged from 4 to 13% (with an average of 7.8%); for the GO-series experiments the equivalent values are: 0, 2.8, and 1.4%, respectively. For the glasses with > 0.5 wt. % H_2O, calculated liquid Na_2O contents increased by 4 to 42%, and the increase is strongly correlated with the water content of the glass; increases in K_2O were much lower (0–5%). These "new" alkali contents are reported in Table 3. With the exception of three experiments (MMGh-1-2, MMGh-3-1, and MMGh-4-1), oxide sums of the glasses including water and the adjusted alkali contents were > 98 wt. % (range: 98.2–99.5 wt. %). In the three experiments with low glass sums, which were also high in water, glass totals remained low (97.0–97.9 wt. %). Although some of the difference (from 100%) can be accounted for by dissolved CO_2, in the eight glasses that we have analyzed for CO_2 by FTIR, CO_2 contents are all < 0.5 wt. %. Furthermore, the solubility of CO_2 in a rhyolite glass (i.e., if CO_2 was the only volatile species present) at the temperatures and pressure of our experiments was calculated using the model of Zhang et al. (2007) to be < 0.5 wt. %. Nevertheless, the compositions of these three glasses are consistent with our other experimental runs in terms of TiO_2 and ZrO_2 contents.

3.3 Attainment of equilibrium

As stated above, all of our experiments are synthesis runs, and thus we have not demonstrated that the compositions of the liquids and coexisting crystals in our experiments represent equilibrium values. However, a number of lines of evidence are consistent with our experiments having approached equilibrium closely. (1) Mass balance calculations for all of our runs are statistically significant. This is a necessary albeit insufficient condition for equilibrium. However, our mass-balance calculations have not established that water was conserved in our experiments since bulk water content was a free parameter. In order to investigate the extent to which water is conserved in our charges, we conducted a time series using mix H-2 (Table 1) at 1200°C (superliquidus for this bulk composition). The nominal bulk water content is 7.0 wt. %. FTIR measurements of the three glasses (run times of 3.1, 21, and 96 h) yield water contents of 5.2, 4.9, and 4.6%. These values suggest that although a relatively large fraction of water is lost very early in the run, H_2O contents appear to remain relative constant in the longer duration time series experiments, and thus we infer that water contents in our other experiments also remained relatively constant. (2) Experiments MMG-2-1 and MMG-2-2 were run at the same temperature for 114 and 191 h, respectively, and produced liquid and crystal compositions that overlap at the 1-sigma level (Tables 2, 3, and 4). The quenched glasses from runs MMGh-1-1 and MMGh-1-2 (1300°C, ~ 48 h, and saturated in zircon and rutile) differ by nearly a factor of two in their water contents but nevertheless contain very similar TiO_2 and ZrO_2 contents. It is well known that water is an excellent flux in silicate crystal-melt systems (e.g., Watson et al. 2006) and the overlap in the compositions of the phases from these two experiments supports a close approach to equilibrium. (3) The consistency of the TiO_2 contents in our rutile-saturated glasses with a much larger body of experimental work (e.g., Figure 5) also supports a close approach to equilibrium. Gaetani et al. (2008) showed that a rhyodacite liquid saturated with rutile approached a constant composition after ~ 3 h at 1350°C and 10 kbar. This suggests that the dissolution of rutile is rapid under these conditions and that our rutile compositions in runs of 48 to 192 h may well have approached equilibrium. This supposition is supported by Zr diffusion coefficients (D_{Zr}) measured in rutile by Sasaki et al. (1985). Using their value of D_{Zr} determined in air at 1200°C, and run times of 168 h (i.e., the run duration of GO-5-1; Table 2), the diffusion distance will be ~ 5 μm. This is on the same order as the size of rutiles in our experiments. This diffusion distance is a minimum estimate since Sasaki et al. (1985) showed that D_{Zr} is negatively correlated with f_{O_2} at 1400°C (changing from 5×10^{-12} in air to 4×10^{-10} at a log(f_{O_2}) of -8.6. However recent measurements of Zr in rutile by Cherniak et al. (2007) are ~ 3 orders of magnitude slower and would lead to a diffusion distance of Zr in rutile in run GO-3-1 of ~ 0.1 μm. (4) Finally, the well-developed, compositionally distinct rims observed on the majority of the zircons from this study suggest that measurable reaction and/or overgrowth has occurred between the zircons and the liquids in our experiments; therefore, the Ti concentrations in these overgrowths may have equilibrated with the surrounding liquid.

3.4 Ti-in-zircon thermometry

Figure 7 compares the Ti (ppm) in zircon overgrowths from this study and Ti concentrations in zircons coexisting with rutile reported by Watson et al. (2006) and Ferry and Watson (2007). These data are measured Ti concentrations only; no correction has been made for either the activities of TiO_2 (a_{TiO_2}) or SiO_2 (a_{SiO_2}) in the coexisting liquid, an issue we will discuss shortly. It should be noted that uncertainties reported by Watson et al. (2006) and Ferry and Watson (2007) are given as two standard errors and, while generally smaller than the standard deviations reported for our measurements, would, we expect, be of similar or larger magnitude if converted to standard deviations. Both data sets show an overall decrease in Ti content in zircon with decreasing temperature. In general, our data plot below those of Watson et al. (2006) and Ferry and Watson (2007)—even for those experiments from both data sets that are rutile-saturated. With one exception, the Ti contents in zircons from our

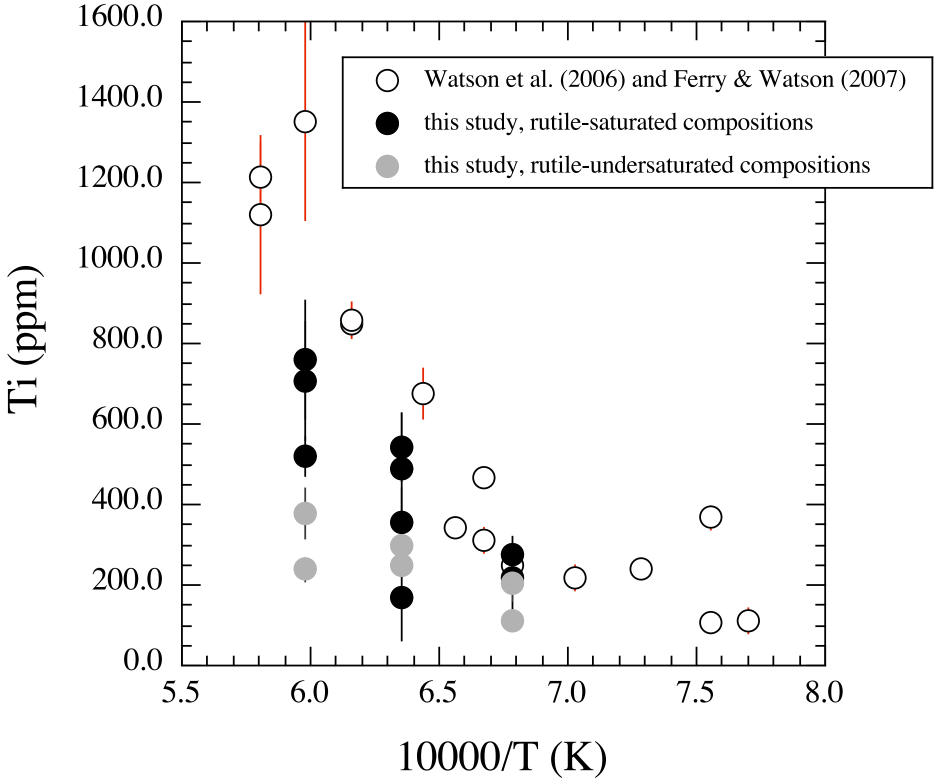

Figure 7. Comparison of Ti concentrations in zircon overgrowths from this study (black and gray circles) and in zircons from Watson et al. (2006) and Ferry and Watson (2007) (open circles). Error bars on data from this study are one standard deviation; error bars on data from Watson et al. (2006) and Ferry and Watson (2007) are two standard errors, as reported. With one exception, zircons grown from bulk compositions undersaturated in rutile (gray circles) contain the lowest Ti. The large error on the single exception (lowest black circle; GO-3-1) suggests that it may not record a fully equilibrated zircon composition.

rutile-undersaturated experiments plot below those from rutile-saturated runs at the same temperature. This is consistent with our expectations: at the same temperature and for similar liquid compositions, rutile-saturated melts should have higher TiO_2 contents, and this in turn should translate into higher Ti in the coexisting zircon. The exception is experiment GO-3-1 where the Ti of the zircon overgrowth is much lower than all other Ti contents in zircons at 1300°C and has a large standard deviation (± ~ 65% of the mean). These observations suggest that zircons in GO-3-1 may not have completely equilibrated with the liquid, and another experimental charge of this composition has been prepared to run in the piston cylinder for a longer duration.

Ferry and Watson (2007) proposed, based on crystal-chemical arguments, that the reaction controlling Ti concentrations in zircon is: $ZrSiO_4^{xtal} + TiO_2^{liq} = ZrTiO_4^{xtal} + SiO_2^{liq}$ where xtal and liq refer to crystal and liquid, respectively. They went on to suggest that the equilibrium constant derived from this expression could be simplified by assuming that $a_{ZrSiO_4} \approx 1$ and that a_{ZrTiO_4} could be approximated by a Henry's Law constant and a factor to covert mole fraction of $ZrTiO_4$ to Ti ppm. Finally, they predicted that log(Ti-in-zircon, ppm) + log($a_{SiO_2}{}^{liq}$) - log($a_{TiO_2}{}^{liq}$) should vary linearly with 1/T and in fact their experimental data define a line in a plot of this index v. 1/T (see their Figure 4). Plotting our data in these same dimensions requires calculating the appropriate activities of SiO_2 and TiO_2 in each of our experiments.

All of our experiments are undersaturated with respect to quartz. Quartz is not present in any of our runs and the normalized silica contents of our quenched glasses (64.2–70.7 wt. %) are substantially lower than 81.8 wt. % SiO_2, the concentration that results from equilibrating a rhyolite glass with quartz at 10 kbar and 1350°C (Gaetani et al. 1998). We calculated the activity of SiO_2 in our experiments with respect to quartz (a_{SiO_2}) using pHMELTS (MELTS mode, superliquidus calculation; Ghiorso and Sack 1995; Smith and Asimow 2005). The activity of SiO_2 was determined from the affinity of quartz (the difference between the chemical potential of silica in the liquid and the chemical potential of the stable phase of quartz at the T and P of interest) for each experimental glass after renormalizing our glass compositions on a ZrO_2-free basis (the MELTS model does not include Zr). We ignored the small correction from β-quartz (the stable phase predicted by MELTS for our experiments) to α-quartz (the reference phase used by Ferry and Watson 2007); these authors report that, in those cases for which experimental temperatures lie in the β-quartz stability field, the correction to the α-quartz reference state is < 0.03 log units for $T \leq 1300°C$. For our liquids, predicted $a_{\mathrm{SiO_2}}$ values range from 0.82 to 0.59. For our rutile-saturated glasses, TiO_2 activities predicted by MELTS range from ~ 0.3 to 0.5, suggesting that MELTS is not well calibrated for Ti in this region of composition space. Instead we have followed Ferry and Watson (2007) and set $a_{\mathrm{TiO_2}}$ equal to the mole fraction of TiO_2 in the coexisting rutile (i.e., we assumed that Raoult's Law holds for TiO_2 mole fractions of 0.93–0.97, the range observed in our experimental rutiles). For our rutile-undersaturated experiments, we followed Hayden and Watson (2007) and assumed that $a_{\mathrm{TiO_2}}$ was equal to the ratio of the measured mole fraction of TiO_2 in the liquid to the predicted mole fraction of TiO_2 in the liquid at rutile saturation. For our rutile-undersaturated experiments, we used the model of Gaetani et al. (2008) to estimate liquid X_{TiO_2} at rutile saturation. Note that the Gaetani et al. (2008) model is calibrated assuming that $X_{TiO_2}^{rt} = 1$; in our rutile-saturated glasses, $X_{TiO_2}^{rt}$ is inversely correlated with 1/T and thus for each of the rutile-undersaturated glasses the ratio ($X_{TiO_2}^{liq} / X_{TiO_2}^{liq}$ at saturation) was multiplied by $X_{TiO_2}^{rt}$ for the temperature of that experiment. Activities of TiO_2 in our rutile-undersaturated glasses range from ~ 0.8 to 0.4.

Figure 8 shows our experimental results plotted as a function of log(Ti-in-zircon, ppm) + $\log(a_{\mathrm{SiO_2}}) - \log(a_{\mathrm{TiO_2}})$ vs. 1/T (K); also plotted is the best-fit regression line from Ferry and Watson (2007). The results of experiments on the synthetic bulk compositions are shown in panel (a), the runs made using the G-2 granite are plotted in (b), and a global fit is shown in (c). Equations for the weighted least-squares fits for each panel are given in the caption and are discussed in more detail below. In all cases, our experimental data plot below the calibration curve for Ti-in-zircon of Ferry and Watson (2007) and generate least-squares fits with steeper slopes. Although our rutile-undersaturated data tend to plot, on average, slightly below our rutile-saturated points, the differences are not great and thus it is unlikely that systematic

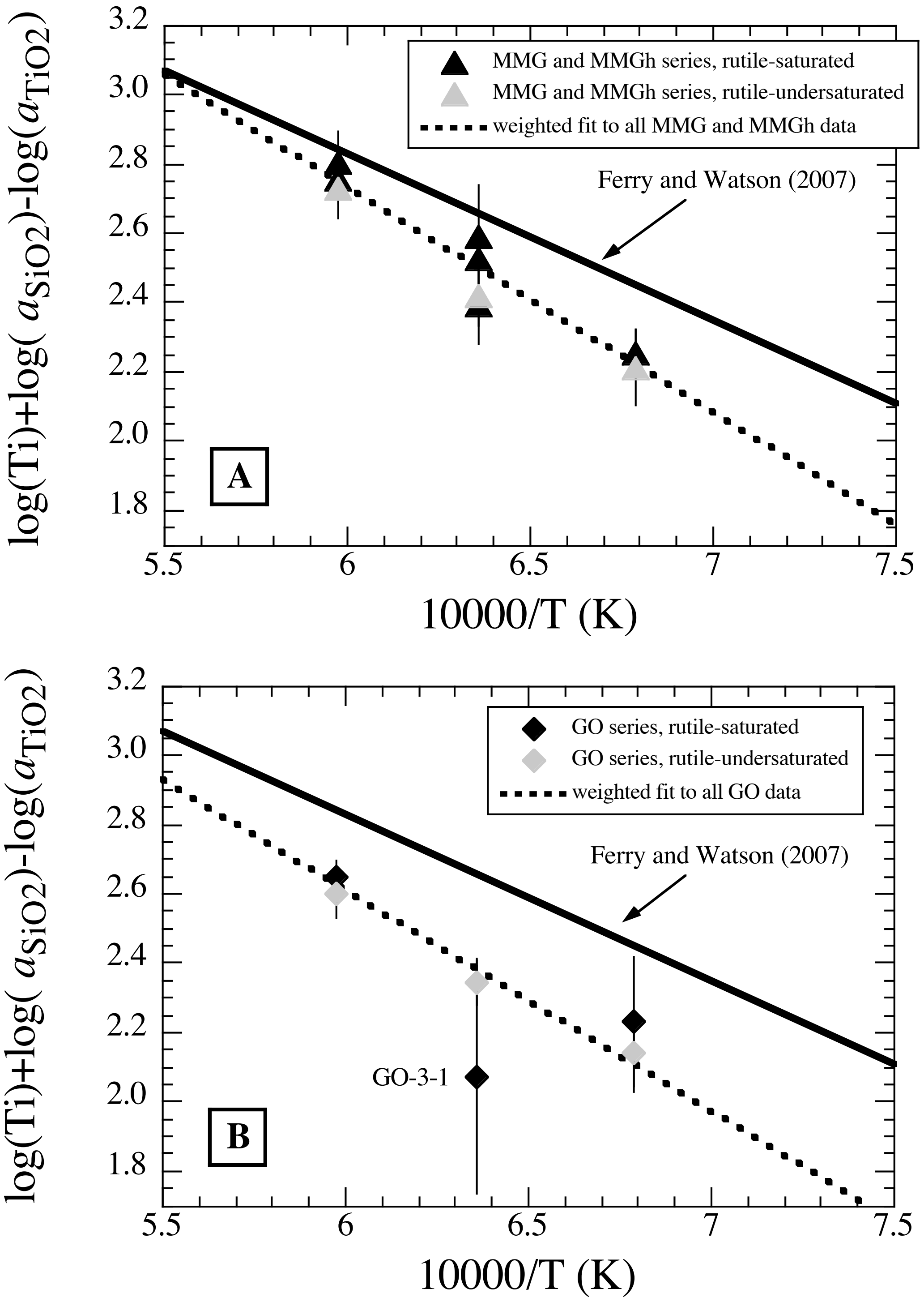
A
MMG and MMGh series, rutile-saturated
MMG and MMGh series, rutile-undersaturated
weighted fit to all MMG and MMGh data
Ferry and Watson (2007)
log(Ti)+log(a_{SiO2})-log(a_{TiO2})
10000/T (K)
3.2
3.0
2.8
2.6
2.4
2.2
2.0
1.8
5.5
6
6.5
7
7.5
B
GO series, rutile-saturated
GO series, rutile-undersaturated
weighted fit to all GO data
Ferry and Watson (2007)
GO-3-1
log(Ti)+log(a_{SiO2})-log(a_{TiO2})
10000/T (K)

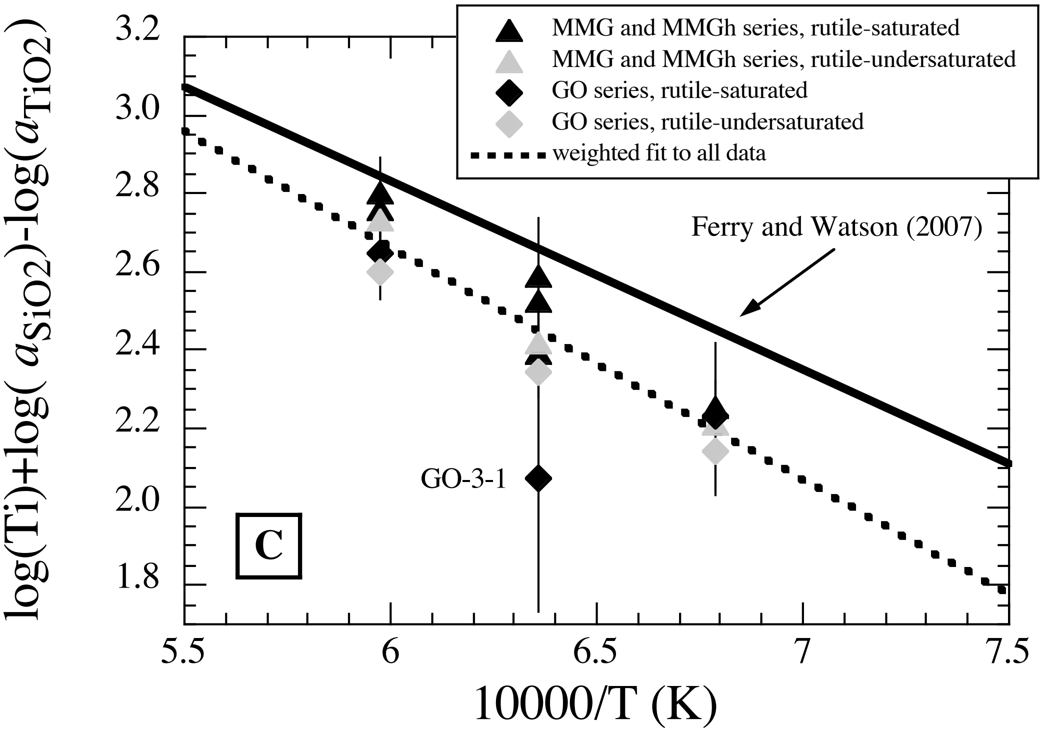

Figure 8. Comparison of the calibration curve reported in Ferry and Watson (2007) to Ti concentrations in zircon overgrowths from this study plus estimates of the activities of SiO_2 and TiO_2 in each experimental system. **a.** Zircons grown from synthetic oxide compositions (MMG and MMGh series), with rutile-undersaturated charges denoted as light gray triangles. **b.** Zircons grown from a modified natural granite compositions (i.e., the GO series), with rutile-undersaturated charges denoted as light gray diamonds. **c.** A global fit to all data from this study. The 1 sigma error bars on log(Ti-in-zrc, ppm) + log(a_{SiO_2}) – log(a_{TiO_2}) reflect uncertainties on the zircon Ti concentrations (Table 2), an estimated 5% uncertainty on a_{SiO_2}, and either the uncertainty on the TiO_2 concentration in the rutile (Table 4) or an error of 10% on the calculated a_{TiO_2} value for the rutile undersaturated experiments (the calculation of a_{TiO_2} for the rutile-undersaturated runs is described in the text). Note that the uncertainty on the Ti content of the zircon contributes the bulk of the error. Weighted linear least-square fits that account for errors in "y" are included in each panel and correspond to the following equations for synthetic compositions (1), natural compositions (2), and all compositions(3):

$$\log(\text{Ti-in-zrc, ppm})+\log(a_{SiO_2})-\log(a_{TiO_2}) = (6.624 \pm 0.579)-(6485 \pm 916)/T\ (K);\ R^2 = 0.94 \quad (1)$$

$$\log(\text{Ti-in-zrc, ppm})+\log(a_{SiO_2})-\log(a_{TiO_2}) = (6.433 \pm 0.704)-(6369 \pm 1144)/T\ (K);\ R^2 = 0.94 \quad (2)$$

$$\log(\text{Ti-in-zrc, ppm})+\log(a_{SiO_2})-\log(a_{TiO_2}) = (6.214 \pm 0.430)-(5918 \pm 689)/T\ (K);\ R^2 = 0.85 \quad (3)$$

Removing the datum for GO-3-1 makes the GO series slope shallower by ~ 2% and the global slope shallower by < 0.5% and improves the R^2 values to 0.96 and 0.87, respectively. The result of a two-sample t-test (P-value = 0.155) performed on the populations fit by equation (1) and equation (2) suggests that the two data series are indistinguishable at the 95% confidence level.

errors in estimating a_{TiO_2} in the under-saturated glasses are affecting our fits. However, differences in estimating a_{SiO_2} between the two studies may account for some of the mismatch seen in Figure 8, and there is also the issue of potential systematic analytical errors.

Figure 9 shows the Zr content in ppm of our experimental rutiles plotted as a function of log(Zr-in-rutile, ppm) + log(a_{SiO_2}) vs. 1/T (K) where a_{SiO_2} has the same value as that used in the corresponding Ti-in-zircon expression. The best-fit line from Ferry and Watson (2007) and a weighted least-squares fit to our data are also shown. Similar to what was seen in Figure 8, our data in Figure 9 plot below the Ferry and Watson line and at a steeper angle. Rutile compositions plotted in Figure 9 were made using the electron microprobe, and therefore the similar direction of offset in rutile-composition space (compared to that observed in zircon-composition space) argues against there being a systematic NanoSIMS analytical error depressing our measurements of Ti in zircon.

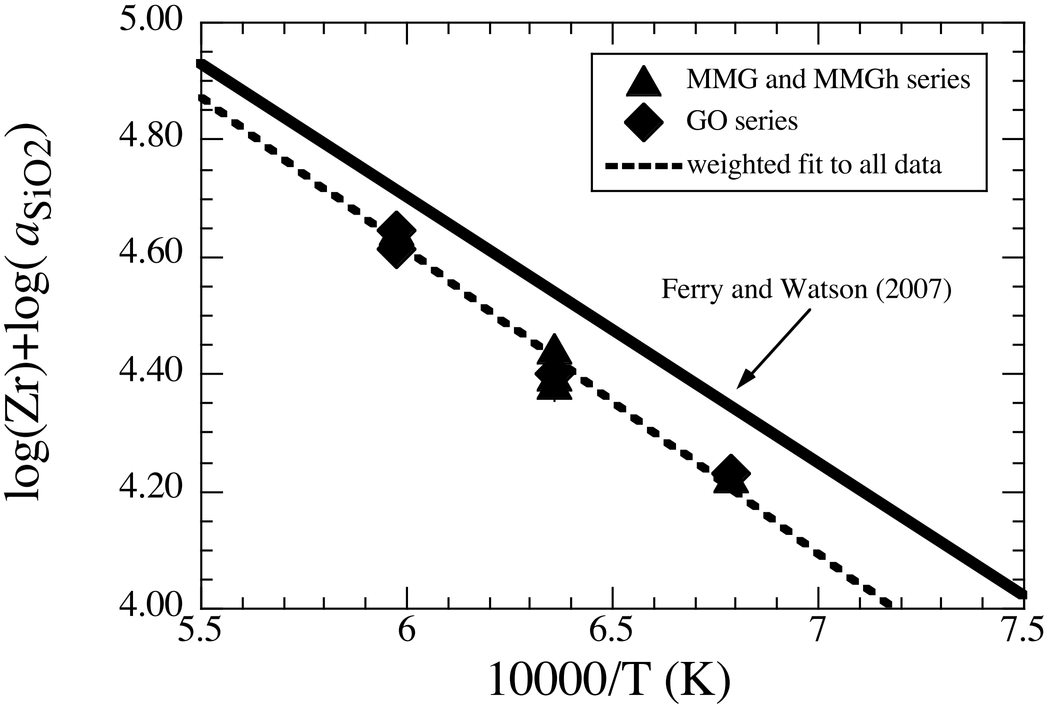

Figure 9. Comparison of the calibration curve reported in Ferry and Watson (2007) to Zr concentrations in rutiles from this study plus the activity of SiO_2 in each experimental system. A weighted linear least square fit that accounts for errors in the log(Zr-in-rut, ppm) + log($aSiO_2$) term is included and correspond to the equation: log(Ti-in-rut, ppm)+log(a_{SiO_2}) = (7.723±0.178)–(5184±284)/T K; R^2 = 0.98. (4) One sigma uncertainties on the log(Zr-in-rut, ppm) + log($aSiO_2$) term reflect uncertainties on the average ZrO2 content of the rutile and an estimated 5% uncertainty on a_{SiO_2}.

In both our experiments and most of those used to calibrate the Ti-in-zircon thermometer (Ferry and Watson 2007), a_{SiO_2} is potentially the least well-constrained parameter. Assuming a systematic offset between our MELTS-based a_{SiO_2} values and those calculated by Ferry and Watson (2007) using either zircon and zirconia equilibrium or Zr-in-rutile, we calculated the a_{SiO_2} activity required to move our coexisting Ti-in-zircon and Zr-in-rutile values for a given experiment onto or close to (given the constraint that a_{SiO_2} must be ≤ 1) the Ferry and Watson (2007) calibration curves; in all cases, an SiO_2 activity of between 0.85 and 1.00 was required. A plot of the difference between our MELTS-calculated a_{SiO_2} values and the a_{SiO_2} required for our experiments to fall on or near the Ferry and Watson (2007) calibration curves is given in Figure 10.

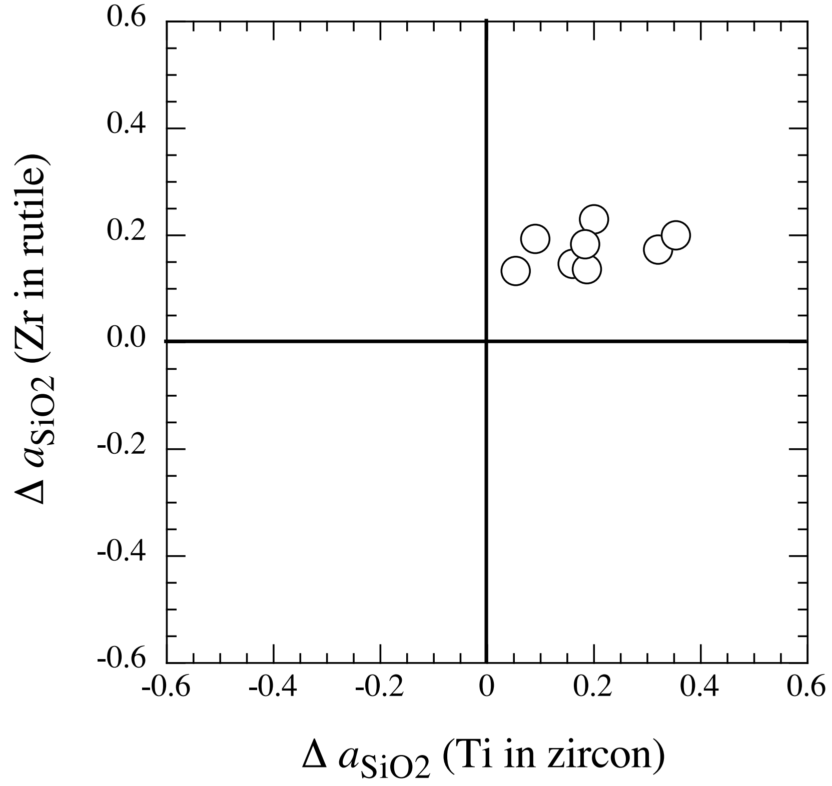

Figure 10. Plot of the change in SiO_2 activity required to move either the log(Ti-in-zrc, ppm)+log(a_{SiO_2})–log(a_{TiO_2}) term or the log(Ti-in-rut, ppm)+log(a_{SiO_2}) term for each rutile+zircon-saturated experiment from this study onto or near (under the constraint that $a_{SiO_2} \leq 1$) the respective calibration line of Ferry and Watson

(2007). Although the data cluster in the upper-right quadrant, the horizontal spread in data (with respect to the zircon calibration) suggests that no single correction factor for a_{SiO_2} will reconcile our data with the calibration lines of Ferry and Watson (2007).

Although the Δa_{SiO_2} values cluster in the upper-right quadrant of Figure 10, the horizontal spread in these values suggest that no single correction term for a_{SiO_2} can reconcile our experimental data with that of Watson et al. (2006) and Ferry and Watson (2007). Without better constraints (e.g., experiments saturated in quartz, zircon, and rutile) or independently testing our a_{SiO_2} calculations, it is difficult to resolve this discrepancy.

3.5 Do trace elements in zircon affect the Ti-in-zircon thermometer?

Although we cannot presently resolve the discrepancies between our data and those of Watson et al. (2006) and Ferry and Watson (2007), we nevertheless can return to the question of whether the presence of trace elements (at concentrations comparable to those found in natural granites) affects Ti partitioning between zircon and melt. Figure 8 is broken into three panels: the uppermost plot is of zircons grown from synthetic oxide compositions, with rutile-undersaturated charges denoted as light gray triangles; the middle plot is of zircons grown from a modified natural granite composition (i.e., the GO series) and rutile-undersaturated charges are denoted as light gray diamonds; the bottom panel displays a global fit to all data from this study. Weighted linear least square fits that account for errors in the log(Ti-in-zircon, ppm) + log(a_{SiO_2}) – log(a_{TiO_2}) term are also plotted in each panel of Figure 8 and correspond to the following equations for synthetic compositions (1), natural compositions (2), and all compositions (3):

$$\log(\mathrm{Ti,ppm}) + \log(a_{SiO_2}) - \log(a_{TiO_2}) = (6.624 \pm 0.579) - \frac{6485 \pm 916}{\mathrm{T\ (K)}};\ R^2 = 0.94 \qquad (1)$$

$$\log(\mathrm{Ti,ppm}) + \log(a_{\mathrm{SiO_2}}) - \log(a_{\mathrm{TiO_2}}) = (6.433 \pm 0.704) - \frac{6369 \pm 1144}{\mathrm{T\ (K)}};\ R^2 = 0.94 \qquad (2)$$

$$\log(\mathrm{Ti,ppm}) + \log(a_{\mathrm{SiO_2}}) - \log(a_{\mathrm{TiO_2}}) = (6.214 \pm 0.430) - \frac{5918 \pm 689}{\mathrm{T\ (K)}};\ R^2 = 0.85. \qquad (3)$$

Deleting the datum for GO-3-1 makes the GO series slope shallower by ~ 2% and the global slope shallower by less than 0.5% and improves the R^2 values for equations (2) and (3) to 0.96 and 0.87, respectively. Extrapolation of these fits to lower temperatures is not advised.

A two-sample F-test on the log(Ti-in-zircon, ppm) + $\log(a_{\mathrm{SiO_2}})$ – $\log(a_{\mathrm{TiO_2}})$ terms from our synthetic and natural composition series experiments indicates that, at the 95% confidence level, the variances are statistically equivalent; therefore, a two-sample t-test was performed on the same two data populations assuming a null hypothesis that the two sample means were equivalent. The result of the t-test (P-value = 0.155) suggests that the two data series are indistinguishable at the 95% confidence interval, and, therefore, the fits for the synthetic series (eqn. 1) and the natural composition series (eqn. 2) are indistinguishable from one another within error. This result suggests—but does not confirm—that, at temperatures greater than 1200°C, Ti partitioning between zircon and melt is not significantly affected by the presence of other trace elements in the liquid, at least at concentrations found in the GO-series melts. However, the effect of other trace elements on Ti partitioning at temperatures relevant to zircon crystallization in nature (~ 600 to 1000°C) remains unknown and is further justification and motivation for performing the cold-seal pressure vessel experiments described above. To explain spatial correlations among Ti and other trace elements observed at micron-to-submicron scales in natural zircons, Hofmann et al. (2009a) suggested that Ti partitioning into zircon may be enhanced in the presence of other trace elements due to changes in the sizes and shapes of cation sites within the zircon crystal lattice that preferentially decrease the activation energy required for Ti substitution. At temperatures > 1200°C, this effect is not observed. The absence of such an effect may be due to configurational entropy, which would "favor" a completely disordered state and dominate the free energy expression (over enthalpy) for these substitutions at high temperatures.

Although we were unable to directly measure other trace elements in the zircon overgrowths from our experiment, we can predict what their concentrations should be given the liquid compositions in our experiments. Using a zircon-melt partition coefficient for phosphorus of 2 from Luo and Ayers (2009) for zircons grown at temperatures ≥ 1200°C and an average GO liquid composition of ~ 3000 ppm P, we should expect P of ~ 6000 ppm in the zircon overgrowths, which should have been detectable even at the low beam currents used in this study. It seems prudent, therefore, to spend additional time tuning the NanoSIMS in an attempt to detect $^{31}P^{16}O^{-}$ when we analyze the new GO series experiments that were not completed in time for inclusion in this thesis. Yttrium and cerium concentrations in the zircon overgrowths are expected to be much lower (< 100 ppm Y and < 30 ppm Ce) based on: 1) the GO series starting compositions containing less than 10 ppm Y and less than 150 ppm Ce (values given for the G-2 bulk composition), and 2) average partition coefficients of 10 and 0.2 for Y and Ce, respectively (Luo and Ayers 2009). When combined with the low ionization potentials of the negative molecular ions $^{89}Y^{16}O^{-}$ and $^{140}Ce^{16}O^{-}$, it seems unlikely that resolvable signals for either ion will be detected even with additional tuning of the NanoSIMS. Because Hf was added to the starting compositions only as a component bound within the zircon seed crystals, no attempt was made to determine Hf contents in the resulting experimental glasses, even though we expect that some dissolution of the seeds occurred. A plot of Hf v. Ti (both in ppm) in the zircon overgrowths for the same starting HfO_2 composition (i.e., only those experiments with bulk HfO_2 = 0.2 wt. %, Table 1) showed neither discernable correlations between Ti and Hf nor differences in the overgrowth Hf concentrations between zircons from the trace-element enriched (i.e., GO) series and the two synthetic series (MMG and MMGh).

We have used the NanoSIMS to make ion maps of natural zircons of known provenance (Chapter 3 of this thesis; Hofmann et al. 2009b) including two zircons from the IG2E unit of the Bishop Tuff (Hildreth 1979; Wilson and Hildreth 1997; Hildreth and Wilson 2007). One of those zircons (BT1-8) shows no apparent spatial correlations between Ti and either other trace elements or cathodoluminescent (CL) banding; this zircon records a range of Ti contents from ~ 5 to 30 ppm. Conversely, the image of the second Bishop Tuff zircon (BT2-10) displays positively correlated Ti, Y, P, and Ce, the distributions of which appear to track oscillatory CL banding, i.e., high trace-element concentrations coincident with CL-dark bands. The Ti range recorded by this zircon is ~ 1 to 4 ppm—over a factor of five less than that recorded in BT1-8. A conservative estimate of the average Ti in two adjacent CL bands from BT2-10 suggests an increase by a factor of two from a CL-bright (~ 1.5 ppm) to a CL-dark (~ 3 ppm) region. With the caveats that 1) zircons extracted from IG2E need not have experienced much, if any, crystallization during their residence in that unit and 2) two adjacent CL bands—taken to indicate a distinct period of zircon growth—can be separated in both time and temperature, we plot in Figure 11 all of our experimental data and the high and low Ti contents from adjacent CL bands in BT2-10 using the average of new magnetite-ilmenite temperatures calculated for samples from the IG2E stratigraphic sequence (Hildreth and Wilson 2007). We interpret the large range in Ti (25 ppm) observed over a 20 × 20 μm area in zircon BT1-8 as evidence of disequilibrium and therefore do not include it in the low-temperature fit presented in Figure 11. The dashed black line in Figure 11 is the global fit to all experimental data (as previously presented in the lower panel of Figure 8) extrapolated to lower temperatures. The dotted gray line shows a linear least-squares fit of all experimental

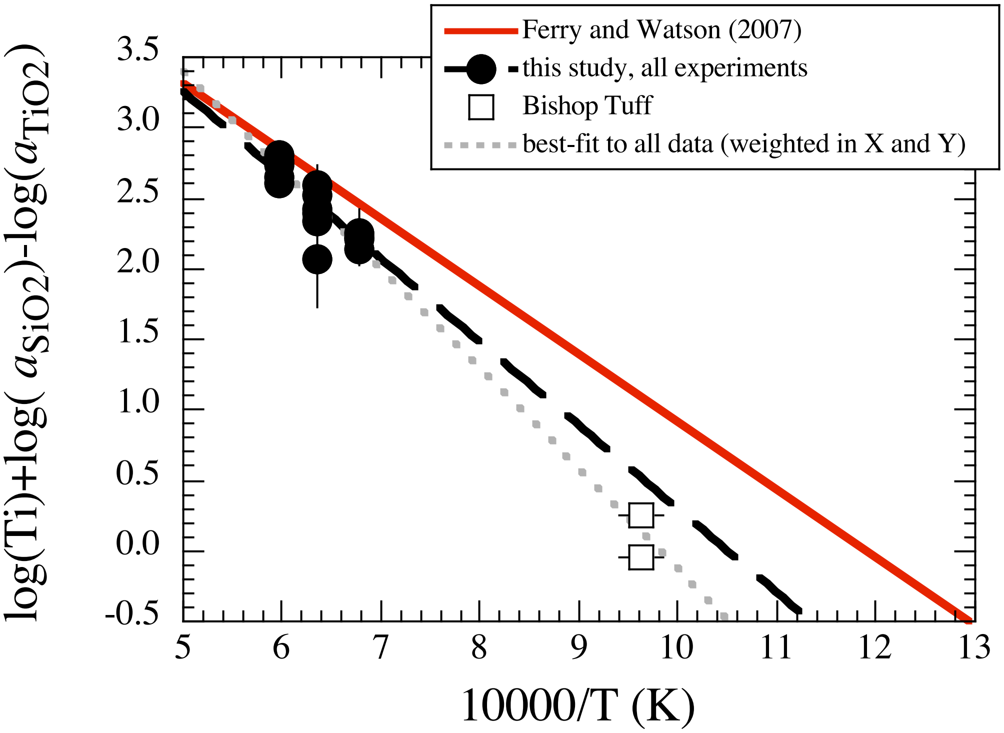

Figure 11. Comparison between the Ferry and Watson global fit (solid red line), the weighted global fit (dashed line) to all of our experiments (filled circles), and a weighted global fit (dotted gray line) to our experimental data and to NanoSIMS data from a Bishop Tuff zircon (open squares). The NanoSIMS data are presented in Chapter 3 and are conservative estimates of the average Ti in two adjacent CL bands from Bishop Tuff zircon BT2-10 from the IG2E unit described by Hildreth (1979), Wilson and Hildreth (1997), and Hildreth and Wilson (2007). Activities were assigned as $a_{\mathrm{SiO_2}}$ = 1 and $a_{\mathrm{TiO_2}}$ = 0.6 based on the presence of quartz and ilmenite and ulvospinel in the IG2E unit. Temperature was assigned based on the updated Fe-Ti oxide thermometry of unit IG2E presented in Hildreth and Wilson (2007); see text. Errors on the NanoSIMS-derived Ti were assigned to be 10%; errors on the temperature were taken to be one standard deviation. The weighted best-fit dotted gray line includes errors in both X and Y and yields the following equation: log(Ti-in-zrc, ppm)+log($a_{\mathrm{SiO_2}}$)–log($a_{\mathrm{TiO_2}}$) = (6.921±0.118)–(7047±292)/T (K). (5)

data and the NanoSIMS Bishop Tuff data for zircon BT2-10, weighted to errors in both X and Y. The calibration curve from Ferry and Watson (2007) is given as the solid red line for comparison. The weighted best-fit line to all data corresponds to the following equation:

$$\log(\mathrm{Ti,ppm}) + \log(a_{\mathrm{SiO_2}}) - \log(a_{\mathrm{TiO_2}}) = (6.921 \pm 0.118) - \frac{7047 \pm 292}{\mathrm{T\ (K)}}. \quad (5)$$

A two-sided t-test shows that the slopes of eqn. 3 and eqn 5 are statistically different at the 95% confidence level. It should be noted that this fit (eqn. 5) includes a 400°C temperature window for which we have no experimental constraints and is essentially a two-point calibration whose slope could be altered by changing the location of the Bishop Tuff data. Given the robustness of our NanoSIMS data (i.e., Ti of experimental zircons were determined from nominally homogeneous plateaus in $^{48}Ti^{16}O^{-}/^{94}Zr^{16}O^{-}$), the fit represented by eqn. 5 suggests that 1) the crystallization temperatures assigned to the natural zircons chosen to calibrate the Ti-in-zircon thermometer (Watson et al. 2006; Ferry and Watson 2007) were too low, 2) that there is a systematic error in the Ti concentrations measured for those zircons, or 3) that estimates of $a_{\mathrm{TiO_2}}$ and/or $a_{\mathrm{SiO_2}}$ were in error. In assigning temperatures to a given populations of natural zircons, Watson et al. (2006) discuss uncertainties in their choices of temperature constraints (e.g., assigning the temperature of a neighboring metamorphic rock assemblage to a zircon population because the population comes from a metamorphic assemblage for which the temperature has not been determined). Additionally, the observed presence of micron- to submicron-scale zoning in Ti spatially correlated with CL banding and other trace-element distributions (e.g., Chapter 3 of this thesis; Hofmann et al. 2009a; Hofmann et al. 2009b) implies that the Ti determined for these naturals using a 15-20 μm diameter beam (Watson et al. 2006) may be skewed to higher values.

3.6 Ti Partitioning Between Zircon and Melt

This study is the first attempt to synthesize zircons from granitic bulk compositions in which both the zircon and the coexisting glass could be analyzed and therefore a partition coefficient for Ti between zircon and melt ($\mathrm{D_{Ti}^{zrc/melt}}$) determined. Previously reported Ti partition coefficients appear anomalously high (e.g., $\mathrm{D_{Ti}^{zrc/melt}} \sim 3$) compared to values from natural zircon-melt pairs (e.g., $\mathrm{D_{Ti}^{zrc/melt}} = 0.001–0.04$, calculated from values provided in Lowery Claiborne et al. (2006)). This discrepancy may be due to the fact that the high apparent Ti zircon-melt partition coefficients were in one case calculated by mass balance (Luo and Ayers 2009) and in the other based on measurements of ^{48}Ti (Thomas et al. 2002; B. Watson and J. Thomas, personal communication), which is known to suffer from multiple isobaric interferences in zircon, most importantly doubly charged ^{96}Zr. Partition coefficients for Ti between zircon and melt from this study are between 0.014 and 0.029 (we have not included the GO-3-1 point; Figure 12), consistent with the apparent incompatibility of Ti in the zircon lattice and with $D_{Ti}^{zrc/melt}$ calculated from natural zircon-glass pairs. In general, Ti partitioning appears to have a slight temperature dependence ($R^2 = 0.1$); however, this temperature dependence disappears (i.e., the trend, which is weighted by errors in Y, becomes horizontal with a value of ~ 0.02) when the datum for GO-3-1 is removed. It should be noted that these partition coefficients are for a limited range of bulk compositions and temperatures; down-temperature extrapolation of the weighted fit is not advised. Data from the Bishop Tuff, which has bulk SiO_2 contents on order ~ 10 wt. % greater than the bulk compositions of our experiments and which crystallized at much lower temperatures, are included for comparison. The bounding box for the Bishop Tuff data was constructing assuming a low value of Ti = 1 ppm based on NanoSIMS observations (Chapter 3) of a zircon from unit IG2E and a high value of Ti = 4.5 based on the average given in Watson et al. (2006) for zircons from the same unit that were used in calibrating the Ti-in-zircon thermometer. An average melt Ti content was determined using melt inclusion analyses from Wallace et al. (1999) from the IG2E unit. The temperature range was assigned based on the most recent compilation Fe-Ti oxide thermometry of the IG2E unit (Hildreth and Wilson 2007).

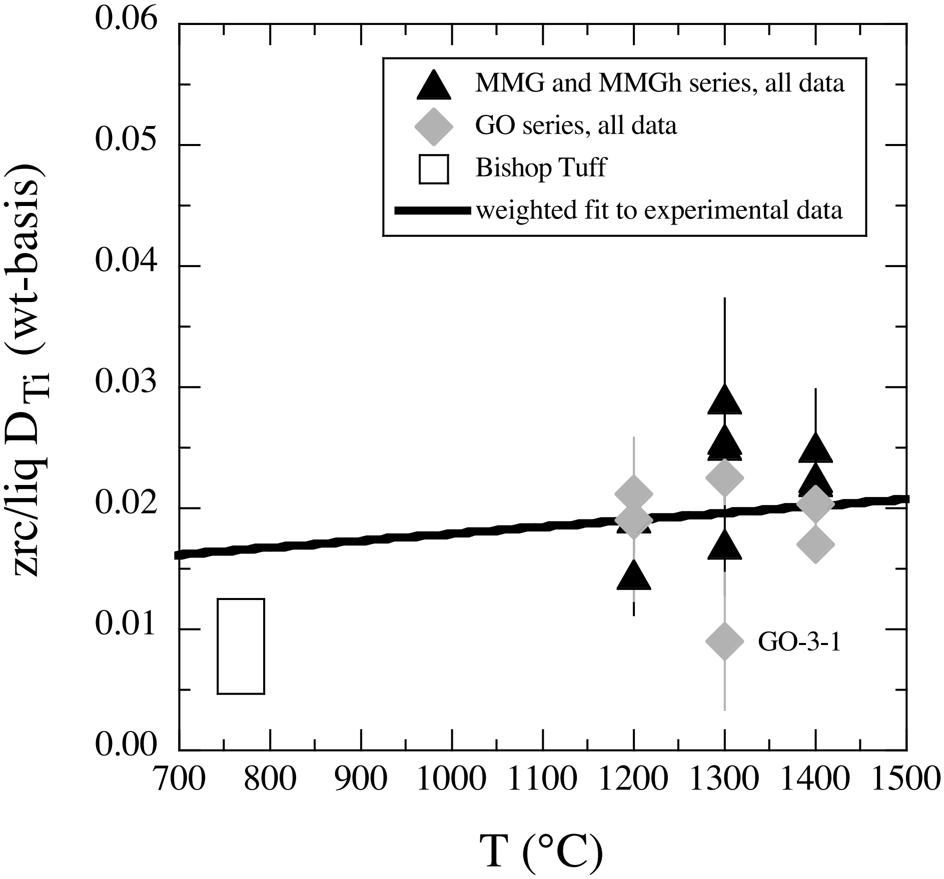

Figure 12. Zircon-melt partition coefficients for Ti as determined from coexisting experimental zircons and glasses (this study). Ti partitioning appears to have a slight temperature dependence, which disappears (i.e., the trend, which is weighted by errors in Y, becomes horizontal with a value of ~ 0.02) when the datum for GO-3-1 is removed. The bounding box for the Bishop Tuff data was constructing assuming a minimum value of Ti = 1 ppm based on NanoSIMS observations (Chapter 3) of a zircon from unit IG2E and a maximum value of Ti = 4.5 ppm based on the average given in Watson et al. (2006) for zircons from the same unit and used for calibration of the Ti-in-zircon thermometer. An average melt Ti was determined using analyses of melt inclusions from unit IG2E (Wallace et al. 1999). The temperature range was assigned based on the most recent compilation Fe-Ti oxide thermometry of the IG2E unit by Hildreth and Wilson (2007).

The fact that the $D_{Ti}^{zrc/melt}$ determined for the Bishop Tuff lies below our weighted best-fit curve suggests three possible interpretations: 1) given the limited temperature range of our experiments, we have not "captured" the true temperature dependence of $D_{Ti}^{zrc/melt}$; 2) $D_{Ti}^{zrc/melt}$ is a strong function of composition and decreases with increasing SiO_2 in the melt; 3) the $D_{Ti}^{zrc/melt}$ values recorded by the Bishop Tuff zircons are disequilibrium values. Testing the first hypothesis requires performing additional experiments at lower temperatures using the same starting compositions; testing the second hypothesis requires changing the initial bulk compositions but performing experiments over the same temperature interval. In the absence of these additional data, we can only suggest that the third hypothesis seems plausible given the fact that zircons from the Bishop Tuff, like all other natural zircons analyzed to date using the NanoSIMS (Chapter 3; Hofmann et al. 2009a; Hofmann et al. 2009b) display complex Ti distributions that are frequently spatially correlated at the micron- to submicron-scale with variable distributions of other trace elements and oscillatory CL (i.e., growth) banding. Given the slow solid-state diffusivities for these elements in zircon (e.g., $< 1 \times 10^{-18}$ mm^2/s for Ti and the rare earths at 1000°C; Cherniak et al. 1997; Cherniak and Watson 2007), it seems unlikely that even two adjacent growth bands would undergo much re-equilibration below this temperature: at 1000°C, diffusion of Ti a distance of 1 μm would take on order ~ 30 million years. On the other hand, the Ti of our experimental zircons were taken from nominally homogeneous plateaus in $^{48}Ti^{16}O^-/^{94}Zr^{16}O^-$ resolvable from a core of even lower $^{48}Ti^{16}O^-/^{94}Zr^{16}O^-$ and therefore represent, to the best of our knowledge, new zircon overgrowths that formed in equilibrium with melt during our high-temperature experiments.

4. Conclusions

Our 10 kbar experiments on a series of synthetic and natural granitic compositions (enriched in ZrO_2) yield zircon-liquid and rutile-liquid pairs over a temperature range of 1400 to 1200°C. The quenched glasses contain between 1.8 and 3.3 wt. % zircon; 6 of the 16 experiments contain between rutile (up to 1.1 wt. %). SiO_2 contents of the quenched glasses range from 64.2 to 70.7 wt. % and water varied from 0.4 to 7 wt. %. TiO_2 contents of the rutile-saturated quenched melts are positively correlated with run temperature, vary from 1.9 to 5.1 wt. %, and are consistent with the recent rutile-saturation model of Gaetani et al. (2008).

At a given temperature, ZrO_2 contents of the liquids are strongly correlated with the cation-based melt parameter used by Harrison and Watson (1983), although our measured concentrations are substantially below what their model would predict. This almost certainly reflects the fact that our run temperatures are substantially outside the range of temperatures of the experiments used to calibrate their model. ZrO_2 contents of the rutiles in our experiments are positively correlated with temperature and range from 7.2 to 3.2 wt. %; these values are nearly a factor of two lower than the measured concentrations of ZrO_2 in rutiles from the experiments of Watson et al. (2006) and Ferry and Watson (2007). NanoSIMS measurements of Ti in zircon overgrowths rims in our experiments range from 760 to 112 ppm and show a positive correlation with TiO_2 content of the quenched glass and run temperature. Our Ti-in-zircon values when "adjusted" for SiO_2 and TiO_2 melt activities (i.e., log(Ti-in-zircon, ppm) + $\log(a_{SiO_2})$ – $\log(a_{TiO_2})$ show a strong inverse correlation with 1/T; however, our data plot below the calibration line of Ferry and Watson (2007). Least squares fits to the two sets of data generated in this study (synthetic bulk compositions and natural bulk compositions) yield equations with slopes that are statistically indistinguishable; however, the least-squares fits are steeper than that of Ferry and Watson (2007). Our Zr-in-rutile data also yields a regression line in composition v. 1/T space that is below and steeper than the equivalent calibration curve in Ferry and Watson (2007). At present we do not have a robust explanation for the discrepancies between the two data sets. Because of our experimental design—water contents not exceeding ~ 7 wt. % in the melts—we were able to quench our liquids, and, coupled with the NanoSIMS's ability to measure compositions from much smaller scale features than a conventional SIMS, thereby determine the first experimental zircon-melt Ti partition coefficient. Our measured $D_{Ti}^{zrc/melt}$ values are 0.014 to 0.029 and are broadly consistent with values determined from natural-zircon glass pairs. Finally, based on the inconsistencies between 1) our experimentally derived Ti-in-zircon calibration curve and that of Watson et al. (2006) and Ferry and Watson (2007) and 2) the Ti content as determined by Hofmann (Chapter 3) and Fe-Ti oxide temperatures of the IG2E Bishop Tuff zircons and those values used to calibrate the Ti thermometer in Watson et al. (2006) and Ferry and Watson (2007), we recommend a re-evaluation of the lower-temperature regime of the calibration curve. This is particularly important given the ambiguity involved in selecting a Ti concentration for a natural igneous zircon that displays oscillatory zoning in Ti. In particular, we suggest that the experimental zircons, which were synthesized at high temperatures and exhibit overgrowths with relatively constant Ti contents, likely represent a closer approach to equilibrium than natural zircons with oscillatory zoning, and long-duration, low-temperature zircon synthesis experiments should be performed to evaluate this hypothesis.

Acknowledgments

The author thanks Yunbin Guan for technical assistance on the NanoSIMS, Rick Hervig (ASU) for assistance on Caltech's 7fGeo SIMS, Chi Ma for assistance on the electron microprobe, and Bruce Watson for illuminating conversations regarding methodology and preliminary results. Financial support for this study was provided by the National Science Foundation to J.M. Eiler and a grant from the Moore Foundation to the Caltech Microanalysis Center.

References

Albarede F, Provost A (1977) Petrological and geochemical mass-balance equations: an algorithm for least-square fitting and general error analysis. Comput Geosci 3:309-326

Armstrong JT (1988) Quantitative analysis of silicate and oxide minerals: Comparison of Monte Carlo, ZAF and $\phi(\rho z)$ procedures. In: Newbury DE (ed) Microbeam analysis, vol. San Francisco Press, San Francisco, pp 239-246

Behrens H, Stuke A (2003) Quantification of H_2O contents in silicate glasses using IR spectroscopy—a calibration based on hydrous glasses analyzed by Karl-Fischer titration. Glass Sci Technol 76:1-14

Behrens H, Tamic N, Holtz F (2004) Determination of the molar absorption coefficient for the infrared absorption band of CO_2 in rhyolitic glasses. Am Mineral 89:301-306

Cherniak DJ, Hanchar JM, Watson EB (1997) Rare-earth diffusion in zircon. Chem Geol 134:289-301

Cherniak DJ, Manchester J, Watson EB (2007) Zr and Hf diffusion in rutile. Earth Planet Sci Lett 261:267-279

Cherniak DJ, Watson EB (2007) Ti diffusion in zircon. Chem Geol 242:470-483

Ferriss EA, Essene EJ, Becker U (2008) Computational study of the effect of pressure on the Ti-in-zircon geothermometer. Eur J Mineral 20:745-755

Ferry JM, Watson EB (2007) New thermodynamic models and revised calibrations for the Ti-in-zircon and Zr-in-rutile thermometers. Contrib Mineral Petrol 154:429-437

Fu B, Page FZ, Cavosie AJ, Fournelle J, Kita NK, Lackey JS, Wilde SA, Valley JW (2008) Ti-in-zircon thermometry: Applications and limitations. Contrib Mineral Petrol 156:197-215

Gaetani GA, Asimow PD, Stolper EM (1998) Determination of the partial molar volume of SiO_2 in silicate liquids at elevated pressures and temperatures: A new experimental approach. Geochim Cosmochim Acta 62:2499-2508

Gaetani GA, Asimow PD, Stolper EM (2008) A model for rutile saturation in silicate melts with applications to eclogite partial melting in subduction zones and mantle plumes. Earth Planet Sci Lett 272:720-729

Ghiorso MS, Sack RO (1995) Chemical Mass-Transfer in Magmatic Processes IV. A revised and internally consistent thermodynamic model for the interpolation and extrapolation of liquid-solid equilibria in magmatic systems at elevated temperatures and pressures. Contrib Mineral Petrol 119:197-212

Gladney ES, Jones EA, Nickell EJ, Roelandts I (1992) 1988 Compilation of elemental concentration data for USGS AGV-1, GSP-1, and G-2. Geostandard Newslett 16:111-300

Gladney ES, Roelandts I (1988) 1987 compilation of elemental concentration data for USGS BHVO-1, MAG-1, QLO-1, RGM-1, SCo-1, SDC-1, SGR-1, and STM-1. Geostandard Newslett 12:253-362

Govindaraju K (1994) 1994 Compilation of working values and descriptions for 383 geostandards. Geostandard Newslett 18(Special Issue):1-158

Hanson B, Delano JW, Lindstrom DJ (1996) High-precision analysis of hydrous rhyolitic glass inclusions in quartz phenocrysts using the electron microprobe and INAA. Am Mineral 81(1249-1262)

Hayden LA, Watson EB (2007) Rutile saturation in hydrous siliceous melts and its bearing on Ti-thermometry of quartz and zircon. Earth Planet Sci Lett 258:561-568

Hiess J, Nutman AP, Bennett VC, Holden P (2008) Ti-in-zircon thermometry applied to contrasting Archean metamorphic and igneous systems. Chem Geol 247:323-338

Hildreth W (1979) The Bishop Tuff: Evidence for the origin of compositional zonation in silicic magma chambers. Geol S Am S 180:43-75

Hildreth W, Wilson CJN (2007) Compositional zoning of the Bishop Tuff. J Petrol 48:951-999

Hofmann AE, Valley JW, Watson EB, Cavosie AJ, Eiler JM (2009a) Sub-micron scale distributions of trace elements in zircon. Contrib Mineral Petrol 158:317-335

Hofmann AE, Baker MB, Eiler JM (2009b) Sub-micron scale Ti variations in zircons of known provenance. Geochim Cosmochim Acta 73:A542

Huggins ML (1940) The density of silicate glasses as a function of composition. J Opt Soc Am 30:420-430

Ihinger PD, Hervig RL, McMillan PF (1994) Analytical methods for volatiles in glasses. In: Carroll MR, Holloway JR (eds) Volatiles in Magmas, vol 30. Mineralogical Society of America, Washington, D.C., pp 67-121

Jakobsson S, Oskarsson N (1994) The system C-O in equilibrium with graphite at high pressure and temperature: An experimental study. Geochim Cosmochim Acta 58:9-17

Krawczynski MJ, Sutton SR, Grove TL, Newville M (2009) Titanium oxidation state and coordination in the lunar high-titanium glass source mantle. In: 40th Lunar and Planetary Science Conference, pp 2164-2165

Kress VC, Carmichael ISE (1991) The compressibility of silicate liquids containing Fe_2O_3 and the effect of composition, temperature, oxygen fugacity, and pressure on their redox state. Contrib Mineral Petrol 108(82-92)

Le Maitre RW (1976) The chemical variability of some common igneous rocks. J Petrol 17:589-598

Lowery Claiborne L, Miller CF, Walker BA, Wooden JL, Mazdab FZ, Bea F (2006) Tracking magmatic processes through Zr/Hf ratios in rocks and Hf and Ti zoning in zircons: An example from the Spirit Mountain batholith, Nevada. Mineral Mag 70:517-543

Luo Y, Ayers JC (2009) Experimental measurements of zircon/melt trace-element partition coefficients. Geochim Cosmochim Acta 73:3656-3679

Maas R, Kinny PD, Williams IS, Froude DO, Compston W (1992) The Earth's oldest known crust: A geochronological and geochemical study of 3900–4200 Ma old detrital zircons from Mt. Narryer and Jack Hills, Western Australia. Geochim Cosmochim Acta 56:1281-1300

Matzen AK, Baker MB, Beckett JR, Stolper EM (2010) Fe-Mg partitioning between olivine and high-magnesian melts and the nature of Hawaiian parental liquids. Submitted to J Petrol

Menneken M, Nemchin AA, Geisler T, Pidgeon RT, Wilde SA (2007) Hadean diamonds in zircon from Jack Hills, Western Australia. Nature 448:917-921

Morgan VI GB, London D (1996) Optimizing the electron microprobe analysis of hydrous alkali aluminosilicate glasses. Am Mineral 81:1176-1185

Newman S, Stolper EM, Epstein S (1986) Measurement of water in rhyolitic glasses: Calibration of an infrared spectroscopic technique. Am Mineral 71:1527-1541

Ohlhorst S, Behrens H, Holtz F (2001) Compositional dependence of molar absorptivities of near-infrared OH- and H_2O bands in rhyolitic to basaltic glasses. Chem Geol 174:5-20

Page FZ, Fu B, Kita NT, Fournelle J, Spicuzza MJ, Schulze DJ, Viljoen F, Basei MAS, Valley JW (2007) Zircons from kimberlite: new insights from oxygen isotopes, trace elements, and Ti in zircon thermometry. Geochim Cosmochim Acta 71:3887-3903

Reid MR, Vazquez JA, Schmitt AK (2009) Zircon-scale insights into the history of a supervolcano, Bishop Tuff, Long Valley, California—With implications for the Ti-in-zircon geothermometer. Eos Transactions AGU 90(52):Abstract V44C-04

Sasaki J, Peterson NL, Hoshino K (1985) Tracer impurity diffusion in single-crystal rutile (TiO_{2-x}). J Phys Chem Solids 46:1267-1283

Smith PM, Asimow PD (2005) Adiabat_1ph: A new public front-end to the MELTS, pMELTS, and pHMELTS models. Geochem Geophy Geosy 6. doi:10.1029/2004GC000816

Stolper E (1982) Water in silicate glasses: an infrared spectroscopic study. Contrib Mineral Petrol 81:1-17

Thomas JB, Bodnar RJ, Shimizu N, Sinha AK (2002) Determination of zircon/melt trace element partition coefficients from SIMS analysis of melt inclusions in zircon. Geochim Cosmochim Acta 66:2887-2901

Tuttle OF, Bowen NL (1958) Origin of granite in the light of experimental studies in the system $NaAlSi_3O_8$-$KAlSi_3O_8$-SiO_2-H_2O. Waverly Press, Inc., Baltimore, MD, 153 pp

Wallace PJ, Anderson Jr. AT, Davis AM (1999) Gradients in H_2O, CO_2, and exsolved gas in a large-volume silicic magma system: Interpreting the record preserved in melt inclusions from the Bishop Tuff. J Geophys Res 104(B9):20097-20122

Watson EB, Harrison TM (1983) Zircon saturation revisited: temperature and composition effects in a variety of crustal magma types. Earth Planet Sci Lett 64:295-304

Watson EB, Harrison TM (2005) Zircon thermometer reveals minimum melting conditions on earliest Earth. Science 308:841-844

Watson EB, Wark DA, Thomas JB (2006) Crystallization thermometers for zircon and rutile. Contrib Mineral Petrol 151:413-433

Wiedenbeck M, Hanchar JM, Peck WH, Sylvester P, Valley J, Whitehouse M, Kronz A, Morishita Y, Nasdala L, Fiebig J, Franchi I, Girard J-P, Greenwood RC, Hinton R, Kita N, Mason PRD, Norman M, Ogasawara M, Piccoli PM, Rhede D, Satoh H, Schulz-Dobrick B, Skår Ø, Spicuzza MJ, Terada K, Tindle A, Togashi S, Vennemann T, Xie Q, Zheng Y-F (2004) Further characterisation of the 91500 zircon crystal. Geostand Geoanal Res 28:9-39

Wilson CJN, Hildreth W (1997) The Bishop Tuff: New insights from eruptive stratigraphy. J Geol 105:407-439

Zhang Y, Xu Z, Zhu M, Wang H (2007) Silicate melt properties and volcanic eruptions. Rev Geophys 45: doi: 8755-1209/07/2006RG000216

Chapter 3

SUB-MICRON SCALE TRACE ELEMENT DISTRIBUTIONS IN ZIRCONS OF KNOWN PROVENANCE: IMPLICATIONS FOR TI-IN-ZIRCON THERMOMETRY

Abstract

Sub-micron-scale zoning of Ti concentrations [Ti] and correlations between concentrations of Ti and other trace elements (P, Ce, and Y) and cathodoluminescent (CL) zonations is observed in 7 of 10 natural zircons of known provenance analyzed in this study. Of the remaining three zircons, one shows [Ti] inversely correlated with P, Y, and Ce concentrations; the oscillatory zoning shown by P, Y, and Ce tracks oscillatory CL bands. The other two zircons show no correlations between CL zones and either Ti or the other trace elements. Hafnium concentrations generally do not track CL banding or [Ti] in all 10 of the zircons that we analyzed. Using our compositional data and the fact that the NanoSIMS allows us to evaluate compositional variations on a much finer scale than a conventional SIMS, we evaluate the hypothesis that Ti concentrations in zircon reflect equilibrium, temperature-dependent partitioning—the premise behind Ti-in-zircon thermometry. We show that, in the case of zircons for which temperatures can be estimated using independent mineral equilibria, the temperatures derived from NanoSIMS [Ti] profiles cannot be explained by existing calibrations of the Ti-in-zircon thermometer.

1. Introduction

Zircon, a nearly ubiquitous accessory mineral in felsic igneous rocks, incorporates many elements of geochemical interest (e.g., Y, P, Ti, rare earth elements (REEs)) into its crystal lattice at concentrations much less than a weight percent, with Hf (on average ~ 2 wt.

% HfO_2) being the primary exception. The concentrations of and quantitative relationships among these minor and trace elements provide information regarding the crystallization environment of the host zircon, such as its parental melt composition and the extent to which that melt underwent fractionation during its emplacement in the crust. Of late, Ti-in-zircon thermometry (Watson et al. 2006; Ferry and Watson 2007) has provided researchers with another potentially powerful tool for extracting petrogenetic data from zircons, which are in some cases the only vestiges of the parent rock.

The Ti-in-zircon geothermometer developed by Watson and colleagues (Watson et al. 2006; Ferry and Watson 2007) has been applied to zircons from rocks of known (e.g. granitoids from the Spirit Mountain batholith, Lowery Claiborne et al. 2006) and unknown provenance (e.g., Jack Hills zircons, Watson and Harrison 2005). The thermometer was initially introduced by Watson and Harrison (2005) as an additional line of evidence for the presence of hydrous granitoid melts on the Earth over four billion years ago (Ga): Ti-thermometry of > 4 Ga Jack Hills zircons suggested mean crystallization temperatures for those zircons of 696 ± 33°C (Watson and Harrison 2005). However, the accuracy of this thermometer is dependent on a knowledge of TiO_2 and/or SiO_2 activities in the parent liquids from which the zircons crystallized (Ferry and Watson 2007); therefore, the application of the thermometer to zircons like those from the Jack Hills may be tenuous given the relatively unknown composition of their parent melt. (It should be noted that mineral inclusions in these zircons provide some constraints on the Jack Hills zircons' parental melt chemistry, e.g., Maas et al. 1992; Menneken et al. 2007.)

It therefore seems prudent to evaluate the temperatures provided by the thermometer for zircons for which independent estimates of the magmatic temperature can be made. Studies to this effect have focused on zircons from various lithologies and of varying petrogenetic histories and have quantified bulk temperatures in one of two ways: either 1) by relying on other mineral-pair geothermometers or, in the case of metamorphic rocks, indicator assemblages in addition to Ti-in-zircon thermometry (e.g., Baldwin et al. 2007; Cates and Mojzsis 2009; Rubatto et al. 2009) or 2) by relying on zircon saturation temperatures as an independent constraint on and benchmark for comparison to Ti-in-zircon temperatures (e.g., Glikson 2006; Nutman 2006). Using zircons from the Tibetan Dala igneous complex, Harrison et al. (2007) argue that zircon saturation temperatures consistently underestimate the temperature of zircon crystallization, although no zircon-independent temperature estimate for the complex is offered. In those cases for which temperatures are known independently of Ti-in-zircon thermometry, no systematic relationship between the two sets of temperature is observed: Ti thermometry has been observed to underestimate (e.g., Baldwin et al. 2007), overestimate (e.g., Cates and Mojzsis 2009), and nearly match (e.g., Rubatto et al. 2009) the independently constrained temperature range. Additional zircon analyses not included in the Ti-in-zircon thermometer's initial calibration but for which crystallization or peak metamorphism temperatures are known were included in the section "Zircon thermometry of selected rocks" of Watson et al. (2006). The Ti concentrations ([Ti]) of these zircons were not included in the thermometer's calibration due to concerns regarding uncertainties in the corresponding bulk rock TiO_2 activities. It should be noted that many of the zircons used in the thermometer's initial calibration were assigned temperatures based on limited external constraints (e.g., in some cases, temperatures were assigned on the basis of neighboring rock assemblages; see the Appendix of Watson et al. 2006).

Zircon's physical and chemical robustness as well as the slow solid-state diffusivity of Ti in zircon (Cherniak and Watson 2007) would seem to guarantee the preservation of previous generations of zircon growth (and their inherent [Ti]); therefore, electron microprobe and most ion microprobe analyses of Ti may be complicated by the poor spatial resolution of these techniques relative to the domain sizes of interest (i.e., cleanly resolving zircon cores from rims). The importance of high (~ micron-scale and smaller) spatial resolution for zircon Ti analyses has recently been confirmed by Hofmann et al. (2009a), who have shown that [Ti] in > 4 Ga zircons from the Jack Hills, Western Australia, are positively correlated with other trace elements (i.e., Y, P, Ce) and cathodoluminescent (CL) banding at the micron to sub-micron scale. Here we consider whether younger zircons for which we know the parent melt composition and/or the crystallization history and that show similarly correlated trace-element distributions. In particular, zircons from volcanic and plutonic provinces were selected from the Toba and Bishop Tuffs, Sierra Nevada batholith, and Quottoon Igneous Complex along with metamorphic zircons from an Adirondack migmatite. Because the compositions of the parent melts have been characterized (and hence the activity of TiO_2 with respect to rutile and SiO_2 with respect to quartz in the system can be estimated), such observations provide further insight into the robustness of the thermometer. Additionally, comparing element distributions and concentrations in these young zircons to those observed in zircons from the Jack Hills should indicate whether growth and crystallization processes inferred for the young zircons can be applied to those that crystallized on the early Earth.

In this study, as in Hofmann et al. (2009a), the NanoSIMS high-resolution ion microprobe was used to evaluate variations of Ti (as well as Y, P, and Ce) in these zircons over the scale of CL banding. Two of four volcanic and all four plutonic zircons we analyzed display positive correlations of [Ti] with other trace elements, conformable to *oscillatory* µm- to sub-µm CL zonations. In these cases, high trace-element concentrations correspond to CL-dark regions, and Ti concentrations vary by a factor of approximately 1.5 to 2 between adjacent oscillatory CL bands. The magnitude of these variations is similar to that observed in

Jack Hills zircons imaged by Hofmann et al. (2009a). In the remaining zircons (two volcanic, two metamorphic), we observe one instance in which there is an apparent spatial relationship between non-oscillatory CL-dark regions and trace element distributions, one case in which [Y], [P], and [Ce] are positively correlated with one another as well as CL banding and *negatively* correlated with [Ti], and two zircons for which no correlations between oscillatory CL zones and trace element distributions are observed, although in one of these zircons there appears to be a spatial relationship between [Y], [Ce], and [Ti]. The [Ti] of zircons that display [Ti] uncorrelated to CL zones span a greater range (6–25 ppm difference between high and low values) than that observed (with one exception) for those zircons that do display positive spatial correlations among Ti, CL banding, and the distributions of other trace elements (2–5 ppm Ti difference).

2. Samples and Analytical methods

2.1 Sample descriptions and preparation

We successfully examined two volcanic zircons from the 76 ka Toba Tuffs eruption (sample 87 from the YTT unit in Chesner (1998)), and two from unit IG2E of the Bishop Tuff, California, described in Hildreth (1979) and Wilson and Hildreth (1997). In all cases, a "successful analysis" is defined as one in which over 50% of the ion image is continuously collected without loss of the NanoSIMS primary beam current. The Youngest Toba Tuff (YTT) unit is of variable composition from rhyodacite to rhyolite with corresponding bulk SiO_2 contents between 68 and 76 wt. %; quartz, plagioclase, sanidine, biotite, amphibole, and orthopyroxene are the major phases; and accessory phases include magnetite, allanite, zircon, and ilmenite in addition to rare instances of highly oxidized fayalite seen only in mineral separates (Chesner 1998). Temperatures determined from Fe-Ti oxide pairs following the approach outlined in Anderson and Lindsley (1988) range from 701 to 780°C (± 20–30°C) in the YTT pumices and welded tuff; the reported temperature for sample 87 is 716°C with the same error envelope of ± 20–30°C (Chesner 1998). Zircons from the YTT are reported to contain 1.36–3.52 wt. % HfO_2 by electron microprobe analysis (Chesner 1998). Unit IG2E of the Bishop Tuff (also referred to as the "Tableland" unit, Hildreth 1979) consists of crystal-rich, two-pyroxene pumices containing accessory titanomagnetite, ilmenite, allanite, apatite, zircon, and pyrrhotite; quartz, plagioclase, sanidine, and biotite are the major phases (Hildreth 1979; Wilson and Hildreth 1997; Hildreth and Wilson 2007). Trace element compositions of the zircons are reported qualitatively with respect to concentrations in other accessory minerals (e.g., zircon is enriched with respect to allanite in U) with the exception of Y, which ranges from ~ 6000 ppm in zircons from low-temperature units (720–730°C) to ~ 2000 ppm in zircons from high-temperature units (~ 790°C) (Hildreth 1979). Updated Fe-Ti oxides temperatures for the IG2E unit are reported in Hildreth and Wilson (2007) to be 718–816°C, with a mean of 761 ± 27°C.

Three plutonic zircons from a quartz diorite in the 56 Ma Quottoon Igneous Complex, British Columbia (Thomas and Sinha 1999) and one from a quartz diorite from the southernmost Sierra Nevada batholith, California were successfully analyzed, as were two zircons from a migmatite unit of the Adirondack Mountains, New York. The two Adirondack zircons we analyzed were provided by collaborators at Rensselaer Polytechnic Institute (RPI) who knew them to be from a migmatite and therefore may have undergone metamorphic temperatures up to at least 790°C based on petrographic assemblages of migmatitic pelites from the southern Adirondack highlands (Storm and Spear 2005), but there is currently no information available regarding the zircons' age or petrogenesis (J. Thomas, personal communication). Likewise, the Sierran zircon is from a lithology whose petrography has not previously been described in the literature: a hypersthene-hornblende quartz diorite with accessory alkali feldspar and biotite in the eastern Tehachapi Mountains (J. Saleeby, personal communication). The Quottoon Igneous Complex consists of mafic to felsic quartz diorites that underwent varying degrees of metamorphism and tectonic deformation (Thomas and Sinha 1999). Major phases include quartz, alkali feldspar, plagioclase, hornblende, and biotite; accessory minerals include magnetite, ilmenite, zircon, titanite, and apatite (Thomas and Sinha 1999). The parental liquid(s) of zircons examined in this study were not identified, and no geochemical analysis of zircon separates was provided. A petrologic study of nearby gneisses (within 2 km of the Quottoon pluton) concluded that the pluton was generated via partial melting of the pre-existing amphibolite-grade gneiss at 775–825°C (Lappin 1976, as cited in Harrison et al. 1979 and Harrison and Clarke 1979).

Quottoon, Toba, Bishop Tuff, and Adirondack zircon separates were mounted in epoxy and polished by colleagues at RPI. Sierra Nevada zircons were mounted in Araldite resin and polished with 0.25 μm diamond grit followed by colloidal silica. Standards included zircon 91500 (Wiedenbeck et al. 2004) and high-Ti synthetic zircons from 'Run 57' of Watson et al. (2006) that were mounted in Araldite resin and polished with 0.25 μm diamond grit followed by colloidal silica. All sample mounts were Au-coated prior to NanoSIMS analysis. All samples examined in this study were imaged using Caltech's LEO 1550 VP FE-SEM in electron backscatter, secondary electron, and CL modes before and after ion microprobe sessions in order to identify prospective locations for NanoSIMS analysis and to identify and document cracks and/or mineral inclusions within those regions. Inclusions greater than ~ 1 μm in diameter were identified prior to NanoSIMS analysis using SEM-EDS. Inclusions observed include apatite (Bishop Tuff, Quottoon, Sierra Nevada, Toba), feldspar (Adirondack, Quottoon, Toba), monazite (Bishop Tuff), corundum and spinel (Adirondack), and possibly a pyroxene (Quottoon). Inclusions less than 1 μm in diameter were only identified in our samples after SIMS analysis, either because they appeared as obvious anomalous features in ion images and/or because they were recognized during post-analytical SEM interrogations.

2.2 Ion microprobe analytical technique

All zircons were analyzed for Ti, P, Y, Ce, Hf, Zr, and Si contents by ion microprobe using the Caltech Microanalysis Center's CAMECA NanoSIMS 50L. The following isotopes were chosen for analysis: ^{28}Si, ^{31}P, ^{49}Ti, ^{89}Y, ^{94}Zr, ^{140}Ce, ^{180}Hf; an explanation of these choices, along with potential interferences can be found in Hofmann et al. (2009a). Two types of analyses were performed: spots and images. Data were collected on the Toba, Quottoon, and Adirondack samples during October 2008; data were collected on the Bishop Tuff and Sierran samples during May 2009 and again in August 2009. The following parameters were typical of the tuning conditions used for data collected during all analyses: For both spot measurements and ion imaging, the primary beam aperture lenses, D0 and D1, were set at 150 μm and 300 μm, respectively, corresponding to a typical probe size of ~ 600 nm. The beam diameter was independently measured in August 2009 to be ~ 650 nm by making a traverse across the interface between a 10 μm wide synthetic zircon and surrounding glass in an adjacent sample mount and evaluating the width of the signal between 16 and 84% of its height. Positive secondary ions were extracted at 8 kV and collected using electron multipliers. The QSA effect was not calculated. No energy offset was applied.

Spot analyses, which refer to measurements of average trace-element concentration within a μm-scale domain, utilized a 500–700 nA O^- primary beam (~ 40–60 pA on the sample surface, after passing through the aperture D1 and the E0 immersion lens stack) in October 2008 and a 200–400 nA O^- primary beam (~ 15–30 pA on the sample surface) in May and

August 2009 focused to a 2 × 2 μm rastered spot on the sample surface. Collected counts were limited to the inner 1 × 1 μm square of the rastered area by electrostatic gating of the secondary ion beam in order to minimize sampling the outermost edges of the analysis area, which are affected by gradients in charge and topography. Zircons were pre-sputtered for 3–5 minutes prior to analysis in an attempt to achieve a relatively steady counting rate on $^{94}Zr^{+}$. Zirconium was chosen over silicon because images of raw $^{94}Zr^{+}$ counts appeared "flatter" than those of $^{30}Si^{+}$, suggesting that the ionization of Zr may be less susceptible than Si to topography or local charging effects. The first ionization potential of Zr (6.84 eV) is closer in magnitude to that of the other metal cations (Ti = 6.82 eV; Y = 6.38 eV; Hf = 7.0 eV; Ce = 5.47 eV), and we would therefore expect the ionization of these elements in the primary column (with the exception, perhaps of P, which has a 1st potential of 10.486 eV) to be more similar to one another than to the ionization of Si (1st ionization potential = 8.151 eV) (all data from Moore 1970).

Ion imaging was performed using the same magnitude primary beam currents as those reported for spot analyses rastered over 20 × 20 μm areas (or, in the case of Bishop Tuff zircon BT2-10, 10 × 10 μm). The choice of raster size depended on the size of the feature of interest and the presence of other sputtered regions, which affect charging at the sample surface and hence interfere with collection. Image data are collected as 256 × 256 linearly discretized spots within the analysis area, resulting in oversampling with respect to the diameter of the primary beam. Zircons were pre-sputtered with a higher beam current, obtained by use of a wider primary beam aperture, for 15–30 minutes (depending on analysis area size) prior to imaging in order to establish a steady counting rate on $^{94}Zr^{+}$.

2.3 Calibration of trace element analyses

Two synthetic, Ti-doped zircons from experimental Run 57 of Watson et al. (2006) were used in conjunction with the natural zircon 91500 (Wiedenbeck et al. 2004) to calibrate ion microprobe analyses. Established values for the two Ti-doped zircons were previously determined by Hofmann et al. (2009a) to be 1393 ± 45 (1σ) and 1646 ± 118 ppm (1σ). The value of [Ti] for zircon 91500 was lower than the detection limit of the electron microprobe and was therefore taken from analyses in Fu et al. (2008) to be 5.2 ppm; concentrations of Y, P, Ce, and Hf were taken from analyses in Wiedenbeck et al. (2004) to be 140 ppm, 35 ppm, 2.5 ppm, and 5325 ppm, respectively. Conversion of $^{49}Ti^+/^{94}Zr^+$ to [Ti] is based on a four-point calibration involving an unweighted linear least-squares fit to the three standards regressed through the origin and should be accepted as preliminary until the code for weighting errors in X and Y is coupled to the bootstrap statistics code used in Hofmann et al. (2009a) (Chapter 1). Conversion of all other ion ratios to concentrations (i.e., $^{31}P^+/^{94}Zr^+$ to [P], $^{89}Y^+/^{94}Zr^+$ to [Y], $^{140}Ce^+/^{94}Zr^+$ to [Ce], and $^{180}Hf^+/^{94}Zr^+$ to [Hf]) relied on two-point calibrations involving a linear fit from the standard value regressed through the origin and should be taken as approximations. Each ion image of a natural zircon was either preceded or followed by analyses of both of the synthetic, high-Ti zircons from Watson's Run 57 experimental charge and zircon 91500; therefore, each image has a corresponding calibration curve for converting ion ratios to concentrations of P, Ti, Y, Ce, and Hf.

2.4 Image processing

Images produced on the NanoSIMS were output as 256 × 256 pixel ASCII matrices, in which each matrix element is the number of ion counts recorded at the corresponding (x, y) position of the image made on the sample. These raw image files were processed using code written in MATLAB by the author. In all cases, the nominal beam diameter on the sample surface (~ 650 nm) was larger than the corresponding width of an individual pixel; therefore, images were smoothed with a 25-pixel moving-average window (i.e., a 5 × 5 pixel image domain) to account for over-sampling. Prior to smoothing, raw images were ratioed pixel-by-pixel to the $^{94}Zr^+$ image in order to reduce variations affected by the efficiency of secondary ion extraction or caused by changes in primary beam intensity. As in Hofmann et al. (2009a) line profiles (Figures 1-8, 10) illustrate variations in ion abundance ratios along one-dimensional image transects. Each point along a line profile is initially the ratio (e.g., $^{31}P^+/^{94}Zr^+$) of the average of all ion counts within a rectangle 3–5 pixels long parallel to the line profile (in which the integration length was determined based on width of features of interest) and 20–250 pixels wide perpendicular to the line profile. These point values were then converted to concentrations using the scheme described in §2.3 above. The rectangular dimensions were selected in order to maximize the number of counts contributing to a line profile without "projecting" obvious compositional variations at some non-perpendicular angle to that line profile. In any single line profile, the area integrated for each point on the line is constant. NanoSIMS images were co-registered for intra-grain location with post-SIMS SEM and CL images using Adobe Illustrator.

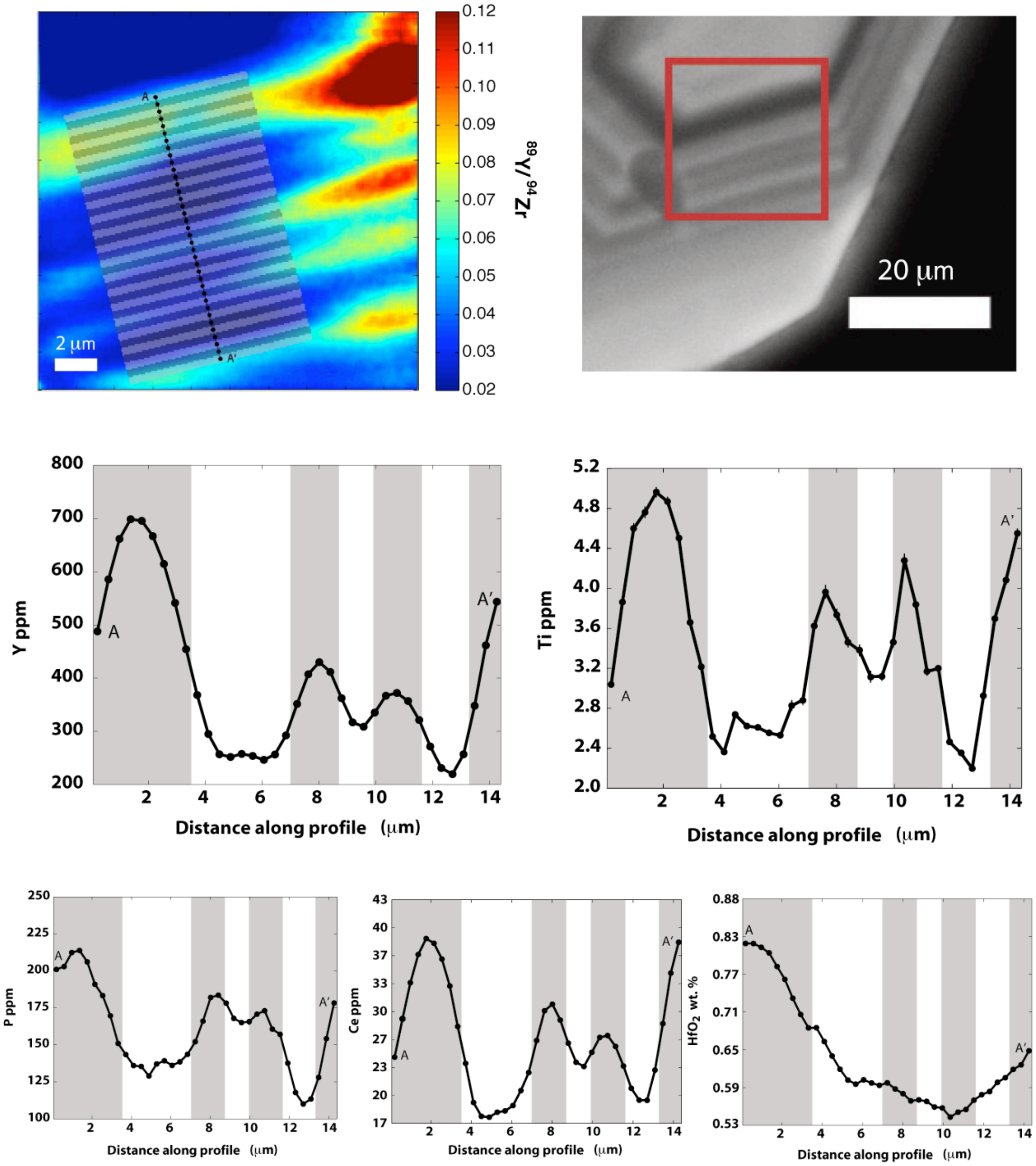

Figure 1. Quottoon zircon Q4 displaying correlations between oscillatory CL zones and all trace elements (but not Hf). *Upper left:* $^{89}Y^{+}/^{94}Zr^{+}$ ion map of the 20 × 20 µm area outlined in the CL image. *Black line* across bands indicates location of line profile. The alternating *gray rectangles* indicate the integration areas (390 nm × 11.7 µm) for counts assigned to each profile point. *Upper right:* CL image of region mapped (outlined in *red*). *Bottom:* Line profiles showing correlated CL and trace element concentrations. The *vertical gray bars* correlate to the CL-dark bands in the analyzed region.

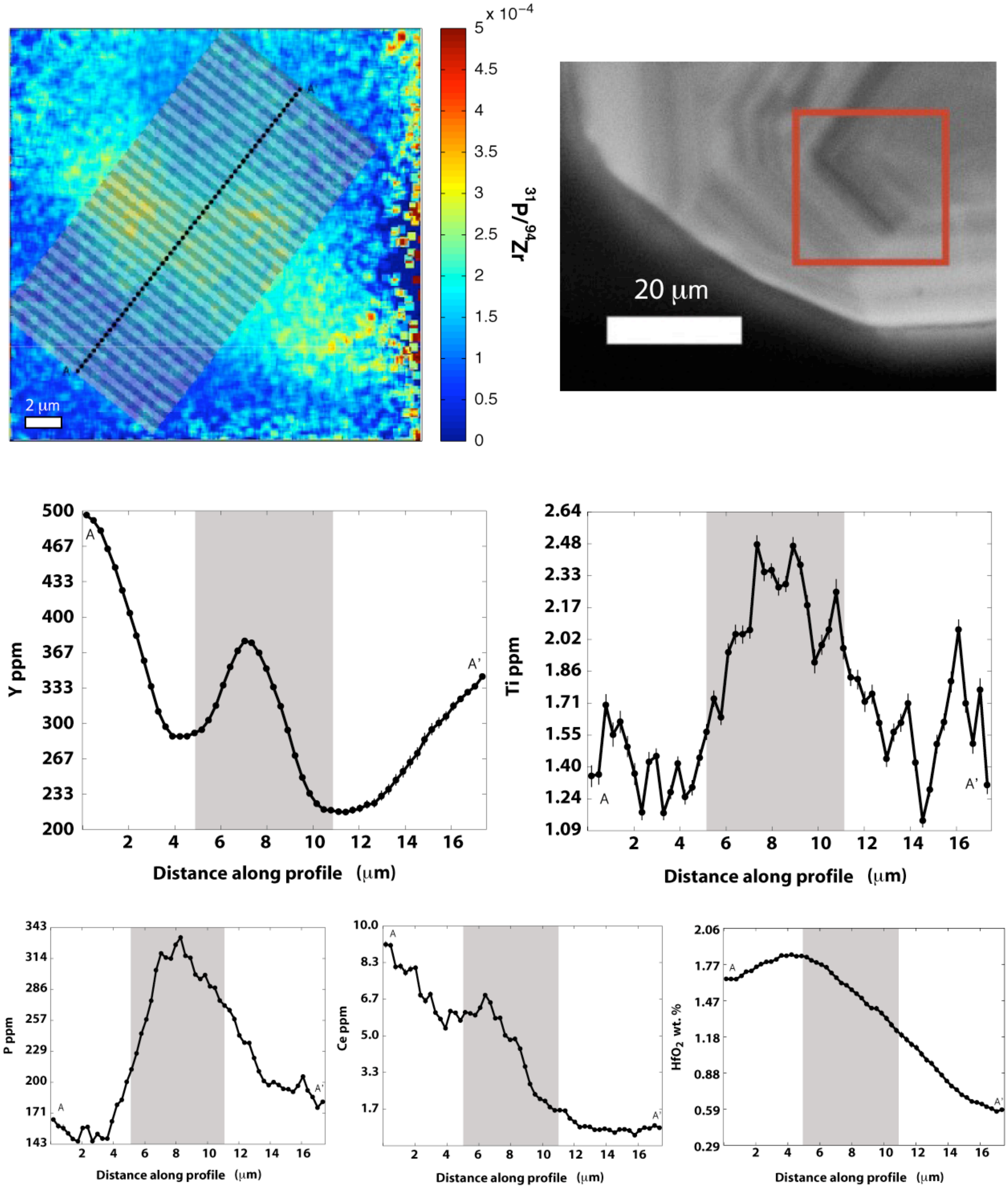

Figure 2. Quottoon zircon Q3 displaying correlations between a CL-dark band and trace elements (but not Hf). *Upper left:* ^{89}Y^{+}/^{94}Zr^{+} ion map of the 20 × 20 μm area outlined in the CL image. *Black line* across bands indicates location of line profile. The alternating *gray rectangles* indicate the integration areas (310 nm × 9.4 μm) for counts assigned to each profile point. *Upper right:* CL image of region mapped (outlined in *red*). *Bottom:* Line profiles showing correlated CL and trace element concentrations. The *vertical gray bars* correlate to the CL-dark bands in the analyzed region.

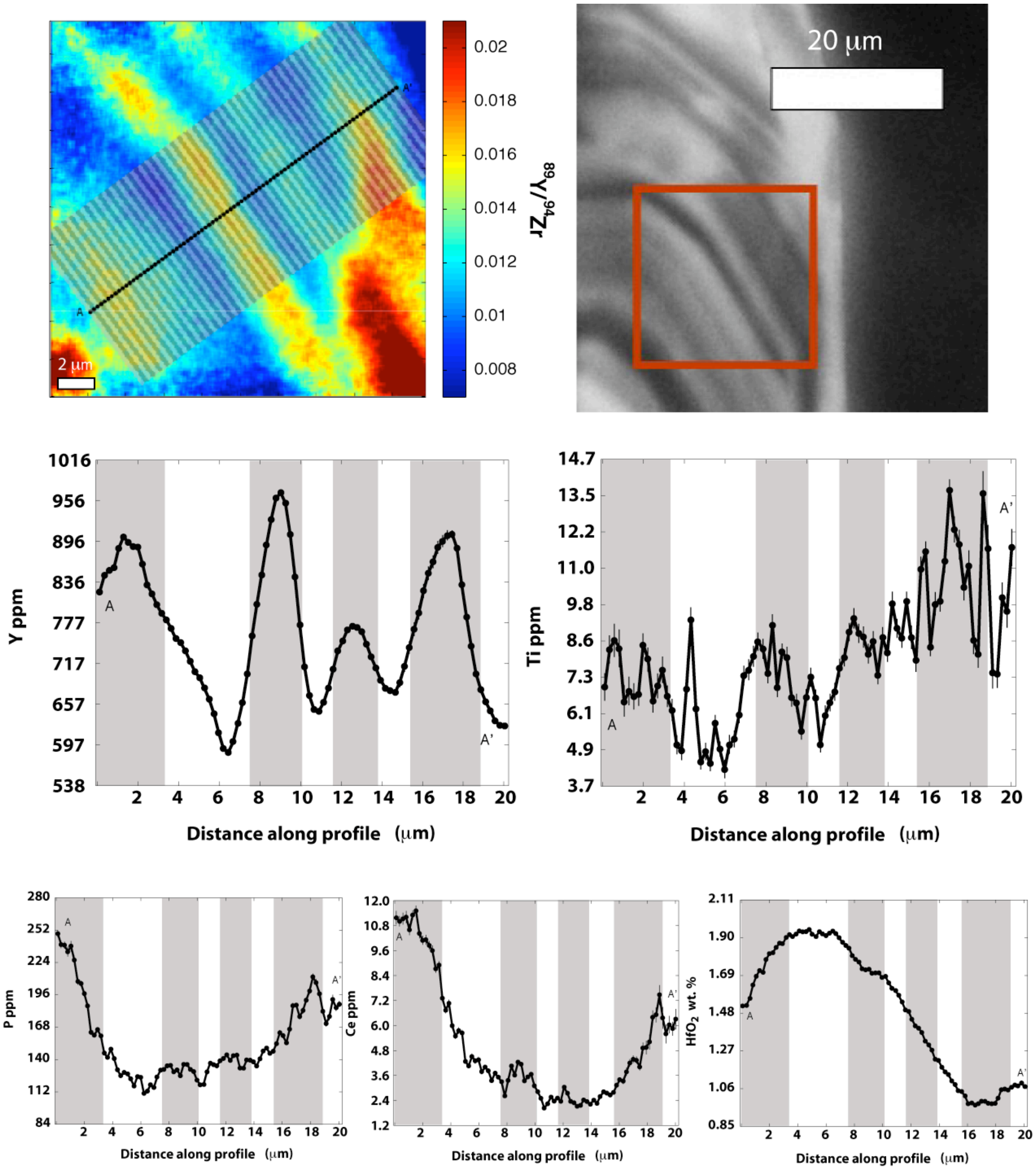

Figure 3. Sierra Nevada zircon 93TH234.11 ("SN11") displaying correlations between oscillatory CL zones and all trace elements (but not Hf). *Upper left:* $^{89}Y^+/^{94}Zr^+$ ion map of the 20 × 20 μm area outlined in the CL image. *Black line* across bands indicates location of line profile. The alternating *gray rectangles* indicate the integration areas (235 nm × 9.4 μm) for counts assigned to each profile point. *Upper right:* CL image of region mapped (outlined in *red*). *Bottom:* Line profiles showing correlated CL and trace element concentrations. The *vertical gray bars* correlate to the CL-dark bands in the analyzed region

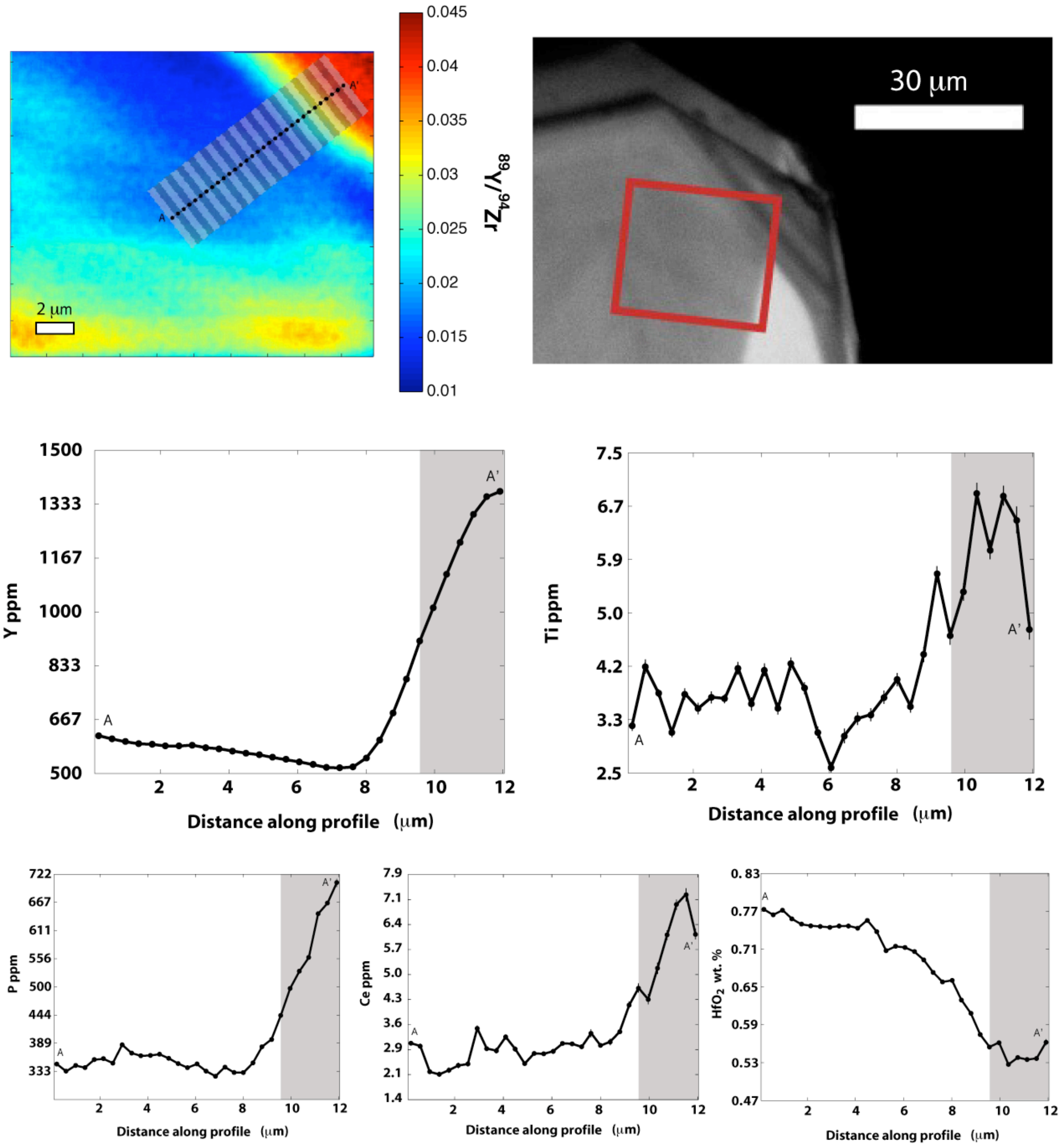

Figure 4. Toba zircon T8 displaying positive correlations between a CL-dark band and all trace elements, all of which appear negatively correlated to Hf. *Upper left:* ^{89}Y^{+}/^{94}Zr^{+} ion map of the 16 × 20 μm area outlined in the CL image. *Black line* across bands indicates location of line profile. The alternating *gray rectangles* indicate the integration areas (390 nm × 3.9 μm) for counts assigned to each profile point. *Upper right:* CL image of region mapped (outlined in *red*). *Bottom:* Line profiles showing correlated CL and trace element concentrations. The *vertical gray bars* correlate to the CL-dark bands in the analyzed region.

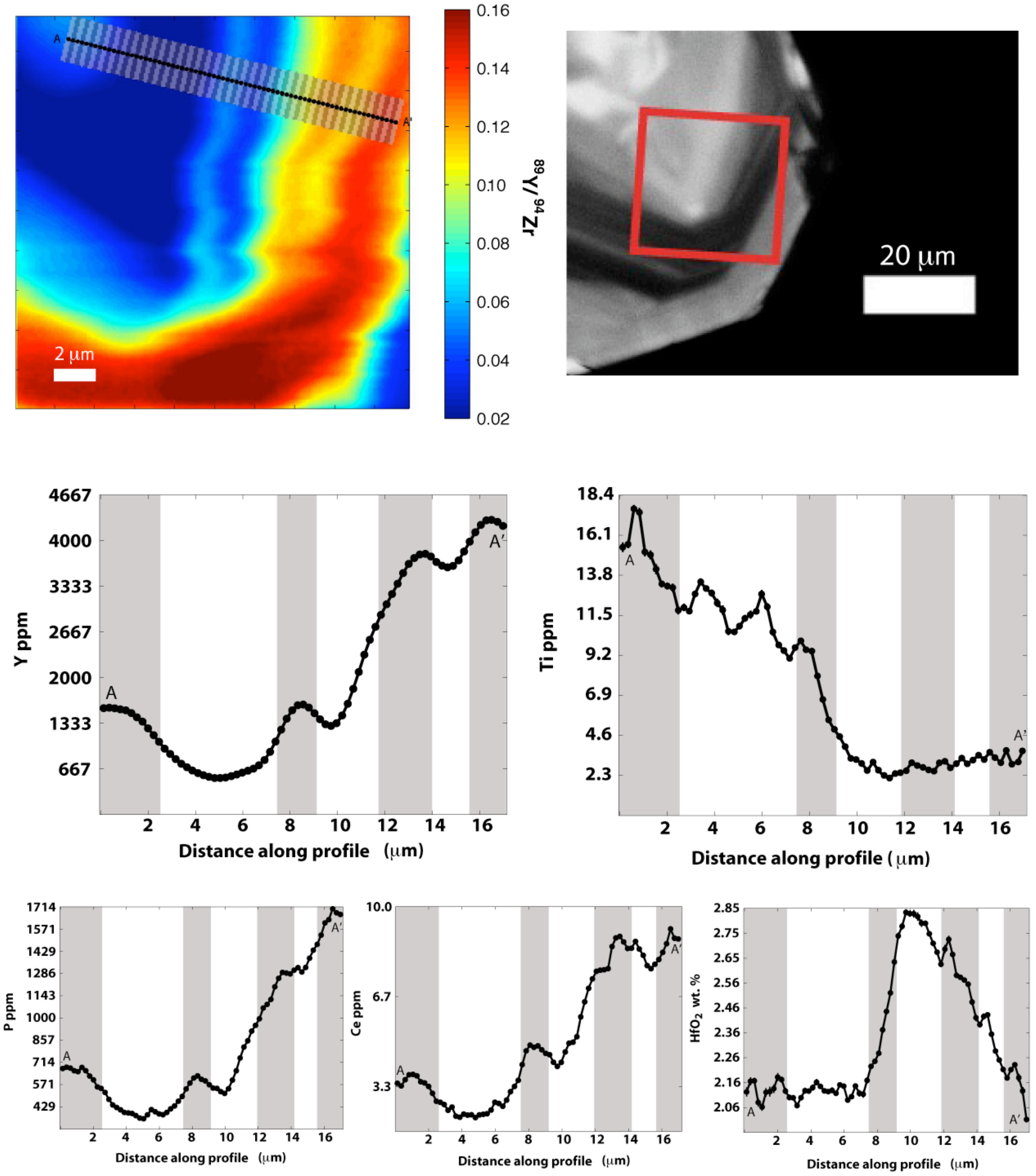

Figure 5. Toba zircon T11 displaying correlations between oscillatory CL zones and all trace/minor elements EXCEPT Ti and Hf. *Upper left:* ^{89}Y$^+$/^{94}Zr$^+$ ion map of the 20 × 20 µm area outlined in the CL image. *Black line* across bands indicates location of line profile. The alternating *gray rectangles* indicate the integration areas (230 nm × 1.6 µm) for counts assigned to each profile point. *Upper right:* CL image of region mapped (outlined in *red*). *Bottom:* Line profiles showing correlated CL and trace element concentrations. The *vertical gray bars* correlate to the CL-dark bands in the analyzed region.

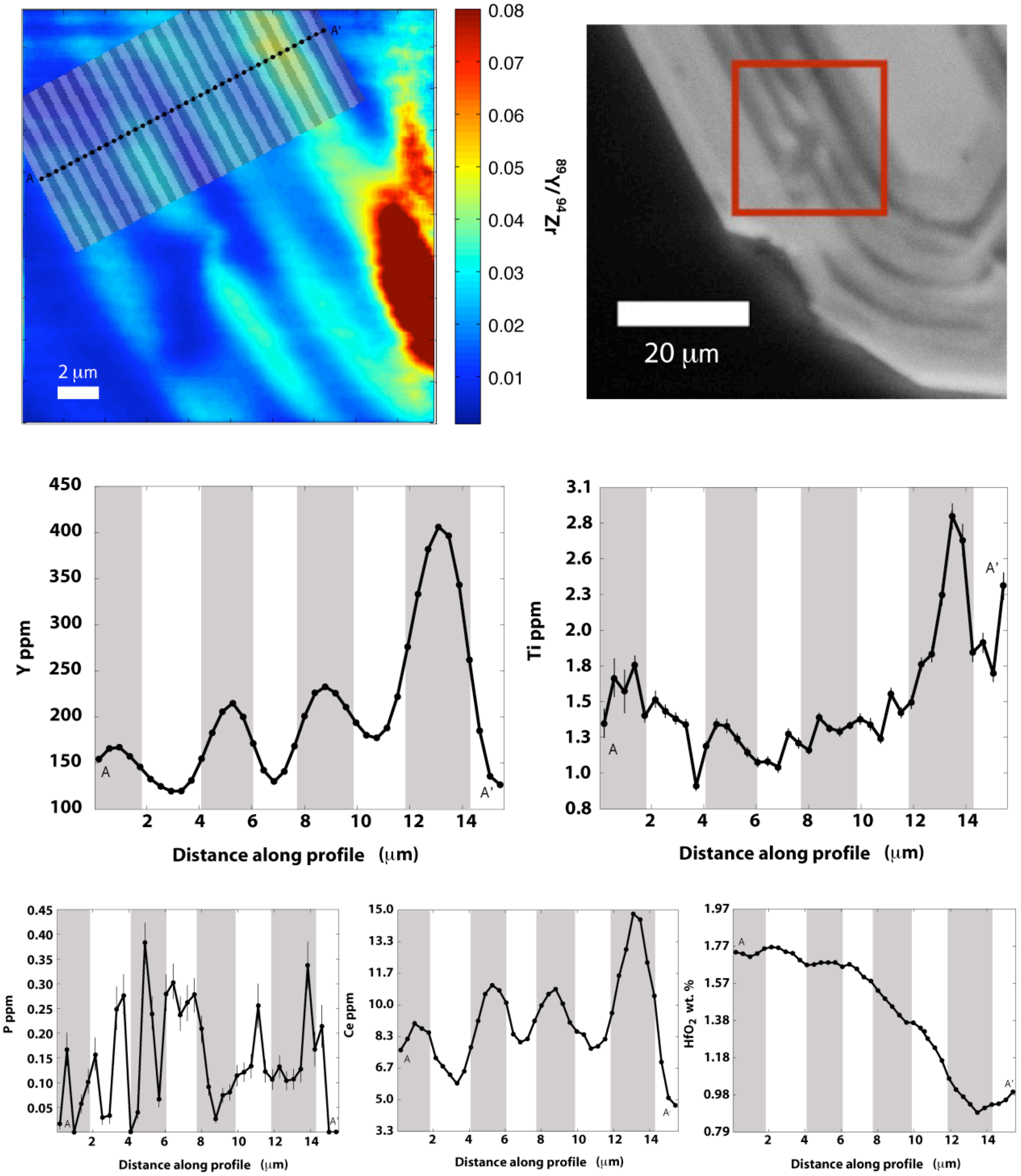

Figure 6. Quottoon zircon Q8 displaying correlations between oscillatory CL zones and all trace elements except P. *Upper left:* $^{89}Y^+/^{94}Zr^+$ ion map of the 20 × 20 µm area outlined in the CL image. *Black line* across bands indicates location of line profile. The alternating *gray rectangles* indicate the integration areas (390 nm × 7.8 µm) for counts assigned to each profile point. *Upper right:* CL image of region mapped (outlined in *red*). *Bottom:* Line profiles showing correlated CL and trace element concentrations. The *vertical gray bars* correlate to the CL-dark bands in the analyzed region.

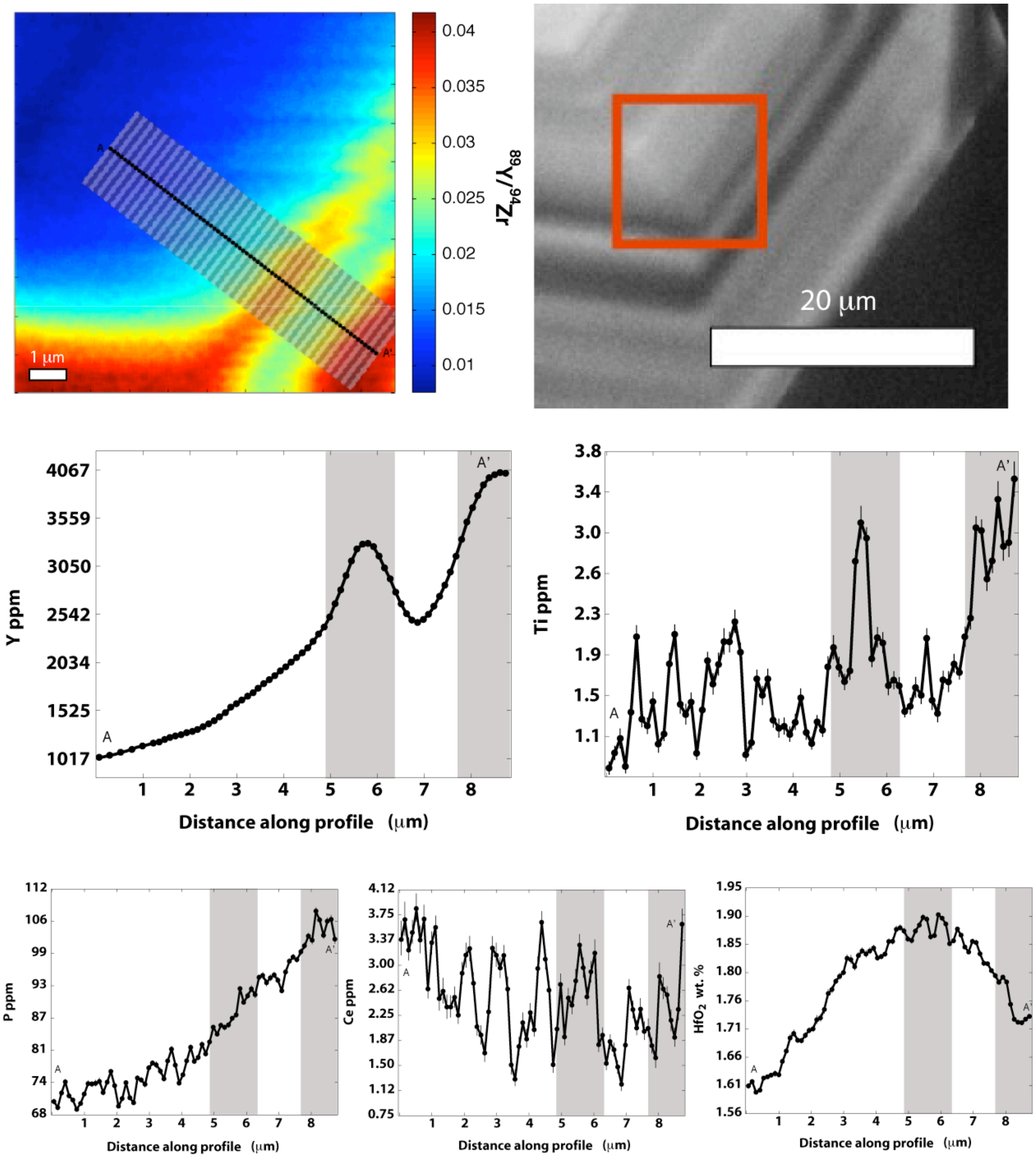

Figure 7. Bishop Tuff zircon BT2-10 displaying correlations between oscillatory CL zones and Y and Ti (but not Hf or other trace elements). *Upper left:* $^{89}Y^+/^{94}Zr^+$ ion map of the 10 × 10 μm area outlined in the CL image. *Black line* across bands indicates location of line profile. The alternating *gray rectangles* indicate the integration areas (120 nm × 2.3 μm) for counts assigned to each profile point. *Upper right:* CL image of region mapped (outlined in *red*). *Bottom:* Line profiles showing correlated CL and trace element concentrations. The *vertical gray bars* correlate to the CL-dark bands in the analyzed region.

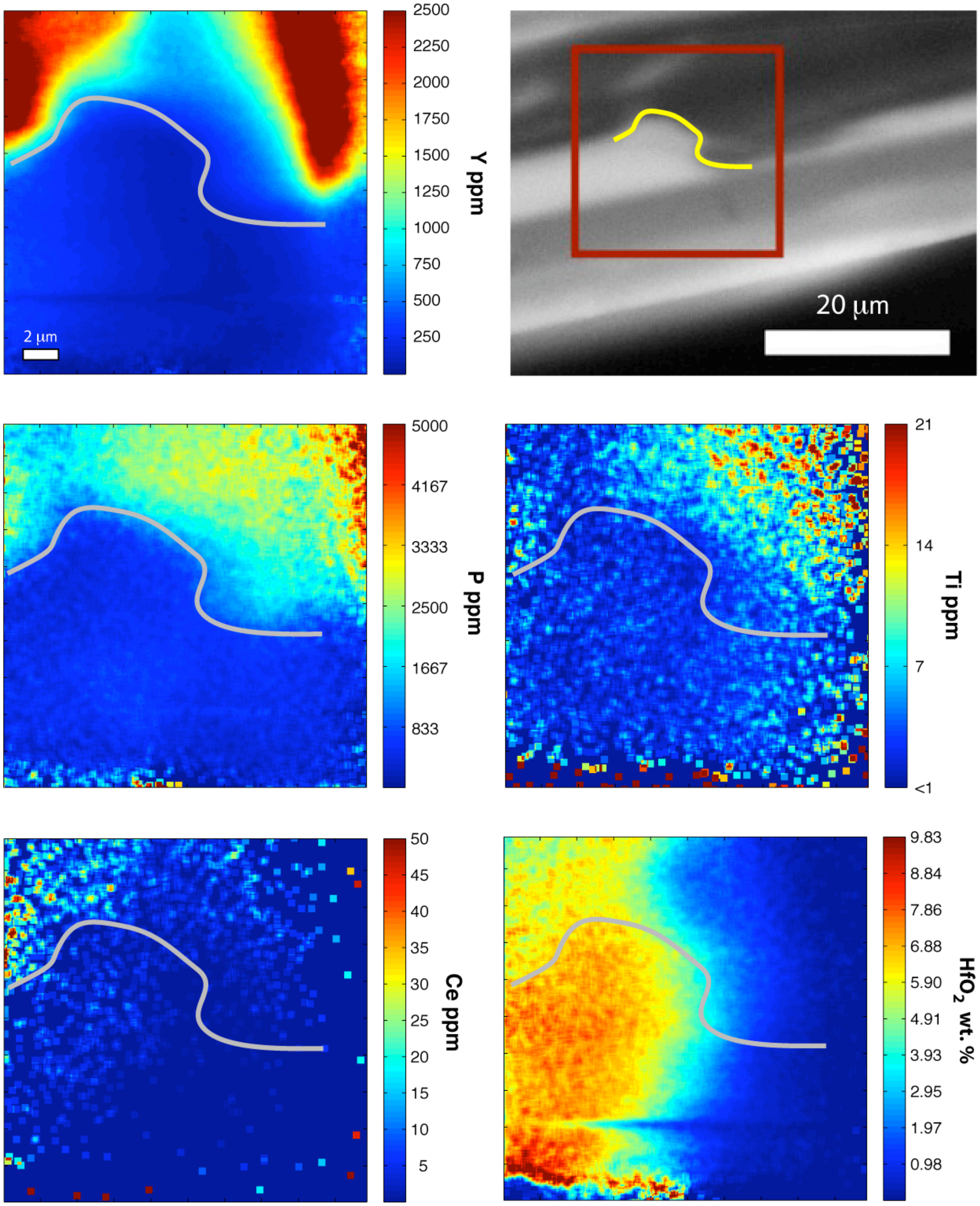

Figure 8. Adirondack zircon M9 displaying an apparent spatial relationship between CL-dark zones and trace element distributions (but not Hf). *Upper right:* CL image of region mapped (outlined in *red*). *Yellow line* traces the interface between a CL-dark and CL-bright zone within the imaged area. *Others:* Ion and concentration maps of trace and minor elements. *Gray line* traces the approximate location of the interface denoted by the *yellow line* in the CL image.

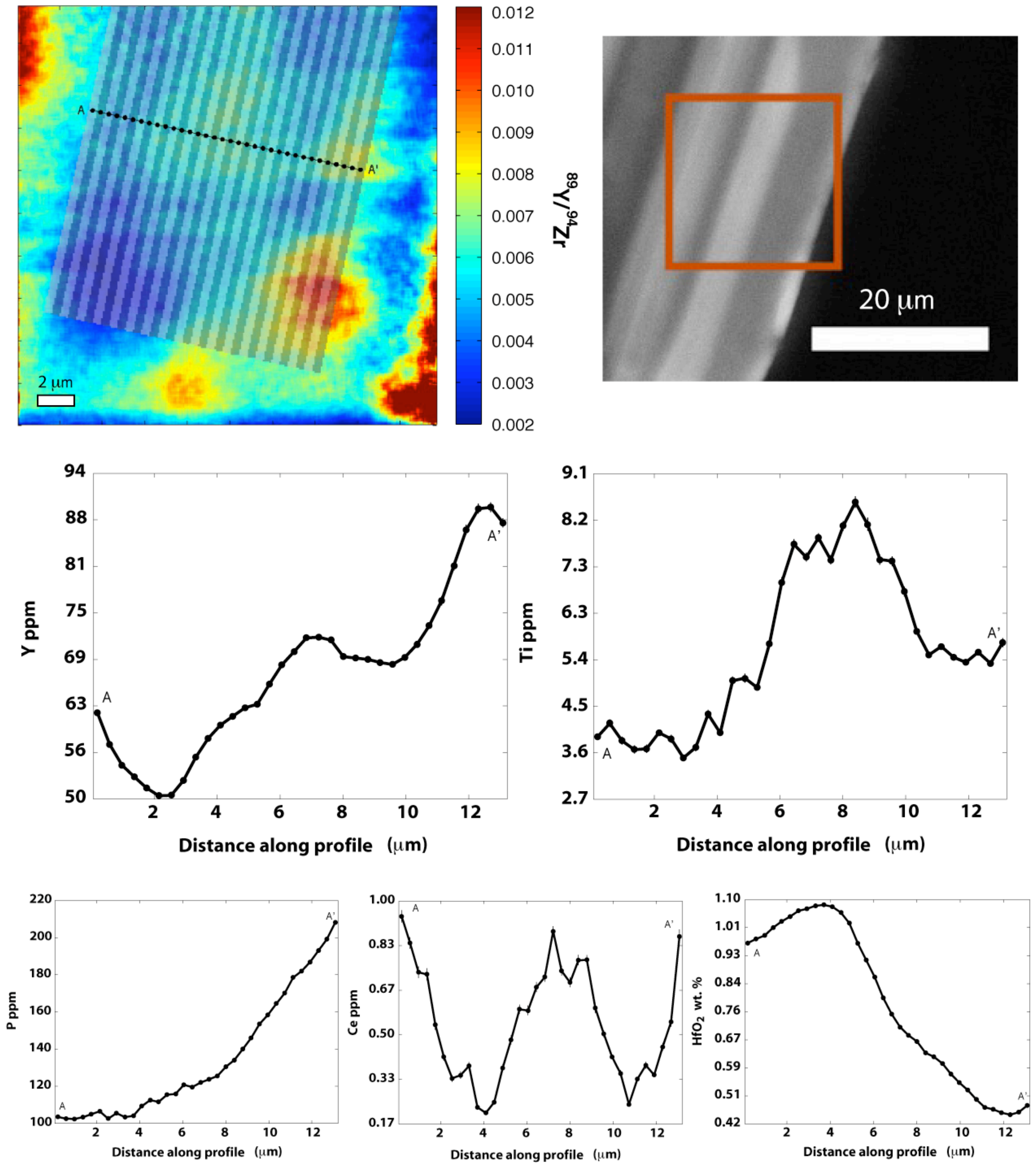

Figure 9. Adirondack zircon M29 displaying no correlations between oscillatory CL zones and trace/minor elements, although there appears to be some spatial relationship between the central Y peak and peaks in Ti and Ce. *Upper left:* $^{89}Y^+/^{94}Zr^+$ ion map of the 20 × 20 μm area outlined in the CL image. *Black line* across bands indicates location of line profile. The alternating *gray rectangles* indicate the integration areas (390 nm × 19.5 μm) for counts assigned to each profile point. *Upper right:* CL image of region mapped (outlined in *red*). *Bottom:* Line profiles showing correlated CL and trace element concentrations. The *vertical gray bars* correlate to the CL-dark bands in the analyzed region.

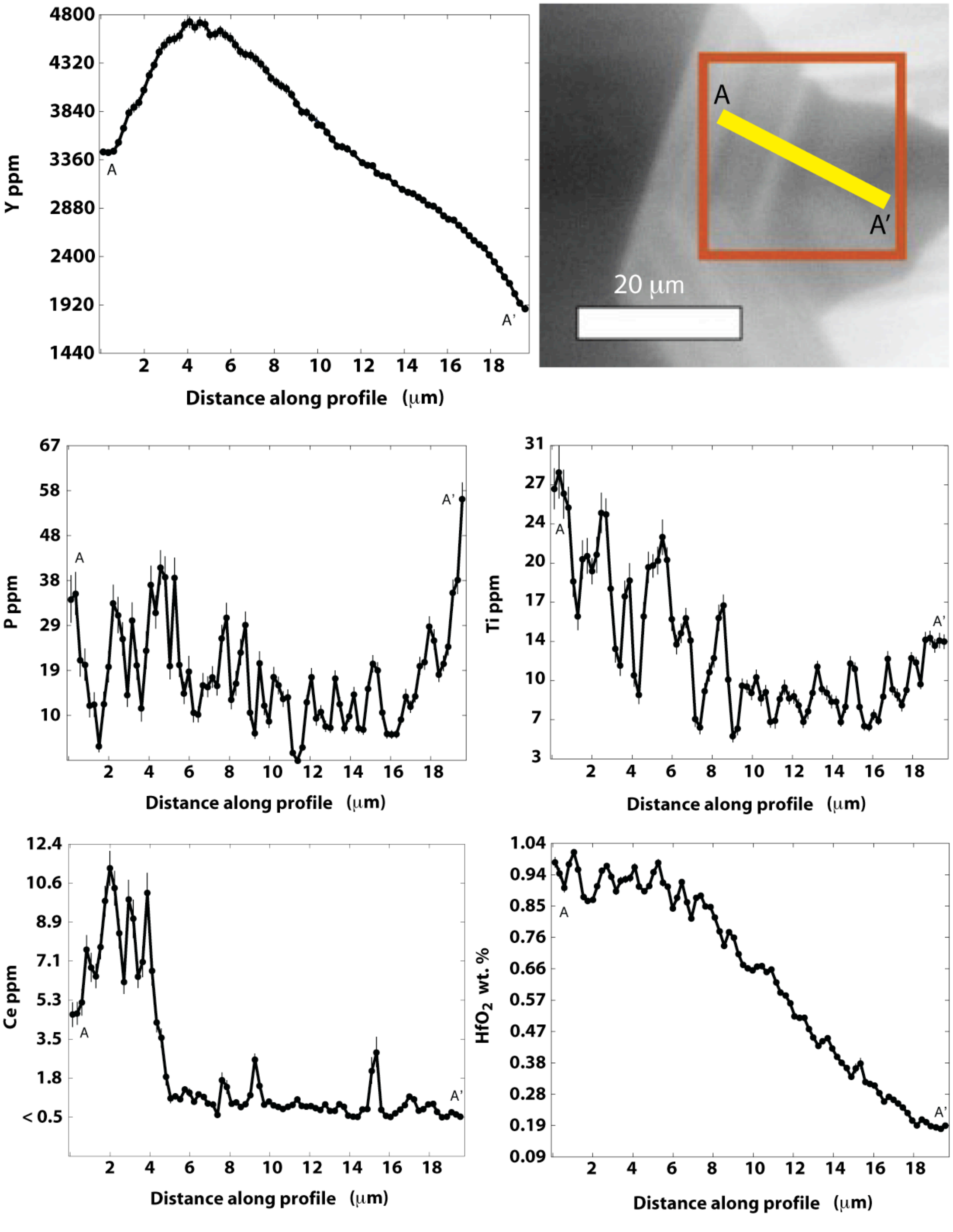

Figure 10. Bishop Tuff zircon BT1-8 displaying no apparent correlations between oscillatory CL zones and trace/minor elements. *Upper right:* CL image of the 20 × 20 μm area mapped (outlined in *red*). Yellow line demarcates approximate location of line profile (perpendicular to CL banding). Profile location is approximate because the $^{89}Y^+/^{94}Zr^+$ ion map showed no discernable features related to the CL image. *Others:* Line profiles showing trace element concentrations.

3. Results and Discussion

3.1 Correlations of Ti and other trace elements with CL banding

Growth features manifested in CL zoning were observed in all ten natural zircons analyzed in this study. Guided by our previous observation that high trace elements concentrations can be spatially correlated with CL-dark bands (e.g., Hofmann et al. 2009a; Hofmann et al. 2009b), we concentrated our NanoSIMS ion-imaging efforts on regions within these zircons that displayed sharp contrasts in CL. In all but one case (grain M9), this approach led us to image locations displaying oscillatory zoning in CL. Overall, seven of ten zircons display positive spatial correlations among CL zones, [Ti], and some subset of P, Y, and Ce. Four of these ten zircons (Figures 1-4, zircons Q4, Q3, SN11, and T8) display positively correlated [Ti], [P], [Ce], and [Y] conformable to oscillatory CL bands. In these cases, as in Hofmann et al. (2009a), high trace-element concentrations correspond to CL-dark regions, and Ti concentrations vary by a factor of approximately 1.5 to 2 between adjacent oscillatory CL bands, similar to variations observed in Jack Hills zircons (Hofmann et al. 2009a). In this study, unlike in Hofmann et al. (2009a), we were able to utilize all seven electron multipliers on the NanoSIMS and therefore collected Hf data in addition to the trace elements previously discussed. In the four zircons that show trace element distributions correlated with CL banding, Hf is observed to generally decrease along the length of the line profile; in all but one case (Q3, Figure 2), [Hf] decreases toward the outer edge of the grain. Hf concentrations in three of the four zircons do not appear spatially correlated with either any of the trace elements or with the CL bands that the trace elements appear to track. In the case of Toba zircon T8 (Figure 4), Hf appears to be inversely correlated with [Y], [Ti], [P], and [Ce]. To the best of our knowledge, no data sets currently exist within the literature for which Hf and the rare earth elements (plus Y and P) were analyzed at the same location within a zircon. Zircon is known to be a good fractionator of Hf, Y, and the heavy rare earths (Hoskin and Schaltegger 2003), but negative correlations among these elements cannot be explained to the zeroth order by magmatic fractionation of zircon. It is therefore unclear what these correlations suggest.

The distribution of trace and minor elements in Toba zircon T8 (Figure 4) can be directly contrasted with that observed in Toba zircon T11 (Figure 5), noting that both zircons are from the same lithologic unit (YTT-87). It should also be noted that grain T11 is *not* included in the six of ten zircons identified above as displaying positive correlations between CL, [Ti], and the other trace elements. Rather, in grain T11, [Y], [P], and [Ce] (all concordant with CL bands) are positively correlated with one another and broadly *negatively* correlated with [Ti]; [Hf] appears to increase at the same point along the profile where [Ti] begins to decrease, with [Hf] increasing toward the outer edge of the grain as [Ti] decreases. The Hf abundance within natural zircons is observed to increase as fractionation of a magma proceeds (e.g., Hoskin and Schaltegger (2003) and references therein); therefore, our observation of negatively correlated Hf and Ti in Toba zircon T11 combined with the decoupling of [Ti] from oscillatory CL banding could be interpreted as indicative of magmatic fractionation towards a lower-T, more felsic (in the case of Toba, less rhyodacitic and more rhyolitic) end-member. In other words, this grain could represent the rare (1 in 10, based on samples examined in this study) instance for which [Ti] can be interpreted as a proxy for crystallization temperatures without requiring counter-intuitive magmatic thermal evolution.

Of the remaining five zircons, three display [Ti] spatially conformable to CL zones. Grain Q8 displays positively correlated [Ti], [Ce], and [Y] conformable to oscillatory CL bands (Figure 6); P concentrations in Q8 are too low to be unambiguously resolved. Hf concentrations appear unrelated to either trace element distributions or to CL banding, and

[Hf] generally increases toward the edge of the crystal in the imaged region. Bishop Tuff zircon BT2-10 displays positively correlated [Ti] and [Y] conformable to oscillatory CL bands (Figure 7); in this zircon, Ce is difficult to resolve and [P] appears to increase toward the crystal's edge. As was true for the imaged region of zircon Q8, [Hf] in BT2-10 increases toward the crystal rim. Zircon M9 from the Adirondack migmatite displays asymmetric CL zones that were not easily translated into MATLAB-analyzable line profiles; therefore, Figure 8 presents the ion maps (converted to concentrations) in addition to the corresponding CL image. The location of the CL-dark / CL-bright boundary (denoted by the yellow line in Figure 8) was co-registered within each individual ion map using Adobe Illustrator. The gray line in each ion map roughly corresponds (i.e., within 10%) to the yellow line on the CL image. The dark blue boundaries near the edges of the ion maps are an artifact of image processing and should not be taken as interpretable data. In these images, [Y], [Ti], and [P] are the most resolvable and appear to track the CL boundary. The Ce content is too low to resolve in this format, and [Hf] does not appear to correlate with either the other trace elements or with CL zonations.

The final two zircons—one from the Adirondack migmatite (grain M29) and one from the Bishop Tuff (BT1-8)—show no correlations between oscillatory CL zones and either trace or minor elements. Of these two zircons, the Adirondack zircon M29 displays no observable correlations between oscillatory CL zones and trace element distributions (Figure 9), although there appears to be some spatial relationship between Y, Ce, and Ti distributions. Post-SIMS imaging on Caltech's SEM did not reveal any cracks or inclusions to be the source of the central peaks in the [Y] image or in the [Y], [Ce], and [Ti] line profiles. As with zircon JH54b.4-1 from the Jack Hills in Hofmann et al. (2009a), the NanoSIMS image of zircon BT1-8 from the Bishop Tuff (Figure 10) was made in a region displaying both sector and oscillatory

CL zonations. However, unlike the image from JH54b.4-1, which displayed well-correlated trace element distributions spatially related to CL banding, this region of BT1-8 displays neither a spatial relationship between trace element distributions and oscillatory CL bands nor any apparent correlations among trace elements. [Hf] and [Y] do appear to be broadly positively correlated and generally increase toward the outer edge of the crystal, perhaps indicating a period of magmatic fractionation. Because oscillatory CL zonations were not observed to correlate spatially with any of the trace elements imaged in this study, the location of the line profile (given by the yellow line on the CL image in Figure 10) is approximate. In processing the image (and making the line profile), every attempt was made to ensure that the line profile would be perpendicular to CL banding.

3.2 Interpretations

Out of the total population of [Ti] images made on zircons using the NanoSIMS (n = 12 including the two Jack Hills zircons imaged and reported in Hofmann et al. (2009a), 67% (n = 8) exhibit positive correlations of [Ti] with other trace element distributions (either one or more of Y, P, and Ce), all of which also appear spatially correlated to oscillatory CL bands. This figure rises to ~ 75% if we include M9, the Adirondack zircon for which [Ti] appears spatially correlated (along with [Y] and [P]) to more broadly defined CL zones (as opposed to oscillatory bands). The remaining 25% show [Ti] generally decoupled from both CL bands and other trace and minor elements. As discussed in Hofmann et al. (2009a), the correlations observed in 75% of zircons analyzed could result from one or more of the following three possibilities: temperature-dependent equilibrium partitioning of all trace elements during cycles in temperature and/or melt composition; episodic, diffusion-limited enrichment of trace elements in the boundary layer between the growing crystal and adjacent melt; kinetically controlled, non-equilibrium partitioning of trace elements into rapidly grown crystal layers. We revisit these hypotheses—particularly equilibrium, temperature-dependent partitioning: the premise behind Ti-in-zircon thermometry—in the context of the new images presented in this study.

Oscillatory CL zonations in zircon have most frequently been attributed to the incorporation and/or rejection of heavy rare earth elements (HREEs), although the type of zone (i.e., CL-dark or CL-bright) varies depending on the element and its electronic properties (e.g., Ohnenstetter et al. 1991; Hanchar and Rudnick 1995; Remond et al. 1995; Corfu et al. 2003; Nasdala et al. 2003). Regardless of the cause, our observations suggest that, in ~ 75% of all zircons (Figures 1-4 and 6-7 of this study and Figures 4 and 5 in Hofmann et al. (2009a), if we take our data set as a representative sampling), [Ti] also partitions in a manner correlated to the formation of oscillatory CL banding. Therefore, to interpret the [Ti] signature of these zircons as an equilibrium temperature phenomenon requires considering the following six possibilities, illustrated in Figure 11, in addition to the assumption that correlated distribution of the other trace elements also reflect temperature-dependent partitioning.

The upper panel of Figure 11 (a) is a cartoon of a NanoSIMS ion image meant to display spatially correlated [Ti] and oscillatory CL banding. The representative line profile on the right (location shown on the ion image cartoon to the left) illustrates how the magnitude of [Ti] is observed to vary across CL bands. The six lower panels (Figure 11 b-g) indicate how one might interpret the [Ti] line profile as temperature. Figure 11b depicts a case in which the actual temperature of crystallization may in fact be an average of the temperatures indicated by the [Ti] peaks of the two CL bands. This interpretation has been favored by individuals who use electron microprobe and conventional ion microprobes, which are unable to resolve variations at the micron-scale like the NanoSIMS can, to quantify [Ti] in zircon. It has been suggested that one can ignore the [Ti] variations observed in NanoSIMS analyses when [Ti] are

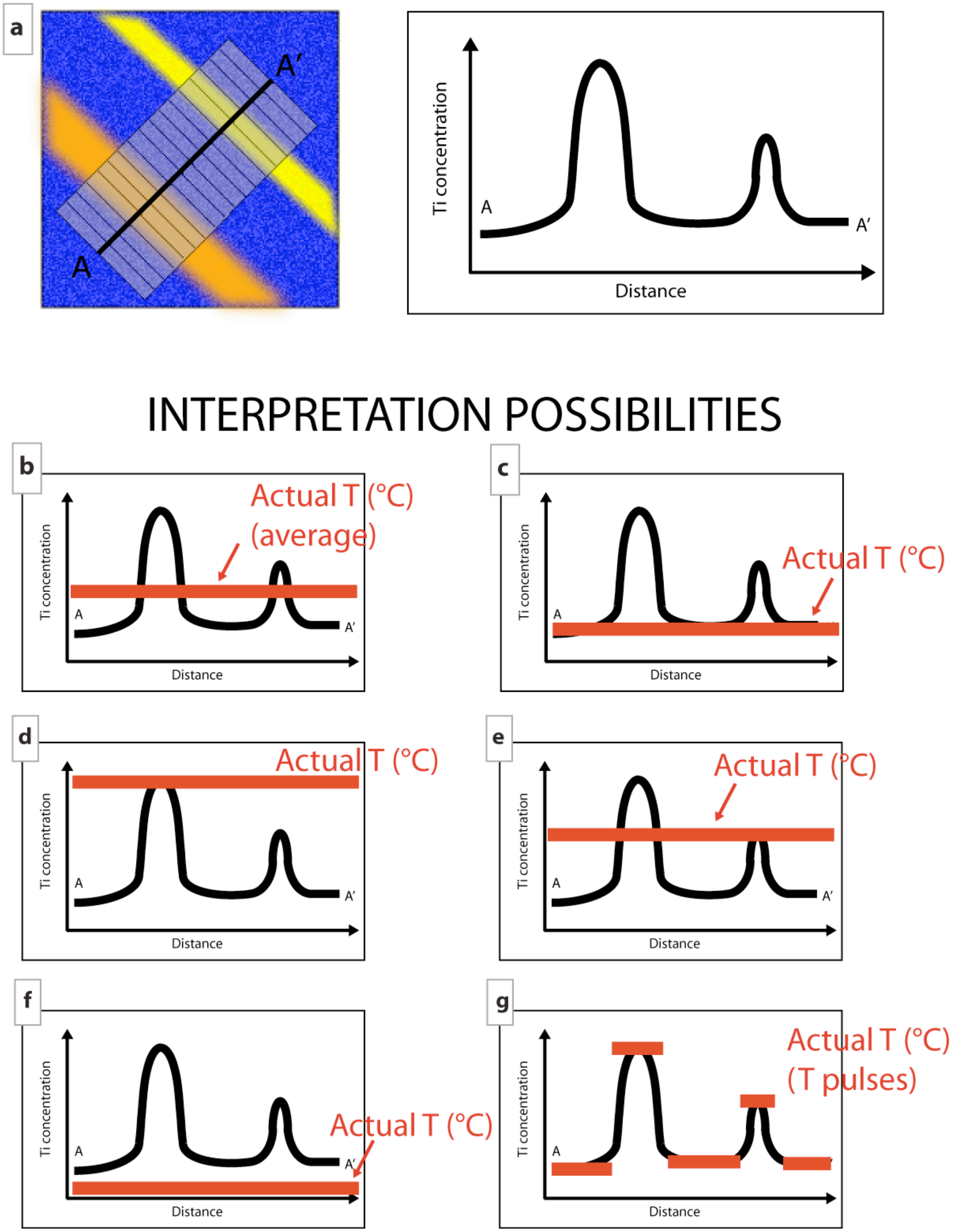

Figure 11. Cartoon illustrating six possible ways in which to interpret [Ti] spatially correlated to CL banding as temperature. **a.** *Left:* Idealized ion image meant to illustrate enriched trace element concentrations (orange and yellow bands) spatially correlated to oscillatory CL banding, as observed in Figures 1–4. The location of the line profile, as well as the integration regimes, is given by the black line denoted A – A'. *Right:* Line profile across ion image showing [Ti] varying in concordance with CL banding. **b.** Interpretation of the line profile suggesting that the actual temperature of crystallization is an average of the temperatures indicated by the [Ti] peaks of the two CL bands. **c.** Interpretation suggesting that the peak [Ti] are in fact anomalous (perhaps a result of kinetic influences on partitioning) and [Ti] of the baseline correspond to the actual temperature of zircon growth or

crystallization. **d.** Interpretation favoring [Ti] of the higher peak as recording actual growth/crystallization temperature of the zircon. **e.** Complementary to panel **d**, this interpretation suggests that [Ti] of the lower peak records the actual growth/crystallization temperature. **f.** Interpretation suggesting that the actual temperature of zircon growth/crystallization corresponds to a [Ti] below the concentration range recorded in the [Ti] image or that, in taking a line profile, we have inadvertently and consistently missed part of the [Ti] distribution within the ion image. **g.** Interpretation suggesting that variations in [Ti] should be taken as evidence for consistent, cyclic temperature fluctuations within a magma chamber. See text for discussion regarding each interpretation's viability.

coupled to CL banding and variations in other trace element distributions because the [Ti] between any two adjacent CL bands are observed to vary by less than a factor of 2. A type of integrating over or "averaging out" these variations—similar to that illustrated in Figure 11b—occurs when using a traditional ion microprobe, which has a beam diameter of ~ 10–20 μm and is the preferred analytical tool for determining [Ti] in zircons. Although not explicitly stated, averaging in this manner disregards resolvable variations in *all* of the analyzed trace elements' concentrations as being the result of processes other than bulk equilibrium and, furthermore, suggests that large-scale equilibrium processes underwrite the bulk trace element budget of a zircon. The latter seems unlikely given that crystal-chemical controls such as coupled substitutions, cation size, charge, and polarizability, intracrystalline strain energies, and kinetic phenomena like surface entrapment are all known to affect the incorporation of trace and incompatible elements in zircon (e.g., Hoskin and Schaltegger (2003) and references therein).

To address how [Ti] ranges determined by NanoSIMS analyses may be affected by "averaging," we have attempted to replicate traditional SIMS analyses—complete with "gating": collecting only the counts from an inner region of the analysis area—on the zircons imaged in this study by averaging the inner 80% of our NanoSIMS 20 × 20 μm and 10 × 10 μm $^{49}Ti^{+}$ and $^{94}Zr^{+}$ ion images, converting the resulting $^{49}Ti^{+}/^{94}Zr^{+}$ ratio to [Ti], and then reporting that mean and one standard error as both [Ti] and temperature in Table 1. We also report similar "faux SIMS" values for the two Jack Hills zircons described in Hofmann et al.

(2009a). In two images (T8 and JH54b.4-1), we were required to integrate over a smaller area due to loss of the primary beam current; the values are reported in the table as percents of the total original image size (e.g., 60% refers to 60% of a 20 × 20 μm image). Temperatures given in Table 1 were calculated using both the Ferry and Watson (2007) Ti-in-zircon calibration and the extrapolated global fit to experiments from Hofmann (Chapter 2). With the exception of the Adirondack zircons, all natural zircons analyzed in this study were known to coexist with quartz, thereby fixing the activity of SiO_2 in the system with respect to quartz at 1.0; an activity of 1.0 was assumed for the zircons from the Adirondack migmatites. The activity of TiO_2 with respect to rutile (a_{TiO_2}) was determined based on coexisting mineral assemblages; when petrographic information was not available, an activity of 1.0 (resulting in a minimum temperature) was assigned (Table 1). Calculations of [Ti] and temperature utilized a Monte Carlo error propagation routine accounting for errors on the slope and y-intercept of the calibration curves, the TiO_2 activity (assigned to be ± 0.1 for those cases in which $a_{TiO_2} = 0.6$), the mean ion ratio (as one standard error), and the $^{49}Ti^+/^{94}Zr^+$-to-[Ti] conversion factor (assigned an error of 15%). For comparison, zircon saturation temperatures were calculated for Quottoon, Toba, and Bishop Tuff zircons using electron microprobe Quottoon bulk rock compositions (Thomas and Sinha 1999), X-ray fluorescence (XRF) glass composition data for Toba unit YTT (Chesner 1998), and XRF data for pumices from the IG2E unit of the Bishop Tuff (Hildreth and Wilson 2007), respectively. With the exception of zircon BT1-8 (which displays [Ti] decoupled from both CL banding and other trace elements), the integrated "average" temperature (and [Ti]) fall well below 800°C, the average maximum temperature observed by Fu et al. (2008) to be recorded in zircon populations from most parent rocks, regardless of composition. Furthermore, even at the 95% confidence level, averages of these

Table 1. Magmatic temperatures calculated using Ti-in-zircon (Ferry and Watson; Hofmann, Chapter 2) and zircon saturation

Zircon ID	**Mean [Ti] (ppm)**	**1 σ (ppm)**	***a*TiO₂**	**Ferry & Watson T (°C)**	**1 σ (°C)**	**Hofmann (Ch. 2) T (°C)**	**1 σ (°C)**	**Zircon saturation T (°C)**
T11	6	1	0.6	749	25	866	169	765 – 875
T8 (60%)*	4	1	0.6	704	23	807	160	
Q8	2	0	0.6	647	21	771	148	715 – 850
Q4	4	1	0.6	711	23	837	161	
Q3	2	0	0.6	646	20	769	148	
M29	6	1	1.0	705	19	831	160	n.d.
M9	4	1	1.0	665	18	790	152	
BT1-8	13	2	0.6	824	29	954	185	770 – 795
BT2-10	2	0	0.6	638	20	761	147	
SN11	9	1	1.0	731	21	858	165	n.d.
JH54b.4-1 (40%)*	5	1	1.0	688	19	814	156	n.d.
JH54b.9-2	3	1	1.0	654	18	778	149	n.d.

Titanium concentrations [Ti] determined by averaging the inner 80% (unless otherwise noted) of all NanoSIMS images (Figures 1-10) in an attempt to reproduce the [Ti] expected from a conventional SIMS analysis. Temperatures calculated using the Ferry and Watson (2007) calibration curve and the global weighted fit to all experiments from Chapter 2; $a_{SiO_2} = 1$ in all cases; a_{TiO_2} is listed and is based on published coexisting mineral assemblages; when no such information is present, a_{TiO_2} set to1.0 (this results in a minimum temperature). Calculations for both [Ti] and temperature utilize a Monte Carlo error propagation routine: for [Ti]—error on the mean ion ratio and the $^{49}Ti^{+}/^{94}Zr^{+}$ to [Ti] conversion factor (assigned an error of 15%); for T—errors on the slope and intercept of the calibration curves, errors on [Ti], error on a_{TiO_2} of 0.1. Zircon saturation temperatures determined using the expression of Watson and Harrison (1983) and liquid compositions given in Chesner (1998), Thomas and Sinha (1999), and Hildreth and Wilson (2007) for Toba, Quottoon, and Bishop Tuff, respectively; maximum and minimum temperatures reflect variations in either glass or bulk rock compositions; T = Toba; Q = Quottoon; M = Adirondack migmatite; BT = Bishop Tuff; SN = Sierra Nevada; JH = Jack Hills (from Hofmann et al. (2009a)).

*Percentage of the total original image integrated to determine the mean [Ti].

n.d. = not determinable.

images consistently fail to capture the range of temperatures inferred from the [Ti] of the line profiles (or images) in Figures 1-10.

Panel c of Figure 11 depicts the case in which peak [Ti] are a result of kinetic influences on partitioning and [Ti] of the baseline correspond to the actual temperature of crystallization. Long-duration, low-temperature experimental syntheses of zircons with resolvable overgrowths from bulk compositions enriched in TiO_2 (similar to those proposed in Chapter 2) may help constrain whether the [Ti] of either the peaks or the valleys (here referred to as the baseline) represent equilibrium values. Panels d and e are complements of one another and suggest that [Ti] of either the highest peak or the lowest peak record the actual growth/crystallization temperature of the zircon. Both arguments are rejected as spurious because, lacking independent evidence implicating one peak's temperature as geologically meaningful, they involve decision-making based on personal preference. Figure 11, panel f depicts the possibility that the actual temperature of zircon growth/crystallization corresponds to a [Ti] below the concentration range recorded in the [Ti] image or that, in taking a line profile, we have inadvertently and consistently missed part of the [Ti] distribution within the ion image. This interpretation would require additional NanoSIMS evidence for a region of zircon homogeneous in [Ti] and justification as to why that region should be preferred over the CL banded region. It should be noted here that many regions of a zircon that appear homogeneous in CL are in fact sector zones, which arise as a result of local disequilibrium (i.e., less compatible cations attach to geometrically/energetically incomplete crystal surface sites, which are in equilibrium with the near-field liquid and/or different growth rates and mechanisms operate along different crystallographic faces (Nakamura 1973; Dowty 1976; Watson and Liang 1995; Watson 1996). Interpreting Ti partitioning (and resultant [Ti]) as an equilibrium phenomenon in sector zones would appear to be contradictory. The last panel (g) of Figure 11 depicts variations in [Ti] as reflecting consistent, cyclic temperature fluctuations within a magma chamber. This interpretation would be viable in the presence of additional, independent evidence for magma mixing, recharge, and/or transportation of the zircon from one region of the magma chamber to another. The [Hf] profiles from zircons in this study that show cyclic [Ti] signatures (Figures 1–4, 6-7) are in general not suggestive of such large-scale magmatic processes.

The remaining four zircons from this study (i.e., grains M9, T11, M29, and BT1-8) show [Ti] decoupled from oscillatory CL zonations. Given the disparate behavior [Ti] in each of the four zircons in this population, it is difficult to develop a single hypothesis to explain our observations. In the case of M9 (Figure 8), the Adirondack migmatite zircon showing CL zones with more complicated, non-linear geometry, [Ti] appears spatially correlated to the CL-dark zone. It is difficult to assess whether these zones "qualify" as sectors or not and what significance they may have, given the zircon's potentially complicated thermal history. As discussed in §3.1, Toba zircon T11 (in which [Ti] is decoupled from other trace element distributions and from oscillatory CL banding) may in fact record a temperature profile, although what type of temperature (e.g., of the parent melt, latent heat of zircon crystallization) is being recorded is unknown. The two zircons (M29 and BT1-8, Figures 9 and 10) for which [Ti] is decoupled from both oscillatory CL banding and other element distributions may be interpreted as recording a range of growth and/or crystallization temperatures, which we investigate in the following section via application of the Ferry and Watson (2007) Ti-in-zircon calibration curve.

3.3 Comparison of natural data to calibration curves

Table 2 provides a comparison of the zircon saturation temperature predicted from bulk rock compositions (when available) with temperatures for the [Ti] ranges presented in line profiles (Figures 1-10) calculated using the Ferry and Watson (2007) Ti-thermometry curve, the Hofmann (Chapter 2) calibration curve extrapolated from high temperature experiments, and a_{TiO_2} as listed in Table 1. For ease of comparison, we reproduce the zircon saturation temperatures reported in Table 1 for bulk analyses of Toba, Quottoon, and the Bishop Tuff. Unlike the examples cited in Harrison et al. (2007), we do not observe Ti-in-zircon temperatures to be higher than zircon saturation temperatures; rather, we observe the opposite: in all cases, zircon saturation temperatures estimate temperatures either higher than or barely encompassed by the high end of the Ti-in-zircon temperatures of an individual zircon. Temperatures calculated using the calibration of Hofmann (Chapter 2) more closely resemble the range of calculated zircon saturation temperatures, although it should be noted that the Quottoon bulk compositions and zircons might not be directly related (i.e., it is unknown which bulk rock sample corresponds to the zircon separates we were provided). Fe-Ti oxide thermometry was applied by Chesner (1998) to YTT unit 87 and by Hildreth and Wilson (2007) to unit IG2E of the Bishop Tuff; those values are reported in Table 1 for comparison. Fe-Ti oxide temperatures appear to more closely approximate the temperature range suggested by zircon saturation temperatures than by either calibration. Most zircons analyzed record an average temperature range of ~ 100°C from data taken over a less than 400 μm^2 area. In general, the Ferry and Watson (2007) calibration estimates growth and crystallization temperatures to be ~ 100°C less than the temperatures predicted by the extrapolation of the global weighted fit to our experiments (Chapter 2). More important than

Table 2. Comparison of magmatic temperatures calculated using Ti-in-zircon (Ferry and Watson; Hofmann, Chapter 2), zircon saturation, and coexisting Fe-Ti oxides

Zircon ID	[Ti] range from line profile (ppm)	T (°C) range (Ferry & Watson)	T (°C) range (Hofmann)	Zircon saturation T (°C)	Fe-Ti oxide T (°C)
T11	2.3 – 18.4	663 – 863	778 – 979	765 – 875	716 ± 30
T8	2.5 – 7.5	670 – 768	785 – 883		
Q8	0.8 – 3.1	583 – 686	696 – 802	715 – 850	n.d.
Q4	2.0 – 5.2	652 – 732	767 – 849		
Q3	1.1 – 2.6	607 – 674	720 – 789		
M29	2.7 – 9.1	637 – 737	751 – 853	n.d.	n.d.
M9	< 1 – 21	< 567 – 821	< 679 – 937		
BT1-8	3 – 31	695 – 926	811 – 1040	770 – 795	761 ± 27
BT2-10	0.75 – 3.75	582 – 703	694 – 819		
SN11	3.7 – 14.7	660 – 783	774 – 899	n.d.	n.d.
JH54b.4-1*	2.5 – 5.5	630 – 693	744 – 808	n.d.	n.d.
JH54b.9-2*	2 – 10	614 – 746	728 – 862	n.d.	n.d.

Temperature ranges predicted for the [Ti] contents of zircons given in NanoSIMS images and line profiles (Figures 1 – 10) determined using the calibration of Ferry and Watson (2007) and the calibration based on the global weighted fit to all experiments from Chapter 2; $a_{\mathrm{SiO_2}} = 1$ in all cases; $a_{\mathrm{TiO_2}}$ from Table 1. Zircon saturation temperatures determined using the expression of Watson and Harrison (1983). Fe-Ti oxide temperatures are from the following sources: Toba, Chesner (1998); Bishop Tuff, Hildreth and Wilson (2007)
See Table 1 for a description of zircon saturation calculations; n.d. = not determinable
*Line profiles and associated [Ti] are from Hofmann et al. (2009a) and are reproduced in Chapter 1, Figures 5 and 6.

these comparisons, however, is whether either fit can simultaneously explain the observed [Ti] of zircons for which temperatures are independently known.

Independent temperature constraints exist for the lithologic units from which two of the three zircons (BT1-8 and T11) showing no correlations between [Ti] and either other trace elements or CL banding: Bishop Tuff unit IG2E and the YTT 87 of the Toba Tuffs. It should be noted that these constraints, which are determined from the chemistry of coexisting magnetite and ilmenite, generally underestimate the zircon saturation temperature (which is presumably closer to the actual zircon crystallization temperature) determined for the same unit (Table 2). The highest and lowest [Ti] from the NanoSIMS ion maps of these two zircons (BT1-8 and T11) were plotted on an Arrhenius diagram in Figure 12 along with 1) the same data for their lithologic counterparts (BT2-10 and T8), which do show positive correlations among [Ti], other trace elements, and CL zonations; 2) all of the experimental zircon analyses from Chapter 2 and the associated weighted linear least squares calibration curve fit to those experiments; and 3) the Ti-in-zircon calibration curve given in Ferry and Watson (2007). Temperatures were chosen to be the average value given in Chesner (1998) for Toba unit 87 (~ 716 ± 30°C) and in Hildreth and Wilson (2007) for Bishop Tuff unit IG2E (~ 761 ± 27°C). Based on these temperature choices, we observe that *neither* fit can explain NanoSIMS [Ti] data from both the Toba and Bishop Tuff zircon populations. As suggested in §3.2, zircons in which [Ti] appears decoupled from both CL banding and the distributions of other trace elements (open diamonds and squares in Figure 12) might record actual magmatic temperature variations, but the corresponding temperatures predicted by both the Ferry and Watson (2007) and the Hofmann calibrations are implausibly high based on independent temperature constraints (Figure 12 and Table 1).

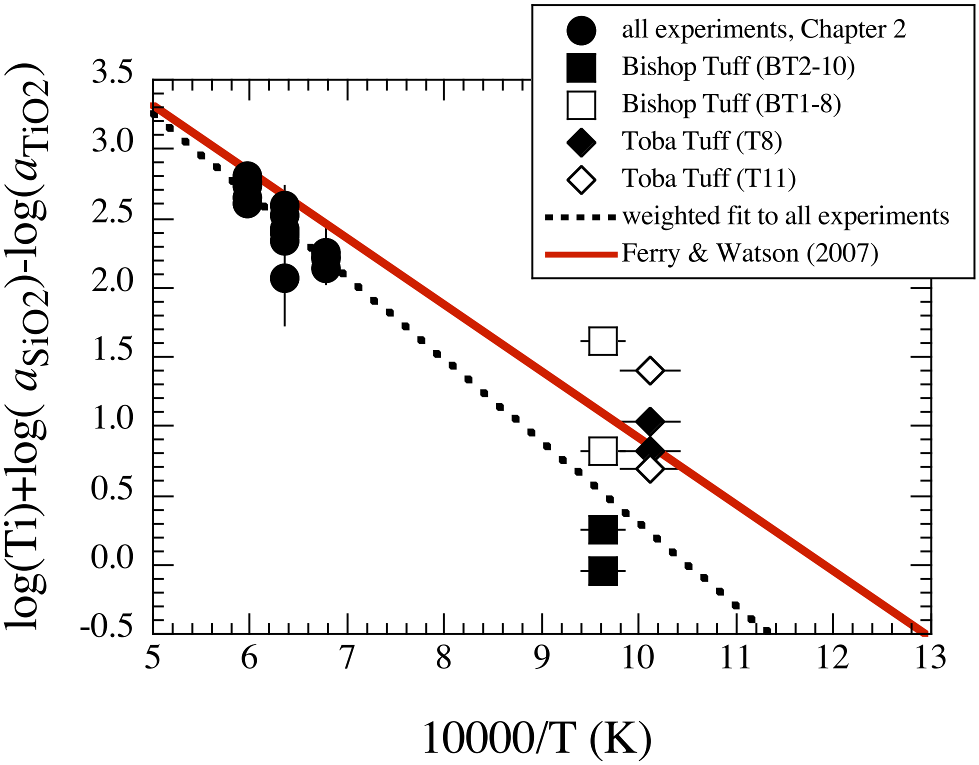

Figure 12. Comparison of NanoSIMS Ti data from this study for zircon populations for which temperatures of the source lithologic unit are independently constrained. Bishop Tuff zircons BT2-10 (Figure 7) and BT1-8 (Figure 10) from unit IG2E are given as square symbols. Toba Tuff zircons T8 (Figure 4) and T11 (Figure 5) from the YTT eruption are given as diamonds. In both cases, filled symbols indicate [Ti] distributions are correlated with both CL zonations and distributions of other trace elements; open symbols indicate decoupled [Ti] distributions. Temperatures were assigned based on the mean value given for each lithologic unit in Chesner (1998) and Hildreth and Wilson (2007). Experimentally grown zircons from Chapter 2 ([Ti] based on NanoSIMS analyses of micron- to sub-micron-scale overgrowths) are represented as filled circles. Trace element distributions were not measured in these zircons. When larger than the symbol size, errors in all cases are one standard deviation. An extrapolation of the weighted global fit to the experiments is given by the black dotted line and corresponds to the equation: log(Ti, ppm) + log(a_{SiO_2}) – log(a_{TiO_2}) = (6.214 ± 0.430) - (5918 ± 689) / T (K); $R^2 = 0.85$. The Ti-in-zircon calibration curve from Ferry and Watson (2007) is given by the solid red line.

Given Figure 12 and its implication that Ti distributions in zircon may be governed by variables other than temperature alone, a decision must be made regarding how to interpret temperatures from zircons showing correlated [Ti], trace element distributions and CL banding (a phenomenon observed in 75% of zircons imaged using the NanoSIMS to date and represented as filled diamonds and squares in Figure 12 for those cases in which temperatures are independently constrained). No one interpretation scheme from Figure 11 will satisfactorily explain both zircons; therefore, in the absence of additional partitioning studies and zircon-independent temperature constraints, concluding that the other trace elements (e.g., Y, P, REEs) *occasionally* proxy for temperature and/or that averaging over the [Ti] variations likely to exist in most CL-zoned zircons provides a robust measure of temperature is unwarranted. These observed distributions and the inability to explain them as equilibrium temperature phenomena suggest that a more rigorous and quantitative understanding of what governs the coupled partitioning behavior of trace elements—including Ti—in zircon is required.

4. Conclusions

The results of this study suggest that Ti distributions in zircons are more complicated than has been generally appreciated: 75% of all zircons imaged to date using the NanoSIMS show [Ti] to be spatially correlated with CL zonations and the distributions of a subset other trace elements. The remaining 25% display either large ranges in [Ti] that translate into > 100°C temperature variations over a small (< 400 μm^2) area or [Ti] decoupled from CL zonations yet spatially related to other trace element distributions. Averaging over these variations in a manner imitating the integration domain of a conventional ion microprobe spot analysis necessarily also removes the potentially useful information of variations in the other trace elements—particularly in those instances when [Ti] positively correlates with [P], [Y], and [Ce]—and results in temperatures (using the calibration of Ferry and Watson (2007)) lower than those predicted by zircon saturation calculations. In the case of zircons for which zircon-independent temperature constraints are known, neither experimentally derived calibration (i.e., Ferry and Watson (2007); Hofmann, Chapter 2) can explain the observed [Ti] variations in the NanoSIMS images, despite the fact that the Ferry and Watson (2007) Ti-in-zircon thermometer calibration was fit using [Ti] of natural zircons. Based on these observations, we urge caution in applying the Ti-in-zircon thermometer, particularly in the case where the host rock not longer exists. Well-characterized experiments using natural compositions and at temperatures relevant to zircon crystallization (< 1000–900°C) are needed before the [Ti] zoning patterns observed in magmatic zircons can be correctly interpreted.

Acknowledgments

The author thanks Yunbin Guan for technical assistance on the NanoSIMS and Bruce Watson, Jay Thomas, and Jason Saleeby for providing zircon samples. Financial support for this study was provided by a National Science Foundation grant to J. Eiler and by a grant from the Moore Foundation to the Caltech Microanalysis Center.

References

Anderson DJ, Lindsley DH (1988) Internally consistent solution models for Fe-Mg-Mn-Ti oxides: Fe-Ti oxides. Am Mineral 73:714-726

Baldwin JA, Brown M, Schmitz MD (2007) First application of titanium-in-zircon thermometry to ultrahigh-temperature metamorphism. Geology 35:295-298

Cates NL, Mojzsis SJ (2009) Metamorphic zircon, trace elements and Neoarchean metamorphism in the ca. 3.75 Ga Nuvvuagittuq supracrustal belt, Quebec (Canada). Chem Geol 261:99-114

Cherniak DJ, Watson EB (2007) Ti diffusion in zircon. Chem Geol 242:470-483

Chesner CA (1998) Petrogenesis of the Toba Tuffs, Sumatra. J Petrol 39:397-438

Corfu F, Hanchar J, Hoskin PWO, Kinny P (2003) Atlas of zircon textures. In: Hanchar JM, Hoskin PWO (eds) Zircon, Reviews in Mineralogy and Geochemistry, vol. 53, pp 469-500

Dowty E (1976) Crystal structure and crystal growth: II. Sector zoning in minerals. Am Mineral 61:460-469

Ferry JM, Watson EB (2007) New thermodynamic models and revised calibrations for the Ti-in-zircon and Zr-in-rutile thermometers. Contrib Mineral Petrol 154:429-437

Fu B, Page FZ, Cavosie AJ, Fournelle J, Kita NK, Lackey JS, Wilde SA, Valley JW (2008) Ti-in-zircon thermometry: applications and limitations. Contrib Mineral Petrol 156:197-215

Glikson A (2006) Comment on "Zircon thermometer reveals minimum melting conditions on earliest Earth" I. Science 311:779a

Hanchar JM, Rudnick RL (1995) Revealing hidden structures: The application of cathodoluminescence and back-scattered electron imaging to dating zircons from lower crustal xenoliths. Lithos 36:289-303

Harrison TM, Armstrong RL, Naeser CW, Harakal JE (1979) Geochronology and thermal history of the Coast Plutonic Complex, near Prince Rupert, British Columbia. Can J Earth Sci 16:400-410

Harrison TM, Clarke GKC (1979) A model of thermal effects of igneous intrusion and uplift as applied to the Quottoon pluton, British Columbia. Can J Earth Sci 16:411-420

Harrison TM, Watson EB, Aikman AB (2007) Temperature spectra of zircon crystallization in plutonic rocks. Geology 35:635-638

Hildreth W (1979) The Bishop Tuff: Evidence for the origin of compositional zonation in silicic magma chambers. Geol S Am S 180:43-75

Hildreth W, Wilson CJN (2007) Compositional zoning of the Bishop Tuff. J Petrol 48:951-999

Hofmann AE, Valley JW, Watson EB, Cavosie AJ, Eiler JM (2009a) Sub-micron scale distributions of trace elements in zircon. Contrib Mineral Petrol 158:317-335

Hofmann AE, Baker MB, Eiler JM (2009b) Sub-micron scale Ti variations in zircons of known provenance. Geochim Cosmochim Acta 73:A542

Hoskin PWO, Schaltegger U (2003) The composition of zircon and igneous and metamorphic petrogenesis. In: Hanchar JM, Hoskin PWO (eds) Zircon, Reviews in Mineralogy and Geochemistry, vol. 53, pp 27-62

Lappin AR (1976) Partial melting and generation of quartz dioritic plutons at crustal pressure and temperature within the Coast Range batholithic complex, B.C. Ph.D. thesis. Princeton University, Princeton, NJ

Lowery Claiborne L, Miller CF, Walker BA, Wooden JL, Mazdab FZ, Bea F (2006) Tracking magmatic processes through Zr/Hf ratios in rocks and Hf and Ti zoning in zircons: An example from the Spirit Mountain batholith, Nevada. Mineral Mag 70:517-543

Maas R, Kinny PD, Williams IS, Froude DO, Compston W (1992) The Earth's oldest known crust: A geochronological and geochemical study of 3900–4200 Ma old detrital zircons from Mt. Narryer and Jack Hills, Western Australia. Geochim Cosmochim Acta 56:1281-1300

Menneken M, Nemchin AA, Geisler T, Pidgeon RT, Wilde SA (2007) Hadean diamonds in zircon from Jack Hills, Western Australia. Nature 448:917-921

Moore CE (1970) Ionization potentials and ionization limits derived from the analyses of optical spectra. In: National Bureau of Standards USDoC (ed), National Standard Reference Data Service, National Bureau of Standards, Washington, D.C., p 22

Nakamura Y (1973) Origin of sector-zoning of igneous clinopyroxene. Am Mineral 58:986-990

Nasdala L, Zhang M, Kempe U, Panczer G, Gaft M, Andrut M, Plotze M (2003) Spectroscopic methods applied to zircon. In: Hanchar JM, Hoskin PWO (eds) Zircon, Reviews in Mineralogy and Geochemistry, vol. 53, pp 427-467

Nutman AP (2006) Comment on "Zircon thermometer reveals minimum melting conditions on earliest Earth" II. Science 311:779b

Ohnenstetter D, Cesbron F, Remond G, Caruba R, Claude J-M (1991) Emissions de cathodoluminescence se deux populations de zircons naturels: tentative d'interpretation. C. R. Acad. Sci. Paris 313:641-647

Remond G, Blanc P, Cesbron F, Ohnenstetter D, Rouer O (1995) Cathodoluminescence of rare earth doped zircons. II. Relationship between the distribution of the doping elements and the contrasts of images. Scanning Microsc Suppl 9:57-76

Rubatto D, Hermann J, Berger A, Engi M (2009) Protracted fluid-induced melting during Barrovian metamorphism in the Central Alps. Contrib Mineral Petrol 158:703-722

Storm LC, Spear FS (2005) Pressure, temperature, and cooling rates of granulite facies migmatitic pelites from the southern Adirondack Highlands, New York. J Metamorph Geol 23:107-130

Thomas JB, Sinha AK (1999) Field, geochemical, and isotopic evidence for magma mixing and assimilation and fractional crystallization processes in the Quottoon Igneous Complex, northwestern British Columbia and southeastern Alaska. Can J Earth Sci 36:819-831

Watson EB (1996) Surface enrichment and trace-element uptake during crystal growth. Geochim Cosmochim Acta 60(24):5013-5020

Watson EB, Harrison TM (2005) Zircon thermometer reveals minimum melting conditions on earliest Earth. Science 308:841-844

Watson EB, Liang Y (1995) A simple model for sector zoning in slowly grown crystals: Implications for growth rate and lattice diffusion, with emphasis on accessory minerals in crustal rocks. Am Mineral 80:1179-1187

Watson EB, Wark DA, Thomas JB (2006) Crystallization thermometers for zircon and rutile. Contrib Mineral Petrol 151:413-433

Wiedenbeck M, Hanchar JM, Peck WH, Sylvester P, Valley J, Whitehouse M, Kronz A, Morishita Y, Nasdala L, Fiebig J, Franchi I, Girard J-P, Greenwood RC, Hinton R, Kita N, Mason PRD, Norman M, Ogasawara M, Piccoli PM, Rhede D, Satoh H, Schulz-Dobrick B, Skår Ø, Spicuzza MJ, Terada K, Tindle A, Togashi S, Vennemann T, Xie Q, Zheng Y-F (2004) Further characterisation of the 91500 zircon crystal. Geostand Geoanal Res 28:9-39

Wilson CJN, Hildreth W (1997) The Bishop Tuff: New insights from eruptive stratigraphy. J Geol 105:407-439

Chapter 4

INSIGHT INTO SPINIFEX TEXTURES VIA ZONING OF PHOPHORUS AND ASSOCIATED ELEMENTS IN NATURAL AND SYNTHETIC KOMATIITIC OLIVINES

Abstract

Spatially correlated P, Al, and Cr zoning is observed in 36 of 40 Gorgona komatiitic olivines from three textural units: a jointed flow top, two random spinifex zones, and two oriented plate spinifex zones. P zoning is observed to be decoupled from or inversely correlated with Al and Cr zoning in some olivines from all three units. Microphenocrysts from the jointed flow top display oscillatory and sector zoning as well as P ± Al ± Cr rich cores with shapes mirroring the overall geometry of a given crystal. Spinifex olivines from both the random and the oriented zones display bands alternatingly enriched and depleted in P, Al, and Cr parallel to the long dimension of these crystals. In the case of oriented plate spinifex olivines, a central high-P band frequently is observed along the a-axis. Cooling-rate experiments were performed on a synthetic haplo-komatiite bulk composition in order to evaluate the physical parameters governing incorporation of P, Al, and Sc (as a proxy for Cr) in spinifex komatiitic olivines. In the absence of a thermal gradient, no spinifex olivines were generated from these experiments; however, the bladed olivines that were produced display spatially correlated sector zoning in P and Sc broadly similar to features observed in P and Cr in the Gorgona olivines. Cation-cation plots of data from the natural olivines reveal strong linear trends between Al and Cr and suggest that Al and Cr enter the olivine crystal lattice in a 2:1 ratio. Trends in P-Al and P-Cr composition space are nearly horizontal in the case of microphenocrysts from the flow top, despite the visual confirmation of P zoning correlated to zoning in Al and Cr. Random spinifex olivines define two trends in both P-Al and P-Cr space:

one that is sub-vertical and one that is sub-horizontal; in many cases, different analyses locations from a single grain can be found in both trends. With one exception, oriented plate spinifex olivines define a sub-horizontal P-Al and P-Cr trend, which suggests that P is being accommodated into the olivine lattice via a substitution mechanism involving both Al and Cr. The outlier from this population is a rare preserved plate spinifex tip, which records much higher P at low Al and Cr concentrations compared to the other plate spinifex grains; we interpret these data as suggestive of P incorporation in excess of equilibrium values due to rapid crystal growth.

1. Introduction

The preservation of trace and minor element zoning (specifically phosphorus (P), often coupled with chromium (Cr) and aluminum (Al)) in igneous olivine may provide insight into the early stages of magma genesis and/or a magma's crystallization history. Milman-Barris et al. (2008), who first pointed out the presence of oscillatory zoning of P in igneous olivine, concluded that rapid crystal growth and the resulting entrapment of slow-diffusing, incompatible trace elements in the crystal-melt boundary layer was responsible for most of the observed high-P zones in analyzed olivines. Due to the high temperatures (> 1400°C) at which komatiites erupt, the diffusive loss of P-zones in komatiitic olivines was thought to be a likely possibility; therefore, Milman-Barris et al. (2008) analyzed two komatiitic olivines from Gorgona Island, Colombia, and one from the Belingwe greenstone belt in Zimbabwe as part of their reconnaissance survey of igneous olivines. Although the average P_2O_5 contents of those komatiitic olivines—a plate spinifex grain and two microphenocrysts—were shown to be between a factor of two and an order of magnitude lower than the P_2O_5 concentrations of Hawaiian tholeiite phenocrysts, the presence of complex zonations in P, Cr, and Al in the komatiitic olivines was nevertheless readily visible in elemental X-ray maps. In this study, we consider a more extensive selection of komatiitic olivines taken from the different layered regions of Gorgona komatiite flows in order to evaluate how phosphorus zoning manifests itself in olivines of different komatiitic textures (e.g., microphenocryst, plate spinifex).

Komatiites are mantle-derived ultramafic igneous rocks that are generally restricted to the Archaean. Although even the freshest of Archaean komatiites are heavily altered, they are nevertheless studied for the potential insights they may yield into the nature of the early Earth's mantle and plume evolution. In this study, we focus on a representative suite of Cretaceous komatiites from the Colombian island of Gorgona. These rocks are the youngest known komatiites, first documented by Gansser et al. (1979). Olivines from the Gorgona Island komatiites, unlike their Archean counterparts, are relatively unaltered by either metamorphism or hydrothermal alteration (Echeverría 1980). Relative to Archean komatiites, erupted compositions of the Gorgona komatiites are depleted in SiO_2 and enriched in Al_2O_3 for any given MgO content and unlike them, Gorgona komatiites contain late-crystallizing plagioclase (Echeverría 1980; Aitken and Echeverría 1984). Basic descriptions of the Gorgona komatiites can be found in Echeverría (1980) and Kerr et al. (1996) and a review of proposed origins in Hastie and Kerr (2010).

Komatiite flows (sometimes referred to as “cooling units” to incorporate both extrusive flows and intrusive sills; Donaldson 1982; Arndt 1994) are layered ultramafic rocks comprised of olivine and pyroxene in a matrix of dendritic pyroxenes, Cr-rich magnetite, and devitrified glass, the majority of which has been replaced by secondary minerals due to hydrothermal alteration; plagioclase is rare in Archean and Proterozoic komatiites but common to Gorgona komatiite flows, most likely due to the higher Al_2O_3 of these lavas (Kerr et al. 1996; Arndt 2008). A typical Gorgona komatiite flow has an upper “flow top” that is usually fractured, brecciated, and displays chilled textures: skeletal to hopper olivine microphenocrysts and a high percentage of devitrified glass and fine-grained to dendritic olivine and pyroxene in the groundmass (Echeverría 1980; Donaldson 1982; Kerr et al. 1996). The flow top grades downward into a "spinifex zone" consisting of an upper, randomly oriented spinifex zone and a lower plate spinifex zone in which the spinifex olivines are oriented subparallel to one another; such olivines are, in the terminology of Donaldson (1976; 1982), classified as skeletal and either tabular (defined crystallographically $c \approx a >> b$) or bladed (i.e., $c > a >> b$) and are observed to grow in elongate bundles subparallel to proximal crystals of the same morphology and perpendicular to the komatiite flow top. Additional phases found in Gorgona spinifex zones include dendritic clinopyroxene, chromian spinel, plagioclase, and small granular olivine (Kerr et al. 1996). The bottom layer of a flow may or may not contain a "B-1" zone of foliated, skeletal-to-hopper olivines (e.g., Donaldson 1982; Kerr et al. 1996) below which lies an olivine cumulate. At Gorgona, such cumulates are rare; when present, they are described as "discontinuous and lenticular" (Kerr et al. 1996). In this study, we analyzed olivine crystals from the jointed flow top and both of the spinifex zones.

The origin of the spinifex texture characteristic of komatiite olivines and pyroxenes has been debated in the literature since it was first described by Viljoen and Viljoen (1969). Briefly, the following, often mutually exclusive, causes for the formation of spinifex-textured crystals have been proposed: instant quenching; slow cooling with slight undercooling; rapid cooling with large undercooling; rapid cooling promoted by convection within the interior of a komatiite flow; slow cooling accompanied by volatile loss; slow cooling in the presence of thermal and compositional gradients (e.g., Viljoen and Viljoen 1969; Nesbitt 1971; Donaldson 1974; Huppert et al. 1984; Kinzler and Grove 1985; Turner et al. 1986; Grove et al. 1994; Parman et al. 1997; Faure et al. 2006). The last of these possibilities (Faure et al. 2006) is the most recent and the only example in the literature in which komatiitic spinifex olivines were produced experimentally. Because those experiments were restricted to haplo-komatiite compositions in the CaO-MgO-Al_2O_3-SiO_2 (hereafter CMAS) system (Faure et al. 2006), further insight into the formation of this texture may be gained by adding minor elements like P, Sc, and Cr to the bulk komatiite starting composition, growing spinifex olivines in a manner similar to that of Faure et al. (2006), and then analyzing the minor element zoning trends present in the synthetic komatiite olivines as was done for natural olivines in Milman-Barris et al. (2008). We observe complex zonations in P, Cr, and Al in natural plate spinifex olivine; therefore, if thermal gradients are required for spinifex formation, then we might expect spinifex olivines grown in a thermal gradient to display similar complex zonations in P, Sc, and Al. The issue of what role—if any—that thermal gradients play in the production of trace element distributions within olivine was not considered by Milman-Barris et al. (2008) in their study of P zoning in olivines or by Faure et al. (2006). To address this issue, we performed a series of cooling rate experiments on a P, Sc (as a proxy for Cr as explained below), and Al-bearing, Fe-free haplo-komatiite bulk composition.

2. Materials and Methods

2.1 Description of Gorgona komatiites

We obtained several samples of Gorgona komatiites from Andrew Kerr at Cardiff University from which polished thin sections were prepared. Throughout the text, we adopt the same nomenclature as can be found for these samples in (Kerr et al. 1996; Kerr 2005). Not all samples published here have been previously reported in the literature. One (GOR94-19) is from a "polyhedrally jointed" flow top (Kerr et al. 1996; Kerr 2005) and consists of polyhedral to skeletal olivine microphenocrysts and chromian spinel in a matrix of devitrified glass and skeletal to chain-like pyroxene. Beneath the flow top is a zone dominated by randomly oriented spinifex olivine (samples GOR94-1 and GOR94-46) but which also includes skeletal olivine phenocrysts, dendritic pyroxene, chromian spinel, and altered interstitial glass. The random spinifex zone is followed with increasing depth by a plate spinifex layer (samples GOR94-29 and GOR94-43) in which bundles of spinifex olivines (up to 15 cm long) are oriented sub-vertically with respect to the top of the flow (Kerr et al. 1996; Kerr 2005); this zone contains skeletal, chain, and dendritic pyroxene, plagioclase needles and laths, hopper olivine microphenocrysts, spinel, and interstitial glass. Eight olivines in each of these five thin sections were analyzed for a total of 40 olivine elemental maps and corresponding quantitative analyses. Kerr (2005) and Kerr et al. (1996) also report the presence of a sharply defined contact between the oriented spinifex zone and an underlying "horizontal olivine zone" as well as a lowermost olivine cumulate zone in some flows; however, we did not have samples from either zone.

2.2 Experimental Materials and Methods

The synthetic haplo-komatiite composition selected for this study (Table 1) was determined via comparison to 1) CMAS bulk compositions used by Faure et al. (2006), 2) a projection of the forsterite-bearing multiply saturated liquidus onto the plane defined by the end-member compositions of silica, diopside, and spinel (Sheng 1992), and 3) trace element abundances in natural Gorgona komatiites (Echeverría 1980; Aitken and Echeverría 1984; Kerr et al. 1996; Kerr 2005). We chose not to use one of the compositions reported in Faure et al. (2006) because their CaO and Al_2O_3 contents were much higher than those from our target Gorgona composition after conversion of our values to the CMAS system. Due to its single valence state for the redox conditions of interest, scandium (Sc) was chosen to replace

Cr in this iron-free mix. Although we pay a lattice-strain penalty with this substitution (i.e., the ionic radius of $^{vi}Sc^{3+}$ is much larger (0.745 Å) compared to that of $^{vi}Cr^{3+}$ (0.615 Å) (Shannon 1976)), the advantage of this substitution lies in knowing that any observations of zoning in Sc are not reflecting behavior related to valence-state partitioning (as they might with Cr^{2+}/Cr^{3+}). The starting material (designated K-1, Table 1) was produced by combining oxide and carbonate powders (Alfa or Alfa Aesar Puratronic $CaCO_3$, MgO, Al_2O_3, SiO_2, Mn_2O_3, and Sc_2O_3) and hydroxy-apatite (Baker's Analyzed Reagent) in appropriate weight ratios and grinding under ethanol in an automated alumina mortar for a total of 4 hours and decarbonated overnight at 800°C.

Table 1. Bulk composition (wt %) of starting material for experiments

Sample ID	SiO_2	Al_2O_3	Sc_2O_3	MnO	MgO	CaO	P_2O_5	Sum
K-1	55.25	6.580	0.395	0.496	29.99	6.885	0.403	100.00

We conducted a series of isothermal experiments at 1450, 1475, 1490, and 1500°C and, in order to reduce the loss of P, which is highly volatile in air (Kilinc et al. 1983), each isothermal experiment was conducted in a vertical one-atmosphere DelTech gas-mixing furnace using an H_2-CO_2 gas mixture matching the f_{O_2} of QFM at 1500°C (Table 2). Under these conditions, log f_{O_2} at 1500 °C was determined to be -5.52.

Table 2. Average glass analyses of isothermal experiments (wt. %)†

Sample ID (K-1-#)	T (°C)	total time (h)	SiO_2	Al_2O_3	Sc_2O_3	MnO	MgO	CaO	P_2O_5	Sum
L1	1500	2.00	54.9(3)	6.90(7)	0.37(2)	0.48(3)	29.3(1)	6.82(7)	0.36(4)	99.1
L2	1450	2.25	56.8(3)	7.84(5)	0.42(1)	0.52(3)	26.1(2)	7.70(5)	0.44(4)	99.4
L3	1450	6.67	56.9(3)	7.9(1)	0.42(2)	0.50(3)	25.3(3)	7.9(1)	0.40(5)	99.4
L4	1475	16.40	55.9(4)	7.50(9)	0.40(1)	0.50(4)	27.7(2)	7.40(9)	0.39(4)	99.8
L5	1425	14.33	57.5(2)	8.37(7)	0.45(1)	0.52(4)	23.3(1)	8.36(6)	0.24(4)	98.8
L6	1495	4.98	54.7(4)	7.25(9)	0.37(1)	0.46(3)	29.2(2)	7.00(8)	0.36(4)	99.3

† Numbers in parentheses adjacent to the analyses are 1σ in terms of the least units cited; e.g., 54.9(3) represents 54.9 ± 0.3.

Experiments were performed by lowering a ~ 200 mg sample of K-1 suspended on a loop using PVA as a binder and 0.0125" diameter Pt wire into the hot spot of the furnace at 1000°C under flowing H_2-CO_2 gas. The sample was then heated to the run temperature at a rate of ~ 500°C/h and allowed to remain at temperature for 2–17 h before being drop-quenched into deionized H_2O. Run products were mounted in epoxy and polished with 0.25 μm diamond powder before electron microprobe analysis. Phase proportions were determined by mass balance. By projecting a linear fit to the experimentally determined liquid fraction as a function of temperature projected to a liquid fraction of one, we obtained a liquidus temperature for the K-1 composition of 1505 ± 5°C.

Three cooling rate experiments were performed in the one-atmosphere furnace using the same experimental set-up and gas mixture as the isothermal experiments described above. Samples were heated from 1000 to 1510°C at a rate of 500°C/h and then held at temperature for 2-4 hours (Table 3). The temperature was then decreased at a rate of either 5°C/h or 20°C/h until the charge reached a temperature of < 1400°C (Table 3), at which point it was drop-quenched into deionized H_2O.

Table 3. Run parameters for cooling rate experiments

Sample ID (K-1-#)	**experimental type**	**starting T (°C)**	**ramp rate (°C/h)**	**peak T (°C)**	**hold time (h)**	**cooling rate (°C/h)**	**ending T (°C)**	**total time (h)**
1	Pt loop	1000	500	1510	2	5	1395	24.50
2	Pt loop	1050	500	1510	4	5	1360	36.20
3	Pt loop	1000	500	1510	4	20	1320	15.00

We attempted to use various modifications of the graphite crucible technique of Faure et al. (2006) to grow olivine within a thermal gradient but these were unsuccessful due to failure of the Pt holding wires. This may reflect volatilization of P due to locally highly reducing conditions within the graphite crucible. Some of the P then alloyed with the Pt holding wires, leading to partial melting (there is a low temperature (588°C) eutectic between

Pt and Pt_5P_2 in the Pt-P system), followed by mechanical failure and auto-quenching of the crucible. In the future, we intend to perform the same type of experiments using a starting composition similar to K-1 but without P; after determining the specific conditions (e.g., superheating time, cooling rate, thermal gradient) on such a composition and analyzing the crystal morphologies and Sc distributions of run products, we will run experiments on K-1 (P-bearing) in platinum crucibles under moderately oxidizing (QFM) conditions.

2.3 Analytical Techniques

K_α X-ray intensity maps of Al, Cr, Fe, P, and Ti in natural olivines and of Al, Sc, P, Ca, and Mn in synthetic olivines were obtained using Caltech's JEOL JXA-8200 electron microprobe. Elemental maps were made under the following operating conditions: 15 kV accelerating voltage, 400 nA beam current, 1 μm beam diameter, and 1 μm pixel step size. All five elemental maps were collected simultaneously, with P and Cr acquired on PET crystals to improve signal-to-noise due to their low (P_2O_5: < 0.04 wt. %; Cr_2O_3: < 0.2 wt. %) concentrations in these olivines. For consistency, Sc and P were acquired on PET crystals for all synthetic olivine analyses as well. Dwell times of at least 800 msec were required in order to observe P zoning in the olivines, but several Gorgona images were collected with dwell times of 2400 msec. Maps required between 2 and 70 h as dictated by map dimensions and the dwell time for each point.

Quantitative analyses of SiO_2, TiO_2, Al_2O_3, Cr_2O_3, FeO* (all Fe as FeO), MnO, MgO, CaO, NiO, Na_2O, and P_2O_5 in natural olivines and of SiO_2, Al_2O_3, Sc_2O_3, MnO, MgO, CaO, and P_2O_5 in synthetic olivines were also acquired using Caltech's JEOL JXA-8200 electron microprobe. Cr (or Sc) and P X-ray maps were used to guide analysis locations. Analyses were made using a 15 kV accelerating voltage, 40 nA beam current, and 1 μm beam diameter.

Standards included Shankland forsterite (Si, Mg); synthetic TiO_2 (Ti); anorthite (Al, Ca); Cr_2O_3 (Cr); fayalite (Fe); tephroite (Mn); Amelia albite (Na); Ni olivine (Ni); Durango apatite (P); and scandium phosphate (Sc). Counting times and spectrometer assignments were chosen to minimize errors on P, Cr, and Al due to their low abundances in olivine and importance to the present study. Data reduction was performed using a modified ZAF procedure (CITZAF, Armstrong 1988). Analyses were accepted on the basis of the following criteria: 1) oxide sums of 100.0 ± 2.0 wt. %; 2) cation sums of 3.000 ± 0.015 per four oxygens; and 3) 1.000 ± 0.015 cations of Si + P per four oxygens. Detection limits and errors based on counting statistics for Al_2O_3, Cr_2O_3 (Sc_2O_3), and P_2O_5 in olivine were $\leq$ 0.01 wt. %.

The crystallographic orientations of nine Gorgona olivines, representative of the observed crystal habits / forms among the analyzed olivines, were determined by electron-backscatter diffraction (EBSD) on Caltech's LEO 1550VP FE-SEM. EBSD patterns were collected under the following conditions: an accelerating voltage of 20 kV, aperture of 60 μm, working distance of 20 mm, and tilt angle of 70°. Three to five points were analyzed on each grain; each point gave indexed solutions within < 1° (mean angular deviation) for forsterite using HKL Channel 5 software. Averaged results are given as equal-area, upper-hemisphere projections looking down the vector normal to the image.

3. Results

3.1 Zoning patterns in natural and synthetic komatiitic olivines

Zoning in phosphorus, as determined via X-ray intensity maps, was observed in two of the four synthetic olivine crystals and in all but four of the 40 natural olivines analyzed. P_2O_5 contents ranged from below our detection limits to ~ 0.035 wt. %, with the highest concentrations in olivine from GOR94-46, a section from the platy spinifex zone. With few

Table 4. Representative olivine analyses (wt. %)

Sample ID	Grain ID	Point #	SiO_2	TiO_2	Al_2O_3	Cr_2O_3	FeO*	MnO	MgO	CaO	NiO	Na_2O	P_2O_5	Sum
GOR94 -19	e	142	40.78	0.015	0.083	0.124	8.34	0.126	50.80	0.337	0.450	< 0.03†	0.013	101.07
		149	40.91	0.012	0.129	0.163	8.14	0.131	50.79	0.308	0.451	< 0.03	0.024	101.06
	g	123	40.32	< 0.01	0.054	0.083	10.38	0.168	48.20	0.363	0.376	< 0.03	0.004	99.95
		126	40.79	< 0.01	0.072	0.118	8.59	0.137	50.07	0.334	0.438	< 0.03	0.011	100.56
		130	40.75	0.013	0.062	0.121	8.34	0.136	49.79	0.332	0.436	< 0.03	< 0.005	99.98
	h	60	40.37	< 0.01	0.066	0.002	8.16	0.127	49.52	0.266	0.443	< 0.03	0.017	99.97
		64	40.40	< 0.01	0.602	0.005	8.01	0.133	49.66	0.276	0.452	< 0.03	0.008	99.95
GOR94 -29	b	62	40.25	< 0.02	0.053	0.114	10.66	0.173	47.44	0.372	0.386	< 0.04	< 0.005	99.45
		66	39.90	< 0.02	0.140	0.181	11.34	0.193	46.71	0.377	0.331	< 0.04	0.021	99.19
	g	78	40.55	< 0.02	0.055	0.104	10.77	0.174	48.47	0.382	0.382	0.145	0.005	101.04
		82	40.46	< 0.02	0.152	0.207	10.15	0.183	48.73	0.371	0.396	< 0.04	0.011	100.66
	h	70	40.24	< 0.02	0.168	0.199	9.94	0.147	48.09	0.376	0.422	< 0.04	0.014	99.60
		72	40.22	< 0.02	0.059	0.117	9.87	0.162	48.15	0.381	0.397	0.045	< 0.005	99.40
GOR94 -43	a	53	40.33	< 0.02	0.051	0.084	11.40	0.174	47.23	0.336	0.372	< 0.03	0.027	100.00
		57	40.45	< 0.02	0.057	0.078	11.15	0.172	47.23	0.333	0.377	< 0.03	< 0.005	99.85
	e	54	41.28	< 0.02	0.039	0.093	9.83	0.169	49.59	0.336	0.415	< 0.03	< 0.005	101.75
		59	41.05	< 0.02	0.083	0.125	9.70	0.162	49.43	0.335	0.418	< 0.03	0.013	101.32
	h	89	40.76	< 0.02	0.088	0.121	10.32	0.168	48.48	0.325	0.415	< 0.03	0.032	100.71
		96	40.65	< 0.02	0.048	0.097	9.65	0.159	48.80	0.316	0.435	< 0.03	0.019	100.17
GOR94 -1	b	55	40.04	< 0.02	0.031	0.069	12.39	0.201	46.86	0.369	0.309	< 0.03	< 0.005	100.27
		61	39.39	< 0.02	0.023	0.062	15.89	0.248	43.94	0.367	0.218	< 0.03	0.008	100.15
	e	84	40.10	< 0.02	0.025	0.067	11.80	0.173	47.00	0.356	0.333	< 0.03	0.007	99.86
		97	40.38	< 0.02	0.019	0.067	11.18	0.178	47.94	0.343	0.344	< 0.03	< 0.005	100.45

Table 4. continued

Sample ID	Grain ID	Point #	SiO_2	TiO_2	Al_2O_3	Cr_2O_3	FeO*	MnO	MgO	CaO	NiO	Na_2O	P_2O_5	Sum
GOR94-46	d	70	39.80	< 0.02	0.063	0.085	12.60	0.184	45.69	0.363	0.287	< 0.04	0.009	99.08
		78	40.02	< 0.02	0.027	0.074	11.78	0.189	46.50	0.360	0.303	< 0.04	0.021	99.27
	f	154	39.64	< 0.02	0.046	0.069	11.79	0.207	45.69	0.334	0.311	< 0.04	< 0.005	98.09
		159	39.72	< 0.02	0.091	0.106	11.61	0.186	46.15	0.337	0.332	< 0.04	0.013	98.55
	c (tip)	53	40.00	< 0.02	0.034	0.072	12.95	0.227	45.43	0.361	0.256	< 0.04	0.021	99.35
		66	38.96	< 0.02	0.048	0.079	16.87	0.261	42.23	0.371	0.188	< 0.04	0.049	99.06
K-1-3	a	109	42.62	-	< 0.02	0.096‡	-	0.396	55.64	0.179	-	-	0.176	99.11
		119	42.76	-	0.021	0.080‡	-	0.392	55.55	0.176	-	-	0.100	99.08
		122	42.94	-	< 0.02	0.049‡	-	0.395	55.66	0.179	-	-	0.029	99.25
		126	42.85	-	< 0.02	0.068‡	-	0.425	56.24	0.196	-	-	< 0.02	99.78
	b	63	42.26	-	< 0.02	0.076‡	-	0.417	55.05	0.182	-	-	0.150	98.14
		72	42.39	-	0.111	0.072‡	-	0.419	56.24	0.207	-	-	< 0.02	99.44
		81	42.16	-	0.029	0.070‡	-	0.340	56.30	0.162	-	-	0.065	99.13

† = below the detection limit
- = not included in mix
‡= as Sc_2O_3, chosen as a proxy for Cr_2O_3

exceptions, Cr and Al zonations were spatially correlated with P zoning; i.e., P-rich regions also display higher Cr and Al concentrations, from below detection limits to < 0.2 wt. % and < 0.15 wt. %, respectively. Chromium zoning is preserved even in altered regions where P and Al zoning is absent or obscured. Most olivines display normal zoning in Fe; in all cases, P, Cr, and Al zoning appeared to be independent of Fe/Mg. No resolvable zonations in Ti were observed in any of the analyzed olivines. Due to their high Cr_2O_3 contents relative to P_2O_5 and Al_2O_3, Cr X-ray intensity maps were often a better guide for our quantitative analyses than P and we used them to help inform our description of the zoning where zoning in the P maps was weakly expressed. Phosphorus / Cr / Al zonation patterns in olivine are observed to vary from layer to layer in the komatiite flows. We describe these patterns below and provide representative quantitative analyses for each olivine type in Table 4.

3.1.1 GOR94-19: Jointed flow top

Microphenocrysts display nearly continuous concentric bands of high- and low-Cr, Al, and P (i.e., oscillatory zoning) parallel to crystal edges (e.g., Figure 1). High-concentration bands range from ~ 2 to 20 μm in width and are spaced at irregular intervals 2 to 40 μm apart. Unlike the oscillatory zoning of phenocrysts and microphenocrysts from Hawaiian basalts described by Milman-Barris et al. (2008), we observe no systematic difference in spacing between bands within crystal interiors and near crystal boundaries. There is, however, a ~ 5–10 μm continuous high-P band along the outer edge of the microphenocryst in four of the eight olivines that we mapped.

The cores of microphenocrysts selected for analysis contain few melt inclusions but the crystals appear more hopper-like closer to the grain boundaries (Figure 1, panels a-f).

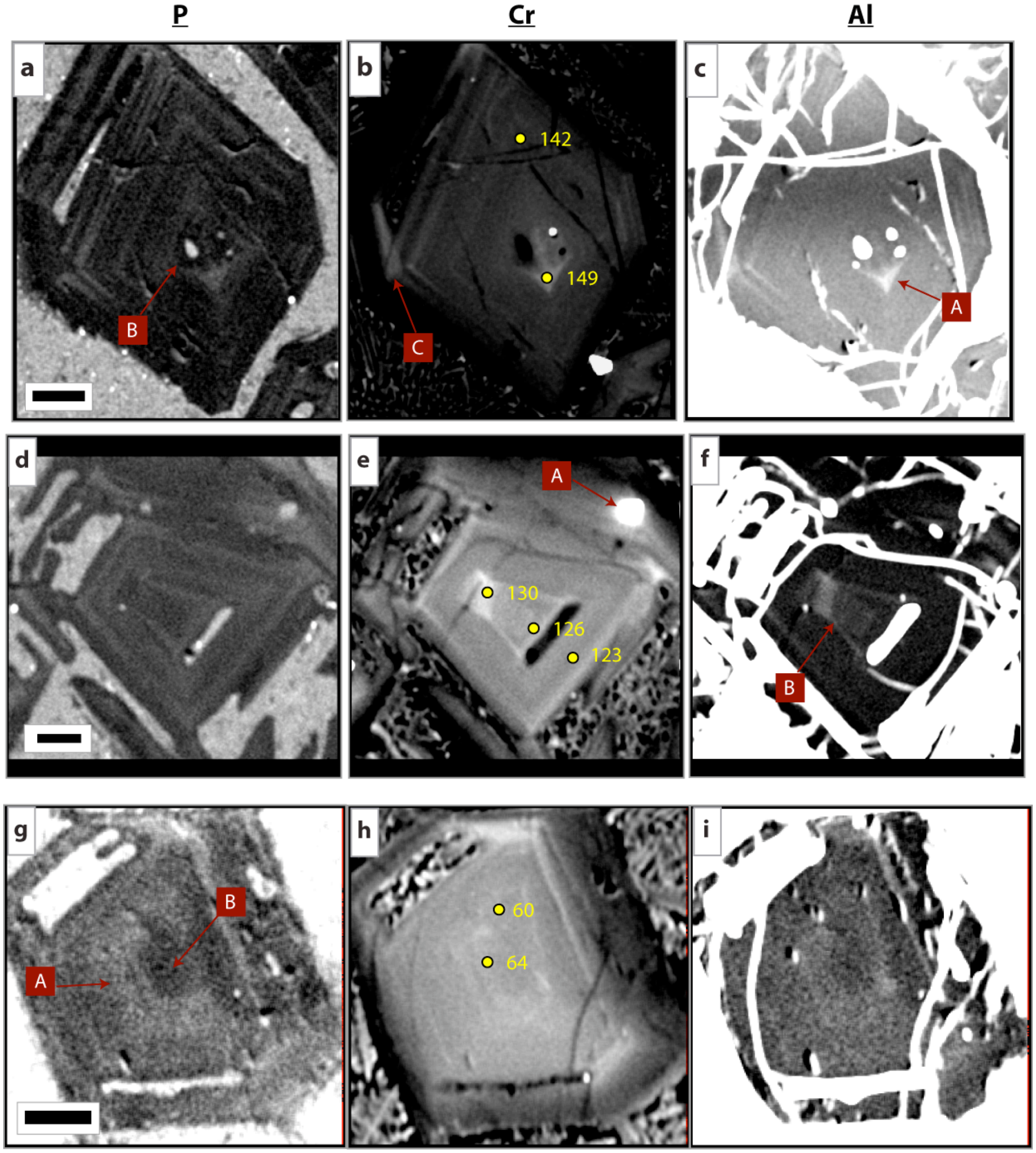

Figure 1. Phosphorus, chromium, and aluminum K_{α} x-ray maps of Gorgona olivine microphenocrysts from sample GOR94-19, taken from the jointed flow top of a komatiite flow. Scale bars (only one shown per grain) are 50 μm for all panels. Pixel intensities are meaningful within a single panel with white corresponding to more x-ray counts and black to fewer. Intensities between panels are not meaningful as the grayscale in each panel has been scaled to emphasize features of interest, which are labeled [A], [B], etc. and indicated by red arrows. Locations of representative quantitative analyses are indicated by numbered yellow dots (see Table 3 for corresponding analyses). **a.-c.** Equant microphenocryst GOR94-19e has a skeletal core [A] with the same geometrical shape as the overall grain and with correlated, high concentrations of P, Cr, and Al; surrounding this core at irregular intervals are concentric bands high in these elements. There are several melt inclusions, which are surrounded by a region low in P [B], and a small sector [C] that displays correlated Cr and Al anticorrelated with P. **d.-f.** Skeletal microphenocryst GOR94-19g contains multiple melt inclusions in addition to a single spinel inclusion [A]. The spinel inclusion appears bright in P due to differences in the background between P in spinel and P in olivine that are not taken into account in the X-ray maps, which are not background corrected. The core of the grain contains a region high in Al and Cr [B] that is low in P. **g.-i.** Equant microphenocryst GOR94-19h contains a core with the same shape as the rest of the grain [A]; however, the core appears skeletal and surrounds a low P, Cr, and Al center [B].

Diminished P, Cr, and occasionally Al signals are observed immediately adjacent to embayments in these crystals (Figure 1, panels d-f). Arrowhead-like regions of high-Cr and P very similar to those described and shown in Figure 3e, feature B of Milman-Barris et al. (2008) are observed in crystals GOR94-19a and GOR94-19e; the features are discontinuous but appears to point toward the terminus of a crystal apex. Three analyzed microphenocrysts (GOR94-19b, c, and h [e.g., Figure 1, panels g-i]) contain a central core low P, Cr, and Al surrounding by diffuse bands of high P, Cr, and Al with the same form as the overall crystal. One olivine imaged (GOR94-19d, first published in Milman-Barris et al. 2008) displays sector zoning through which oscillatory zoning from outside the sector continues. Cr and Al are elevated and P is diminished within the sector relative to the rest of the crystal. When present, cracks are filled with Al-rich material.

3.1.2 GOR94-29 and GOR94-43: Random spinifex zones

Concentrations in these olivines range from below detection limits to 0.20 wt. % for Cr_2O_3, 0.15 wt. % for Al_2O_3, and 0.035 wt. % for P_2O_5. Compared to olivine microphenocrysts in the flow top, olivines from random spinifex zones have elongate habits and appear less skeletal. Because crystals from these zones have no preferred orientation, occasionally equant crystals are observed (e.g., GOR94-29g, Figure 2, panels d-f); in the absence of EBSD data, it is unclear whether the two-dimensional image is a cross-section of an elongate spinifex grain cut perpendicular to a long axis (a or c) or a cross-section of a more euhedral microphenocryst. Some olivine crystals in these thin sections appear, based on morphology to be microphenocrysts rather than end-on views of spinifex olivines in the long-dimension. Elongate olivines display bands 5–35 μm wide and 5–20 μm apart parallel to the long dimension of the crystal. In most cases, these bands appear correlated in Cr, Al, and P;

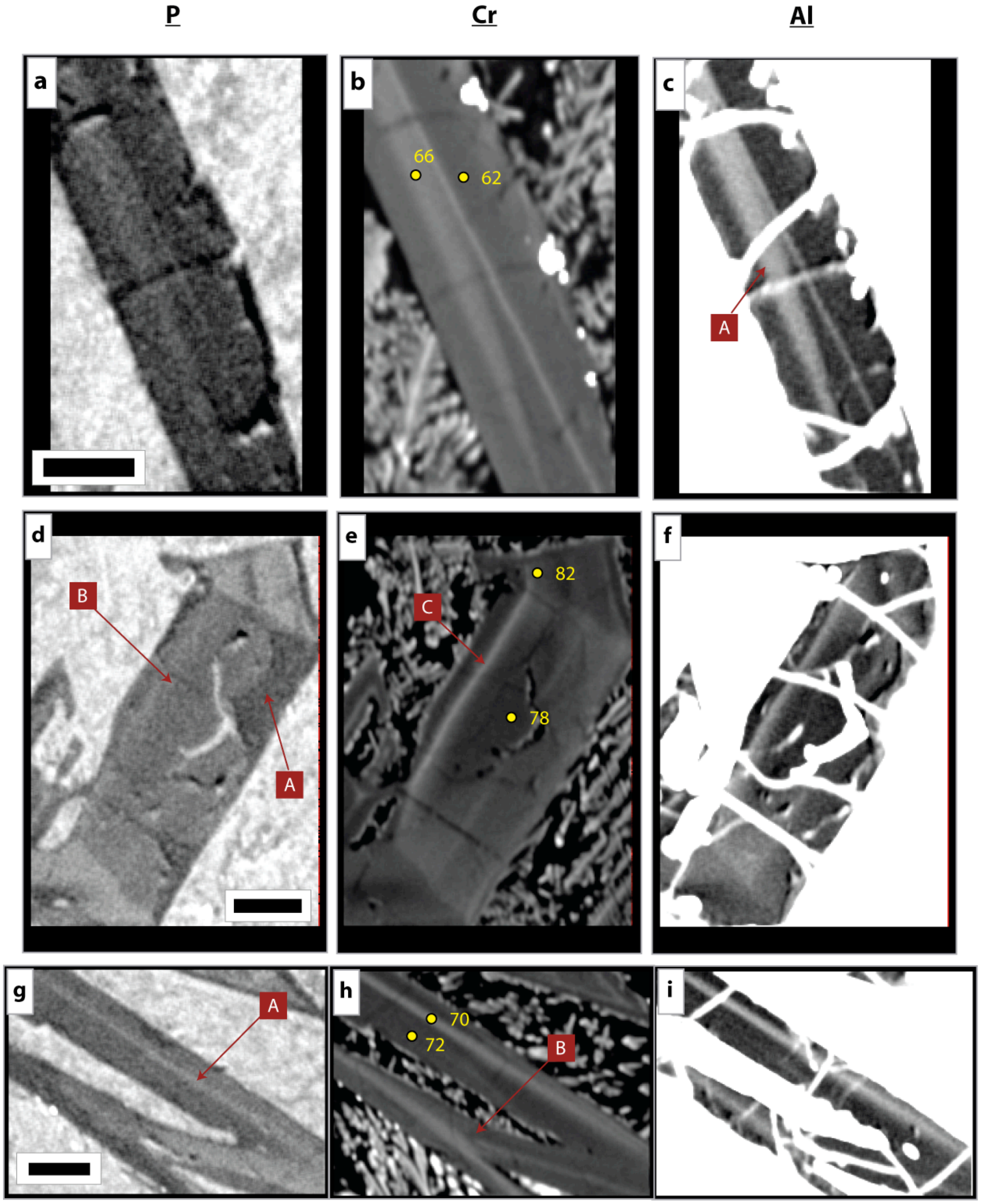

Figure 2. Phosphorus, chromium, and aluminum K_α x-ray maps of Gorgona olivines in sample GOR94-29, from a random spinifex zone of a komatiite flow. Scale bars are 50 μm for all panels. Other explanatory details are given in the caption for Figure 1. **a.-c.** Elongate spinifex olivine GOR94-29b displays a central band high in P, Cr, and Al [A] parallel to the grain's long axis. The band bifurcates, with the thicker band thinning to a sharp point in the lower right of the image. **d.-f.** Skeletal microphenocryst GOR94-29g contains multiple sectors. Note that the low-P region [A] has been altered, which is apparent in the Al map (panel f) but the grain appears continuous and the original zoning is preserved in Cr (panel e). The zone denoted [B] appears to be a single sector in P (panel d); however, distinct bands [C] are apparent in both the Cr and Al maps that are not visible in P. **g.-h.** Elongated spinifex olivine GOR94-29h contains a central band [A] elevated in P, Cr, and Al parallel to the grain's long axis. The banding appears continuous in P but there is a discontinuity in Cr [B].

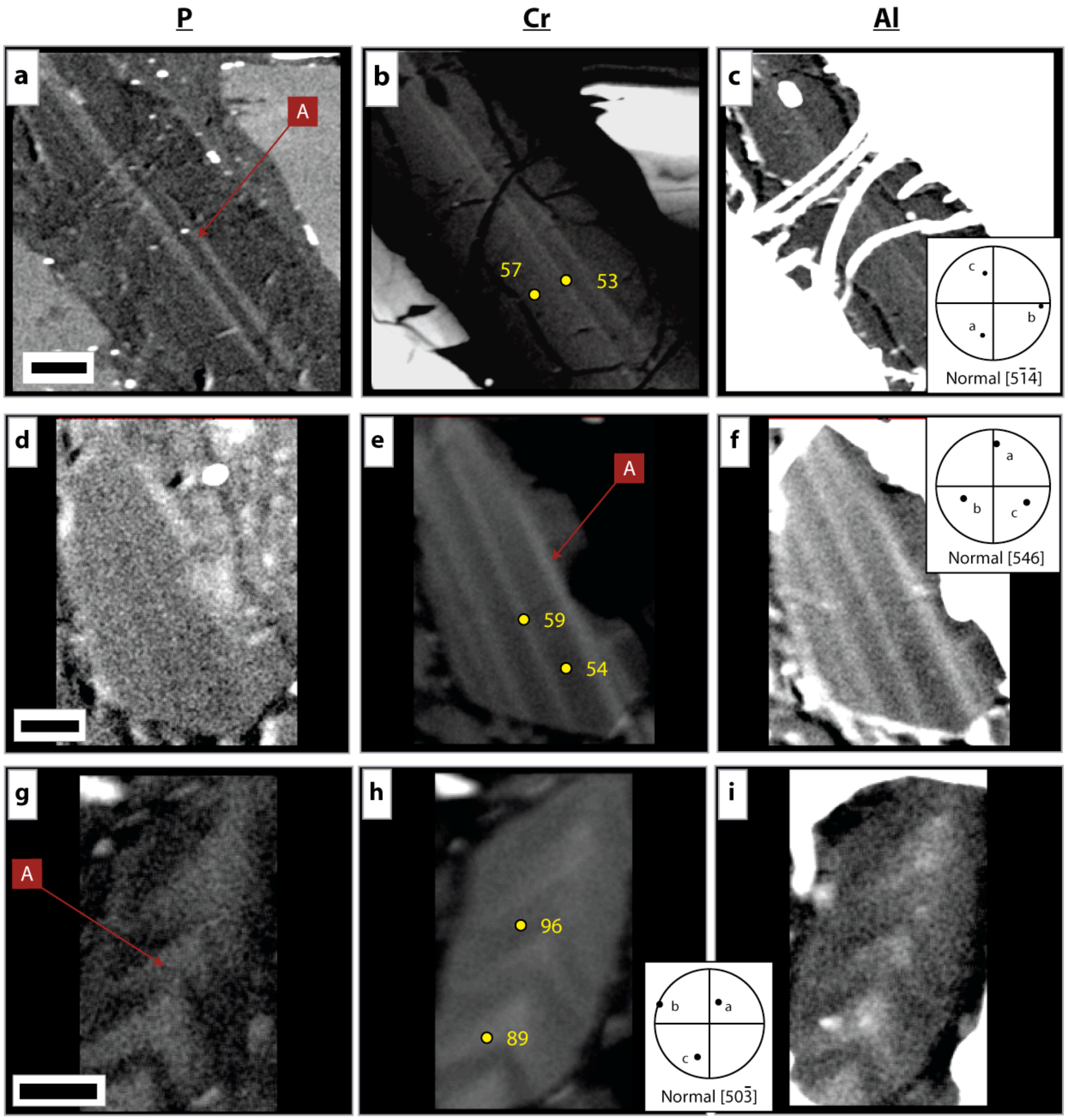

Figure 3. Phosphorus, chromium, and aluminum K_α x-ray maps of Gorgona olivines from sample GOR94-43, taken from a random spinifex zone of a komatiite flow. Scale bars are 50 μm for all panels. Other explanatory details are given in the caption for Figure 1. Crystal orientations based on EBSD, when available in this and succeeding figures, are inset as upper hemisphere equal-area projections of the crystallographic axes; the normal to the imaged plane is also given. **a.-c.** Elongate spinifex olivine GOR94-43a contains multiple thin bands high in P, Cr, and Al parallel to the long dimension of the crystal [A]. **d.-f.** Olivine GOR94-43e displays bands of high Cr and Al that appear sub-parallel to one another [A] and track the long dimension of the grain. It is unclear whether those bands persist in P. **g.-i.** Olivine GOR94-43h displays herringbone zonations high in P, Cr, and Al [A].

however, in two grains there is no resolvable evidence for P banding. In a few cases, thin bands of high Cr (and Al, P) diverge at an angle from wider bands parallel to the long dimension of the crystal (e.g., Figure 2, panels a-c and panels g-i). In one case (GOR94-29g, Figure 2, panels d-f), Cr and Al are inversely correlated with high-P sectors. A high P, Cr, and Al herringbone pattern, very similar to the "arrowhead" pattern described in GOR94-19a above, was also observed in one grain (GOR94-43h, Figure 3, panels g-i).

3.1.3 GOR94-1 and GOR94-46: Oriented plate spinifex zones

All imaged olivines from oriented plate spinifex zones have elongated habits and display oscillatory bands that vary in width (4–40 μm) parallel to the apparent long dimension of the crystal (Figures 4 and 5). Where orientations were determined using EBSD, the crystals were elongated in the a-direction (e.g., olivine GOR94-1b as shown in Figure 4c). In some cases, only one band is present, and it either runs along the center-line of the olivine or along an outer edge but it remains parallel to the long dimension of the crystal; in other cases, low-P/Cr/Al and high-P/Cr/Al bands alternate. As in several olivines from random spinifex layers, high-Cr bands are observed in two spinifex grains to diverge at an angle from other bands parallel to a crystal's long dimension. We observe no evidence of preserved zoning in Cr, Al, or P in GOR94-1c and GOR94-46b. Based on our observations of central thin, single bands in some plate spinifex olivines, these unzoned crystals may represent entirely altered olivine (although this is not borne out compositionally), a two-dimensional slice through an unzoned volume of crystal, or an "end-member" representing cases in which zoning has been diffusively homogenized, as we initially hypothesized for all komatiitic olivines.

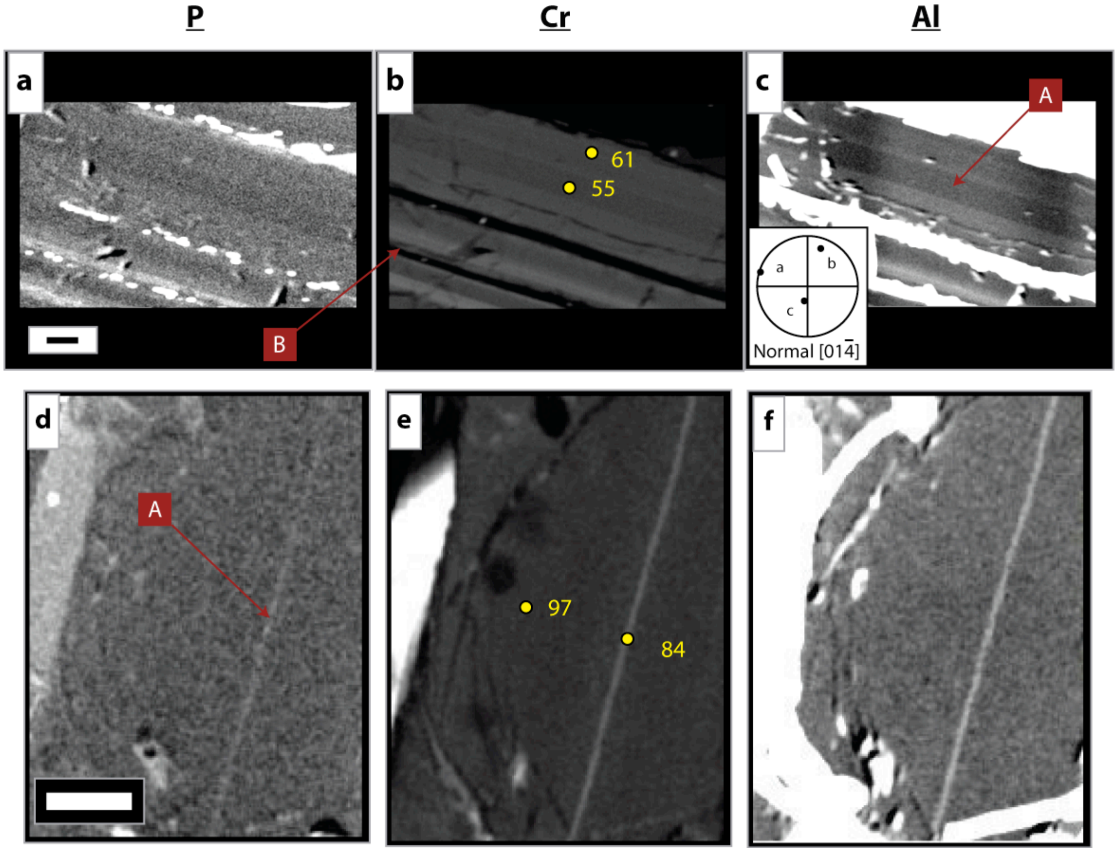

Figure 4. Phosphorus, chromium, and aluminum K_α x-ray maps of Gorgona spinifex olivines in sample GOR94-1 from an oriented plate spinifex zone of a komatiite flow. Scale bars are 50 μm for all panels. Other explanatory details are given in the caption for Figure 1 or 3. **a.-c.** Elongated plate spinifex olivine GOR94-1b is from a plate parallel to the plate containing the spinifex olivine previously imaged and published in Figure 5 panels d-f of Milman-Barris et al. (2008). This crystal displays a similar prominent, correlated banding parallel to its long dimension (the a-axis as determined by EBSD) [A]. In this orientation, the plane of the section is nearly perpendicular to the c-axis. Plate spinifex olivines grow with either their a- or c-axis perpendicular to the top of the komatiite flow and hence to the cooling front, suggesting that the central band low in P, Cr, and Al is denoting the center of the crystal; without a tip, it is, however, difficult to use trace and minor element banding like these to suggest a genetic relationship between element distributions and growth direction. Two thinner, distinct spinifex grains [B] lie to the lower left of 94-1b; EBSD of these grains indicates that they are in the same orientation as 94-1b. **d.-f.** In contrast to 94-1b, elongated plate spinifex olivine GOR94-1e contains a single thin band of high P, Cr, and Al through its center [A].

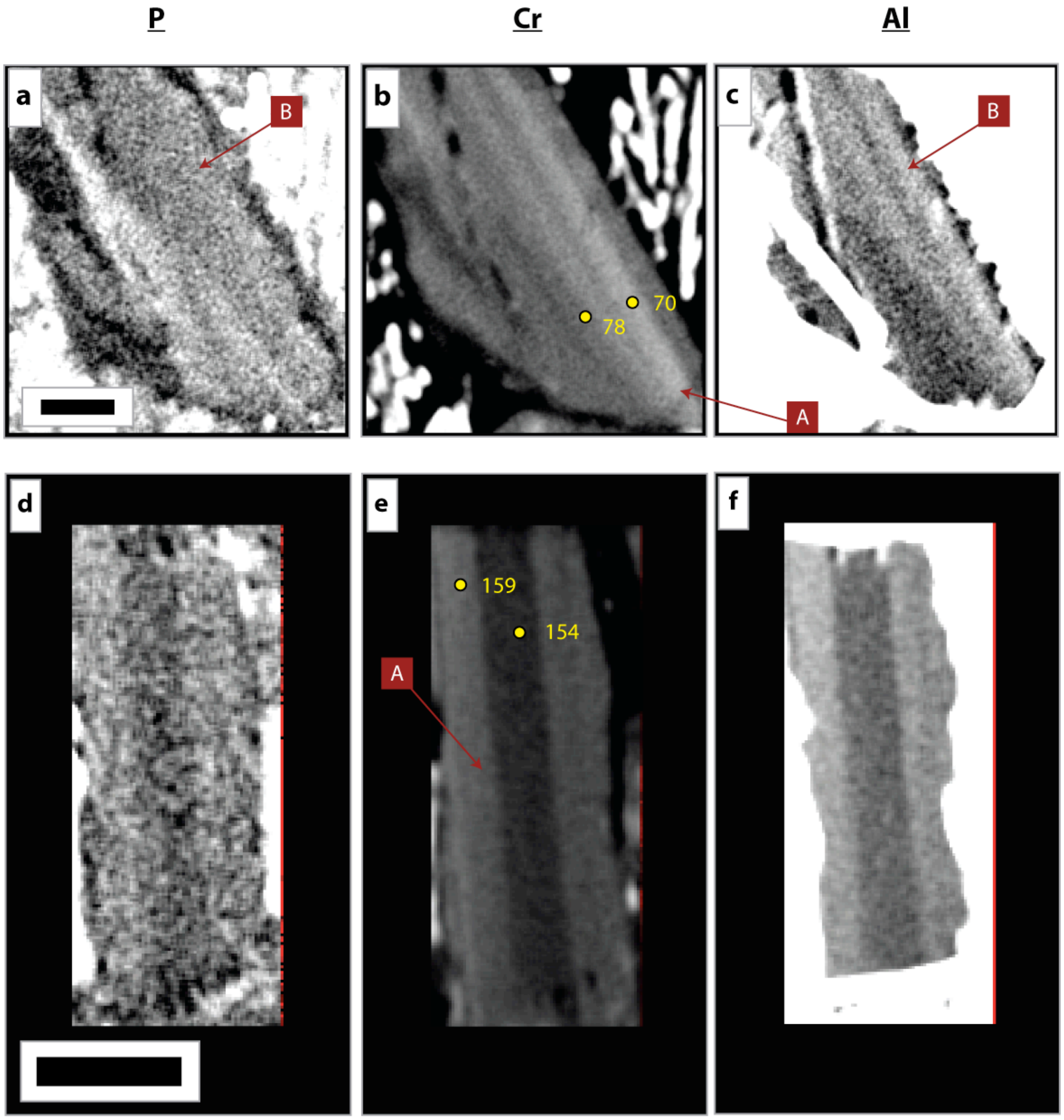

Figure 5. Phosphorus, chromium, and aluminum K_α x-ray maps of Gorgona spinifex olivines in sample GOR94-46 from an oriented plate spinifex zone of a komatiite flow. Scale bars are 50 μm for all panels. Other explanatory details are given in the caption for Figure 1. **a.-c.** Spinifex grain GOR94-46d displays bifurcating banding [A] similar to that seen in GOR94-29b (Figure 4, panels a-c). Bands that are bright in Cr and Al [B] are dark in P. **d.-f.** Elongated plate spinifex grain GOR94-46f, although much smaller than GOR94-1b (Figure 5, panels a-c), displays the same correlated P, Cr, and Al zonations parallel to the long dimension of the crystal, including a central band low in these three trace elements [A].

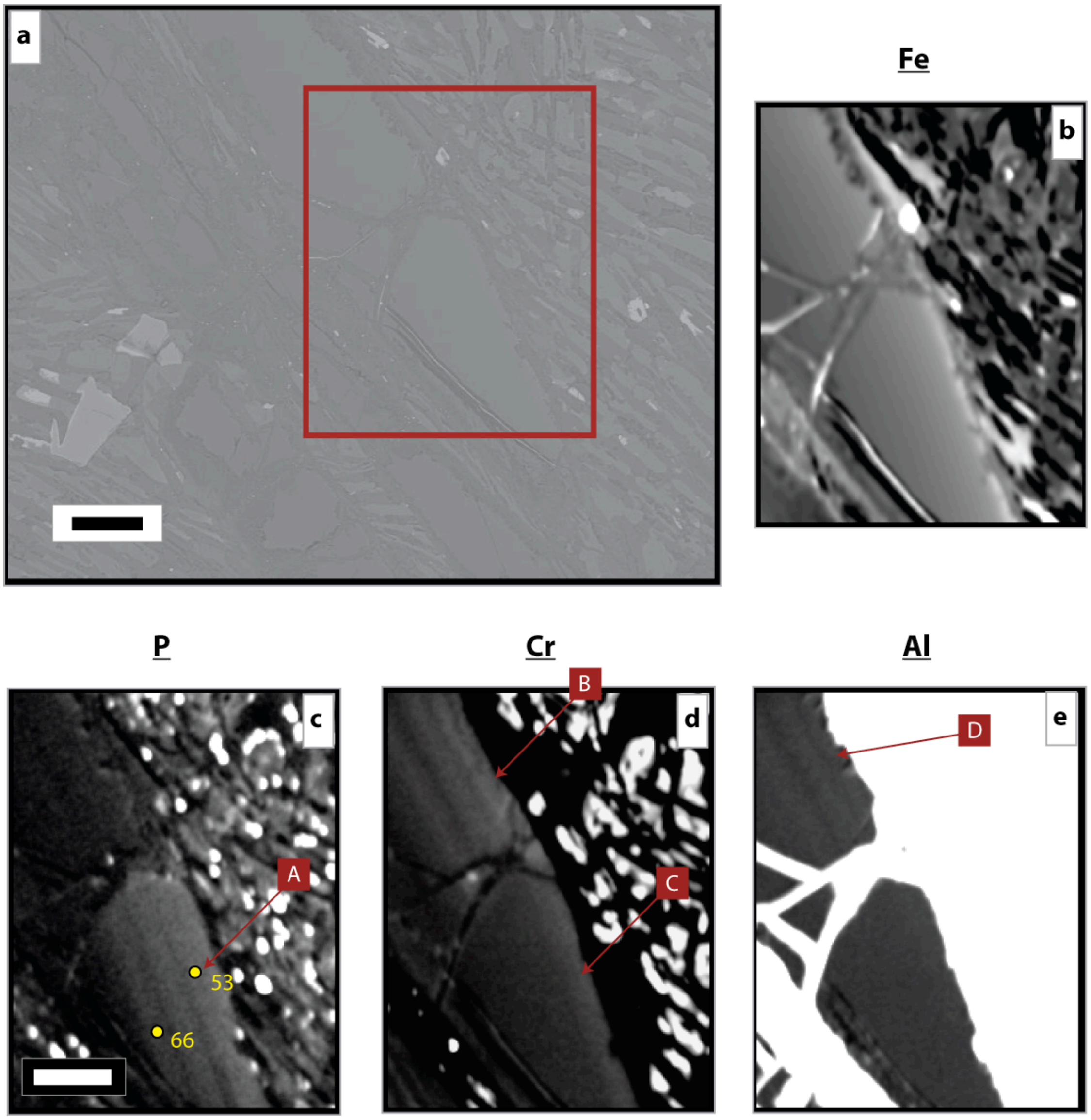

Figure 6. SEM backscatter electron image and iron, phosphorus, chromium, and aluminum K_{α} x-ray maps of the tip of spinifex olivine GOR94-46c. Scale bars are 50 μm for all panels. Other explanatory details are given in the caption for Figure 1. **a.** Backscatter FE-SEM image of the crystal. The red box indicates approximate location of imaged area given in (**b**). The actual terminus of the tip was inadvertently omitted from the x-ray maps. **b.** Fe K_{α} x-ray intensity map of 94-46c showing no discernable zoning. **c.** P K_{α} x-ray intensity map of 94-46c showing three parallel bands [A] bright in P; note that the bands are not concentric with respect to the crystal boundaries in this two-dimensional slice through the grain. The high-P bands also do not appear to continue into the crystal away from the tip. **d.** Cr K_{α} x-ray intensity map of 94-46c showing three parallel bands in the upper left of the crystal [B]; only one Cr-bright band appears continuous [C] from the upper left through into the apex of the grain near the tip. **e.** Al x-ray intensity map of 94-46c showing three parallel bands in the upper left of the crystal [D]; there is no apparent continuation of these bands into the crystal tip.

The preservation of spinifex olivine tips is rare (e.g., Renner et al. 1994); however, one was observed in the plate spinifex thin section GOR94-46. An initial map produced with an 800 msec per pixel dwell time revealed parallel banding along the posterior extent of the crystal; however, zoning in the tip was obscured, particularly in P; therefore, the same grain was mapped with a 2400 msec/pixel dwell time. The resultant Al, Cr, and P X-ray maps from this second analysis are presented in Figure 6. Although the exact terminus was inadvertently not captured in the image, both the parallel posterior bands and the likely extension of those bands into the proximity of the tip were observed.

3.1.4 Synthetic komatiite olivines

Quenched experimental run products K-1-1 and K-1-2 each consists of a single large olivine crystal surrounded by glass; neither olivine shows evidence of zonations in P, Sc, or Al, and, therefore, both the glass and the olivines were inadvertently omitted during electron microprobe analysis. Experiment K-1-3 produced several olivines, some of which appear bundled together; however, because K-1-3 exists as a grain mount and not a thin section, we cannot use the petrographic test of observing whether all the blades go extinct together under crossed polars to determine the number of actual crystals grown. Regardless of their relationships to one another, K-1-3 olivines show zonations in Sc and P only. Two distinct olivines (denoted ‘a’ and ‘b’) from experiment K-1-3 were chosen for mapping based on their elongate morphology and termination in a pointed tip (Figures 7 and 8, panel a). K-1-3a contains visible melt inclusions (Figure 7); K-1-3b may contain an Al-rich mineral inclusion (Figure 8, panels a and d). The melt inclusions in K-1-3a are surrounded by a low-P, low-Sc region that appears feathery or scalloped along its distal extent (with respect to the melt inclusions); this low-P, low-Sc region is intercalated by fingers of higher P and Sc that appear

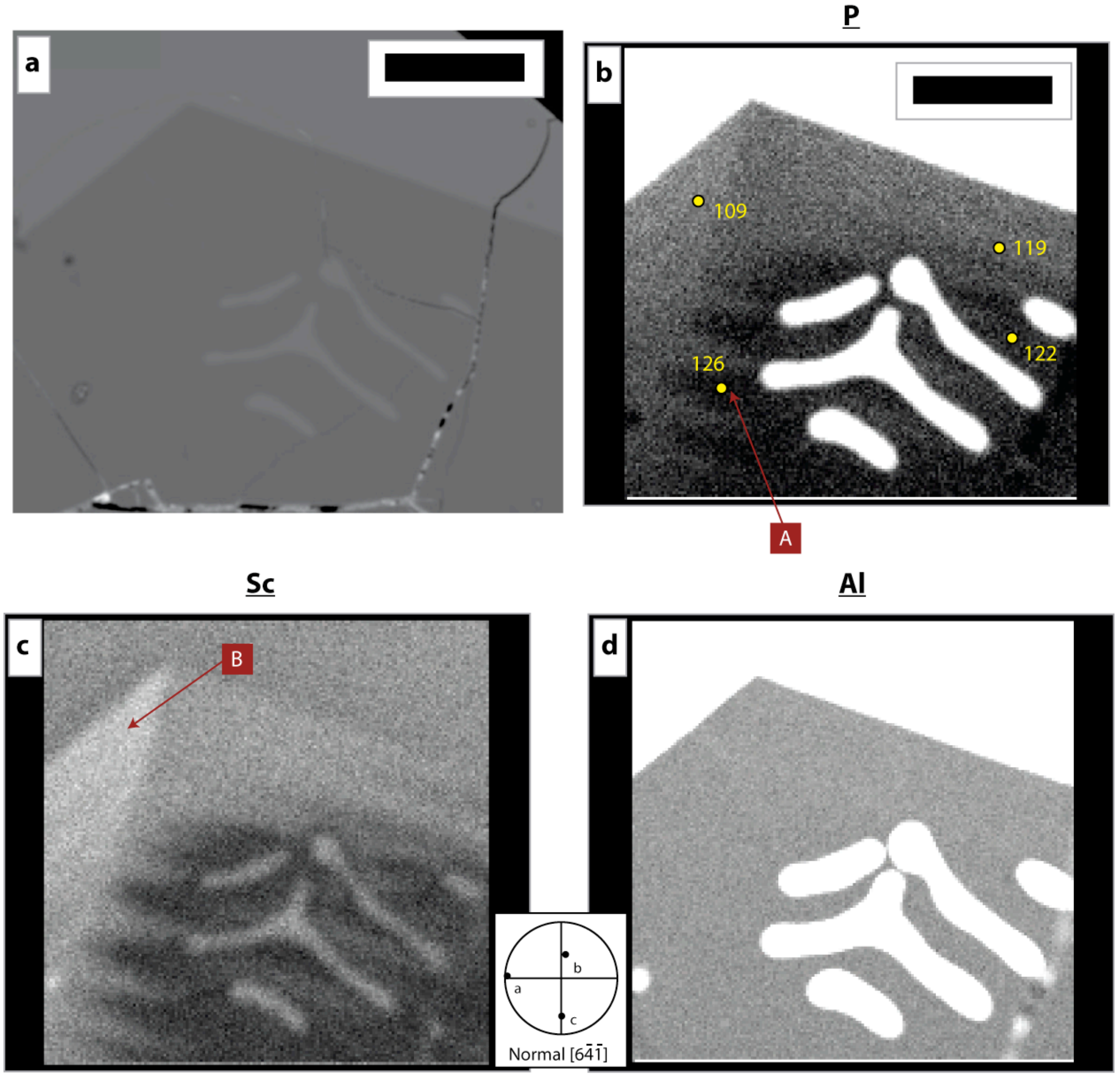

Figure 7. Backscatter electron image and phosphorus, scandium, and aluminum K_α x-ray maps of synthetic olivine K-1-3a grown during cooling rate experiment K-1-3. Scale bars are 50 μm for all panels. Other explanatory details are given in the caption for Figures 1 and 3. **a.** Backscatter FE-SEM image of the crystal. Melt pools appear as lighter gray blebs within the interior of the grain. **b.** P K_α x-ray intensity map of K-1-3a showing distinct dark "fans" (suggesting lower P content than surrounding, lighter areas) between melt pools [A]; brighter fingers appear to touch the terminus of each melt pool. **c.** Sc K_α x-ray intensity map of K-1-3a showing the same fanning observed in (**b**). A bright sector [B] appears near the left edge of the crystal; this feature is also visible in P (**a**). **d.** Al K_α x-ray intensity map of K-1-3a showing no discernable zonations within the olivine.

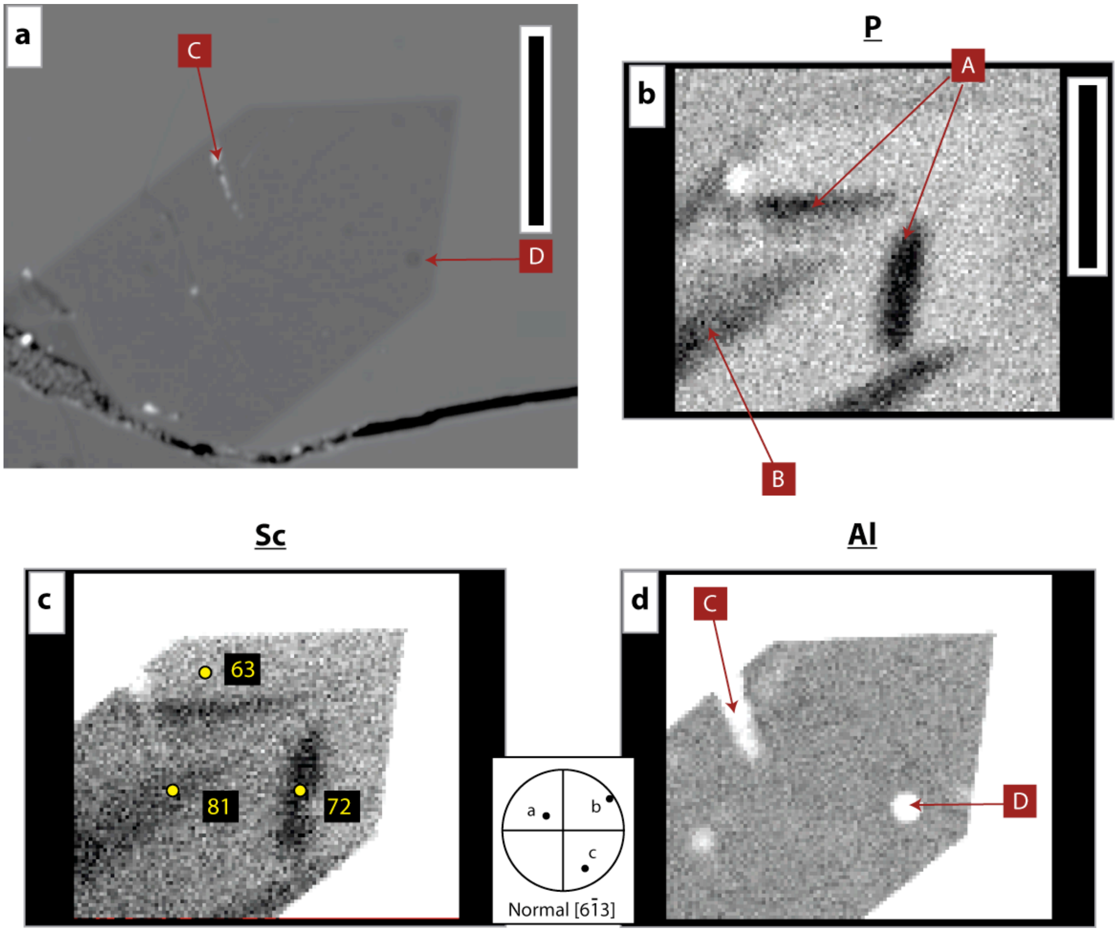

Figure 8. Backscatter electron image and phosphorus, scandium, and aluminum K_α x-ray maps of synthetic olivine K-1-3b grown during cooling rate experiment K-1-3 in the presence of a thermal gradient. Scale bars are 50 μm for all panels. Other explanatory details are given in the caption for Figure 1. **a.** Backscatter FE-SEM image of the crystal. No apparent melt pools are visible. A potential "hot spot" (either a mineral or melt inclusion?) is visible as a darker gray circle within the middle-right of the grain; this feature appears white in (**d**). **b.** P K_α x-ray intensity map of K-1-3b showing two dark sectors "pointing" toward the tip [A] and two others parallel to the long dimension of the grain (one denoted as [B]). These features are also visible in (**c**) but do not correspond to any features visible in the backscatter electron image (**a**). **c.** Sc K_α x-ray intensity map of K-1-3b showing the same features observed in (**b**). **d.** Al K_α x-ray intensity map of K-1-3b showing the presence of a crack [C] and potential mineral or melt inclusion [D] but no discernable zonations.

to nearly touch the distal extent of each melt pool (Figure 7, panels b and c, feature [A]). Of interest in both crystals is the presence of correlated Sc- and P-rich (or poor) sectors (Figure 7, feature [B] and Figure 8, features [A] and [B]) that do not appear in backscatter electron images or other elemental x-ray maps. The EBSD pattern of K-1-3a is difficult to interpret regarding elongation direction (important in distinguishing plate spinifex olivines); however, that of K-1-

3b implies elongation along the b-axis, suggesting that, despite its bladed appearance, K-1-3b is not a plate spinifex olivine.

A comparison of synthetic olivines grown in this study to those grown from Hawaiian basalt bulk compositions by Milman-Barris et al. (2008) and McCanta et al. (2008) reveals several morphological similarities despite the differences in bulk compositions. K-1-3 was quenched after cooling from 1510°C to 1320°C at a rate of 20°C/h, comparable to the cooling interval and cooling rates of experiments 1, 3, and 4 published in Milman-Barris et al. (2008). In all cases, included melt pools are surrounded by low-P olivine (see, for example, Figures 6 and 7 in Milman-Barris et al. (2008) and Figure 7 in this study). Elongated crystals were grown in all experiments, regardless of bulk composition, although the Hawaiian experiments appear more skeletal than ours. The elongated crystals in K-1-3, despite having been grown from a haplo-komatiite bulk composition, are not spinifex olivines because they were grown in the absence of a thermal gradient and therefore show no preferred orientation. Sector zones high in P and oscillatory bands displaying correlated P and Cr (or Sc, in the case of K-1-3) are observed in all of the experimental charges imaged. Unlike the Hawaiian-based synthetics of Milman-Barris et al. (2008), no zonations in Al were observed in olivines from K-1-3. Also, only two phases—olivine and glass—were identified in K-1-3; experiments on Hawaiian bulk compositions in Milman-Barris et al. (2008) resulted in the three-phase assemblage of olivine, glass, and chromian spinel. This absence of spinel in K-1-3 is likely due to the fact that Sc was substituted in place of Cr in our experiments.

3.2 Relationship of P zoning to zonations in other elements

In the Gorgona olivines, P zoning is independent of Fe/Mg zonations but, as evidenced by the x-ray maps, it is generally spatially correlated to zoning in Al and Cr. For the synthetic olivines, which were grown from a starting composition free of Fe, P zoning appeared spatially correlated to Sc only; no zonations were observed in any of the other elements. Quantitative analyses of those synthetic olivines showing P-Sc zoning (run K-1-3), there is a strong linear correlation between P and Sc (Figure 9, global correlation coefficient of 0.66) with P/Sc ~ 3. Figure 10 compares Sc-P relations for olivines in K-1-3 with Cr-P from synthetic olivines analyzed by Milman-Barris et al. (2008). Most of the Milman-Barris et al. data with above-background concentrations of P lie along a trend with P/Cr ~ 16 but a subset is consistent with a slope of 3 (i.e., the same as for K-1-3). Note that it is the higher bulk P experiments that contain olivine compositions plotting within the high P/Cr trend (1.18 wt% P_2O_5 in experiments 3 and 4 *versus* 0.40 in K-1-3 and 0.16 in experiment 1), suggesting that the substitution mechanism may in part be driven by bulk P in the melt.

Quantitative analyses of the Gorgona olivines show a distinctly linear trend in Al-Cr space for each of the three major textures: microphenocrysts, randomly oriented spinifex, and plate spinifex olivines (Figure 11). The slopes of these trends fall between 0.4 and 0.44 for all the Gorgona olivines analyzed, suggesting a potential genetic correlation for their incorporation into the olivine lattice independent of texture and, hence, mechanism of formation.

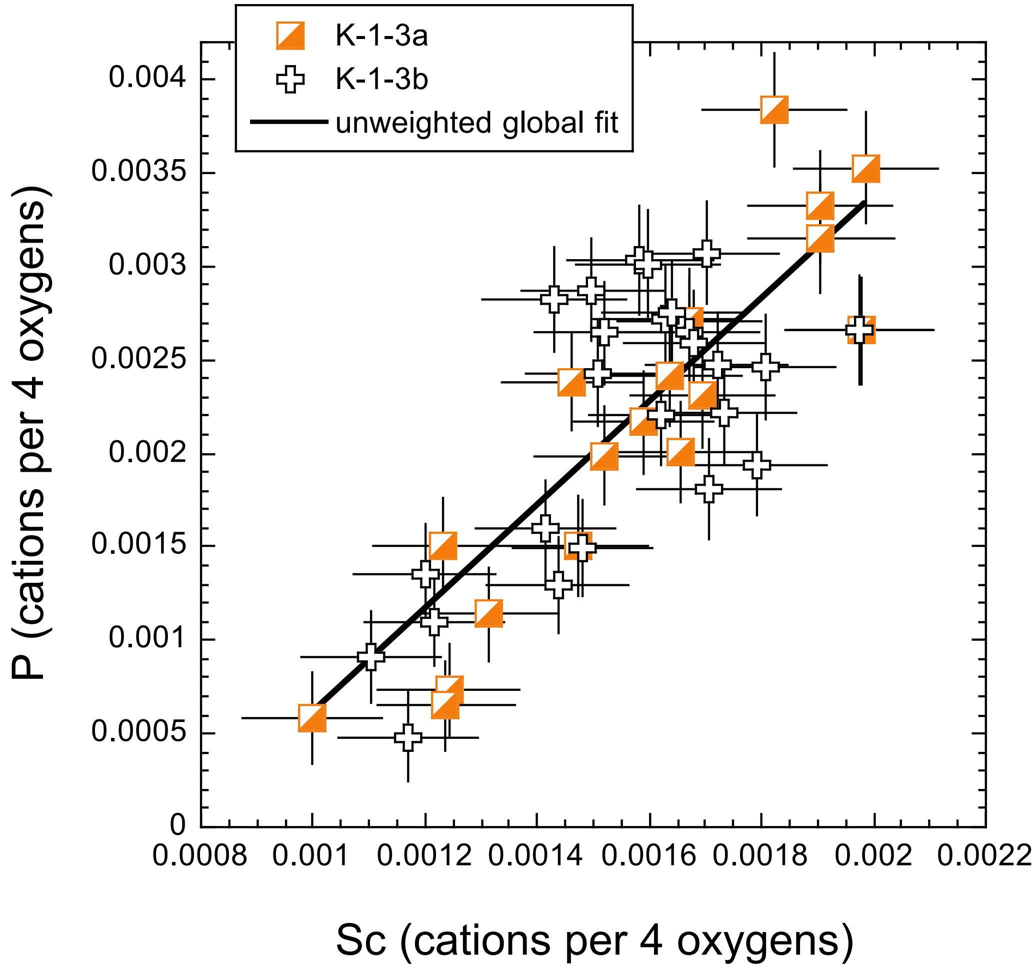

Figure 9. Relationship between Sc and P concentrations expressed as cations per four oxygens in synthetic olivines K-1-3a (half-filled squares) and K-1-3b (crosses) based on background-corrected electron microprobe analyses. Error bars are one standard deviation of the mean based on counting statistics. Best-fit line shown is an unweighted linear regression of all data corresponding to equation: $P = -0.0022 + 2.769 * Sc$ ($r^2 = 0.66$). Equations and correlation coefficients derived from unweighted linear regressions for individual grains (not shown) are: K-1-3a: $P = -0.0028 + 3.114 * Sc$ ($r^2 = 0.83$); K-1-3b: $P = -0.0015 + 2.344 * Sc$ ($r^2 = 0.47$).

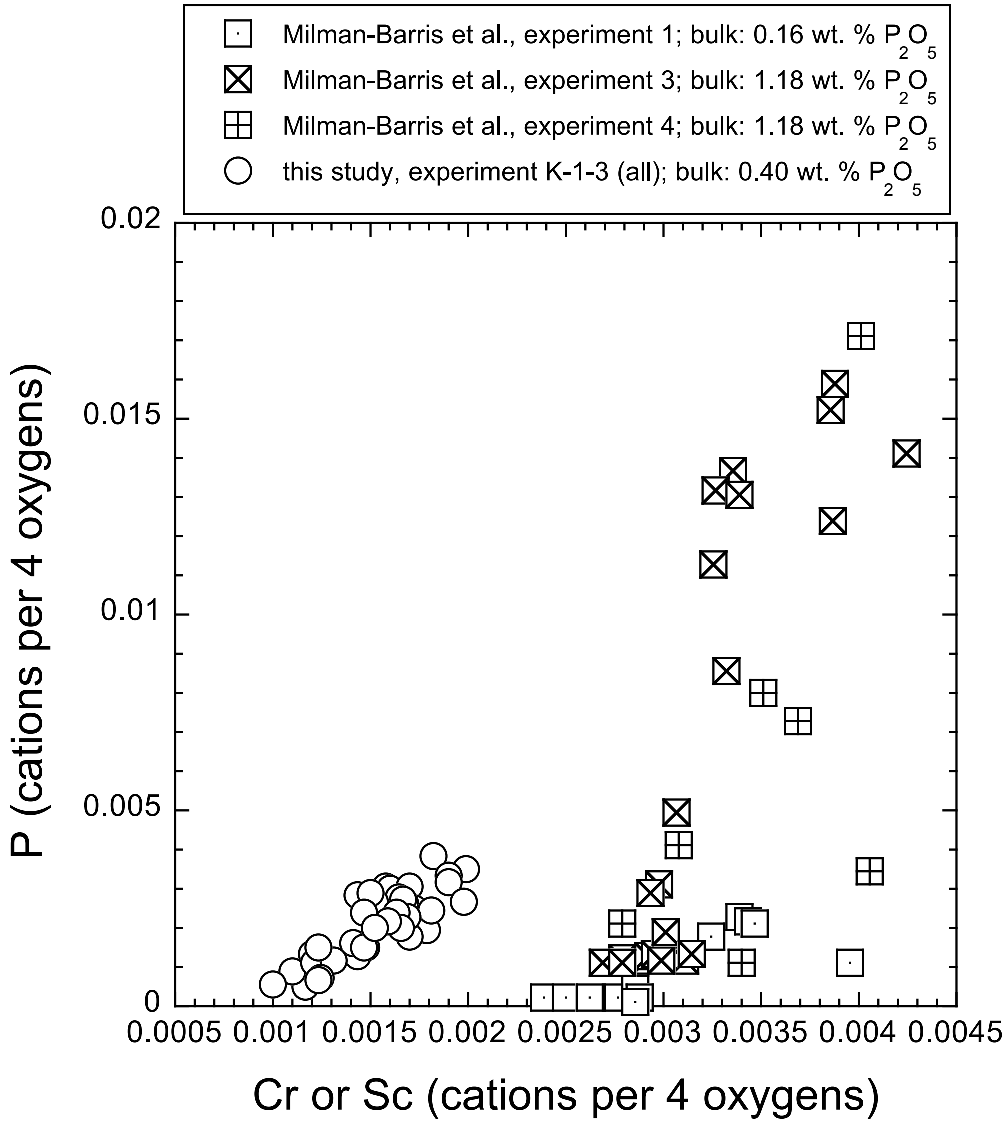

Figure 10. Comparison of experimentally synthesized olivines from Milman-Barris et al. (2008) and this study. Olivines from K-1-3 (this study; open circles) were synthesized from an Fe-free haplo-komatiite bulk composition doped with 0.40 wt. % each of P_2O_5 and Sc_2O_3 (rather than Cr_2O_3); the charge was quenched after cooling from 1510 °C to 1320 °C at 20 °C/h. Olivines from Milman-Barris et al. (2008) were synthesized from a Hawaiian basalt analog containing Cr_2O_3 and variable amounts of P_2O_5: 0.16 wt. % (open squares with central dot) and 1.18 wt. % (squares with crosses and Xs); charges were cooled from 1400 °C to ~ 1200 °C at rates of 15, 15, and 30 °C/h, respectively.

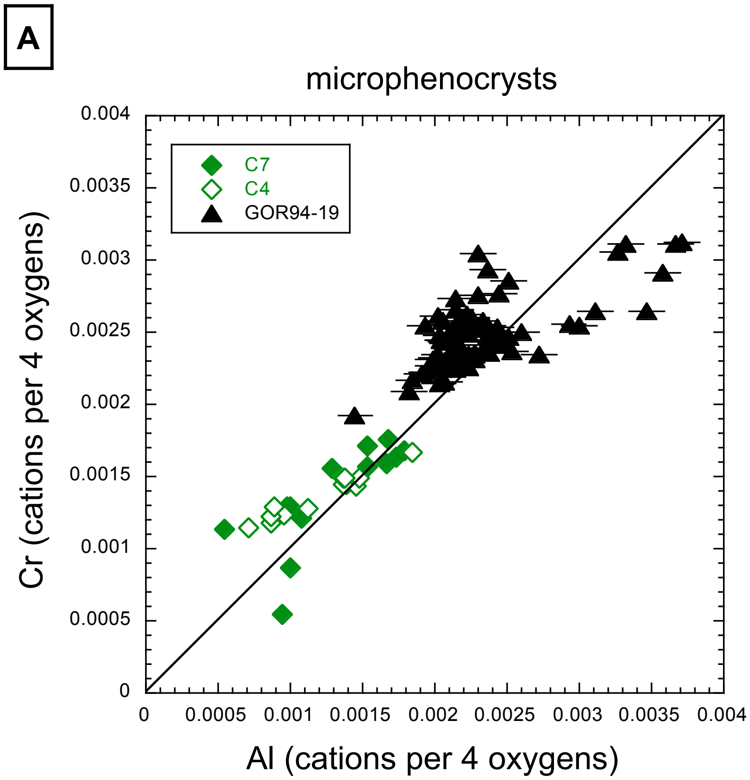
A
microphenocrysts
C7
C4
GOR94-19
Cr (cations per 4 oxygens)
Al (cations per 4 oxygens)
0
0.0005
0.001
0.0015
0.002
0.0025
0.003
0.0035
0.004

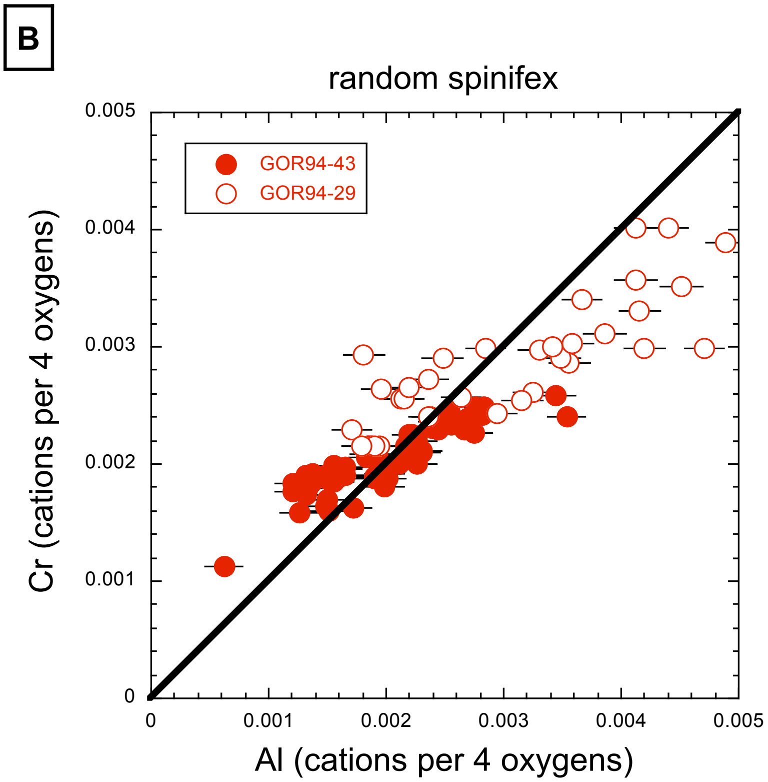
B
random spinifex
GOR94-43
GOR94-29
Cr (cations per 4 oxygens)
Al (cations per 4 oxygens)
0
0.001
0.002
0.003
0.004
0.005

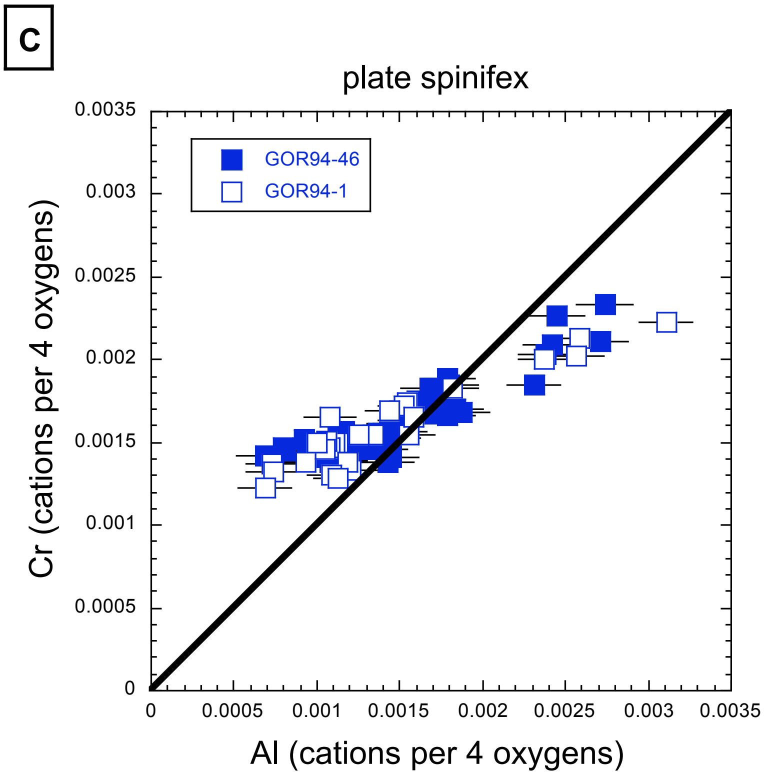

Figure 11. Relationship between Al and Cr concentrations in natural (i.e., Gorgona) komatiite olivines based on background-corrected electron microprobe analyses. Error bars are one standard deviation based on counting statistics. A 1:1 line is drawn in for comparison. **a.** Al v. Cr (cations per four oxygen atoms) in Gorgona microphenocrysts (filled triangles) from sample GOR94-19, the jointed flow top. Also shown are data from two Hawaiian microphenocrysts (C7 [filled diamonds] and C4 [open diamonds], as given in Milman-Barris et al. 2008). Equations and correlation coefficients based on unweighted linear regressions (not shown) are: GOR 94-19: $Cr = 0.0016 + 0.4002 * Al$ $(r^2 = 0.50)$; Hawaii C7: $Cr = 0.0005 + 0.6858 * Al$ $(r^2 = 0.60)$; Hawaii C4: $Cr = 0.0008 + 0.4576 * Al$ $(r^2 = 0.95)$. **b**. Al v. Cr in olivines from Gorgona random spinifex sections GOR94-43 (filled circles) and GOR94-29 (open circles). Equations and correlation coefficients based on unweighted linear regressions (not shown) are: GOR94-43: $Cr = 0.0012 + 0.4250 * Al$ $(r^2 = 0.77)$; GOR94-29: $Cr = 0.0016 + 0.4248 * Al$ $(r^2 = 0.66)$. **c**. Al v. Cr in olivines from Gorgona plate spinifex sections GOR94-46 (filled squares) and GOR 94-1 (open squares). Equations and correlation coefficients based on unweighted linear regressions (not shown) are: 94-46: $Cr = 0.001 + 0.4416 * Al$ $(r^2 = 0.83)$; 94-1: $Cr = 0.001 + 0.4096\ Al$ $(r^2 = 0.88)$.

It should be mentioned that the Gorgona microphenocryst data that plot outside the central cluster in Figure 11a appear to define two trends. Although no discernable differences exist between the analysis locations of one trend compared to those corresponding to the other, the olivine grains that contribute to these trends are all observed to contain much smaller melt inclusions that at least in backscatter electron images do *not* look like the encapsulated melt pockets along the hopper exteriors of GOR94-19 olivines. Note that data in Milman-Barris et al. (2008) for Hawaiian microphenocryst C4 has a similar slope (0.46) as does most of the data from C7 (slope of 0.51 if the two outliers in Figure 11a are excluded); however, the Cr intercepts for the bulk Hawaiian and Gorgona microphenocryst populations differ by almost a factor of two. Figures 12-13 show Al-P and Cr-P in olivine from Gorgona komatiites. The distribution for each textural type of olivine can be described as being composed of a high P/(Al or Cr) and a low P/(Al or Cr) trend that intersect at low Al (or Cr) although this is not well developed in the jointed flow top sample. Al (or Cr) at the intersection of the two trends (or minimum concentration for the jointed flow top) generally increases in the order oriented plate spinifex < random spinifex < jointed flow top. This trend can be explained in the case of Cr by whole rock Cr concentrations that increase in the same manner; however, whole rock Al_2O_3 data are similar for all three unit types (A. Kerr, personal communication) and may depend more on the modal abundances of plagioclase in these particular samples. Not every sample shows both trends (e.g., GOR94-46c versus GOR94-1) but in the aggregate, both trends are present. Hawaiian phenocryst C7 (Milman-Barris et al. 2008) may show a similar pattern but C4 appears to have sampled only a high P/(Al or Cr) trend. Microphenocryst olivines from Gorgona komatiites have significantly less P than their Hawaiian counterparts (e.g., Figures 11a, 12a, 13a and Table 3 in Milman-Barris et al. 2008), a trend consistent with the order of magnitude higher bulk P_2O_5 content of Hawaiian lavas (0.2–0.4 wt. % compared to 0.03–0.06 wt. % in Gorgona, as reported in Stolper et al. (2004) and Kerr (2005), respectively).

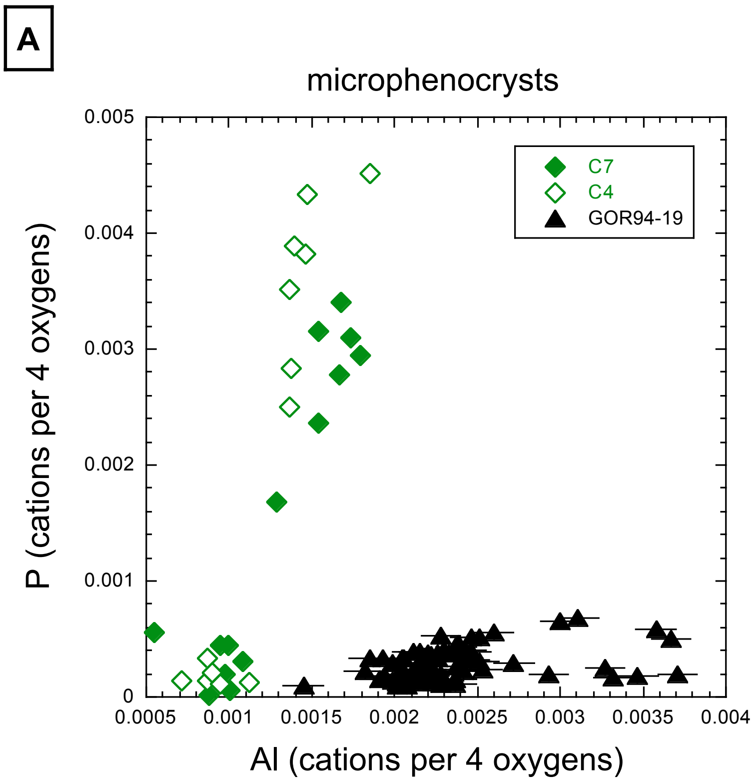
A
microphenocrysts
C7
C4
GOR94-19
P (cations per 4 oxygens)
0.005
0.004
0.003
0.002
0.001
0
0.0005
0.001
0.0015
0.002
0.0025
0.003
0.0035
0.004
Al (cations per 4 oxygens)

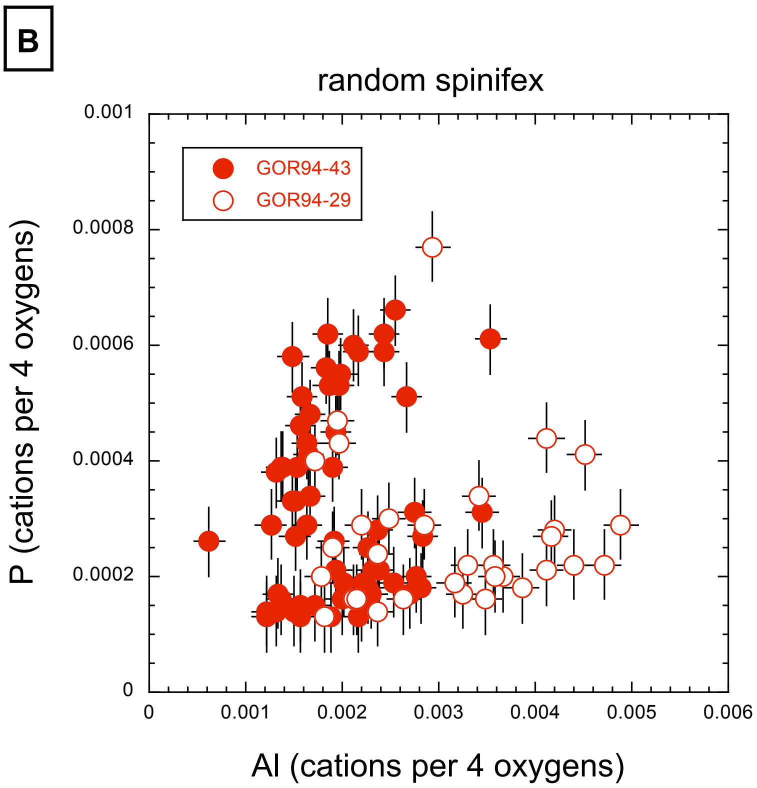
B
random spinifex
GOR94-43
GOR94-29
P (cations per 4 oxygens)
0.001
0.0008
0.0006
0.0004
0.0002
0
0
0.001
0.002
0.003
0.004
0.005
0.006
Al (cations per 4 oxygens)

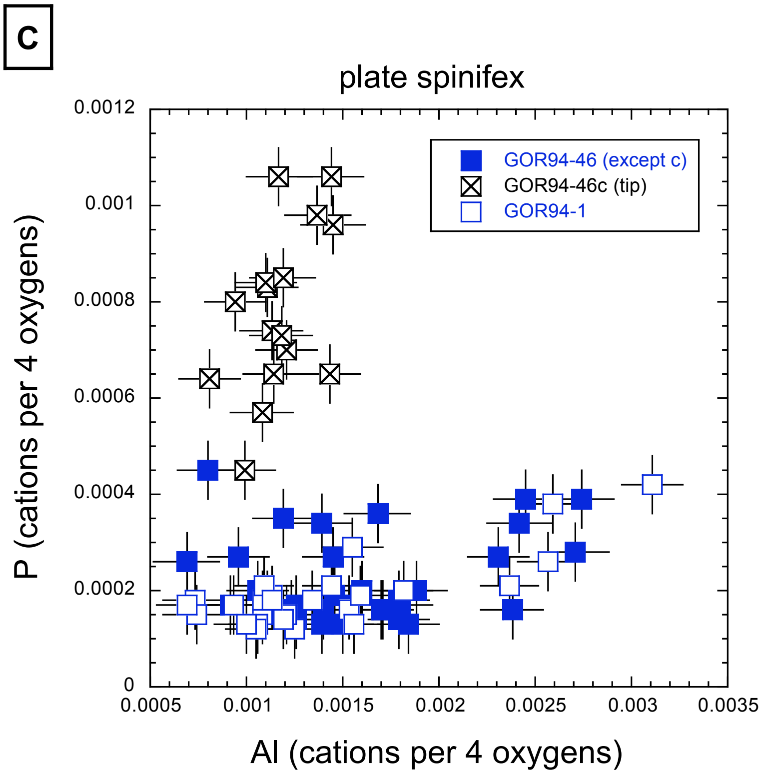

Figure 12. Relationship between Al and P (cations per four oxygen atoms) in Gorgona komatiite olivines based on background-corrected electron microprobe analyses. Error bars are one standard deviation of the mean based on counting statistics. **a.** Gorgona microphenocrysts (filled triangles) from GOR94-19, a jointed flow top sample. Also plotted are two sets of Hawaiian microphenocrysts (C7 [filled diamonds] and C4 [open diamonds], as given in Milman-Barris et al. 2008). Equations and correlation coefficients based on unweighted linear regressions (not shown) are: GOR94-19: $P = -3.302e\text{-}5 + 0.1314 * Al$ $(r^2 = 0.16)$; Hawaii C7: $P = -0.0025 + 3.173 * Al$ $(r^2 = 0.84)$; Hawaii C4: $P = -0.0043 + 5.238 * Al$ $(r^2 = 0.85)$. **b**. Al v. P in olivines from Gorgona random spinifex sections GOR94-43 (filled circles) and GOR94-29 (open circles). **c**. Al v. P in olivines from Gorgona plate spinifex sections GOR94-46 (filled squares) and GOR94-1 (open squares). Equations and correlation coefficients based on unweighted linear regressions (not shown) are: GOR94-46 (except c): $P = 0.0002 + 0.0283 * Al$ $(r^2 = 0.03)$; GOR94-46c (tip): $P = 0.0002 + 0.5097 * Al$ $(r^2 = 0.28)$; GOR94-1: $P = 6.0165e\text{-}5 + 0.0937 * Al$ $(r^2 = 0.62)$.

A

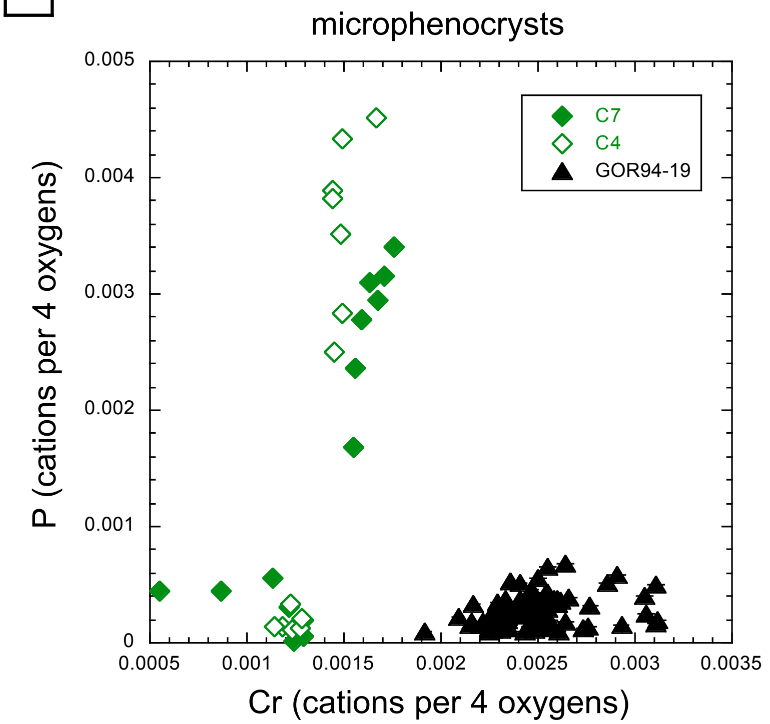
microphenocrysts

B

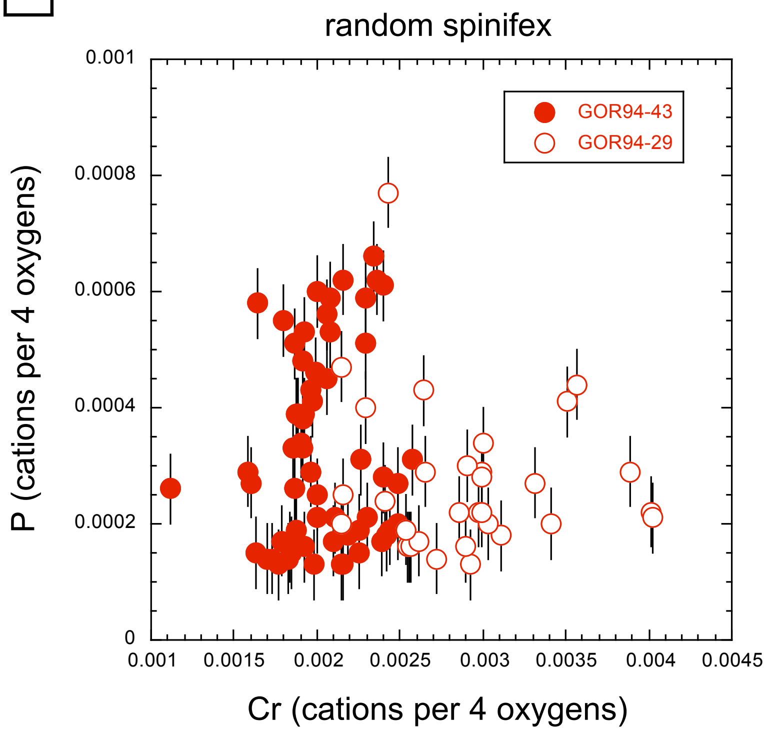
random spinifex

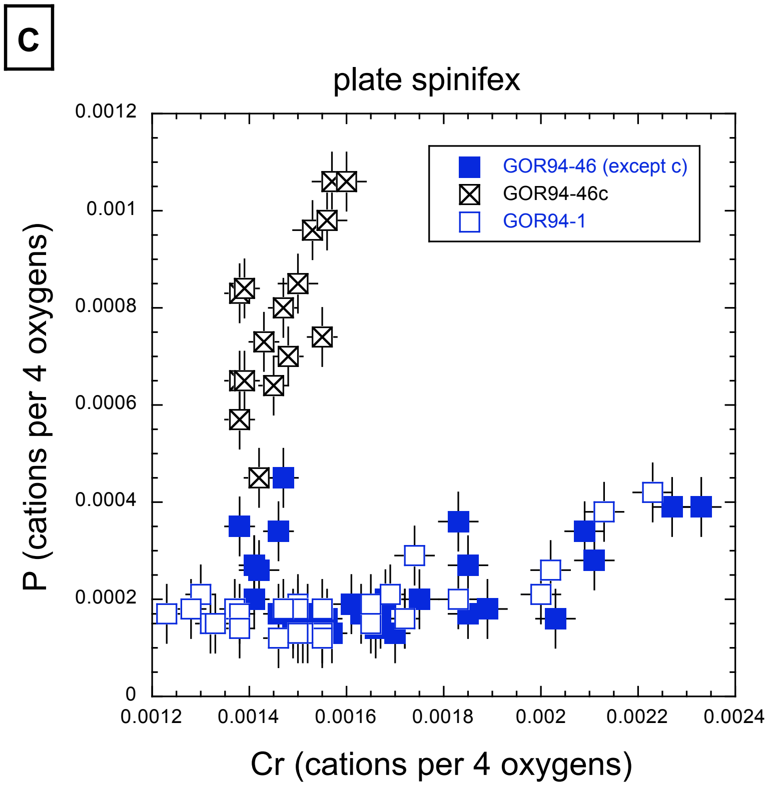

Figure 13. Relationship between Cr and P concentrations in Gorgona komatiite olivines based on background-corrected electron microprobe analyses. Error bars are one standard deviation of the mean based on counting statistics. **a.** Al v. P (cations per four oxygen atoms) in Gorgona microphenocrysts (filled triangles) from sample GOR94-19 taken from a jointed flow top. Also plotted are data for two Hawaiian microphenocrysts (C7 [filled diamonds] and C4 [open diamonds], as given in Milman-Barris et al. 2008). Equations and correlation coefficients based on unweighted linear regressions (not shown) are: GOR94-19: $P = -0.0002 + 0.1766 * Cr$ ($r^2 = 0.09$); Hawaii C7: $P = -0.0027 + 3.083 * Cr$ ($r^2 = 0.63$); Hawaii C4: $P = -0.0132 + 11.14 * Cr$ ($r^2 = 0.85$). **b.** Cr v. P in olivines from Gorgona random spinifex sections 94-43 (filled circles) and GOR94-29 (open circles). **c.** Cr v. P in olivines from Gorgona plate spinifex sections GOR94-46 (filled squares) and GOR94-1 (open squares). Equations and correlation coefficients based on unweighted linear regressions (not shown) are: GOR94-46 (except c): $P = 5.736e\text{-}5 + 0.1017 * Cr$ ($r^2 = 0.08$); GOR94-46c (tip): $P = -0.0016 + 1.65 * Cr$ ($r^2 = 0.52$); GOR94-1: $P = -0.0001 + 0.2036\ Cr$ ($r^2 = 0.56$).

4. Discussion

4.1 Review of hypotheses regarding spinifex texture formation

In their initial classifications of komatiite textures, both Viljoen and Viljoen (1969) and Nesbitt (1971) postulated that spinifex olivines were quench phenomena. In his work on Archean spinifex olivines, however, Donaldson (1974) argued against the quench hypothesis; rather, he asserted that—despite their skeletal and dendritic resemblances—spinifex textures resulted from rapid crystallization due to the high concentration of olivine components in komatiite melts and were in fact a product of slow cooling and slight undercooling below the olivine liquidus. Subsequent investigations involving the extrapolation of cooling rates and undercooling required for the formation of skeletal and dendritic olivine textures in basaltic (as opposed to ultramafic) liquids as determined experimentally by Donaldson (1976) led some authors to infer that the development of spinifex textures in komatiites resulted from extremely rapid cooling rates and correspondingly large degrees of undercooling (Arndt 2008). Kinzler and Grove (1985) performed cooling rate experiments on synthetic komatiite bulk compositions and concluded, based on phase assemblages, pyroxene compositions and that at least the pyroxenes in spinifex-bearing layers formed in response to cooling rates between 10 and 100°C/h. Further experimental work by Grove et al. (1994) and Parman et al. (1997) on water-bearing komatiite compositions led those authors to conclude that the slow cooling rates (<< 1°C/h) presumed to act in the interior of a several-meter thick, anhydrous, hot, high-MgO komatiite flow could not alone produce spinifex textures; they additionally postulated that spinifex formation required the degassing of a volatile-rich intrusive magma body at shallow depths (e.g., ~ 6 wt. % H_2O at 190 MPa; Parman et al. 1997), a process by which the melt would become supersaturated and nuclei-poor with respect to olivine. Based on crystallization experiments and heat flow calculations, both Huppert and Sparks (1984) and Turner et al. (1986) concluded that komatiites must cool by a combination of conduction and both compositional and thermal convection in order to achieve rapid cooling rates (10s–100s of °C/h) and undercooling on the order of hundreds of degrees they believed to be necessary for at least the onset of formation of spinifex olivines. They showed for simple aqueous solutions that carbonate, nitrate, and sulfate dendrites (as an analog for spinifex olivine) grew nearly vertically through the depleted melt zone forming around them and into the warmer convecting layer below; this warmer lower layer was observed to be supersaturated with respect to solute constituents, and the authors hypothesized that the temperature and compositional gradients present across the depleted solvent / supersaturated solvent interface were what enabled the dendrites to pierce through the depleted layer and access the supersaturated layer below (Turner et al. 1986).

Olivine, which is anisotropic, preferentially conducts heat fastest along [100] and [001]: 3.25 ± 0.12 and 2.60 ± 0.03 mm^2/s, respectively, for a single crystal of $Mg_{1.84}Fe_{0.16}SiO_4$ at ambient temperatures (Pertermann and Hofmeister 2006); although the absolute magnitudes of the diffusivities decrease with increasing temperature, thermal diffusivities remain highest parallel to [100] followed by [001] at least up to ~ 1100 °C (Pertermann and Hofmeister 2006). Assuming radiative cooling of a molten komatiite and calculated thermal conductivities for anisotropic olivine and komatiitic melt, Shore and Fowler (1999) proposed that plate spinifex olivine—in which the a- or c-axis is perpendicular to the cooling front—formed by growing down into (and thereby transporting heat away from) a hotter, residual melt. This type of growth would increase the thermal gradient "seen" by the propagating olivine tip and result in melt pockets depleted in olivine constituents between plates. Olivines growing in orientations other than normal to the cooling front would potentially grow more slowly due to lower gradients and slower heat transfer; ultimately, these olivines would intersect the plates and cease growth, potentially to settle out into the cumulate layer. To test the hypotheses rendered by Turner et al. (1986) and Shore and Fowler (1999)—namely, that sub-parallel spinifex-textured crystals form at low cooling rates in the presence of a thermal gradient—Faure et al. (2006) performed a series of one-atmosphere experiments on anhydrous synthetic haplo-komatiitic compositions in which they varied both the cooling rate (generally 2–10°C/h, with one at 1428°C/h) and thermal gradient (from ~ 2.5–30°C/cm) experienced by the experimental charge. Dendritic olivine plates were observed oriented perpendicular to the cooling front in those experiments cooled at rates of ~ 2–5°C/h in the presence of thermal gradients on the order of 20°C/cm (Faure et al. 2006); at faster cooling rates, the olivine morphologies were observed to be more equant and hopper-shaped, regardless of the thermal gradient; the same equant habit was observed at slow cooling rates (~ 2–5°C/h) and low thermal gradients (< 5°C/cm).

Based on all of the calculations and experiments outlined above, plate spinifex olivines in which the a- or c-axis is oriented perpendicular to the flow top (and hence to the cooling front) appear to form as a result rapid crystal growth under slow cooling rates (e.g., 1–5°C/h; Donaldson 1982; Faure et al. 2006) in the presence a thermal gradient (e.g., ~ 10–20°C/cm; Shore and Fowler 1999; Faure et al. 2006; Arndt 2008). Spinifex olivines are believed to grow rapidly due to supersaturation of the undercooled melt in olivine-normative components coupled to low nucleation rates and fast diffusivities of those components facilitated by the high eruption temperatures (~ 1400–1700°C; Arndt 2008) and ultramafic MgO contents (> 18 wt. %; Arndt 2008) of komatiite liquids (Donaldson 1976; Donaldson 1982; Arndt 1994; Shore and Fowler 1999).

4.2 The formation of P-enriched zones in komatiitic olivines

The jointed flow top microphenocrysts are similar in morphology and zonation patterns to Hawaiian microphenocrysts described by Milman-Barris et al. (2008), suggesting that both most likely grew rapidly upon eruption. In particular, most Gorgona microphenocrysts display fine-scale oscillatory zoning in P, Cr, and Al; oscillatory bands high in these elements may form by events leading to increased crystal growth rates with the resulting incorporation of slow diffusing incompatible elements that build up at the interface between a growing crystal and the surrounding melt (e.g., Tiller et al. 1953; Shore and Fowler 1996). The appearance of high- and low-P sectors is particularly pronounced in our synthetic olivines (Figures 7 and 8) as well as in Gorgona microphenocrysts from the jointed flow top (GOR94-19) and in one proposed microphenocryst from the random spinifex zone GOR94-29 (GOR94-29g, Figure 2, panels d-f). In the synthetic olivines, P and Sc appear spatially correlated within single sectors; however, in the natural olivines, P is often inversely correlated with Cr and Al within sectors (e.g., Figure 1, panels a-f), suggesting an independent substitution mechanism for P. Sector zoning in other mineral phases has been explained as being due to the different growth rates (or growth mechanisms) along different crystal faces (e.g., Nakamura 1973; Dowty 1976; Watson and Liang 1995; Watson 1996) and/or the preferential attachment of incompatible elements to incomplete "sites" (i.e., not fully coordinated) on particular crystal faces as a result of the different free energies of such sites, which are presumed to be in equilibrium with the near-field liquid (e.g., Nakamura 1973; Dowty 1976; Watson 1996).

All Gorgona microphenocrysts and both of the mapped K-1-3 synthetic olivines contain melt inclusions surrounding by low-P olivine; following Milman-Barris et al. (2008), we suggest that the low-P regions surrounding melt pools may in fact be the result of previous, slow crystallization along the walls of the melt inclusions. This hypothesis may be insufficient to explain the feathery low-P, low-Sc region that surrounds melt inclusions in one of our synthetic olivines (K-1-3a, Figure 7); in that olivine, the left terminus of each melt inclusion appears to be nearly touching a finger-like projection of high-P, high-Sc olivine. Although a fine rim of low-P, low-Sc olivine appears to separate the melt pools from these fingers, there is little to explain why the melt inclusions would crystallize in this fashion. Because these experiments were run at a single height within the one-atmosphere furnace, there is at most a very small thermal driving force other than the heat of crystallization to promote melt inclusion migration following dissolution and reprecipitation, as proposed by Schiano et al. (2006).

As noted in the introduction to this paper, a layer of randomly oriented spinifex olivines with minor microphenocrystic olivine lies below the jointed flow top. As indicated in Figures 2 and 3, it is frequently difficult to ascertain from two-dimensional morphology and minor element zonation whether an imaged grain is a microphenocryst or part of a larger (usually fragmented) spinifex olivine. The lack of EBSD patterns, particularly for grains from GOR94-29, and thin sections cut perpendicular to the direction of those presented here makes it difficult to make accurate textural identifications. The presence of one or several high-P bands parallel to the long axis of an olivine from these thin sections is at best suggestive of a spinifex texture and rests primarily on the ubiquitous presence of such bands in oriented plate spinifex olivines (Figures 4 and 5). Randomly oriented spinifex olivines were generated in the experiments by Faure et al. (2006) under large thermal gradients and fast cooling rates; at these conditions, crystal growth would be rapid. If equilibrium partitioning is at play, then incompatible element concentrations (like P) should increase at the interface between the growing crystal and the melt. When the crystal begins to grow at a rate faster than the speed at which incompatible cations like P in the liquid can diffuse away from the advancing interface, such cations will become engulfed by the growing crystal, creating a region in the crystal that is elevated in incompatible elements (i.e., "solute trapping" as described in, e.g., Reitano et al. 1994). Higher-than-equilibrium concentrations of incompatible elements at the growing crystal-liquid interface will also slow crystal growth by "blocking" the arrival of major element olivine constituents to the interface. Once the growing crystal incorporates the incompatible-enriched layer, growth rates should once again increase due to the apparent increase in available major elements. The repetition of this process may cause some of the apparent banding in both the microphenocrysts (Figure 1) and the olivines from the random spinifex zone (Figures 2 and 3); in particular, given the low concentrations of P_2O_5 and the high concentrations of MgO in these melts, we may expect to see “thinner” bands of elevated P concentrations relative to “thicker” bands low in P, which is true in some, but not all, of the imaged olivines.

Given that oriented plate spinifex textures appear to form in slow-cooling, non-convecting systems (Faure et al. 2006) and retain sub-parallel orientations to one another (and, hence, orientations normal to the flow top), it seems unlikely that P zoning in these olivines formed as a result of P_2O_5 concentrations in the melt varying over time as a function of magma mixing or olivine settling. However, as suggested by Turner et al. (1986) and Shore and Fowler (1999), the presence of a thermal gradient and the anisotropic heat transfer of the growing crystal may have induced a compositional gradient in the surrounding melt, leading to regions between olivine plates depleted in major olivine constituents. Without information regarding the thickness of the Gorgona spinifex plates (i.e., the third dimension of our thin sections), it is difficult to assess this hypothesis. Adjacent crystals (Figure 4, panels a-c) do not consistently exhibit either low-P or high-P zones along their outermost edge, nor do the bands consistently increase or decrease in thickness towards the edges. The glass surrounding natural crystals is too altered to allow comment on the near-grain-boundary minor element concentrations in a meaningful way. Despite the fact that plate spinifex olivines grow under slow cooling rates (which alone would suggest slow growth rates), the preferential conduction of heat along individual crystals’ long axes (a and/or c) promotes fast crystallization at each crystal’s leading tip. Without orientation information, it is difficult to determine how the zonations in P, Cr, and Al in the preserved tip from plate spinifex section GOR94-46 (Figure

6) can aid in understanding mechanisms of spinifex formation. Unfortunately, section GOR94-46 was damaged during preparation with colloidal silica on the vibration polisher and, as a result, an EBSD pattern cannot be obtained.

As indicated above, the thermal conductivity of olivine is similar along the a and c directions; therefore, we might expect rapid growth in both directions within the plate spinifex region of a komatiite flow. (In some komatiite flows, the a-axis is implicated as the long axis of plate spinifex olivines; however, the c-axis has also been identified as the long axis of plate olivines. In all cases, the b-axis is denoted as the plate's smallest dimension.) The presence of a 10s of microns thick low-P zone in the center of plate spinifex olivines GOR94-1a (presented in Figure 5, panels d-f of Milman-Barris et al. 2008), GOR94-1b (Figure 4, panels a-c), and GOR94-46f (Figure 5, panels d-f) contrasts with the thin, high-P central band in plate spinifex olivine GOR94-1e. It is possible that GOR94-1e is cut in a different orientation than 94-1a and GOR94-1b, both of which are elongated in the a-direction. Assuming the a-axis to be the long axis in GOR94-1b (and GOR94-1a) as suggested by the EBSD patterns, we might expect the zonations to continue in both directions out of the plane of the section; in other words, a slice through these plates parallel to the c-axis may appear relatively zone-less. Without oriented thin sections cut perpendicular to those described in this paper, we cannot say with certainty how or whether zonations in plate spinifex persist into the third dimension. The presence of alternating high- and low-P bands in the b-direction does suggest that P may be either excluded from (in the case of GOR94-1a and b and GOR94-46f) or incorporated into (as in the case of GOR94-1e) the initial crystallite, with P building up in concentration along the crystal-liquid boundary for the former case; "slow" growth in the b-direction may still be rapid enough to engulf slow-diffusing P. Ideally, experiments in which we grow plate spinifex olivines from bulk compositions including P should illuminate the growth and incorporation process, presuming that such crystals incorporate P.

The lower cumulate section of a komatiite flow is believed to form as olivines from the upper sections of the flow (including the spinifex sections) settle out; unfortunately, we do not have any cumulate olivines from Gorgona to examine, but we might expect their P_2O_5 contents (particularly between zones) to vary as a function of their changing location in the flow, provided that the crystals spend enough time in each textural region to grow analyzable overgrowths. Without sufficient residence times in the upper zones, olivines from the cumulate zone should display one prominent overgrowth from the adcumulus process. With the potential exception of cumulate komatiite olivines, the conclusion of Milman-Barris et al. (2008), namely that extrinsic processes like magma mixing and olivine settling cannot be responsible for the observed P zonations, likely applies to komatiite olivines as well.

4.3 Effect of bulk composition on zoning patterns in synthetic olivines

As indicated in Figure 10, there appear to be sub-parallel, linear trends in Cr(Sc)-P space for K-1-3 synthetic komatiite olivines and olivines of nominally Hawaiian bulk composition from the low-P (0.16 wt. % P_2O_5) experiment #1 of Milman-Barris et al. (2008). It should be noted that the experiments performed by Milman-Barris et al. (2008) were run in Fe-bearing systems at QFM, and, although most Cr should exist as Cr^{3+} under those experimental conditions in part due to electron transfer with iron, Cr may exist in both 2+ and 3+ valence states (e.g., Hanson and Jones 1998; Papike et al. 2005). In Fe-free systems at QFM—like that of experiments performed on bulk composition K-1—significant concentrations of both divalent and trivalent Cr would be expected (Hanson and Jones 1998). Mixed valency would restrict the amount of Cr^{3+} available to charge balance P^{5+} and thereby affect P-Cr cation relationships; this problem was avoided in all cooling rate experiments performed in this study by the replacement of Cr by Sc, which is completely trivalent under the experimental conditions. Experimentally determined partition coefficients (D_i, where *i* is the element of interest) between olivine and melt for Cr are quite similar over a range of oxygen fugacities and melt compositions: D_{Cr} ~ 0.5–1 (Kennedy et al. 1993; Hanson and Jones 1998). Partitioning of Sc between olivine and melt, however, appears more variable: one-atmosphere experiments by Grant and Wood (2010) indicate that Sc is moderately to strongly incompatible in Fe-free systems (average forsterite-melt partition coefficient of 0.42 ± 0.31) but previous work by Kennedy et al. (1993) indicate D_{Sc} ~ 0.5–0.8. Chromium partitioning between olivine and melt is complicated by multiple valences so that the partition coefficient varies as a function of f_{O_2} in addition to temperature and liquid composition (Hanson and Jones 1998). For neither Sc or Cr does partitioning of the given element between olivine and melt appear to be a strong function of cooling rate so long as the rate is $\leq$ 100°C/h: experimentally determined partition coefficients varied from 0.45 to 1.3 for Cr and from 0.47 to 0.84 for Sc (Kennedy et al. 1993) between isothermal and dynamic cooling experiments. Given these data, the physical similarities of our experiments to those of Milman-Barris et al. (2008), and the similar starting compositions of the two experiments with regard to Sc_2O_3 and Cr_2O_3, it is difficult to explain the linear offset in the x-direction observed in Figure 10 as a function of differences in olivine-melt partition coefficients alone. It seems more likely that the presence and concentrations of other elements in the liquid play a substantial role in determining the actual partitioning of Sc and Cr between olivine and the surrounding melt.

Colson et al. (1989) speculated that Al^{3+} enters the olivine lattice coupled to another trivalent cation such as Cr^{3+}; it would appear—on the basis of charge alone—that Sc^{3+} would also couple with Al^{3+} but its significantly larger radius (0.745 Å in octahedral coordination versus 0.615 for Cr^{3+}; all radii from Shannon 1976) may cause significant site strain in a coupled substitution with $^{vi}Al^{3+}$ (0.535 Å) on adjacent M-sites. We note that all of the olivines from K-1-3 appear featureless in Al, whereas there is a linear relationship between Sc^{3+} and P^{5+} (Figure 9); it may be that Sc and P are partially charge-compensating for one another, possibly in a substitution like $^{iv}Si^{4+} + 2\ ^{vi}Mg^{2+} = {}^{iv}P^{5+} + {}^{vi}Sc^{3+} + {}^{vi}[\ ]$—although it is unclear why this would result in a 1:3 ratio of P to Sc as observed in Figure 9—and Al-Sc substitutions are energetically unfavorable. Perhaps the combination of a lower bulk Al_2O_3 in K-1 relative to the Hawaiian basalt experiments of Milman-Barris et al. (2008) (6.58 v. 10.54 wt. %) and a strong preference for Sc^{3+} - P^{5+} coupling relative to Al^{3+}- P^{5+} leads to the absence of Al incorporation into our synthetic olivines.

4.4 Substitution mechanisms in natural komatiitic olivines

As described in the §3.2, we observe linear correlations between Al and Cr corresponding to slopes between 0.4 and 0.44 (Figure 11). This relationship suggests that in komatiitic olivines, as in olivines from other bulk compositions (e.g., Milman-Barris et al. 2008), Al and Cr enter the olivine lattice via a coupled substitution mechanism involving approximately two Al to every Cr. This mechanism has previously been suggested for forsterite as $^{iv}Si^{4+} + {}^{vi}M^{2+} = {}^{iv}Al^{3+} + {}^{vi}Cr^{3+}$ in which M is one of the divalent metal cations (Bershov et al. 1983; Maas et al. 1995). Regardless of olivine textural type (i.e., microphenocryst, random spinifex, plate spinifex), the intercepts of all best-fit lines to the Al-Cr data are positive (Figure 11), indicating that at least some of the Cr in these crystals has entered the olivine lattice independent of Al. The same two observations were also made by Milman-Barris et al. (2008) and therefore may indicate a global olivine substitution mechanism. The main difference between olivines analyzed in this study and those plotted on Al-Cr diagrams in Figures 9c and 10a in Milman-Barris et al. (2008) appears to be the magnitude of the Cr-intercept. To a zeroth order, it seems unlikely that crystal growth rate significantly affects the relative magnitude of the Cr-intercept: the intercept for plate spinifex, which appear to indeed be slow-growth textures based on experiments by Faure et al. (2006), is nearly identical to that for the jointed flow top microphenocrysts, which display crystal habits indicative of rapid growth (see the caption to Figure 11). Although Cr concentrations of the spinifex and flow top bulk rock units differ by several 100s of ppm, it seems likely that the Cr content of the liquid has a larger effect on the magnitude of the Cr-intercept. Gorgona whole rock analyses give Cr_2O_3 concentrations between 0.12 and 0.26 wt. % and Al_2O_3 concentrations between 9.75 and 12.52 wt. % (A. Kerr, personal communication), whereas the bulk starting compositions of experiments by Milman-Barris et al. (2008) contained ~ 0.22 wt. % Cr_2O_3 and ~ 10.4 wt. % Al_2O_3. The factor of two increase in the Cr-intercept (of Al-Cr plots) between Gorgona and Hawaiian olivines and the Milman-Barris et al. synthetic olivines (Figure 10a in Milman-Barris et al. 2008) cannot be explained by differences in the Cr and Al contents in the liquids and may instead be a function of a parameter inherent to the experiments (e.g., f_{O_2}).

The relationships among P, Al, and Cr are more difficult to assess in terms of substitution mechanisms based on the observed trends in P-Al and P-Cr space (Figures 12 and 13). Previous studies of P in olivine have suggested that the P^{5+} cation, which is generally believed to substitute for $^{iv}Si^{4+}$, does so via charge-balancing vacancies, either in the tetrahedral (e.g., Self and Buseck 1983; Agrell et al. 1998) or the octahedral (e.g., Boesenberg and Hewins 2010) sites. The apparent spatial correlations among P, Al, and Cr as observed in X-ray maps (Figures 1-6), albeit not in all olivines that we imaged, implies some type of coupled substitution mechanism involving all three cations. The most tenuous relationships among these elements seem to be in the flow top microphenocrysts, which display nearly horizontal trends in plots of both Al v. P (Figure 12a) and Cr v. P (Figure 13a). Crystals from this unit display both correlated P, Al, and Cr and decoupled P, Al, and Cr distributions (Figure 1). The low P concentrations in these olivines may be a result of rapid crystallization (although this hypothesis is difficult to rectify with oscillatory zoning in P unless the oscillatory zoning indicates periods of growth while in a lower-P magma source) and/or a lower P content in the liquid compared to that of the stratigraphically lower flows. Whole rock analyses of the jointed flow top do not bear out the latter line of reasoning, and the coexisting glasses have largely been altered and devitrified, rendering this hypothesis untestable.

The random spinifex olivines display the most complicated relationships between P-Cr and P-Al. As shown in Figures 12b and 13b, two apparent trends are present (one sub-horizontal and one sub-vertical), although some analyses do plot between the two trends and analyses from a single olivine crystal be found along both trends. Given these data, which are limited to olivines from only two units, it is unclear what these plots signify regarding substitution mechanisms involving P, Al, and Cr. The plate spinifex olivines also display two trends in plots of Al v. P and Cr v. P, although the majority of analyses plotting along the sub-vertical trend come from a single crystal: the preserved spinifex tip. It is possible that this trend is representative of growth entrapment of P into the olivine lattice due to rapid growth rates in the presence of a thermal gradient. We are in the process of testing this hypothesis. In the case of plate spinifex olivines, the P-intercepts for the sub-horizontal trends in both P-Al and P-Cr space are nearly zero, suggesting that all of the P is charge compensated by a substitution mechanism involving Cr and Al, which may in turn involve additional lattice defects.

5. Summary

We observed spatially correlated P-, Al-, and Cr-zoning in 36 of 40 natural komatiitic olivines imaged in this study and coupled P- and Sc-zoning in two of four olivines crystallized from a synthetic haplo-komatiitic bulk composition. In the case of the natural komatiitic olivines, zoning patterns vary based in part on the textural sub-unit of the flow (i.e., jointed flow top, random spinifex, oriented plate spinifex) from which the grain originated. Correlated P-Al-Cr zoning as well as correlated Al-Cr zoning in the absence of or decoupled from P zoning are observed in olivines from all three textural units. Microphenocrysts from the jointed flow top display oscillatory zonation patterns similar to those observed in Hawaiian microphenocrysts (Milman-Barris et al. 2008), despite the order-of-magnitude difference in bulk rock P_2O_5 concentrations between komatiites and Hawaiian tholeiites. Microphenocrysts from the random spinifex zone display more complicated zoning patterns. Spinifex olivines from both the random and the oriented plate textural units display zonations that alternate between high and low concentrations of P, Al, and Cr parallel to a crystal's long-axis. If the presence of such zonations can be replicated experimentally in oriented plate spinifex olivines, which are believed to grow rapidly along their a- and c-axes in the presence of a thermal gradient, it might further illuminate mechanisms of spinifex crystal growth and the physical parameters at play within the central zones of a komatiite flow.

All natural olivines display an ~ 2:1 relationship between Al and Cr cations, with a positive Cr-intercept, suggesting that only part of an olivine's Cr budget enters the lattice in a coupled substitution with Al. These same observations were previously made on a more petrologically diverse suite of olivines by Milman-Barris et al. (2008). We therefore suggest that the 2:1 Al to Cr substitution may represent a relatively universal zoning feature in olivines that grow from Cr- and Al-bearing melts under terrestrially relevant f_{O_2}s. Despite visual confirmation via X-ray maps of spatially correlated P, Al, and Cr in most olivines, the quantitative relationships between P and these other cations are more tenuous. Olivines from random spinifex units appear to display two trends in P-Al and P-Cr space—one sub-horizontal and one sub-vertical—that do not appear to be related to a particular crystal textural type or zoning pattern. With the exception of a preserved tip, which has high concentrations of P with respect to Al and Cr compared to other olivines from the oriented plate spinifex sections, plate spinifex olivines define a single trend in P-Al and P-Cr space. The P-intercepts are essentially zero in plots of Al v. P and Cr v. P for all spinifex olivines, suggesting that, although the trends are not in all cases well-defined, P is compensated in some way by both Al and Cr in the olivine crystal lattice.

Cooling-rate experiments performed on a synthetic haplo-komatiitic bulk composition produced bladed olivines with sector zoning in P and Sc, which was used as a proxy for Cr to avoid the complicating effects of mixed valency on zonations and substitutions. The factor of two difference between the Al_2O_3 bulk compositions of natural komatiites and our synthetics (~ 12 wt. % vs. ~ 6.5 wt. %) may explain why zoning in Al in the synthetics was not observed. Based on EBSD patterns, we conclude that these synthetic olivines, despite crystallizing from a komatiitic melt, are not spinifex, and, therefore, we recommend pursuing thermal gradient experiments in order to assess the incorporation of trace elements in spinifex olivines.

Acknowledgments

The author thanks Chi Ma for technical assistance on the FE-SEM and electron microprobe and Andrew Kerr for providing Gorgona komatiite samples. Financial support for this study was provided by the National Science Foundation and NASA grants to E.M. Stolper.

References

Aitken BG, Echeverría LM (1984) Petrology and geochemistry of komatiites and tholeiites from Gorgona Island, Colombia. Contrib Mineral Petrol 86:94-105

Armstrong JT (1988) Quantitative analysis of silicate and oxide minerals: Comparison of Monte Carlo, ZAF, and *Φ (ρz)* procedures. In: Newbury DE (ed) Microbeam analysis—1988. San Francisco Press, San Francisco, pp 239-246

Arndt N (1994) Archean komatiites. In: Condie KC (ed) Archean Crustal Evolution, Elsevier, pp 11-44

Arndt N (2008) Komatiite. Cambridge University Press, Cambridge, 467 pp

Bédard JH (2005) Partition coefficients between olivine and silicate melts. Lithos 83:394-419

Colson RO, McKay GA, Taylor LA (1989) Charge balancing of trivalent trace elements in olivine and low-Ca pyroxene: A test using experimental partitioning data. Geochim Cosmochim Acta 53:643-648

Donaldson CH (1974) Olivine crystal types in harrisitic rocks of the Rhum Pluton and in Archean spinifex rocks. Geol Soc Am Bull 85:1721-1726

Donaldson CH (1976) An experimental investigation of olivine morphology. Contrib Mineral Petrol 57:187-213

Donaldson CH (1982) Spinifex-textured komatiites: a review of textures, compositions and layering. In: Arndt NT, Nisbet EG (eds) Komatiites, George Allen & Unwin, London, pp 213-244

Dowty E (1976) Crystal structure and crystal growth: II. Sector zoning in minerals. Am Mineral 61:460-469

Echeverría LM (1980) Tertiary or Mesozoic komatiites from Gorgona Island, Colombia: Field relations and geochemistry. Contrib Mineral Petrol 73:253-266

Faure F, Arndt N, Libourel G (2006) Formation of spinifex texture in komatiites: an experimental study. J Petrol 47:1591-1610

Grant KJ, Wood BJ (2010) Experimental study of the incorporation of Li, Sc, Al and other trace elements into olivine. Geochim Cosmochim Acta 74:2412-2428

Grove TL, Gaetani GA, deWit MJ (1994) Spinifex textures in 3.49 Ga Barberton Mountain Belt komatiites: Evidence for crystallization of water-bearing, cool magmas in the Archean. Eos Transactions AGU: Spring Meeting 75:354

Hanson B, Jones JH (1998) The systematics of Cr^{3+} and Cr^{2+} partitioning between olivine and liquid in the presence of spinel. Am Mineral 83:669-684

Hastie AR, Kerr AC (2010) Mantle plume or slab window?: Physical and geochemical constraints on the origin of the Caribbean oceanic plateau. Earth-Science Reviews 98:283-293

Huppert HE, Sparks RSJ, Turner JS, Arndt N (1984) Emplacement and cooling of komatiite lavas. Nature 309:19-22

Kennedy AK, Lofgren GE, Wasserburg GJ (1993) An experimental study of trace element partitioning between olivine, orthopyroxene and melt in chondrules: equilibrium values and kinetic effects. Earth Planet Sci Lett 115:177-195

Kerr AC (2005) La Isla de Gorgona, Colombia: A petrological enigma? Lithos 84:77-101

Kerr AC, Marriner GF, Arndt NT, Tarney J, Nivia A, Saunders AD, Duncan RA (1996) The petrogenesis of Gorgona komatiites, picrites and basalts: new field, petrographic and geochemical constraints. Lithos 37:245-260

Kilinc I, Carmichael ISE, Rivers ML, Sack RO (1983) The ferrous-ferric ratio of natural silicate liquids equilibrated in air. Contrib Mineral Petrol 83:136-140

Kinzler RJ, Grove TL (1985) Crystallization and differentiation of Archean komatiite lavas from northeast Ontario: phase equilibrium and kinetic studies. Am Mineral 70:40-51

Milman-Barris MS, Beckett JR, Baker MB, Hofmann AE, Morgan Z, Crowley MR, Vielzeuf D, Stolper E (2008) Zoning of phosphorus in igneous olivine. Contrib Mineral Petrol 155:739-765

Nakamura Y (1973) Origin of sector-zoning of igneous clinopyroxene. Am Mineral 58:986-990

Nesbitt RW (1971) Skeletal crystal forms in the ultramafic rocks of the Yilgarn Block, Western Australia: Evidence for an Archaean ultramafic liquid. Geological Society of Australia Special Publication 3:331-347

Papike JJ, Karner JM, Shearer CK (2005) Comparative planetary mineralogy: Valence state partitioning of Cr, Fe, Ti, and V among crystallographic sites in olivine, pyroxene, and spinel from planetary basalts. Am Mineral 90:277-290

Parman SW, Dann JC, Grove TL, de Wit MJ (1997) Emplacement conditions of komatiite magmas from the 3.49 Ga Komati Formation, Barberton Greenstone Belt, South Africa. Earth Planet Sci Lett 150:303-323

Pertermann M, Hofmeister AM (2006) Thermal diffusivity of olivine-group minerals at high temperature. Am Mineral 91:1747-1760

Reitano R, Smith PM, Aziz MJ (1994) Solute trapping of group III, IV, and V elements in silicon by an aperiodic stepwise growth mechanism. J Appl Phys 76:1518-1529

Renner R, Nisbet EG, Cheadle MJ, Arndt NT, Bickle MJ, Cameron WE (1994) Komatiite flows from the Reliance Formation, Belingwe Belt, Zimbabwe: I. Petrography and Mineralogy. J Petrol 35:361-400

Schiano P, Provost A, Clocchiatti R, Faure F (2006) Transcrystalline melt migration and Earth's mantle. Science 314:970-974

Shannon RD (1976) Revised effective ionic radii and systematic studies of interatomic distances in halides and chalcogenides. Acta Crystallogr A 32:751-767

Sheng YJ (1992) Origin of plagioclase-olivine inclusions. Ph.D. thesis. California Institute of Technology, Pasadena, CA

Shore M, Fowler AD (1996) Oscillatory zoning in minerals: a common phenomenon. Can Mineral 34:1111-1126

Shore M, Fowler AD (1999) The origin of spinifex texture in komatiites. Nature 397:691-694

Stolper E, Sherman S, Garcia M, Baker M, Seaman C (2004) Glass in the submarine section of the HSDP2 drill core, Hilo, Hawaii. Geochem Geophy Geosy 5(7):1-67. doi: 10.1029/2003GC000553

Tiller WA, Jackson KA, Rutter JW, Chalmers B (1953) The redistribution of solute atoms during the solidification of metals. Acta Metall Mater 1:428-437

Turner JS, Huppert HE, Sparks RSJ (1986) Komatiites II: Experimental and theoretical investigations of post-emplacement cooling and crystallization. J Petrol 27:397-437

Viljoen MJ, Viljoen RP (1969) The geology and geochemistry of the lower ultramafic unit of the Onverwacht Group and a proposed new class of igneous rocks. Geological Society of South Africa Special Publication 2:55-85

Watson EB (1996) Surface enrichment and trace-element uptake during crystal growth. Geochim Cosmochim Acta 60(24):5013-5020

Watson EB, Liang Y (1995) A simple model for sector zoning in slowly grown crystals: Implications for growth rate and lattice diffusion, with emphasis on accessory minerals in crustal rocks. Am Mineral 80:1179-1187

Come, my friends,
'Tis not too late to seek a newer world.
Push off, and sitting well in order smite
The sounding furrows; for my purpose holds
To sail beyond the sunset, and the baths
Of all the western stars, until I die.

– Alfred, Lord Tennyson, "Ulysses"

Fait accompli.